Synthesis, microstructure, and deformation mechanisms of CuZr-based bulk metallic glass composites

Von der Fakultät Maschinenwesen der Technischen Universität Dresden

zur Erlangung des akademischen Grades

Doktoringenieur (Dr. -Ing.)

Vorgelegte

DISSERTATION

Von Kaikai Song

geboren am 07. 08. 1982 in Shandong, China

TECHNISCHE
UNIVERSITÄT
DRESDEN

Leibniz Institute
for Solid State and
Materials Research
Dresden

Tag der Einreichung: July 23th, 2013

Tag der Verteidigung: November 11th, 2013

1. Gutachter: Professor Dr. Jürgen Eckert

2. Gutachter: Professor Dr. Weimin Wang

Contents

Abstract

In the past, it has been found that CuZr-based BMG composites containing B2 CuZr crystals in the glassy matrix display significant plasticity with obvious work hardening. In this work, it was tried to provide a strategy for pinpointing the formation of CuZr-based BMG composites, to modify the microstructures of these composites, and to clarify their yielding and deformation mechanisms.

In order to pinpoint the formation of CuZr-based BMG composites, the phase formation and structural evolution of 11 kinds of CuZr-based alloy systems, altogether 36 different compositions, during heating and quenching processes were investigated. An endothermic event between the crystallization and melting peaks was found to be associated with a eutectoid transformation of the B2 CuZr phase. With the addition of elements to the CuZr-based alloys, this endothermic peak(s) shifts to lower or higher temperatures, implying that minor element additions can change the thermal stability of the B2 CuZr phase. By considering the thermal stability of the supercooled liquid, i.e. its resistance against crystallization, and the thermal stability of the B2 CuZr phase, a new strategy to select compositions, which form metastable CuZr-based composites consisting of an amorphous phase and B2 CuZr crystals, is proposed. It is characterized by a parameter, $\boldsymbol{K} = T_f / T_L$, where T_f and T_L are the final temperature of the eutectoid transformation during heating and the liquidus temperature of the alloy, respectively. Based on this criterion, the present CuZr-based alloys are classified into three types. For Type I alloys with lower $\boldsymbol{K}$ values, it is difficult to obtain bulk metallic glass (BMG) composites. For Type III alloys with higher $\boldsymbol{K}$ values, BMG composites with larger dimensions are prone to be fabricated, whereas only moderate-sized BMG composites can be obtained for Type II possessing intermediate $\boldsymbol{K}$ values. Accordingly, CuZr-based BMG composites containing B2 CuZr phase in the glassy matrix for different alloy systems were successfully fabricated into different dimensions.

For the sake of controlling the formation of the B2 CuZr phase in the glassy matrix and then changing the deformability of CuZr-based BMG composites, different methods were also used to fabricate these composites by: (1) introducing insoluable/high-melting particles; (2) appropriate re-melting

treatments of master alloys; and (3) a new flash heating and quenching method. It was demonstrated that the volume fraction, size and distribution of the B2 phase in the glassy matrix can be controlled as well using the methods above.

In order to clarify the excellent mechanical properties of CuZr-based BMG composites, the yielding and plastic deformation mechanisms of CuZr-based BMG composites were investigated based on SEM, XRD, and TEM observations. With the volume fraction of amorphous phase (f_{amor}) decreasing from 100 vol.% to 0 vol.%, a single-to-“double”-to-“triple”-double yielding transition was found.

For the monolithic CuZr-based BMGs and their composites with the $f_{amor} \geq 97.5 \pm 0.5$ vol.%, only one yielding at a strain of ~2% occurs, which is due to the formation of multiple shear bands in the glassy matrix, and the associative actions of the shear banding and the martensitic transformation (MT), respectively. When the f_{amor} is less than 97.5 ± 0.5 vol.%, a “yielding” occurs at a low strain of ~1%, which results from the yielding of B2 CuZr phase and the onset of the MT within B2 CuZr phase. When the f_{amor} is larger than 55 ± 3 vol.%, a “yielding” observed at strains >8% is ascribed from the operation of dislocations with a high density as well as partial de-twinning. It was also found that with the f_{amor} decreasing, the deformation mechanism gradually changes from a shear-banding dominated process, to a process being governed by the MT in the crystalline phase, resulting in different plastic strains.

Owing to the importance of the MT and the shear banding to the deformation of CuZr-based BMG composites, the details of the MT and the shear banding process were investigated.

On one hand, it was found that the MT temperatures of CuZr-based martensitic alloys have a clear relationship with the respective electronic structure and the lattice parameter of the equiatomic CuZr intermetallics. The MT temperatures of the studied alloys can be evaluated by the average concentration of valence electrons. Additional elements with larger atomic radius can affect the stacking fault energy and the electronic charge density redistribution, resulting in the difference of the electronic structures.

On the other hand, the formation and multiplication of shear bands for CuZr-based BMG composites is associated with the storage and dissipation of the partial elastic energy during the plastic deformation. When microstructural

inhomogeneities at different length scales are introduced into the glassy matrix, the elastic energy stored in the sample-machine system during the plastic deformation is redistributed, resulting in a transition of shear banding process from a chaotic behavior to a self-organized critical state.

All in all, our studies and observations provide an understanding of the formation, deformation, and microstrcutural optimization of CuZr-based BMG composites and give guidance on how to improve the ductility/toughness of BMGs.

Kurzfassung

In letzter Zeit zeigte sich, dass massive Cu-Zr-basierte metallische Glaskomposite, welche B2 CuZr-Kristallite in der amorphen Matrix enthalten, eine ausgeprägte Plastizität mit klarer Kaltverfestigung aufweisen. Im Rahmen dieser Arbeit wurde versucht, eine Strategie zur zielgenauen Einstellung der Phasenbildung und des dazugehörigen Gefüges von massiven CuZr-basierten Glas-Matrix-Kompositen bereitzustellen, sowie deren Fließ- und Verformungsmechanismen aufzuklären.

Es wurden elf verschiedene CuZr-basierte Legierungssysteme, insgesamt 36 verschiedene Zusammensetzungen, während Heiz- und Abschreckprozessen untersucht, um die Phasenbildung samt Gefüge von massiven CuZr-basierten Glas-Matrix-Kompositen zielgenau einzustellen. Bei CuZr-basierten metallischen Gläsern kann eine endotherme Reaktion zwischen Kristallisation und Schmelzvorgang der eutektoiden Umwandlung von B2 CuZr zugeordnet werden. Mit Zugabe verschiedener Elemente zur CuZr-Basislegierung kann diese Umwandlung zu höheren bzw. niedrigeren Temperaturen verschoben werden. Bereits geringe Beimischungen beeinflussen die thermische Stabilität der B2 CuZr-Phase. Unter Berücksichtigung der thermischen Stabilität, sowie des Widerstands gegen Kristallisation der unterkühlten Schmelze und der B2 CuZr-Phase wurde eine neue Strategie zur Auswahl des Zusammensetzungsgebiets metastabiler CuZr-Legierungen verschiedener Durchmesser vorgeschlagen. Dieser Widerstand kann durch den Parameter $\boldsymbol{K}=T_f/T_L$ beschrieben werden, wobei T_f die Endtemperatur der eutektoiden Umwandlung und T_L die Liquidustemperatur sind.

Basierend auf diesem Parameter können die untersuchten CuZr-basierten Legierungen in drei Klassen unterteilt werden. Für Legierungen vom Typ I mit niedrigeren ***K***-Werten, ist es schwer massive metallische Glas-Komposite (BMG-Komposite) zu erhalten. Im Gegensatz dazu lassen sich für Legierungen vom Typ III, mit höheren ***K***-Werten, BMG-Komposite mit größeren Probendurchmessern herstellen und Legierungen vom Typ II mit einem mittleren ***K***-Wert mit moderaten Probendurchmessern erzeugt werden.

Folglich wurden CuZr-basierte Glas-Matrix-Komposite verschiedener Legierungssysteme mit B2-Phase in der amorphen Matrix erfolgreich in unterschiedlichen Geometrien hergestellt.

Zur Kontrolle der Ausbildung der B2-Phase in der amorphen Matrix wurden unterschiedliche Methoden verwendet, um duktile CuZr-basierte BMG-Komposite herzustellen: (1) Einbringen von unlöslichen, hochschmelzenden Partikeln; (2) geeignete Wiederaufschmelzbehandlungen der Vorlegierungen; (3) eine neue Schnellerhitzungs- und -Abschreckmethode. Es konnte gezeigt werden, dass der Volumenanteil, sowie die Größe und Verteilung der B2-Phase in der amorphen Matrix durch die oben genannten Methoden kontrolliert werden können. Um die mechanischen Eigenschaften hinsichtlich des Fließens und der plastischen Deformationsmechanismen von CuZr-basierten BMG-Kompositen aufzuklären, wurden diese näher mittels Rasterelektronenmikroskopie, Röntgenbeugung und Durchstrahlungs-elektronenmikroskopie untersucht. Mit sinkendem Volumenanteil der amorphen Phase (f_{amor}) von 100 vol.% auf 0 vol.% kann ein Übergang von einer über zwei zu drei Fließgrenzen beobachtet werden. Für monolithische CuZr-basierte BMGs und ihre Komposite mit einem Anteil f_{amor} ≥ 97.5 ± 0.5vol.% erfolgt das Fließen ab einer Stauchung von ~2% durch Ausbildung von mehreren Scherbänden in der amorphen Matrix bzw. dem Zusammenwirken des dazugehörigen Scherens und der Martensitumwandlung. Bei einem Anteil f_{amor} unter 97.5 ± 0.5 vol.% findet ein Fließen bei niedrigerer Stauchung von ~1% statt. Dies geschieht aufgrund des Fließens und der beginnenden martensitischen Umwandlungen der B2 CuZr-Phase. Bei einem Anteil f_{amor} größer als 55 ± 3 vol.% kann ein Fließen oberhalb einer Stauchung von 8% durch die Interaktion von Versetzungen bei hoher Versetzungsdichte sowie partiellem „Entzwillingen“, beobachtet werden. Es wurde herausgefunden, dass mit sinkendem f_{amor} der Verformungsmechanismus schrittweise von einem Scherband dominierten zu einem von der martensitischen Umwandlung dominierten Mechanismus übergeht. Dieser Übergang führt zu Unterschieden in der plastischen Verformung.

Da für das Verformungsverhalten von CuZr-basierten BMG-Kompositen die deformationsinduzierte martensitische Umwandlung und die Entstehung sowie

Ausbreitung von Scherbändern von herausragender Bedeutung sind, wurden sie näher untersucht.

Einerseits wurde herausgefunden, dass die Umwandlungstemperatur der martensitischen Umwandlung von CuZr-basierten martensitischen Legierungen in klarer Beziehung zur entsprechenden Elektronenstruktur und der Gitterkonstanten der äquiatomaren intermetallischen CuZr-Phasen stehen. Die martensitischen Umwandlungstemperaturen der untersuchten Legierungen können über die mittlere Valenzelektronenkonzentration ausgewertet werden. Zusätzliche Elemente mit größerem Atomradius können die Stapelfehlerenergie und die Ladungsdichteverteilung ändern, was in unterschiedliche Elektronenstrukturen mündet.

Andererseits ist die Entstehung und Vervielfachung von Scherbändern in CuZr-basierten BMG-Kompositen verbunden mit der Speicherung und Dissipation der partiellen elastischen Energie während der plastischen Verformung.

Durch das Einbringen von Gefügeinhomogenitäten unterschiedlicher Größe in die Glasmatrix, wird die elastische Energie, die im System Probe-Maschine gespeichert ist, während der plastischen Deformation umverteilt. Dies führt zu einem Übergang des Schervorgangs von chaotischem Verhalten zu einem selbstorganisierten kritischen Zustand.

Insgesamt stellen unsere Untersuchungen und Beobachtungen ein Verständnis der Ausbildung, Verfomung und Gefügeoptimierung von CuZr-basierten BMG-Kompositen bereit und sollen als Leitfaden zur Verbesserung der Duktilität bzw. Zähigkeit von BMGs dienen.

1 Theoretical background

1.1 Development of metallic glasses

A glass in general is a non-crystalline solid material that lacks the long-range order characteristic of a crystal [1, 2] and which still is one of the most important materials for applications ranging from arts to optoelectronics (Fig. 1.1a). The most familiar type of glass is soda-lime glass, which is usually used for windows and drinking vessels for instance [2].

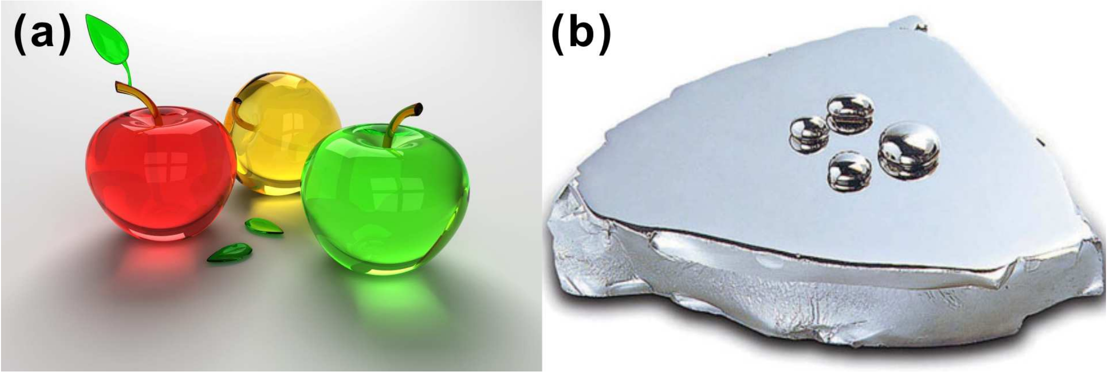

Figure 1.1 *Pictures of (a) the traditional soda-lime glass and (b) MGs. Taken from Refs. [3, 4].*

Only recently, metallic glasses (MGs) (Fig. 1.1b) have been fabricated to join the group of amorphous materials [5-11]. This relatively young class of MGs has been first reported by Klement *et al.* at Caltech in 1960 using a rapid quenching technique for cooling metallic melts at very high rates of 10^5 - 10^6 K/s [12]. During quenching, the nucleation and growth of crystalline phases are suppressed so that the structural configuration of the melt is frozen-in [5, 6, 13, 14].

Since then, remarkable progresses have been made in exploring new alloy compositions being able to vitrify easily [7], which indicates the fundamental scientific importance and the potential engineering applications of MGs [15-17]. During the period from the 1960s to the early 1970s, only MG ribbons, wires, and sheets [18] were developed due to the limited glass-forming ability (GFA) of the MGs and the limited cooling rate of the processing devices. A breakthrough was first achieved by Chen in 1974 relevant to the synthesis of bulk metallic glasses (BMGs) (≥ 1mm) [19]. Through a simple suction casting method, a new Pd-Cu-Si

MG was cast into rods with a diameter of 1 mm under a cooling rate as low as 10^3 K/s [19]. Afterwards, Turnbull, Drehman, Kui, Greer and other collaborators [20, 21] started to focus on Pd-based BMGs by quenching Pd-Ni-P melts covered with a boron oxide fluxing medium in a quartz crucible to purify the melts. As a result, the heterogeneous nucleation was suppressed, and a centimeter-sized MG was fabricated at cooling rates in the 10 K/s region [20, 21]. However, such kinds of BMGs contain too much high-priced noble metals so that it is necessary to develop other BMGs for the possible applications.

Since the late 1980s, Inoue and his co-workers have succeeded in developing new multicomponent alloy systems with the relatively high GFA in Mg-, Ln-, Zr- , Fe- , PdCu-, PdFe-, Ti- and Ni-based alloy systems using suction casting into water-cooled copper molds [22-30]. Especially in 1993, one alloy extensively studied to date, i.e. $Zr_{41.2}Ti_{13.8}Cu_{12.5}Ni_{10}Be_{22.5}$, has been found, which exhibits an excellent GFA [31] and can be made into bulk rods ranging up to 14 mm in diameter. Since the year 2000, significant progress has been also achieved in Cu-, Fe-, Ti-, Rare earth metal- Mg-, and Ca-based BMGs and the critical diameter for fully glass formation (D_c) has been improved over to 20 mm in given alloy systems [32-38]. Recently, the D_c of some Pd- and Zr-based BMGs has been found to be larger than 70 mm in diameter [39, 40].

So far, MGs with different dimensions and compositions have been developed using the microalloying method or introducing different fabrication methods [41-55]. The preparation methods mainly consist of the rapid solidification and the solid-state amorphization [41-55]. The former includes the melt spinning, the gas atomization, the suction casting, the centrifugal casting, and the injection casting, which involves a high velocity of the solidification front and cooling rates from 10 K/s to 10^9 K/s [52, 55]. As a result, the atomic mobility within the melt is rather limited and thus a disordered structure can be obtained.

On the other hand, a crystalline solid can transform into an amorphous state by introducing chemical and/or structural disorder, which is known as solid-state amorphization [51-55], such as the mechanical alloying and the mechanical milling. It has been shown that the fabrication of MGs relies on many internal factors such as purities and atomic size of the constituent elements and external factors such as cooling rate [56].

1.2 Formation of metallic glasses

Upon quenching of a melt [12], the supercooled liquid and crystalline phases compete with each other [57-59]. During this process, the change of volume or enthalpy with respect to temperature for the liquid decreases abruptly but continuously to a value comparable to that of a crystalline solid upon cooling, resulting in a strong viscosity increase (Fig. 1.2) [57-59]. Therefore, the mobility of the atoms in the supercooled liquid is not high enough to arrange them into a periodic lattice so that the melt cannot transform into a crystalline state which is a thermodynamically stable state during quenching. In such a case, from the thermodynamic point of view, the glass transition is only a necessary condition. If the glass transition did not occur at Kauzmann temperature, the volume, the enthalpy, and the configurational entropy of the amorphous state are expected to be lower than those of the more stable crystalline solid, which is impossible [14].

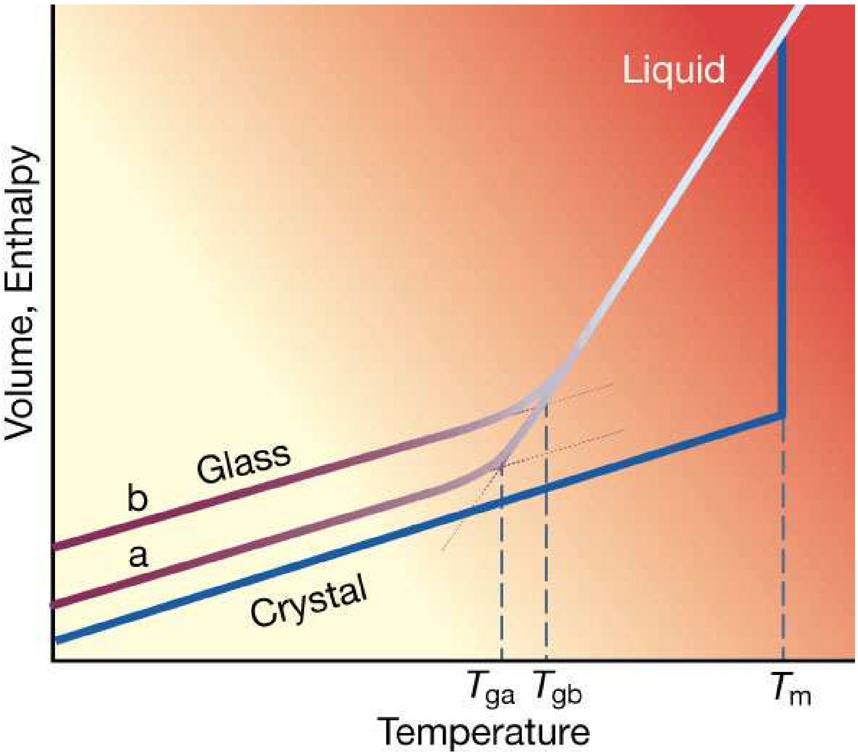

Figure 1.2 *Changes of volume and enthalpy as a function of temperature and cooling rate. Here,* T_m *is the liquidus temperature. With the cooling rate increasing from a to b, the glass transition temperature increases from* T_{ga} *to* T_{gb}*. Taken from Ref. [60].*

As shown in Fig. 1.2, the glass transition temperature (T_g) is defined as the intersection of the extrapolated liquid and vitreous portions of the volume *vs.* temperature curve [60]. As the cooling rate decreases, T_g shifts to a lower value

[60] (Fig. 1.2). When the applied cooling rate further decreases, the liquid can not be vitrified into an amorphous state, and then be transformed into a crystalline state. Therefore, the critical cooling rate for fully glass formation (R_c) respects the GFA of the present MGs [61]. However, it is difficult to accurately measure the real R_c during quenching process. Therefore, the critical casting thickness, D_c, is often used to evaluate the R_c of MGs [61, 62]. Furthermore, other methods to predict or evaluate the GFA have also been proposed based on the intrinsic factors of the alloys (i.e. constituent elements) [7, 56].

For example, three empirical rules [7] derived from extensive experimental results have been proposed to explain the glass formation of metallic alloys: (1) Glass-forming alloy systems generally contain more than three elements; (2) There is a significant difference in atomic size ratios of more than 12% among the three main constituents; and (3) There is a negative heats of mixing among the three main constituents. Any metallic liquid, which satisfies the three empirical rules, is expected to have a denser randomly-packed atomic configuration [5, 7, 15, 57, 58, 61, 63, 64], new local atomic configurations and more homogeneous atomic configurations compared with those of the crystalline counterpart. Such kind of structure features can effectively suppress the crystallization of the supercooled liquid, i.e. slow down the nucleation and growth of the crystalline phase(s), which is equivalent to the GFA of the glass-forming alloys [8]. Therefore, the competition between the liquid phase and crystalline phases plays an important role in the formation of MGs [7, 8, 65], and consequently the suppression of crystallization requires also to be considered. If a steady-state nucleation is assumed, the nucleation rate is determined by the product of the thermodynamic and kinetic factors as follows [8, 66, 67]:

$$I = N_v^0 v D \exp\left(-\frac{\Delta G^*}{kT} \right), \tag{1.1}$$

where $N_v{}^0$ is the monatomic number per volume, v is the frequency rate, and k is the Boltzman's constant, D is the effective diffusion coefficient, and T is the absolute temperature, respectively. At high temperatures, the diffusivity D is proportional to the inverse of the viscosity [8, 66, 67], i.e. $v = kT / 3\pi a_0^3 \eta$. a_0 is the average atomic or ionic diameters and the η is the viscosity. The activation barrier for nucleation, ΔG^*, is given as $\Delta G^* = 16\pi\sigma^3/\Delta G^2$ [8], where σ is the interfacial energy between liquid and solid, and ΔG is the driving force for crystallization. Therefore, the glass formation is governed by the thermodynamic (i.e. the driving force for crystallization) and kinetic (i.e. the viscosity and diffusion) factors as well as the structural contributions (i.e. the configurations).

1.2.1 Thermodynamic considerations

The crystallization temperature of MGs is heating rate dependent (Fig. 1.2) because the nucleation is a thermally activated process [68]. When the driving force for crystallization in the supercooled liquid is low enough, MGs can form during quenching because the low driving force results in a low nucleation rate and a growth rate, and then suppresses the crystallization [69]. The driving force for crystallization (ΔG) is approximated by the Gibbs free energy difference $\Delta G_{l\text{-}s}$ between the supercooled liquid and the crystals, which is given by the heat of fusion and of the difference in the specific heat capacity $\Delta C_p(T)$ between the supercooled liquid and crystals [70-73]:

$$\Delta G_{l-s}(T) = \Delta H_f - \Delta S_f T_0 - \int_T^{T_0} \Delta C_p^{l\text{-}s}(T)dT + \int_T^{T_0} \frac{\Delta C_p^{l\text{-}s}}{T} dT \,, \tag{1.2}$$

where T_0 is the temperature at which the crystals and the liquid are in equilibrium, ΔH_f and ΔS_f are the enthalpy and entropy of fusion at the temperature T_0, respectively. Busch *et al.* [70-73] have investigated the thermodynamic functions of different glass-forming liquids as a function of temperature [74]. The thermodynamic functions of different MGs were determined by measuring ΔS_f as well as the $\Delta C_p(T)$. As shown in Fig. 1.3, the $\Delta G_{l\text{-}s}$ values of a selection of other eutectic, or close-to-eutectic glass-forming systems are compared. The alloys show different R_c between 1 K/s for the Vit 1 MG and about 10^4 K/s for the binary $Zr_{62}Ni_{38}$ MG [70-73]. Most of the glass formers with a lower R_c usually possess a smaller Gibbs free enthalpy difference with respect to the crystalline counterparts than the glass formers with a smaller GFA, which originates mainly from the small entropy of fusion, the relatively large configurational entropy of mixing, the small free volume, and the significant short-range ordering at the melting point (T_L) [8, 70, 71, 74].

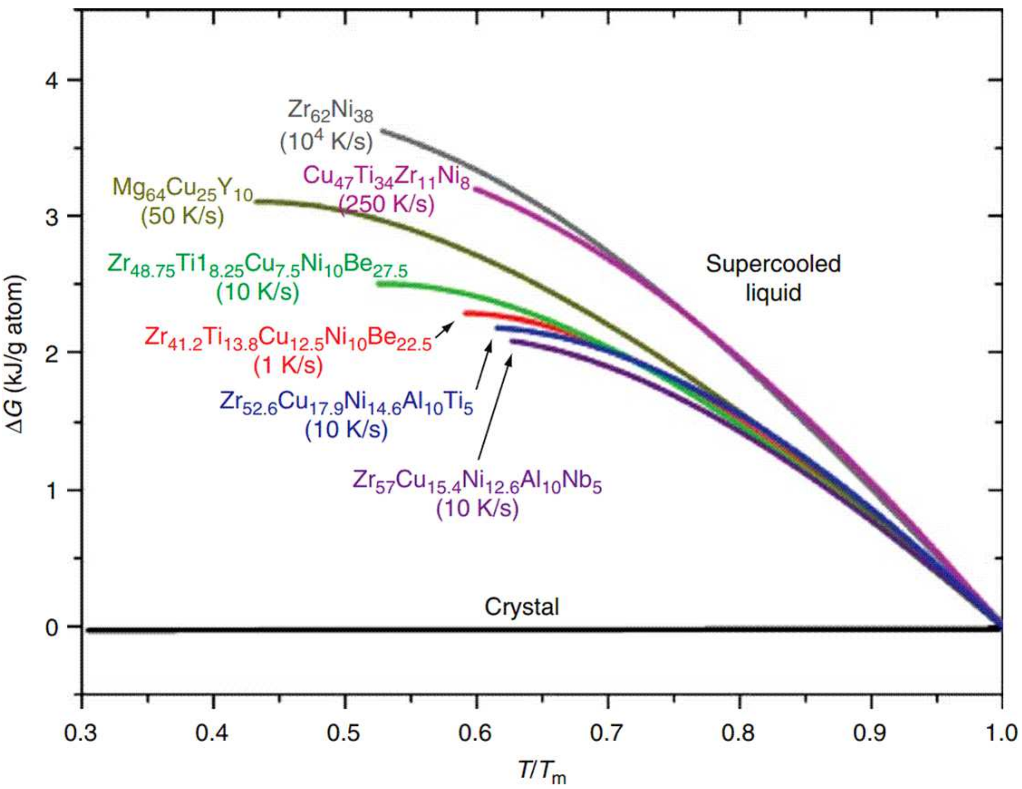

Figure 1.3 *Difference in Gibbs free energy between the liquid and the crystalline state for glass-forming liquids. Taken from Ref. [74].*

From thermodynamic considerations, some parameters were derived to evaluate the GFA of MGs, such as $T_{rg} = T_g/T_L$, $\Delta T_x = (T_x - T_g)$, $\gamma = T_x/(T_L + T_g)$ [7, 61, 62, 75, 76]. The value of T_x indicates the onset temperature of crystallization for MGs during heating. When a metallic melt is cooled down to T_g, the viscosity of the melt increases to a value of about 10^{12} Pa·s, resulting in the formation of a MG [75, 76]. In view of this, a higher T_g and a lower T_L for the glass-forming liquids are favorable for the formation of the glassy phase. Turnbull [57] was the first to apply this idea to evaluate the GFA and proposed a parameter, i.e. $T_{rg} = T_g/T_L$. When the value of T_{rg} is larger than 2/3, the nucleation rate becomes low and then the homogeneous crystal nucleation is suppressed, which supports the vitrification of a liquid (Fig. 1.4a). However, this criterion only considers the condition under which glass is formed without accounting for the thermal stability of MGs. Therefore, the concept of the supercooled liquid region (ΔT_x), which is the difference between the T_x and T_g, was suggested to evaluate the thermal stability of MGs [7]. On this basis, ΔT_x also can be used to evaluate the GFA of MGs to some extent. However, both of these parameters show significant discrepancies in some alloy systems [62]. By considering the stability of the liquid phase and the resistance to the crystallization, Lu and Liu [61, 62] suggested a new parameter ($\gamma = T_x/(T_L + T_g)$), which is now widely used for the assessment of GFA. As shown in Fig. 1.4b [61], a linear relationship is observed between γ values and R_c, which is confirmed by the statistical correlation parameter, $R^2 = 0.9$.

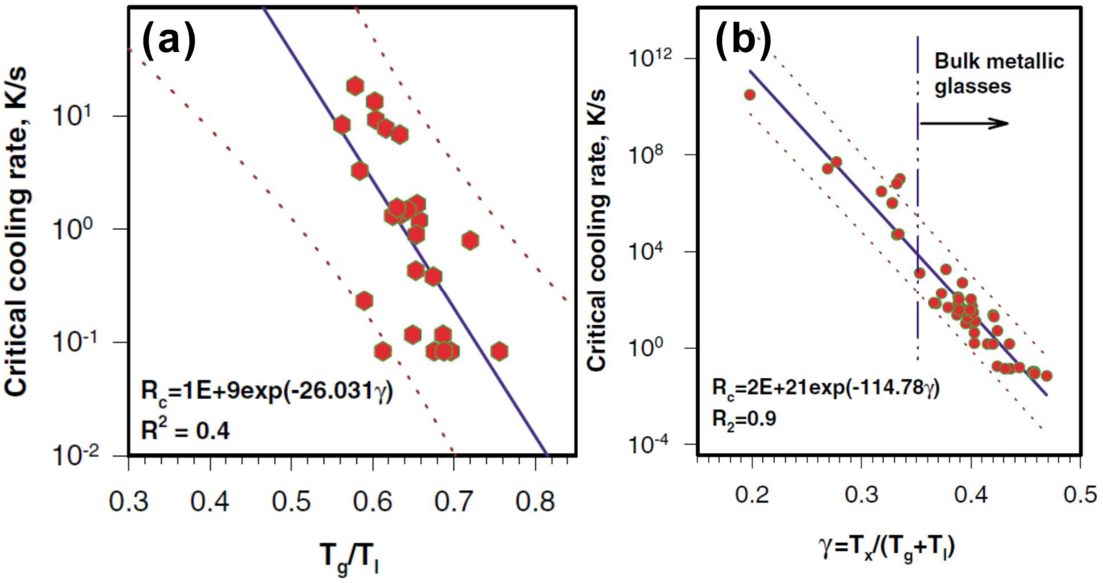

Figure 1.4 The correlation between the R_c, (a) the T_g/T_L parameter, and (b) the γ parameter for MGs. Redrawn from Refs. [61, 62].

1.2.2 Kinetic considerations

From the perspective of kinetics, a key issue is to understand the large and continuous increase in viscosity of the supercooled liquid as the melt is cooled to the T_g [77, 78]. Different techniques have been used to measure the viscosity from the equilibrium liquid down to the deeply supercooled liquid near T_g [70, 71, 74, 77, 79] or the viscosity of the melt above T_L [80-83]. The behavior of the viscosity can be characterized by the concept of liquid fragility, i.e. the fragility of supercooled liquids (m) at temperatures just below T_g [60, 74, 84-88], and the fragility of superheated melts (M) at high temperatures near T_L, respectively [80-83]. It is believed that the fragility strength has a correlation with the GFA of MGs because the liquid fragility manifests the characteristic of the structural evolution during the cooling process [81, 89].

Fig. 1.5 shows a "fragility plot" in the form proposed by Angell [13, 86]. It can be seen that for kinetically "strong" glass-forming liquids (e.g. SiO_2), the viscosity data *vs.* the temperature scaled by T_g can be described by an Arrhenius relation [13, 86], while the kinetically "fragile" liquids exhibit a non-Arrhenius behavior, which is fitted well by the Vogel-Fulcher-Tammann (VFT) relation [13, 86]:

$$\eta = \eta_0 \exp\left[\frac{DT_0}{(T-T_g)}\right], \tag{1.3}$$

where T_0 is the VFT temperature, D is the strength parameter connected with the property of a liquid, and η is the viscosity. The equation of m is described as:

$$m = \left.\frac{d\log\eta}{d(T_g/T)}\right|_{T=T_g}. \tag{1.4}$$

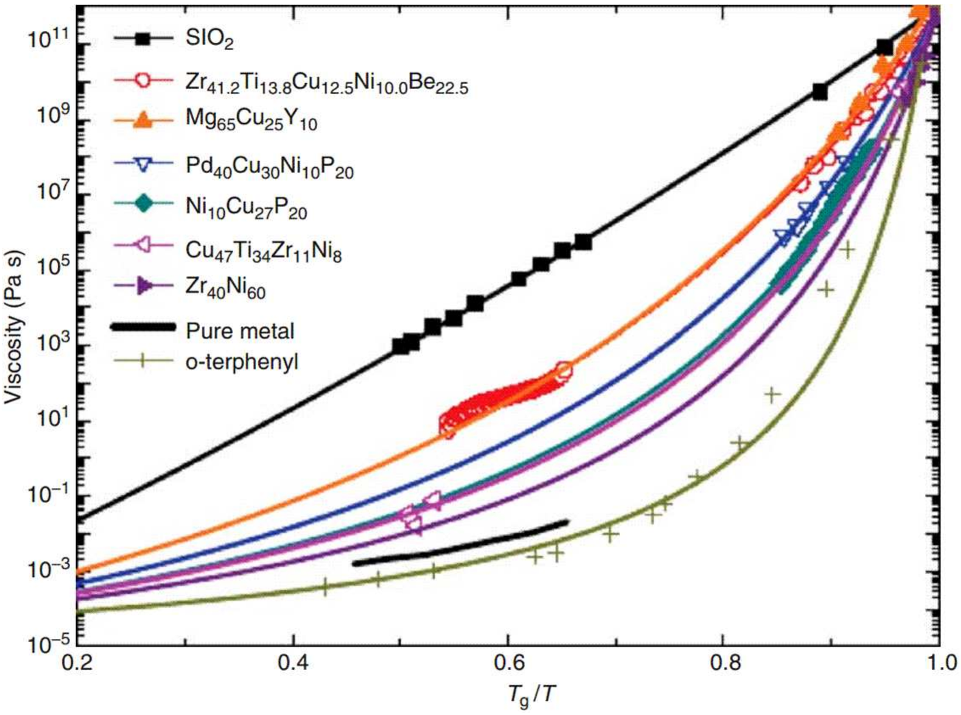

Figure 1.5 *Angell plot over the entire temperature range. All the temperatures were scaled by T_g for the alloys. Taken from Ref. [74].*

Consequently, the value of m is obtained. When the value of m becomes larger, the supercooled liquid becomes more fragile, and the GFA becomes worse for most of MGs [89, 90]. Fig. 1.5 shows the viscosities of some metallic glass-forming liquids together with some typical nonmetallic liquids. SiO_2 is the strongest glass former with a smallest m (i.e. 17.9) of the depicted systems [91]. On the contrary, the viscosity data available for BMG forming liquids indicates that MGs such as $Zr_{41.2}Ti_{13.8}Ni_{10}Cu_{12.5}Be_{22.5}$ are closer to strong glasses than fragile glasses [13, 74, 77].

However, even though many families of BMGs which possess a relatively extensive experimental temperature and time window to measure the viscosity of supercooled liquids have been explored, it is difficult to fabricate bulk samples for marginal glass formers using the conventional suction casting [80]. Yet, bulk amorphous samples are required to accurately measure the viscosity of the supercooled liquids using a thermal mechanical analyzer or the three-point beam bending devices and so on [92, 93]. Hence, there is few available viscosity data for the supercooled liquids of marginal MGs. Recently, Bian *et al.* have proposed a parameter [79-83], i.e. the fragility of superheated melts (M), based on the viscosity data of marginal metallic melts above T_L. In a wide temperature range above T_L, the viscosity of the superheated melts generally obeys the Arrhenius relation [81, 94]:

$$\eta = \eta_0 \exp\left(\frac{E}{RT}\right), \tag{1.5}$$

where η_0 is a pre-exponential constant, which is associated with the nature of the liquid, E is the activation energy for viscous flow, and R is the molar gas constant. According to their analysis, T_L and the viscosity at T_L were used to scale the temperature and the viscosity of the metallic melts, respectively. Then the scaled Arrhenius equation is given by [80-82]:

$$\eta_r = \eta_{r0} \exp(E/RT_L T_r), \tag{1.6}$$

Where $\eta_r = \eta/\eta_L$, $\eta_{r0} = \eta_0/\eta_L$, and $T_r = T/T_L$. Therefore, the fragility of the superheated melt (M) is defined as [80-82]:

$$M = \left|\frac{\partial\eta(T)/\partial\eta(T_L)}{\partial T/\partial T_L}\right|_{T=T_L} = \left|\frac{\partial\eta_r}{\partial T_r}\right|_{T_r=1}. \tag{1.7}$$

Fig. 1.6 shows the scaled viscosity of various Al-based melts [81]. It was found that M has a close relationship with the formation of MGs [79-83]. When the value of M become larger with the temperature decreasing, the viscosity of the melts decrease more quickly, which implies that the thermal stabilization of clusters in melts become worse. In an opposite way, the clusters in the melts with a smaller M trend to be kept to low temperatures. Based on the experiments and simulation results, it has been demonstrated that during the rapid solidification, some structural information carried by the SRO and/or MRO clusters is inherited from a melt to an amorphous solid [95, 96], which promotes the glass formation [9, 97]. Therefore, it is reasonable to believe that a superheated melt with a smaller M is prone to be frozen into the glassy phase [81]. Namely, the smaller the M is, the stronger the superheated melt is, and the better the GFA becomes.

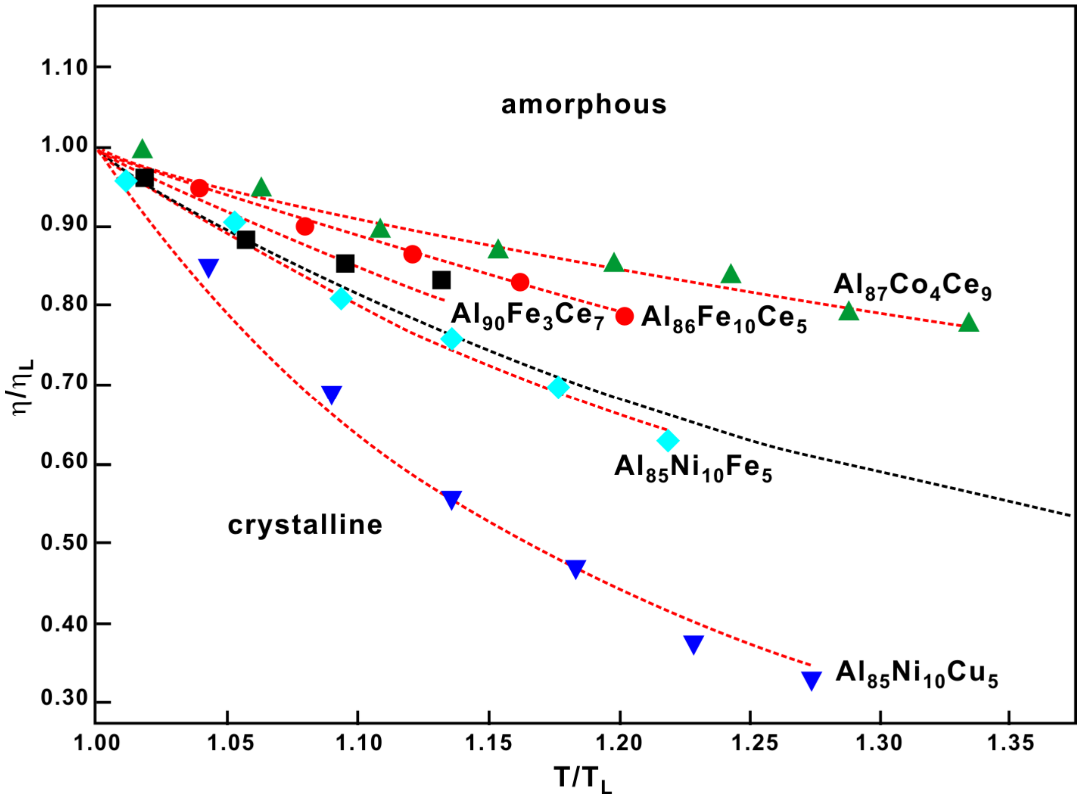

Figure 1.6 *Experimental viscosity scaled by the viscosity at the liquidus temperature (T_L) vs. the temperatures scaled by T_L for Al-based alloys. Redrawn from Ref. [81].*

1.2.3 Structural considerations

It has often been argued that the atomic and electronic structures of MGs are key factors for the glass formation in metallic alloys [98-103]. Turnbull suggested one general guiding principle to design MGs with a good GFA is to select elements with large differences in their sizes [57]. Based on Miracle's solute-centered packing model [63], when the size difference between the atoms exceeds than 12%, a denser randomly-packed atomic configurations and new local atomic configurations can be induced [7, 63]. Egami *et al.* [104, 105] also proposed a topological instability criterion (λ), and explained the glass formation by a concept of the gradual incorporation of solute atoms into a crystalline host lattice. The gradual incorporation of solute atoms into a crystalline host lattice results in the destabilisation of the lattice, which might lead to the collapse of the lattice and even amorphisation [104, 105]. Therefore, the ratio of solvent and solute radii plays a critical role on the glassy formation [63]. The λ criterion represents the atomic mismatch of a crystalline host lattice with the insertion of a given atomic fraction of solute [63, 104-106]:

$$\lambda = \sum c_i \left| \frac{r_i^3}{\sum_A n_j r_j^3} - 1 \right|, \tag{1.8}$$

where c_i and r_i are the molar fraction and the atomic radii of the solute element and n_j and r_j are the number and the atomic radius of each element in the chemical equation of the compound, respectively. The λ criterion indicates compositions with maximum topological instability for which vitrification trends to be easier [107, 108].

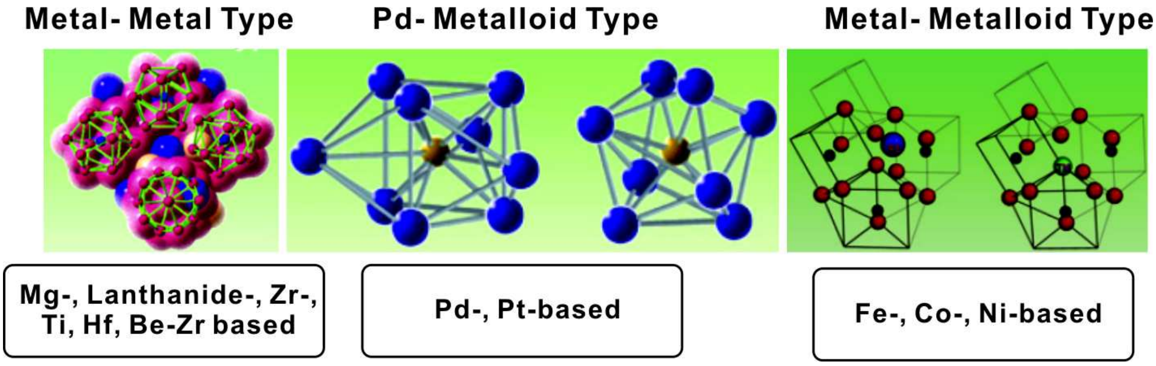

Figure 1.7 *Diagrammatic sketches of the structural features of metal-metal, Pd-metalloid and metal-metalloid types of glassy alloys. Redrawn from Ref. [109].*

Recently, by investigating different MGs, Inoue *et al*. classified the MGs into three types [7, 109, 110] (Fig. 1.7): (1) Metal-metal alloys [111, 112] consist of a large amount of icosahedral clusters. When the size of the icosahedral clusters is larger than about 8 nm [112], the icosahedral clusters transform into icosahedral phase (i.e. quasicrystals); (2) For metal-metalloid alloys, it was found that a network atomic configuration (Fig. 1.7) consists of some trigonal prisms which are connected with each other through “glue atoms” [110]; (3) For Pd- or Pt-based MGs, structural investigation has revealed that two large clustered units of a trigonal prismcaped with three half-octahedra and a tetragonal dodecahedron exist [7-9, 109, 110] (Fig. 1.7). When these two different, large clusters coexist in the glass-forming alloys, the atomic motion in supercooled liquids is no longer spatially homogeneous during quenching to low temperatures. Therefore, the mobility of atoms exhibits a heterogeneous distribution in space, leading to significant spatial partitioning and dynamic isolation between slow-dynamics regions and fast-dynamics regions. Nevertheless, these chemical or structural clusters are expected to be associated to the glass formation of metallic alloys [9].

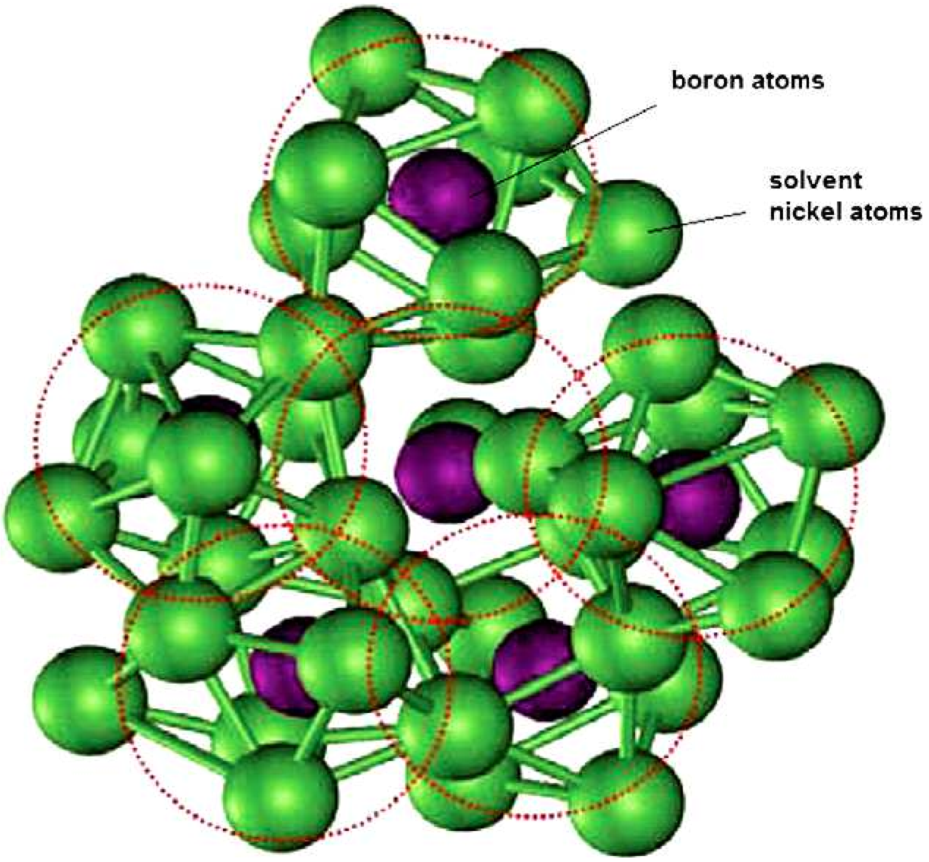

Figure 1.8 *Structure of* $Ni_{81}B_{19}$ *MG obtained from ab initio MD simulation [113].*

Many experiments and various simulation methods have been applied to further analyze the structure of MGs [10] so that the atomic structures of MGs have been better understood (Fig. 1.8). A compelling evidence of the local atomic order in disordered materials is provided [9, 10, 63, 113, 114]. In MGs, chemical short-to-medium range orders are expected to be pronounced. The short-range order (SRO) has been proposed to be solute-centered clusters in MGs, which can be described by the efficient atomic packing in clusters or polyhedra (Fig. 1.8). The packing or correlation of these quasi-equivalent clusters give rise to a distinct medium-range order (MRO) [64, 113, 115, 116]. Recently, nanobeam electron diffraction (NBED) with a coherent electron beam smaller than 1 nm in diameter was applied to detect the local atomic structure of a $Zr_{66.7}Ni_{33.3}$ MG [117]. The method used is schematically given in Fig. 1.9. A coherent electron beam with a minimum of ~ 0.3 nm (full-width at half-maximum (FWHM)) was accurately used to record the NBED pattern from an atomic cluster in MGs using a state-of-the-art spherical aberration-corrected transmission electron microscope (TEM).

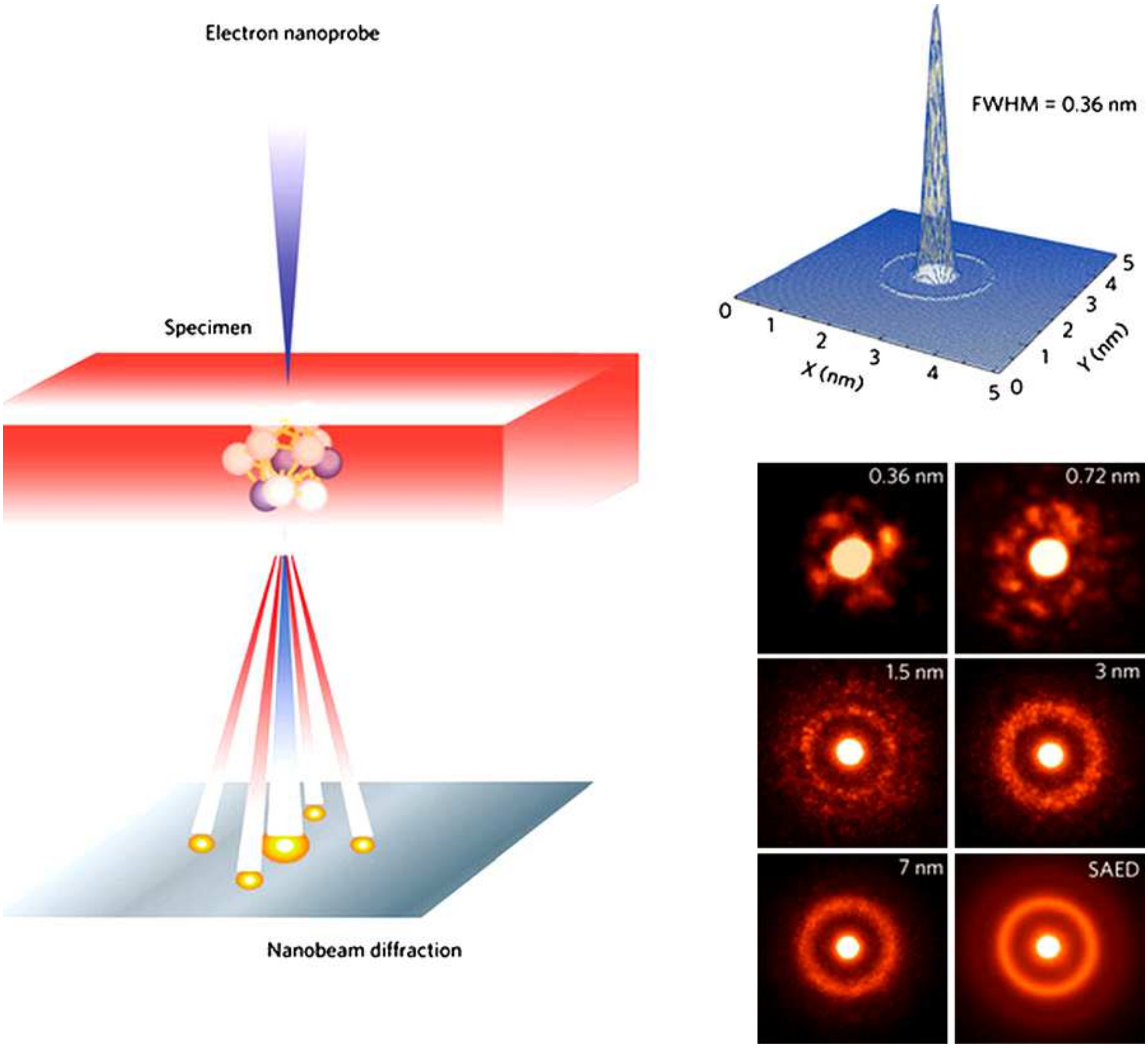

Figure 1.9 *The schematic method used in NBED. Taken from. Ref. [117].*

By using coherent electron beam with a normal FWHM size, a typical halo can be observed (Fig. 1.9). However, when the electron beam gradually decreases to a FWHM size of ~0.72 nm [117], distinct diffraction spots are observed instead of halos (Fig. 1.8). As the coherent electron beam is further reduced to ~0.36 nm in diameter, diffraction patterns similar to a single crystal are frequently observed [117], implying that atoms are packed in a certain regular manner (i.e. SRO). Combined with *ab initio* an MD simulation, the structure of the Zr$_{66.7}$Ni$_{33.3}$

MG was investigated [117]. Individual and interconnected atomic polyhedra were characterized, whose possible configurations were determined in the form of a face-sharing assembly. Their observations further support the assumption that MGs possess specific the SROs and MROs [9, 10, 117], which is further confirmed in Cu-Zr binary MGs. For CuZr binary MGs, the dominated SRO can be treated to be Cu centered icosahedral clusters. These icosahedral clusters in the MGs exhibit a stronger spatial correlation compared with other polyhedra, suggesting a string-like icosahedral MRO. Therefore, the MRO exist in the face-sharing or interpenetrating way for icosahedral clusters. These observations further confirm that the SROs/MROs play a crucial role in the formation of MGs.

Moreover, the relationship between the atomic and the electronic structures also have an effect on the structural stability of a solid phase [98-103]. Nagel and Tauc suggested that a MG can be regarded as a nearly free electron metal and proposed that a MG is stabilized when the Fermi level is located at a minimum in the density-of-state curve [98-103]. Therefore, the electronic structure displays more fundamental information on the thermal stability of MGs. Dong *et al.* [118] indicated that the GFA and thermal stability of MGs are associated with the conduction electron concentration and the atomic size factor. By considering the relationship between the atomic and the electronic structures, a new criterion, $\lambda+(\Delta h)^{1/2}$, was proposed to predict the GFA of MGs [119, 120]. In order to account for electronic effects on the GFA, the average work function difference, $\Delta ø$, and the average electron density difference, $\Delta n_{ws}{}^{1/3}$, between elements are used to calculate the electronic criterion, Δh. The correlation between R_c and $\lambda+(\Delta h)^{1/2}$ [104, 105, 107, 108, 119-122] has been reported to predict the GFA well [119-121]. It can be concluded that the GFA criteria based on both the atomic and electronic structural feathers provide a good tool to select the composition range in a given system.

1.3 Mechanical properties of metallic glasses

Due to their disordered and hence dislocation-free structure [7, 63, 64, 113, 123] as shown in Fig. 1.8, MGs process some excellent mechanical, physical and chemical properties, which are promising for current and future applications [9, 10, 15, 109, 124-126]. Their mechanical properties are among the most interesting characteristics of MGs. Generally, when a MG is mechanically loaded, it first undergoes an elastic deformation followed either by fracture or by plastic deformation [126, 127]. As shown in Fig. 1.10, different BMGs generally show a large strength with about 2% elastic strain [4, 5].

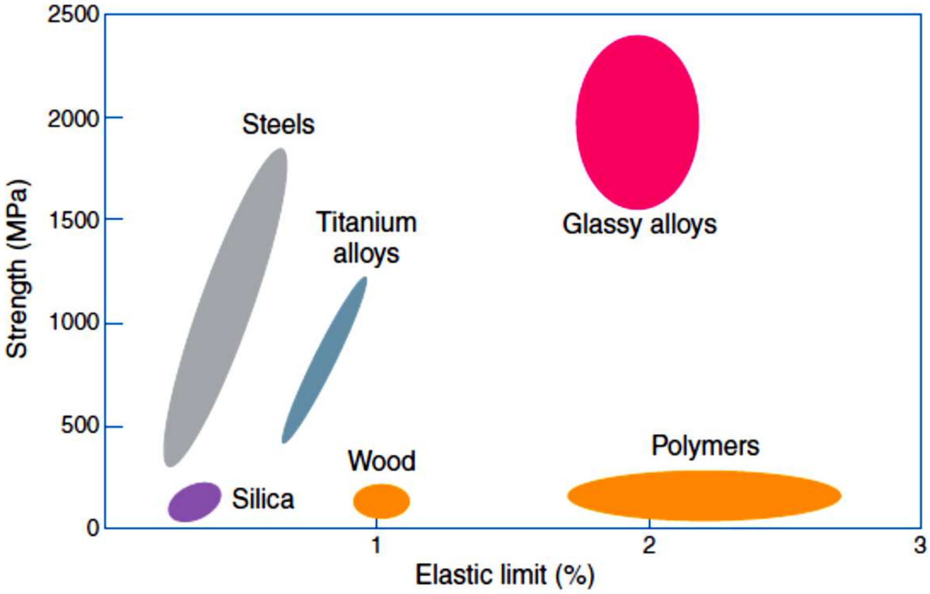

Figure 1.10 *The strength and elastic limit of metallic crystalline alloys and MGs [4]*

When the dimensions of MGs are decreased to micro- or nano-scale, the yield stress and the corresponding yield strain show an increasing tendency as shown in Fig. 1.11a [128]. Surprisingly, extraordinarily high elastic limits can be observed in nano-scaled MG samples and they are about twice as high as the elastic limit observed in conventional BMG samples, which corresponds well with the ideal elastic limit of MGs [129, 130]. Ashby and Greer [131] collected data including the elastic limit (yield stress) and the Young's modulus for 1507 metals, alloys, metal-matrix composites, and MGs, and then found that BMGs can store more elastic energy per unit volume than other materials. It can be seen that the fracture stress (σ) has a clear linear relationship with the Young's modulus (E) of all the studied materials, i.e. $E/\sigma \approx 50$, further confirming previous observations [4, 128].

It was also found that the elastic constants and the compressive yield strengths of about 30 BMGs obtained at room temperature also reveal a linear relationship between shear stress at yielding (τ_Y) and the shear modulus (G): $\tau_Y = \gamma_c G$, and $\gamma_c = 0.0268$ (γ_c value for a single glass are associated with the T_g) [89].

Based on the ratio of uniaxial stress to strain in the solid's elastic regime, the shear modulus [132, 133] is regarded as the strain response of a solid under shear stress. Therefore, the shear modulus can reflect the inherent stiffness of atomic bonds to some degree. Recent reports [132, 134] have shown that the elastic moduli of MGs primarily depend on their solvent metals (Fig. 1.11b), and the elastic deformation of MGs mainly occurs at the solvent-solvent junctions among solute-centered clusters and/or superclusters [132, 134].

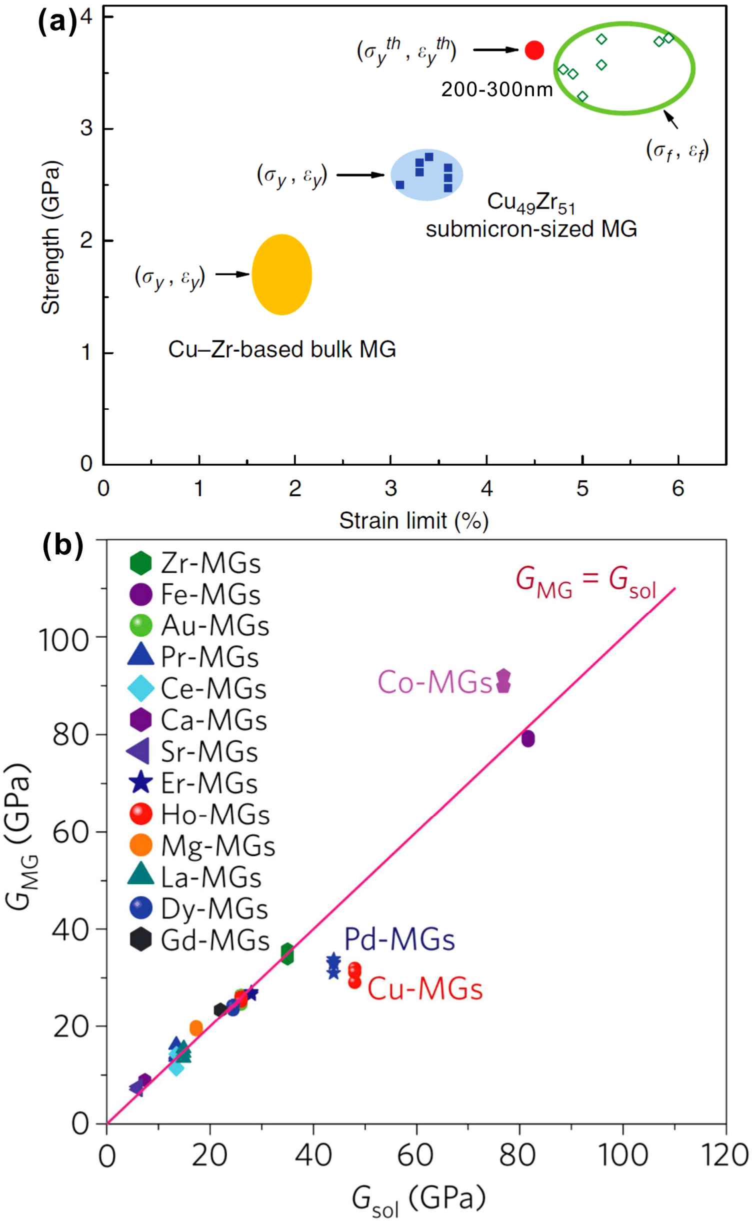

Figure 1.11 *(a) Strength and strain limit of different scaled CuZr-based MGs, (b) average ratio of shear modulus for MGs (G_{MG}) and their solvents (G_{sol}) is close to 1, indicating that moduli of MGs are primarily determined by ther solvent metals. MGs markedly deviate from G_{sol}. Taken from Ref. [128, 132].*

The subsequent plastic stage of some ductile BMGs depends on external and internal factors during deformation [126, 127, 135, 136]. The former includes the testing conditions (i.e. strain rate, temperature, machine stiffness etc.), and the aspect ratio of the samples [126, 127, 135, 136]. During the compression test, as the testing temperature or the strain rate is changed, there is a brittle-ductile transition during deformation of MGs [137-141]. With the machine stiff increasing, the multiple shear bands are prone to form, which further affect the deformation behavior of MGs [142, 143]. With the aspect ratio of the samples decreases from 2:1 to 1:2, the corresponding plasticity of the samples gradually increases [144, 145]. The internal factors which affect the plastic stage of some ductile BMGs is the atomic-level features in the glassy structures such as different relaxation states, different amounts of free volume, or different scaled structural heterogeneities [126, 127]. As nano- or micro-scaled structural heterogeneities are introduced into the glassy matrix, the formation and propagation of shear bands can be changed, resulting in the increase of the mechanical stability of the samples even under tension conditions [135, 136].

It has been demonstrated that when both the external and internal factors are changed, the highly localized shearing process within narrow bands can be governed by one main shear banding or by multiple shear banding [146, 147]. Therefore, it becomes very important to understand the deformation and failure mechanisms of shear bands in order to illustrate the plasticity/ductility of MGs. Recently, it has been found that the dynamic instability of shear bands and the plastic deformation of MGs at a constant strain rat and at an constant temperature can be evaluated by a shear-band instability index, λ_{crit} [142, 143]:

$$\lambda_{crit} = L\left(1+\frac{\pi d^2}{4LK_M}E_y\right), \tag{1.9}$$

where L, d, and E_y are the height, the diameter, the stiffness and the Young's modulus of the sample, respectively, while K_M is the machine stiffness. The values of Poisson's ratio have been demonstrated to have a relationship with the intrinsic plasticity or brittleness for most of MGs, e.g. lower Poisson's ratio usually favors brittleness and vice versa [148, 149]. When the value of Poisson's ratio exceeds a critical value, BMGs become ductile, which may be attributed to different plastic process zone sizes for various MGs [150, 151]. Then the value of

E_y can reflect certain structural information of MGs. It has been pointed out that MGs inherit their E_y and G from the solvent components. This phenomenon is due to the preferential straining of locally solvent-rich configurations among tightly bonded atomic clusters, which gives rise to the weakest link in an amorphous structure. Nevertheless, this criterion can effectively evaluate the plasticity or brittleness for most of MGs during deformation to some degree by partly considering the external and internal factors.

1.4 Deformation mechanisms of metallic glasses

During deformation of MGs, a local rearrangement of atoms can accommodate the shear strain. The volume or size of the accommodated atoms during deformation strongly depends on different alloy systems [9, 17]. As mentioned by Spaepen [17, 152, 153], these groups of atoms and the corresponding localized directional bonding play an important role in the mechanical properties of MGs. Even though many glass-forming alloys have been developed in recent years, a fundamental knowledge on the relationship between structure and deformation behavior of MGs is still lacking. So far, different theories have been suggested to address the correlation between the glassy structures and the deformation mechanisms of MGs.

1.4.1 Shear transformation zone theory

It has been demonstrated [154, 155] that the large flow units in a solid may induce the nonlinear resistance to deformation of a solid (be different from the linear-viscous resistance of most liquids), which implies the importance of the local atomic motions in deforming MGs [9, 126, 127, 152]. Relatively large flow units (about 0.2-0.7 nm^3) in the matrix may produce large internal stress concentrations during plastic deformation [156, 157]. Around these sites, new local flow events are preferentially activated with the applied stress increasing [9]. Argon and Kuo [158, 159] suggested that these small clusters of close-packed atoms spontaneously and cooperatively rearrange to accommodate the applied shear strain, which are termed as a shear transformation zone (STZ) as shown schematically in Fig. 1.12 [158, 160-164]. During shearing, the STZ essentially involves a cluster of atoms that undergoes an inelastic shear distortion from one low-energy configuration to another configuration with relatively low energy through an intermediate activated state with a high energy and a large volume [165, 166]. With the applied shear strain further increasing, more STZs will be triggered, which results in the formation of shear bands [165, 166].

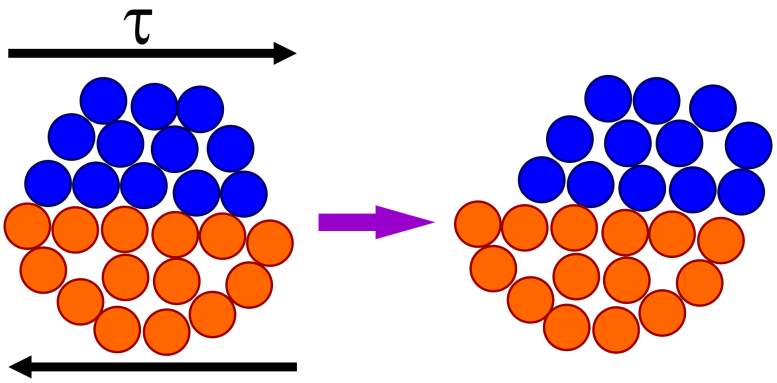

Figure 1.12 *A two-dimensional schematic of a shear transformation zone in MGs [164].*

A quantitative model of STZ behavior has been proposed [159, 167], indicating that the STZ operation is allied to the elastic confinement of the glass matrix and the stress and strain redistribution around the STZs. The free energy for STZ activation in terms of the elastic constants of the MGs is given by [159, 167]:

$$\Delta F_0 = \left[\frac{7-5\nu}{30(1-\nu)} + \frac{2(1+\nu)}{9(1-\nu)}\beta^2 + \frac{1}{2\gamma_0} \cdot \frac{\tau^0}{\mu(T)} \right] \cdot \mu(T) \cdot \gamma_0^2 \cdot \Omega_0 , \tag{1.10}$$

where ν is Poisson's ratio, τ_0 is the athermal shear stress at which the STZ transforms, and $\mu(T)$ is the temperature-dependent shear modulus. The parameters in the brackets contain the dilatational energy related to STZ action, *ß* is the ratio of the dilatation to the shear strain, γ_0 is generally adopted to be of order ~0.1, and Ω_0 usually consists of a few up to perhaps ~100 atoms [127, 130, 159, 163, 168, 169]. Hence, the energy of an STZ is estimated to be on the order of 1 - 5 eV, or ~ 20 - 120kT_g [127], with k being the Boltzmann constant. Based on the original analog model of Argon *et al.* [152, 153, 158, 159, 168], a dynamical theory related to STZ operation has been developed, which contains the following characteristics [9, 17, 126, 127, 164, 165, 169]: (1) The transformed STZ is irreversible along the same shear direction due to saturation effects and jamming of the system; (2) The creation and annihilation rates of STZs are proportional to that of the irreversible plastic deformation as the creation rate of newly formed STZs is as high as their transformation rate of pre-existing STZs; (3) The attempt frequency of the transition is related to the noise in the system, being driven by the strain rate, while random motions associated with the disorder in the system result in the stochastic nature of these fluctuations; (4) The applied stress has a strong influence on the transition rates between jammed and flowing zones. Furthermore, it has been suggested that STZs consists of a few to perhaps ~100 atoms [9, 17, 126, 127, 164, 165, 169].

1.4.2 Free volume model

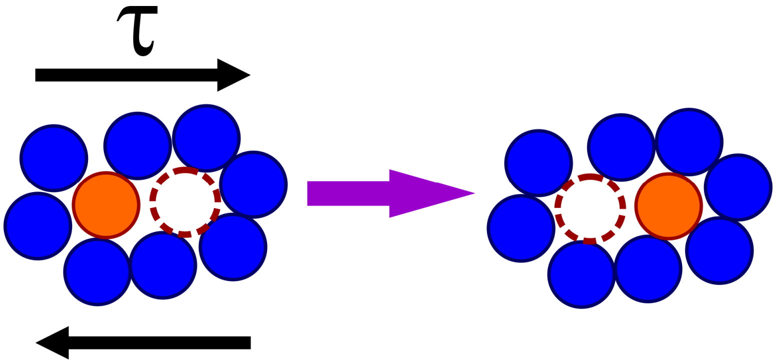

Figure 1.13 *A two-dimensional schematic of free volume model in MGs. Redrawn from Ref. [152].*

As an alternative mechanistic theory describing the plastic flow and deformation behavior of MGs, the "free-volume" model has been proposed by Spaepen *et al.* [152]. Free volume is defined as the part of the thermal expansion or excess volume which is redistributed without energy change [76], which is proposed based on the Doolittle equation in order to account for the molecular transport behavior of liquids and glasses during relaxation as a function of temperature. At the atomic scale, the accommodation of the shear strain in MGs under an applied stress occurs as a series of diffusion-like local atomic jumps into vacant sites in regions with large free volume [152]. The localized plastic deformation is treated as a series of discrete atomic jumps in the amorphous structure as depicted schematically in Fig. 1.13 [152].

The empty space around constituent atoms is called the free volume and is assumed to be distributed statistically among all the atoms in MGs [75, 170, 171]. Due to the weak mechanical coupling to the surrounding of regions with large free volume, the inelastic relaxation is prone to occur by local atom rearrangements [17, 127, 152, 165]. These regions can act as preferred sites where the destabilization of the glassy structure occurs with the applied stress increasing. At low stresses, the annihilation rate of the free volume is exactly equal to its creation rate so that the free volume keeps constant [17, 127, 152, 165]. At high stresses, as the creation rate is larger than the annihilation rate, the softening occurs together with the increase of free volume. With the applied stress decreasing, the driving force for the creation of free volume decreases until the formation of new free volume achieves a steady state [17, 127, 152, 165].

1.4.3 Potential energy landscape theory

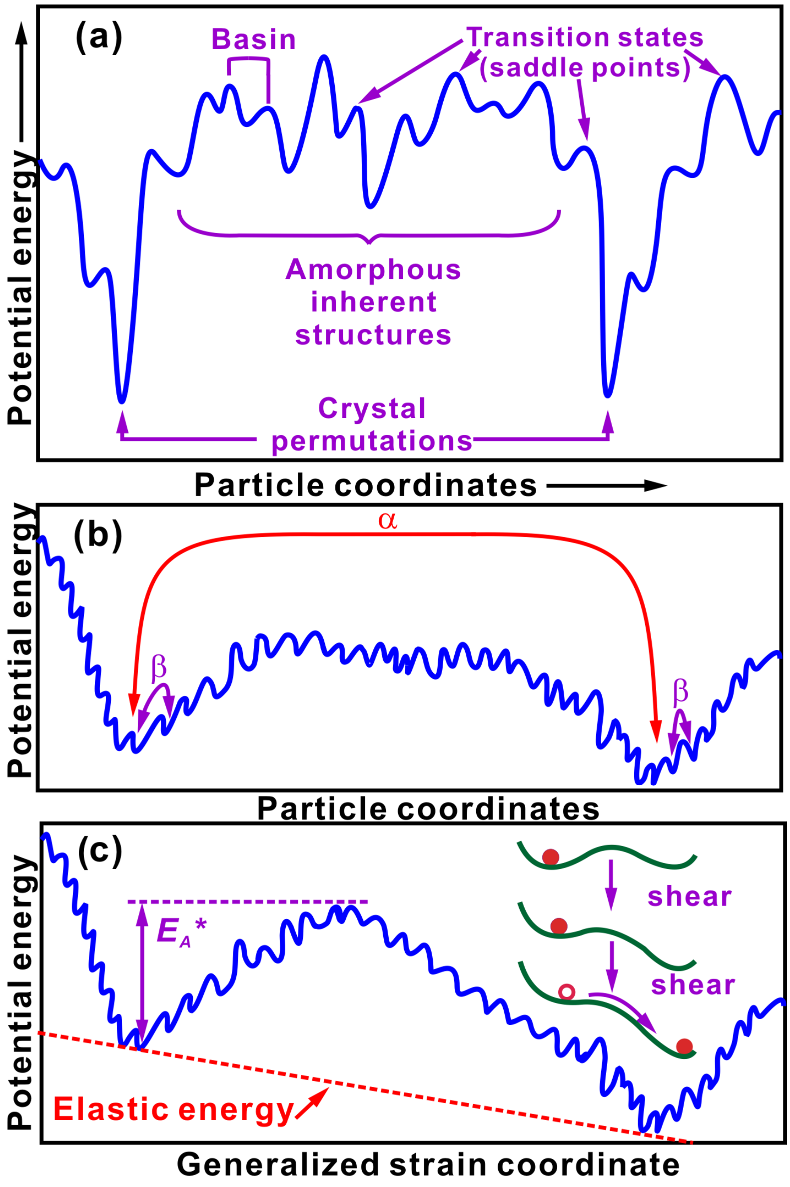

Figure 1.14 *Schematic diagram of the PEL theory. Redrawn from [172, 180, 182].*

The potential energy landscape (PEL) theory is a statistical model to describe the energetic landscape of disordered systems [173-183]. The PEL consists of inherent states (basins) associated with local energy minima that correspond to the different (meta)stable configurational states of the glass [13, 172-179]. The saddle points represent transition states from one (meta)stable configurational state to another (Fig. 1.14a). The extended local minimum is determined to be a (mega)basin. A glassy structure with a configuration close to that of a crystal has a lower energy, and can be called an "ideal glass" [13, 172-179]. As shown in Fig. 1.14a-b, there are two kinds of length-scales exist in the PEL picture. One is the minor configurational changes, which are associated with relatively small energy barriers and are called reversible β-relaxations [13, 172-179]. The hopping events from one basin to the next are determined to be irreversible α-relaxations. It has been proposed that the α-relaxations in MGs are associated with the percolation of STZs while the β-relaxations are connected with the transition of STZs

Assuming that the average potential energy *vs.* shear strain in the vicinity of a basin is a sinusoid, the PEL theory becomes a useful tool to capture the underlying flow mechanism of glass-forming alloys [172, 174, 175]. In order to further illustrate the deformation behavior of MGs, the effect of elastic energy (Fig. 1.14c) on the PEL is considered. As shown in the inset in Fig. 1.14c, the shear stress can decrease and even eliminate the energy barrier separating two inherent states [180-182]. As a result, the atomic rearrangement can be changed to a more stable state upon the applied load. Nevertheless, experimental observations have proven that the STZ theory corresponds well with the classical thermodynamic theories of liquids and glasses based on the PEL theory [183].

1.4.4 Cooperative Shearing Model

Even though free volume and STZ models provide explanations for the strain softening and the heterogeneous deformation of MGs, it is difficult to quantitatively describe the strength and ductility of MGs at room temperature [15]. It has been suggested that plastic yielding in MGs can be explained by a cooperative yielding for flow accommodations by cooperative shearing of atomic clusters [130, 184]. Based on this concept and the energy landscape theory [130, 174, 183, 184], Johnson and Samwer [130, 183] have proposed a cooperative shearing model for STZs, which can elucidate the temperature dependence of yield strength in the form of $T^{2/3}$, and provide an effective interpretation of the ductility and strength of MGs. A quantitative equation is given as follows [183]:

$$\alpha\eta\dot{\gamma}^2\delta W/\delta\varepsilon = \frac{(W-W_e)(W/W_0)^q}{\eta/G_0}, \tag{1.11}$$

where $\dot{\gamma}$ is the strain rate and α is a parameter incorporating two unknown proportionality constants: the conversion efficiency of dissipated energy into potential energy and a factor quantifying the deviation of the system's relaxation rate from Maxwellian [130, 174, 183, 185, 186], η is the viscosity, W is the activation barrier for the shear flow which involves with the shear modulus given by the curvature of the energy density function, ε is the flow-induced shift in the specific configurational potential energy of shear zones [130, 174, 183, 185, 186]. By linking the cooperative shear model with classical deformation thermodynamics through the variable of the activation volume [157], the measured STZ volumes of MGs are determined to be 2.5 nm^3 ~ 6.6 nm^3, then the STZs are estimated to comprise about 200 - 700 atoms based on the assumption of a dense packing of hard spheres in MGs [157].

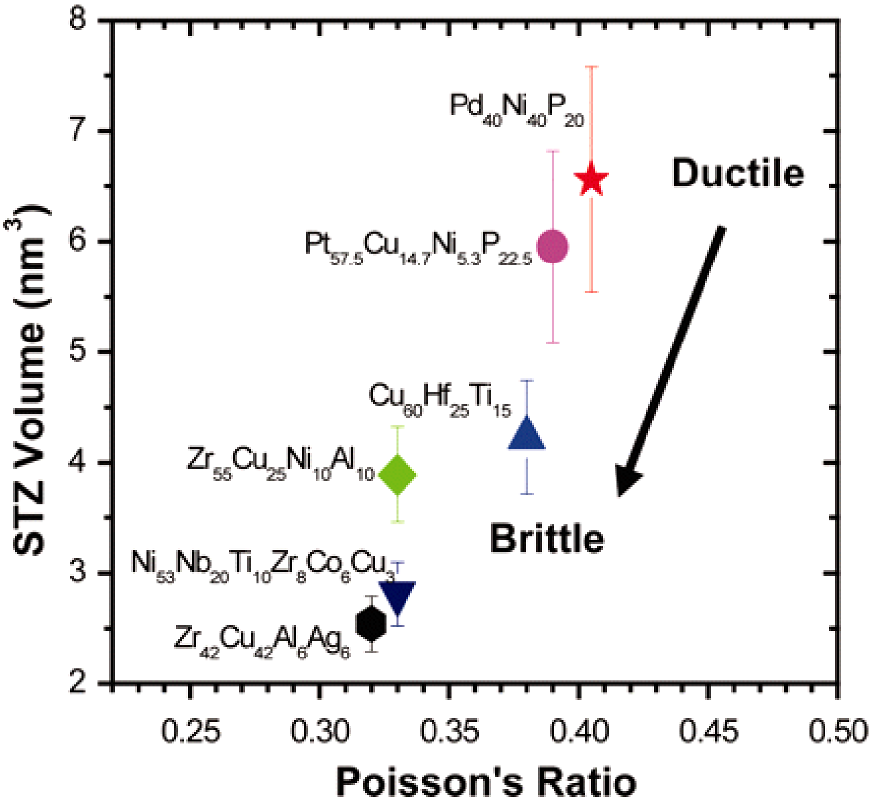

Figure 1.15 *Correlation between ductility, STZ volume, and Poisson's ratio [157].*

Fig. 1.15 shows that the calculated STZ volumes correspond with the increases of the ductility of MGs [157], implying that a larger STZ volume during deformation can promote the formation of multiple shear bands. Nevertheless, the calculation of the volume of STZs based on energetic considerations [15, 157, 183] is helpful for understanding the atomic-scale mechanisms responsible for the mechanical properties of BMGs.

1.5 Strategies to improve the ductility of metallic glasses

So far, a lot of attention has been paid to improve the plasticity since BMGs usually fail in a brittle manner under quasistatic uniaxial loading at room temperature due to highly localized deformation within shear bands [4, 5, 12, 22, 31, 35, 127], which severely restricts their applications as new-generation engineering materials. Johnson and Samwer [130, 183] pointed out that plastic yielding of MGs at room temperature can be roughly described by an average shear strain limit of 0.0267 ± 0.0020, implying that the elastic strain is required for the formation of a shear band nucleus in MGs that contain a local collection of STZs [157]. Therefore, a larger STZ volume enables a smaller number of STZs to be activated for the nucleation of a shear band compared to a smaller one. Moreover, the larger-sized flow units can induce larger internal stress concentrations and thermally activated production of new flow becomes easier [187]. Therefore, larger STZs result in the increase of the shear capability of the MGs and facilitate the formation of multiple shear bands during plastic deformation. This analysis is accordance with the increase of Poisson's ratio (Fig. 1.15), which represents the increase of the possibility for the material to shear under applied stress [188]. So if the large STZ volume in MGs is obtained, it is prone for the multiple shear bands to be induced, resulting in the improvement of the mechanical instability of MGs during deformation. It has been found that as different scaled crystalline/amorphous phases (i.e. microstructural inhomogeneities) at different length scales [188-261] are introduced into the glassy matrix, the STZ volume can be changed, resulting in the change of the shear banding process and the increase of the ductility of BMGs.

1.5.1 Nano-scaled microstructural inhomogeneities

With nano-scaled microstructural heterogeneities being introduced into the glassy matrix, plasticity can be enhanced in different BMGs by inducing the extensive shear band formation and the multiplication of shear bands during deformation [188, 217-261]. Structural heterogeneities observed from experiments still have not been accurately defined. Here, different types of microstructural heterogeneities were introduced based on the previous results, which can be obtained by the following methods [188, 217-261]:

(1) Different microstructural heterogeneities such as free volume, phase separation, nanocrystallization, short-/medium- ranged clusters can be introduced into the glassy matrix by controlling the casting process [188, 217-242].

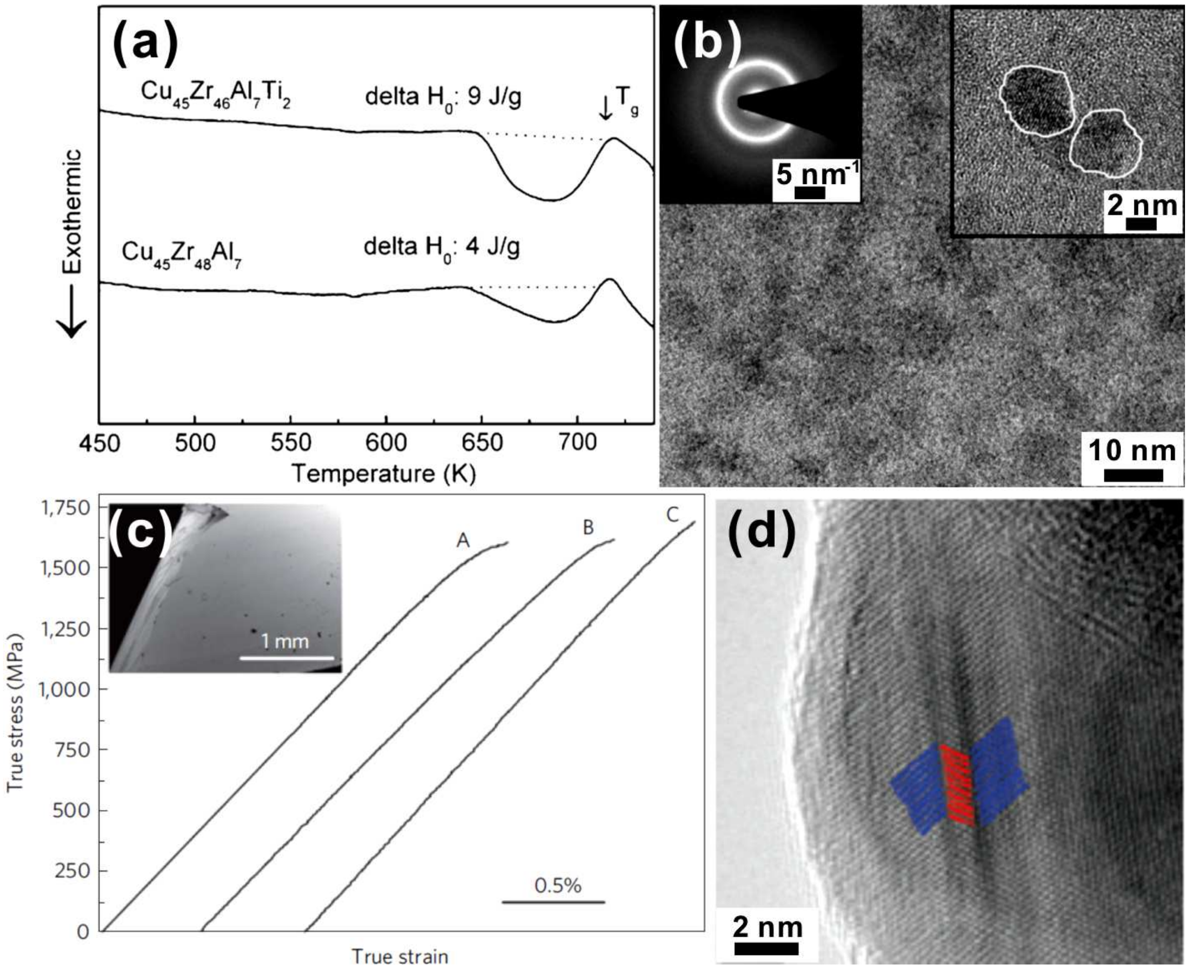

Figure 1.16 *DSC traces of (a)* $Cu_{45}Zr_{48}Al_7$ *and* $Cu_{45}Zr_{46}Al_7Ti_2$ *BMGs (areas indexed by the dotted line indicate the free volume), (b) the nanocrystals in the glassy matrix for* $Cu_{46}Zr_{46}Al_8$ *samples, (c) the tensile stress-strain curves (Inset: the deformed surface) of* $(Cu_{0.5}Zr_{0.5})_{100-x}Al_x$ *(x = 5, 6, and 8) samples, and (d) the twinned crystals in the glassy matrix for the deformed samples [136, 235].*

As shown in Fig. 1.16a, it has been found that by introducing minor amounts of Ti into the glassy matrix, a plasticity of up to 32.5% can be achieved in a $Cu_{45}Zr_{46}Al_7Ti_2$ BMG which can be attributed to a large amount of randomly distributed free volume [237]. The enthalpy change (ΔH_0), i.e. the area of the exothermic event over a broad temperature range below T_g, distinctly increases from 4 J/g to 9 J/g with the Ti addition. The exothermic event prior to T_g is closely associated with the existence of free volume in BMGs as $\Delta H_0 = \beta \Delta v_f$, where β is a constant and Δv_f is the change of free volume per atomic volume [262]. Hence, the increment of ΔH_0 indicates the increase of the free volume in the samples with the Ti addition.

Additionally, it also has been found that when nanocrytals are introduced into Zr-based, CuZr-based or other MGs [188, 218, 219, 221-223, 225, 228-230, 232-234, 237-241], the plastic strain of MGs can be enhanced (Fig. 1.16b). With the applied stress increasing, these microstructural heterogeneities can effectively change the stress distributions [222], and then result in the multiplication of shear bands and the increase of the mechanical instability of BMGs during deformation. For CuZr-based BMGs, even tensile plasticity can be achieved, which can be mainly attributed to a transformation from nanocrystals to nano-twinned crystals during deformation (Figs. 1.16c-d) [136]. For the phase separated BMGs, the microstructural heterogeneities are the nano-scaled, second amorphous phase distributing in the glassy matrix. During deformation, the second amorphous phase can also act as a barrier for shear bands and thus hamper their instantaneous propagation. Therefore, a remarkable macroscopic plastic strain at room temperature can be observed for some of the phase-separated BMGs [220, 226, 227, 231, 242].

It has been found that the local ordering (SRO/MRO) clusters are present in all BMGs [9]. However, some BMGs with a large ductility process large amounts of clusters, while brittle BMGs exhibit a homogenous microstructure. Recently, the relation between icosahedral SROs and plastic deformation [225] has been investigated in Zr-Nb-Cu-Ni-Al BMGs. It was found [225] that the icosahedral SROs increase and the unusual plastic deformability become more obvious with Nb content gradually increasing. During deformation, the icosahedral SROs can mediate the local distribution of free volume and promote the deformation-induced crystallization, which is beneficial for the stress redistribution and the multiplication of shear bands [225]. These observations imply that the introduction of different amounts of local ordering in MGs strongly influences shear transformations and the shear banding behavior during deformation [9, 10, 117, 224].

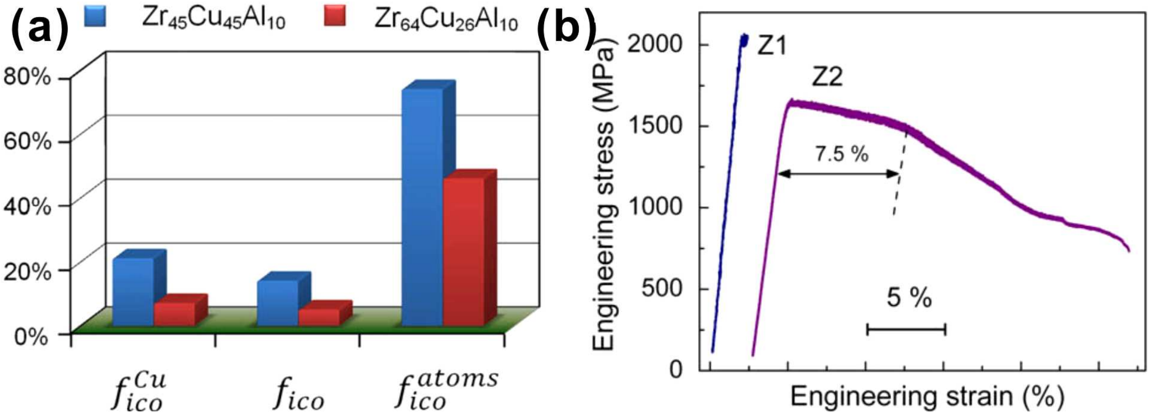

Figure 1.17 *(a) Comparison of the degree of full icosahedal packing and (b) compressive stress-strain curves of* $Zr_{45}Cu_{45}Al_{10}$ *(Z1) and* $Zr_{64}Cu_{26}Al_{10}$ *(Z2), respectively. Taken from Ref. [224].*

According to a computational analysis of the composition-dependent internal structures, the local coordination/the density of certain clusters was proposed to determine the deformation behavior of certain BMGs [224]. As shown in Fig. 1.17a, it can be seen that $Zr_{45}Cu_{45}Al_{10}$ and $Zr_{64}Cu_{26}Al_{10}$ BMGs process different amounts of local clusters [224]. For the brittle $Zr_{45}Cu_{45}Al_{10}$ BMG, the content of Cu-centered full icosahedra is 21%, the total content of full icosahedra around all atoms is 14%, and the fraction of atoms involved in full icosahedra is 74%. In contrast, all these values decrease to 7%, 5%, and 46%, respectively, for the ductile $Zr_{64}Cu_{26}Al_{10}$ BMG [224], implying that the development of full icosahedral local order strongly influences the shear banding during deformation (Fig. 1.17b) [9, 10, 117, 224].

(2) By using pre-deformation methods such as cold-rolling, imprinting, ball milling or shot peening [243-261], the microstructural heterogeneities also can be introduced into the glassy matrix.

It has been demonstrated that pre-deformation can effectively promote the ductility of BMGs [243-261]. Even tensile plasticity can be achieved using these methods. For example, tensile plasticity of about 0.5% and 0.27% in $Zr_{50}Cu_{30}Ni_{10}Al_{10}$ and $Zr_{64.13}Cu_{15.75}Ni_{10.12}Al_{10}$ BMGs can be achieved by cold-rolling with thickness reductions of 10% and 50%, respectively [247, 260]. Interestingly, a little tensile plasticity of 0.7 ± 0.1% in a monolithic $Cu_{47.5}Zr_{47.5}Al_5$ BMG can be attained with a very small thickness reduction of only 2.9 ± 0.3% by cold-rolling [254]. After pre-deformation with different thickness reductions, multiple shear bands are obtained (Figs. 1.18a-b) [243, 260, 263]. Han *et al.* [255] have shown that the activation of pre-existing shear bands predominate the formation of new shear bands during tensile loading. It is believed that the pre-existing shear bands [254, 260, 263] can promote the increase of ductility of BMGs. Meanwhile, it is also shown that pre-deformation can introduce both residual stresses and structural heterogeneities [243, 246, 254, 259]. The former can result in the increase in microhardness [243, 247, 254, 260, 263] while the latter was proven by using high-energy X-ray diffraction techniques. As shown in Figs. 1.18c-d, the structure of BMGs which underwent severe plastic deformation indeed shows the rearrangements of the both short- and long-scaled clusters [259].

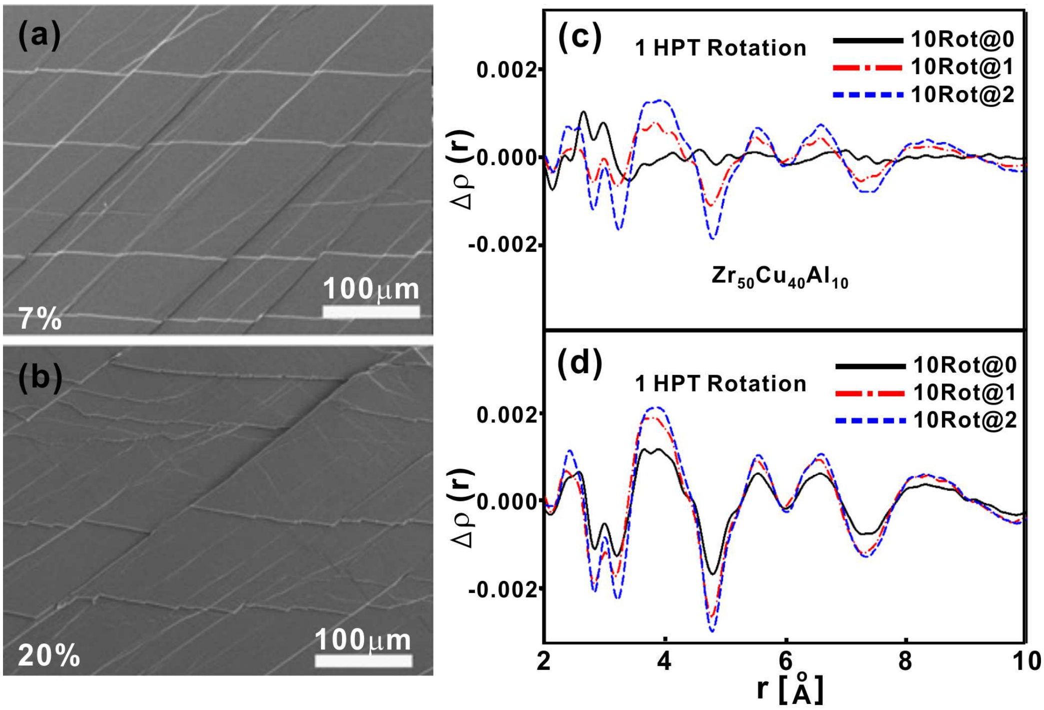

Figure 1.18 *SEM pictures of $Zr_{46.5}Cu_{45}Al_7Ti_{1.5}$ specimens with different thickness reductions of (a) 7% and (b) 20%, and (c-d) the differences of the microstructures for the samples with different degrees of pre-deformation. Taken from Ref. [259, 263].*

1.5.2 Micro-scaled microstructural inhomogeneities

Owing to the inherent brittleness of monolithic BMGs, the development of BMG composites containing micro-scaled, ductile crystalline phase in the glassy matrix becomes a good method to improve the ductility of MGs [204]. In 1982, one of the first BMG composites [264] was fabricated in Zr-based alloys. Since then, a series of BMG matrix composites have been developed, including Zr-, Ti-, Cu-, Pd-, La-, Fe-, Mg-based and other BMG composites [189-193, 195, 196, 198-203, 205, 207-210, 213-217, 265-269] by using *ex situ* and *in situ* methods.

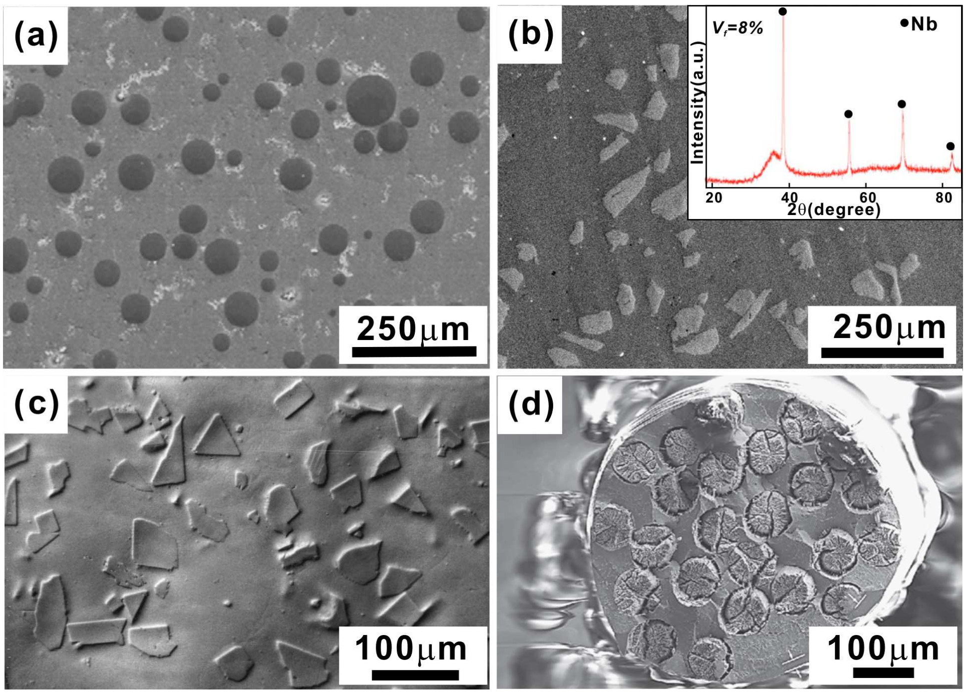

Figure 1.19 *Microstructures of Mg-based BMG composites (a) with 20 vol.% Ti particles, (b)with 8 vol.% Nb particles (Inset: the corresponding XRD pattern), (c) Microstructures of Zr-based BMG composites containing 10vol.% WC particles, and (d) fracture surface of Zr-based BMG composites with 61.4vol.% tungsten wires. Adopted and redrawn from Refs. [205, 270-272].*

By *ex situ* introducing particles, fibers or wires into the glass-forming liquids during casting, BMG composites can be manufactured. Widely used reinforcements are W, Ta, Ti, Nb and others [190, 204, 205, 217, 266, 269-272], which have a higher melting temperature than the glass-forming liquids. As shown in Figs. 1.19a-c, it is possible to control the sizes, shapes, and volume fractions of the reinforced phase. Some *ex situ* BMG composites show good compressive plasticity combined with large strength due to the formation of multiple shear bands during deformation [273]. For example, by changing the orientation of W fibers in a glassy Zr-based matrix, different plastic strains can be observed for these BMG composites [274]. However, in some cases, their mechanical properties are not better than those of the monolithic BMGs [273].

Large stress concentrations are usually induced at the interface between the glassy matrix and the particles [273, 275], which often lead to the rapid propagation of shear bands, and the formation of micro-cracks within the brittle particles and the glassy matrix (Fig. 1.19d) during compression, bending or tensile tests [273]. Furthermore, *ex situ* BMG composites [189, 203, 204, 212] can also be fabricated by a secondary treatment (i.e. thermal treatment, high pressure torsion treatment, and hot extrusion treatments and so on) of amorphous samples. *Ex situ* BMG composites with different crystalline volume factions and relatively homogenous distribution of crystals using annealing treatments can be fabricated. However, most of these composites do no show a large improvement of their mechanical properties [192, 208] when the micro-scaled crystalline phases are more brittle than the glassy matrix and free volume in the glassy matrix is annihilated after heat treatments.

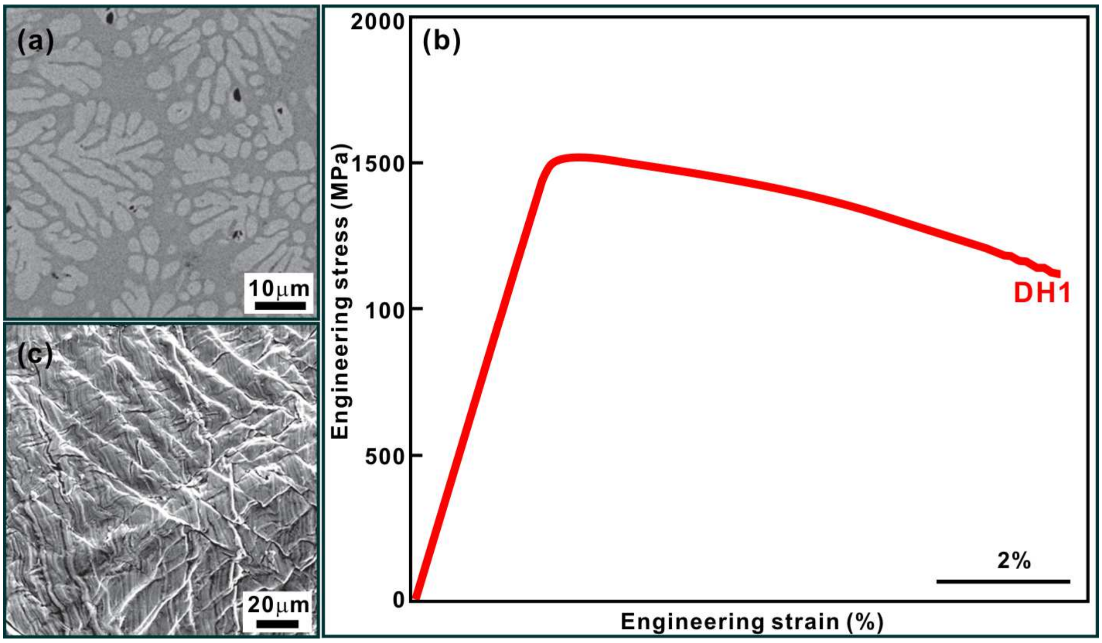

Figure 1.20 *(a) Microstructures and (b) the stress–strain curves of* $Zr_{36.6}Ti_{31.4}Nb_{7}Cu_{5.9}Be_{19.1}$ *(DH1), (c) the shear bands after deformation. Redrawn from [213].*

On the other hand, there are another strategy to fabricate *in situ* BMG composites [189, 203, 204, 212, 213, 215], which can be obtained directly from their melts during solidification. A large success has been the fabrication of Zr-based BMG composites with the presence of ductile *ß*-type crystals with a *bcc* structure in a Zr-Ti-Nb-Cu-Ni-Be glassy matrix obtained during rapid cooling [214] (Fig. 1.209a). As shown in Fig. 1.20b, tensile plasticity of Zr- and Ti-based

BMG composites has been reported [213, 215, 273]. The volume fractions, length scales, and the distribution of the ductile phase can be tailored by adjusting the casting process, which effectively change the toughness and ductility of the BMG composite [215, 276]. By introducing a ductile phase into the brittle glassy matrix, the ductility of the BMG composites is improved due to the formation of multiple shear bands and the deformation of the ductile phase [214] (Fig. 1.20c). During deformation, the ductile phase in the glassy matrix may initiate the formation of individual shear bands, act as attraction or pinning centers for shear bands during their propagation, and then result in the increase of plasticity of BMG composites [213-215, 267, 273, 276, 277].

Additionally, the Young's modulus of the glassy matrix and the second crystalline phase need also to be considered. The difference of the Young's modulus of the dual phases in the composites can result in a mismatch between the coefficient of thermal expansion of the crystalline phase and the glassy matrix and thus affect the misfit of the deformation modes of the crystalline phase and the glassy matrix upon loading. [199, 273, 278] In some cases, the composites with the ductile *bcc* precipitates show improved compressive plasticity, but no tensile ductility can be observed [199, 273]. A comparison of all these *in situ* BMG composites indicates that the shear modulus of the second crystalline phase ought to be lower than that of the glassy matrix [199, 273]. Based on these insights, different BMG composites such as Fe-, La-, and Mg-based alloys [195, 200, 201, 203, 211, 216, 268, 277] have been developed and they show excellent tensile plasticity and relatively large strength.

1.5.3 CuZr-based BMG composites

So far, various BMG composites containing crystalline phases with different length scales and crystalline volume fractions have been fabricated [213-215, 267, 273, 276, 277]. However, these BMG composites only exhibit a limited work-hardening effect during the elastic-plastic stage and subsequently show a macroscopic strain-softening behavior during the plastic stage under tensile conditions [213, 215, 267, 273, 276, 277], which severely limits the application of such kinds of BMG composites. Therefore, it is necessary to develop a new strategy to optimize the deformability of BMG composites.

It has been demonstrated that a diffusionless phase transformation during deformation can significantly enhance the ductility/toughness of different crystalline materials [279], known as TRIP effect (Transformation-Induced Plasticity) and TWIP effect (Twinning-Induced Plasticity), respectively. As shown in Fig. 21, a certain amount of metastable retained austenite in TRIP steels can transform into martensite under mechanical loading, while the deformation of fully austenitic TWIP are predominantly controlled by twinning [280, 281]. It can be seen that obvious work hardening can be seen in addition to the improved plasticity of the materials [280, 281]. If this concept can be applied into the fabrication of *in situ* BMG composites, the dominant work softening of the glassy matrix may be overcompensated. So far, the MT can be found in traditional Fe, Ti, and Cu-based alloy and other alloys, for most of which it is difficult to obtain fully amorphous bulk samples [9, 15, 16, 39, 109].

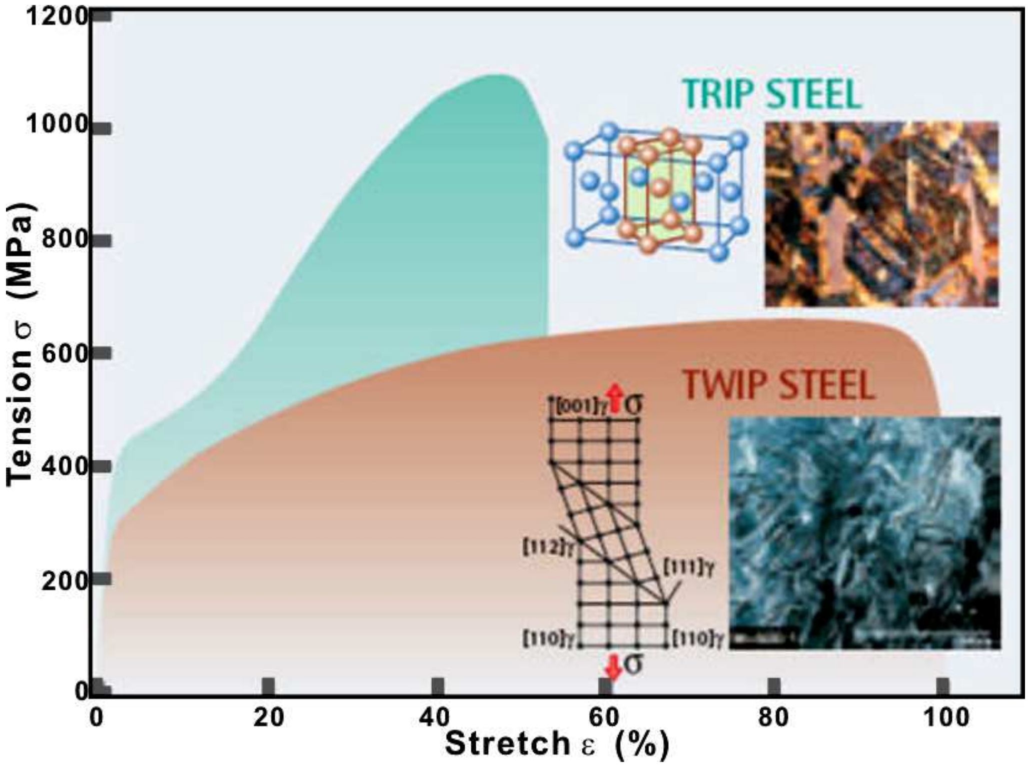

Figure 1.21 *Stress-strain diagram shows the differing characters of TRIP and TWIP steels [282].*

Fortunately, it has been demonstrated that the GFA of CuZr-based alloys is relatively large [283-287]. Especially, for CuZr-based alloys, even a $Cu_{50}Zr_{50}$ binary alloy can be made into bulk amorphous samples [288-291]. As a little Al, Ag, or RE (rare earth metals) are added to a CuZr-based alloy, its GFA can be dramatically improved [284, 292]. Fig. 1.22a shows the glass-forming compositions of Cu-Zr-Al ternary alloys based on calculations using the extended Miedema's model [284, 292]. All the simulated Cu-Zr-Al alloys were classified into the three structure states, i.e. the crystal state, the transition state and the amorphous state as shown in Fig. 1.22a. The whole composition triangle is divided into seven regions by six critical solubility lines, i.e. AB, CD, EF, GH, IJ, and KL, respectively [284, 292]. It was found that only with the addition of Al less than 10 at.%, CuZr-based BMGs can be fabricated [284, 292]. As shown in Fig. 1.22b, for the $Cu_{47}Zr_{45}Al_8$ alloy, even fully amorphous rods with diameters more than 1 cm can be obtained [284, 292].

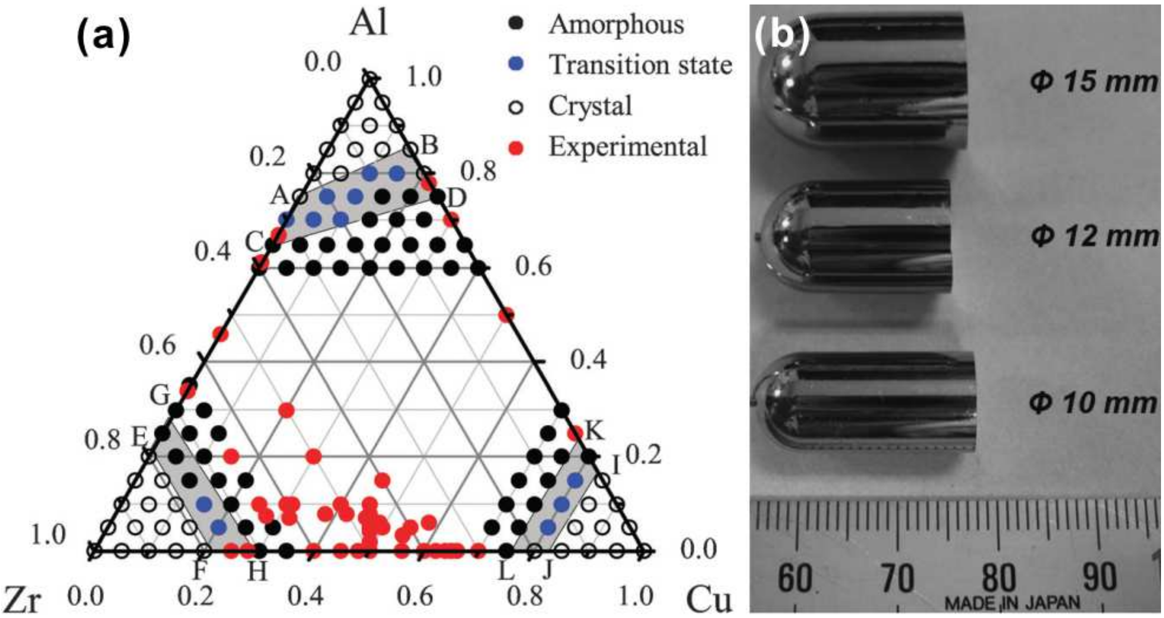

Figure 1.22 *(a) The crystal-amorphous state phase diagram for the Cu–Zr–Al ternary system, (b) outer shapes of as-cast* $Cu_{47}Zr_{45}Al_8$ *rods with diameters of 10-15 mm [284, 292, 293].*

Additionally, the equiatomic CuZr intermetallic compound has different metastable structures, i.e. the high-temperature B2 CuZr phase with a cubic primitive structure (Pm-3m), and monoclinic martensites ($P2_1/m$ and Cm) [294] (Figs. 1.23a-c). As shown in Figs. 1.23, the lattice parameter of the parent B2 CuZr phase is a = 0.3262 nm. Meanwhile, the lattice parameters of the basic structure and of the superstructures of the martensites are a = 0.3278 nm, b = 0.4161 nm, c = 0.5245 nm and β = 103.88°, and a = 0.6316 nm, b = 0.8562 nm, c = 0.5331 nm and β = 105.27°, respectively [294].

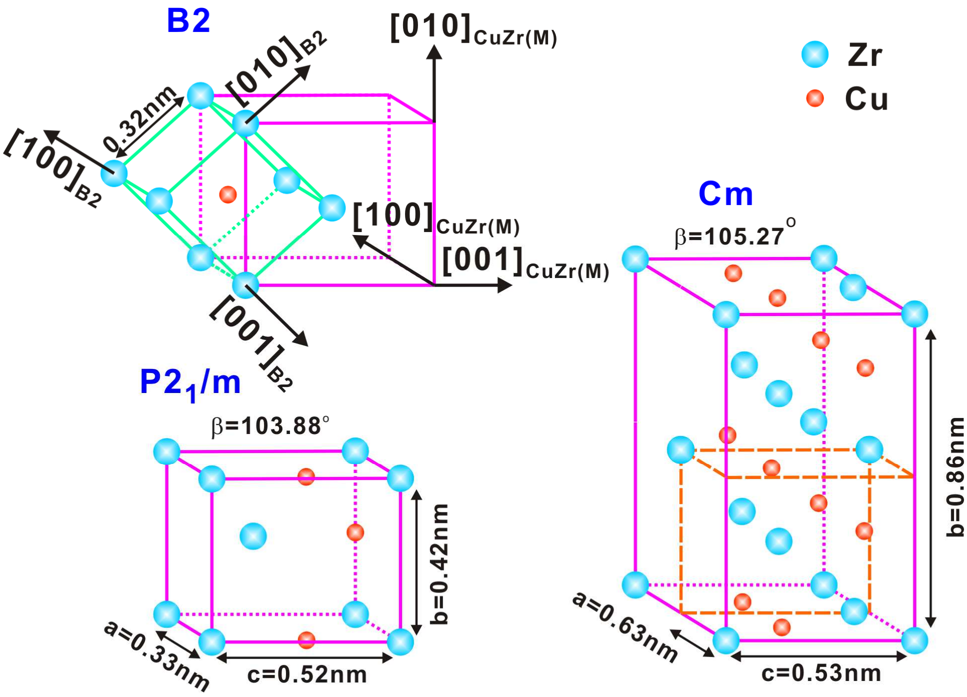

Figure 1.23 *The crystalline structures of the B2 CuZr, $P2_1/m$, and Cm phases [294].*

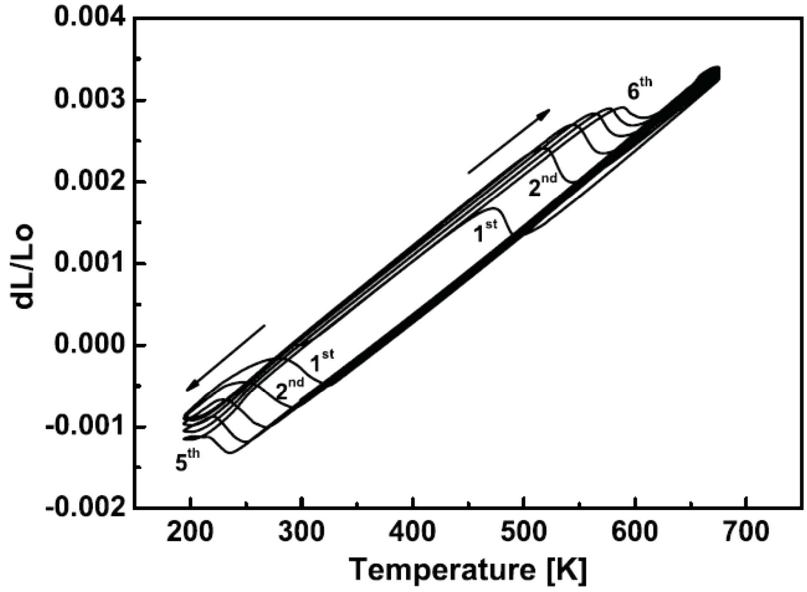

Figure 1.24 *Dilatometer results of a $Cu_{47.5}Zr_{47.5}Al_5$ sample annealed for 16 h at 1073 K [295].*

During deformation or cooling [295, 296], the B2 CuZr phase transforms into martensites (Fig. 1.24). However, it was found that only CuZr-based alloys with a Cu-to Zr ratio of 1:1 exhibit the MT during deformation or thermal treatment [294, 297-299]. Furthermore, the B2 CuZr phase is a line compound. Hence, any compositional deviation will affect the MT when the minor elements are introduced into $Cu_{50}Zr_{50}$ binary alloys. On the other hand, the B2 CuZr phase is not stable at room temperature for most of CuZr-based alloys [294, 297-299].

For example, the B2 CuZr phase in binary $Cu_{50}Zr_{50}$ alloy exists above the temperature 988 K [293], and below it, the B2 CuZr phase decomposes into the low-temperature equilibrium phases, such as $Cu_{10}Zr_7$ and $CuZr_2$. However, under rapid quenching conditions, this eutectoid decomposition may be avoided and thus the B2 CuZr phase may be reserved to room temperature [294, 297-299]. In other words, CuZr-based glass-forming alloys are good candidates to fabricate BMG composites showing the TRIP effect.

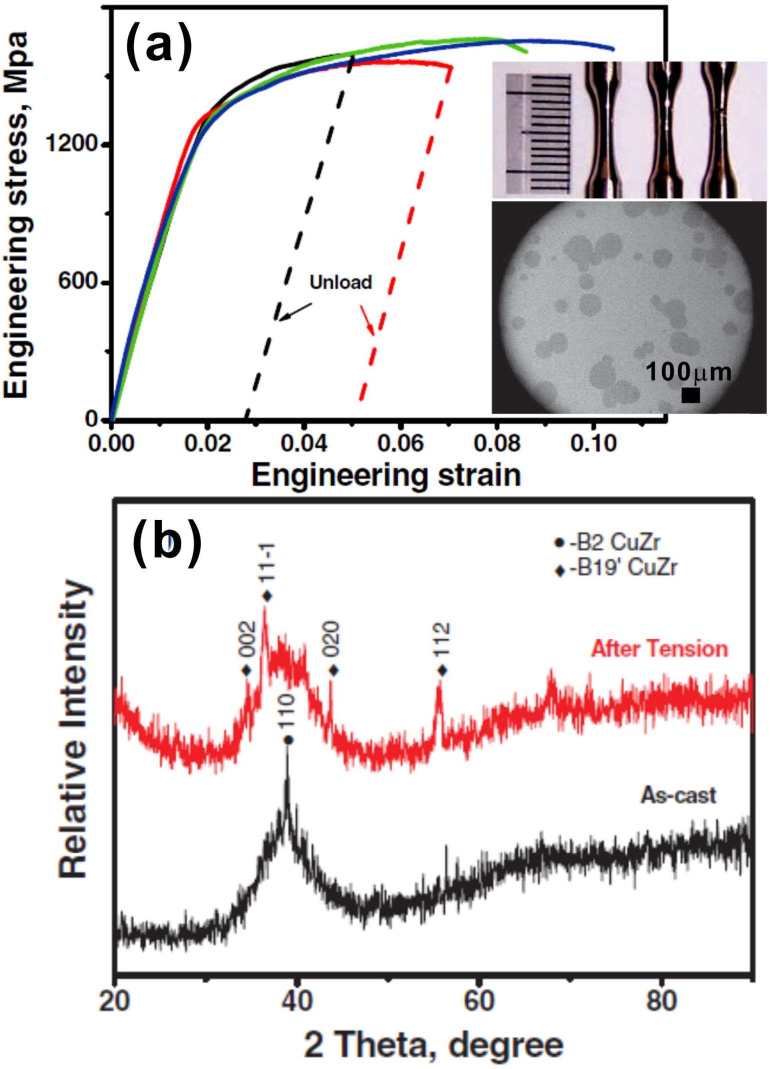

Figure 1.25 *(a) Tensile stress–strain curves of Cu-Zr-Al-Co BMG composites, (b) XRD pattern from the as-cast and the deformed samples, respectively. Redrawn from [301].*

So far, a series of ductile CuZr-based BMG composites with significant plastic deformability and pronounced work hardening have been tested under both compression and tension tests (Fig. 1.25a) [295, 300, 301]. It can be seen (the lower insets) that the B2 CuZr phase (dark areas) precipitates in the glassy matrix, which was also confirmed by the XRD measurement (Fig. 1.25b). Only a sharp crystalline peak of the B2 CuZr phase superimposed on a diffuse diffraction maximum shows that the samples consist of some B2 CuZr crystals and a small amount of amorphous phase. Compared with the as-cast samples (Fig. 1.25b), the samples after tension shows some crystalline peaks of martensitic CuZr crystals, implying that the B2 CuZr phase can undergo the MT from a B2 structure into its martensitic phases, a process which is accompanied by the formation of nano-scaled twins (Fig. 1.26a) [295, 300, 301]. Furthermore, it can be seen from Fig. 1.26b that multiple shear bands deflect at the interface between the crystals and the glassy matrix and then divide into many shear bands around the B2 CuZr phase. A finite element analysis results have shown that the presence of the B2 CuZr phase in the glassy matrix can effectively distribute the plastic strain more homogeneously in the glassy matrix during deformation (Fig. 1.26c) [300].

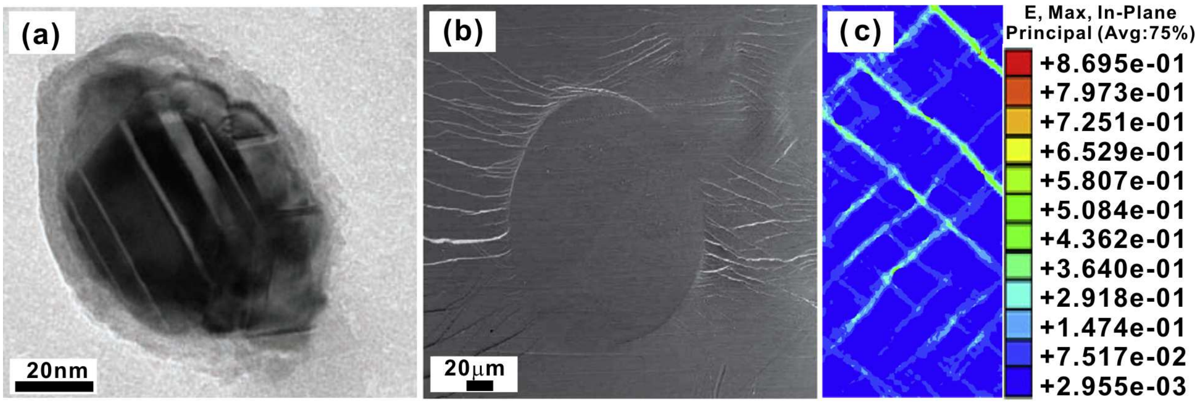

Figure 1.26 *(a) the formation of twins, (b) the formation of multiple shear bands, and (c) the stress distribution induced by the B2 CuZr phase during deformation. Taken from [300, 301].*

Nevertheless, it can be concluded that the existence of the B2 CuZr phase is vital for the fabrication of CuZr-based BGM composites with good deformability. However, there are still many open questions, which motivate this work: (1) to measure the tendency of CuZr-based alloys to form BMG composites containing the B2 CuZr phase, (2) to fabricate novel CuZr-based BMG composites, (3) to effectively optimize the microstructures of CuZr-based BMG composites, i.e. the distribution and size of the B2 CuZr phase, in order to improve the mechanical properties, (3) to understand the physical mechanisms determining the yielding and subsequent plastic deformation of CuZr-based BMG composites.

2 Experimental techniques

2.1 Sample preparation

In order to achieve a systematic understanding of the formation and thermal stability of CuZr-based glass-forming alloys, different CuZr-based alloy systems were chosen as follows: $Cu_{50}Zr_{50-x}Co_x$ (x =2 and 5), $Cu_{45}Zr_{45}Co_{10}$, $(Cu_{0.5}Zr_{0.5})_{100-x}Ag_x$ (x = 0, 2, 6 and 10), $(Cu_{0.5}Zr_{0.5})_{100-x}Al_x$ (x = 4, 5, 6, 8 and 10), $Cu_{50}Zr_{50-x}Ti_x$ (x = 2.5, 7.5 and 10), $(Cu_{0.5}Zr_{0.5})_{100-x}A_{10}Co_x$ (x = 4, 5 and 6), $Cu_{47.5}Zr_{48}Al_4Co_{0.5}$, $(Cu_{0.5}Zr_{0.5})_{100-x}(Al_{0.5}Ag_{0.5})_x$ (x = 1, 2, 3, 4, 5, 6, 7, 8 and 10), $(Cu_{0.5}Zr_{0.5})_{100-x}(Al_{0.5}Ni_{0.5})_x$ (x = 3, 4 and 5), $Cu_{42}Zr_{46}Co_8Ti_4$, $Cu_{46}Zr_{42}Al_7Y_5$, $Cu_{43}Zr_{57}Al_{11}Y_{4.6}$, $Cu_{45}Zr_{42.55}Al_9Y_{3.45}$ and $Cu_{46.25}Zr_{44.25}Al_{7.5}Er_2$, $(Cu_{47.5}Zr_{47.5}Al_5)_{0.98}(T_{50}W_{50})_{0.02}$.

Prior to pre-alloying, all the constituting elements (≥ purity 99.99%) were ground using a grinding paper and then cleaned with ethanol in an ultrasonic bath. The amounts of the constituting elements were weighed using a Mettler Toledo AT200 and the accuracy is about 0.001 g.

2.1.1 Arc melting/suction casting

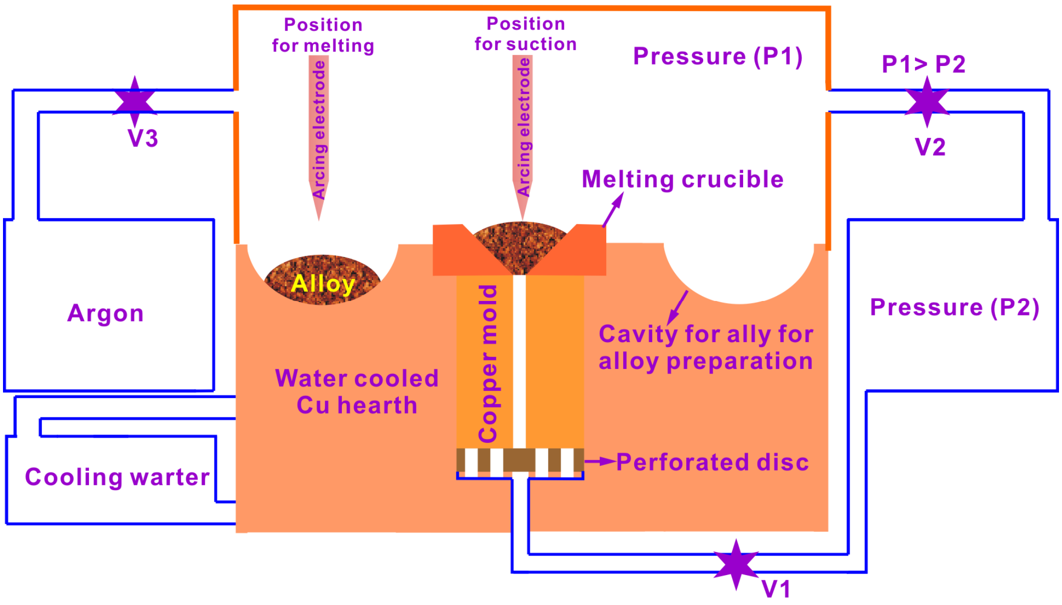

Figure 2.1 *Schematic diagram of the arc melting/casting machine [302, 303].*

Arc melting/suction casting was used in the preparation of BMGs and their composites [302, 303]. The device contains four main components as shown in Fig. 2.1. The first part is a large chamber connected with a mechanical vacuum pump and a molecular vacuum pump. Using these pumps, the vacuum pressure of the chamber can be achieved to be 10^{-5} - 10^{-6} mbar in 40 - 90 min. The second part is the water-cooled copper hearth together with a cavity for the Cu-mold. The third part is the arcing electrode to melt the ingots. The casting temperature is controlled by changing the maximum power, i.e. the melting current/time. The melting current can be increased from 0 A to 280 A, while the melting time is controlled by the operator using a stopwatch. The fourth part is the cooling system. Using this machine, rods with different diameters and a length of about 80 mm and the plates with dimensions of 1 (or 1.5 or 2) mm × 10 mm × 60 mm can be fabricated. A mini suction casting device (Edmund Bühler GmbH) was also used.

2.1.2 Centrifugal casting

Fig. 2.2 shows the centrifugal casting equipment. As the chamber with the copper mold is rotated around its axis after ingots are melted totally, the molten metal is centrifugally thrown towards the inside copper mold wall where it solidifies after cooling quickly. This casting machine mainly contains two components: (1) a centrifugal chamber where the centrifugal arm and the induction coil are located; (2) a high-frequency generator (Fig. 2.2a).

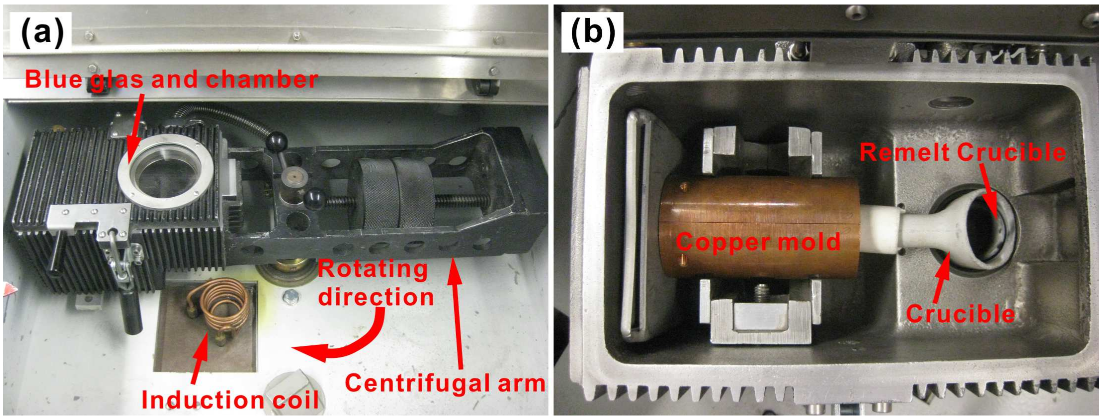

Figure 2.2 *(a) The centrifugal casting facility and (b) the melting and casting parts.*

Prior to the experiment, a smooth run was obtained by adjusting the counter weight, and then the copper mold and the ceramic (Al_2O_3) crucible were put into the chamber (Fig. 2.2b). When the vacuum of the chamber reached 10^{-5} - 10^{-6} mbar using a mechanical vacuum pump and a molecular vacuum pump, argon was filled into the chamber. After that, the high-frequency generator heated the sample to the required temperature which is measured by an infrared-spectral pyrometer. Then the generator was switch off and the centrifugal casting can be started. The melting temperature is about 1523 K for CuZr-based alloys, and the working vacuum pressure is about 250 mbar. The rotation speed is about 500 rpm.

2.1.3 High-frequency melting/injection casting

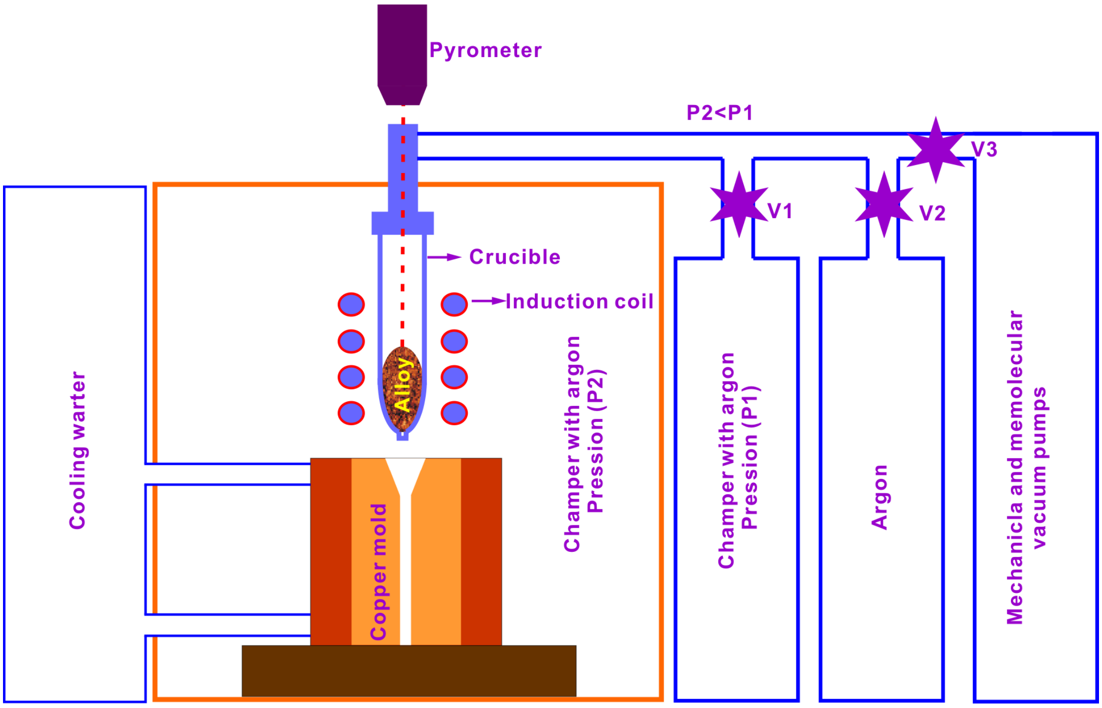

Figure 2.3 *The schematic diagram of the high-frequency melting/injection casting machine [304].*

As shown in Fig. 2.3, the high-frequency melting/injection casting machine has two chambers, i.e. one chamber where the induction coil and copper mold are set up, and another chamber containing argon gas at a larger pressure (P1). The chamber is evacuated to 10^{-5} - 10^{-6} mbar using a mechanical vacuum pump and a molecular vacuum pump. A cylindrical quartz tube with a hole of about 1-6 mm in diameter at the bottom was used. During experiments, argon filled the chamber until the pressure P2 was less than P1. After the high-frequency furnace started to heat the sample to about 200 K above T_L, the V1 was opened while the V2 and V3 were shut down. The melt was ejected into the water-cooled copper mold.

2.1.4 Melt spinning

Melt spinning is a widely used technique to prepare glassy metallic ribbons (Fig. 2.4). Pieces of ingots are put into a quartz tube having a rectangular slit at its bottom. The position between the tip of the tube and the top surface of the copper wheel was adjusted manually. When the vacuum was evacuated to 10^{-5} - 10^{-6} mbar, the vacuum pump was stopped, and then the argon was filled into the chamber whose pressure was less than in the ejecting chamber. After ingots were heated to about 200 K above T_L using an induction coil, the copper wheel was rotated at an angular velocity of 40 ms^{-1}. As the melt spinning started, a thin stream of liquid was dripped onto the wheel and cooled, resulting in the formation of ribbons with a width of approximately 3 - 4 mm and a thickness of 35 ± 5 μm.

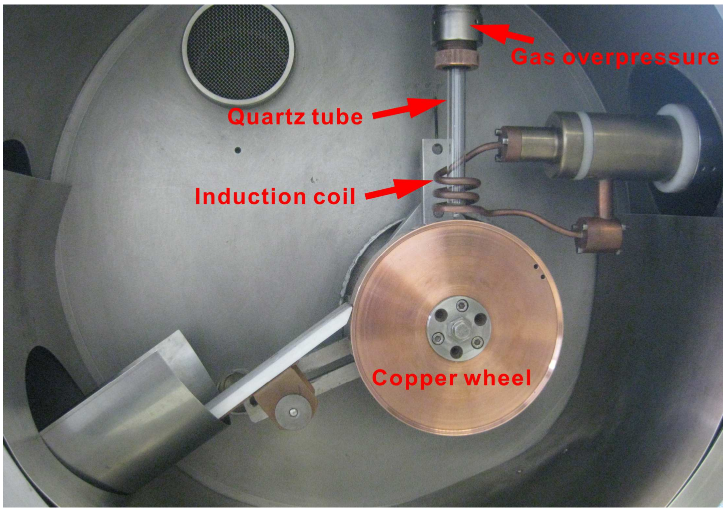

Figure 2.4 *Picture of a melt spinning machine.*

2.1.5 Ball milling and powder consolidation

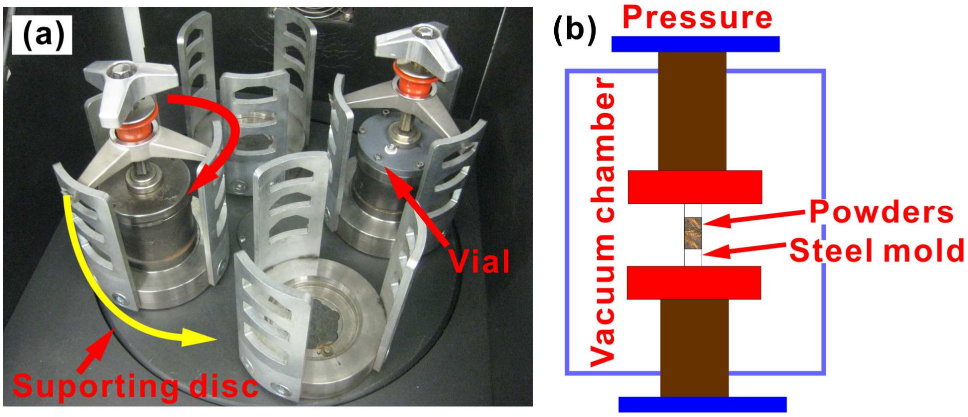

Figure 2.5 *(a) Picture of a ball mill machine and (b) the schematic diagram of a powder consolidation machine [305].*

A ball milling machine (Fig. 2.5a) is one of the grinders used to grind materials into extremely fine powder [305]. The milling experiment begins with loading the pre-materials and the steel balls into a milling vial. The rotating speed is 150 rpm. The pre-material used is about 15 - 25 g and the size of the steel balls is about 10 mm in a diameter. The ball-to-alloy mass ration is 10:1. The milling was carried out in 15 min milling intervals interrupted by 15 min breaks, and the total milling time was about 6 hours. In the following step, the powders were extruded to be a bulk sample without sintering using a consolidation machine (Fig. 2.5b).

2.2 Structure characterizations

2.2.1 X-ray diffraction

A standard X-ray diffraction (XRD) analysis was carried out to identify the phase formation of the samples. The crystalline phases can be identified using the PDF-4+ 2010 database of the International Center for Diffraction Data (ICDD) [306]. Three types of XRD machines were used. The first one is an XRD device (STOE STADI P) equipped with Mo-$K\alpha_1$ radiation (λ = 0.07093187 nm) working in a transmission geometry, and the other is a XRD device (PANalytical X'Pert Pro Diffraction) in reflection mode using Co-K_α radiation (λ = 0.178897 nm). For the former XRD, the samples for this XRD machine were ground to thicknesses less than 100 μm. The diffracted intensities were recorded between 5 and 50 degrees (2θ) in a step mode with a step size of 2θ = 0.5° and the data acquisition time per step was 30 - 40 s. For the latter, the surface of the sample was ground using 800 and 1200 grit grinding papers, respectively. The measurements were conducted in a step mode with a step size of 0.05° and 10 - 20 s per step between 20 and 110 degrees (2θ). The diffractometer is operated at a voltage of 40 kV and a current of 40 mA. Moreover, the *in situ* deformation of CuZr-based alloys were also investigated by high-energy X-ray diffraction (λ = 0.0123984 nm) at the beam line BW5 of HASYLAB in Hamburg, Germany.

2.2.2 Optical microscopy and scanning electron microscopy

The optical microscope (OM) is one of the fundamental tools for phase identification [302]. In our case, OM experiments were performed with a Zeiss Axiophot microscope (Carl Zeiss AG). The samples were mounted in a special conductive resin by using a Bühler Simplimet 3000 apparatus, and ground and polished carefully using a Struers Rotopol polishing machine. After being polished, the samples were cleaned with ethanol in an ultrasonic apparatus and then dried with hot air. A scanning electron microscope (SEM) is an instrument that produces magnified images of a sample using a focused beam of electrons [307, 308] . As shown in Fig. 2.6, a beam of electrons is produced by an electron gun, and passes through the microscope under high vacuum conditions. During this process, several electromagnetic lenses focus the beam down toward the sample. When the beam reaches the surface of the samples, different electrons and rays are ejected, which are collected and then converted into signals. Two types of SEMs were employed. One is a Zeiss Gemini 1530 (Carl Zeiss AG) microscope equipped with an energy-dispersive X-ray (EDX) device (Bruker AXS) and the electron backscatter diffraction (EBSD) device (Oxford). The other one is a Hitachi TM1000 SEM machine attached with an energy-dispersive X-ray (EDX) device. All the samples were cleaned well with the ethanol in an ultrasonic apparatus before observations.

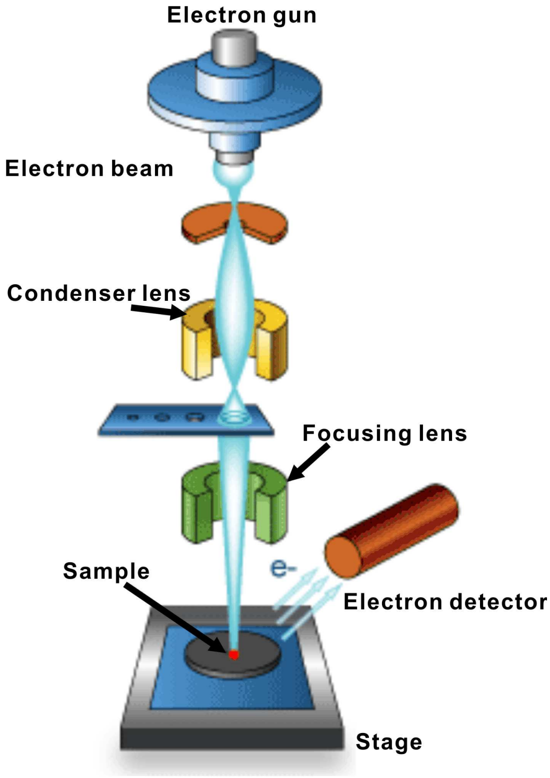

Figure 2.6 *Sketch map of the working principle of SEM. Redrawn from Ref. [308].*

2.2.3 Transmission electron microscopy

For the transmission electron microscope (TEM), the electron source is produced by heating a tungsten filament. The beam of electrons is transmitted through an ultra thin sample, interacting with the sample as it passes through. According to the electrons transmitted through the specimen, an image is formed, magnified, and focused by an objective lens and appears on an imaging screen. Prior to the observations, an ion-milling machine is used to thin the samples. A thin slice for TEM observations is first cut from the original sample, and then thinned to a thickness of approximately 1 μm using a grinding machine. The pre-thinned sample is attached to a Cu-grid and thinned to less than 100 nm by an ion-milling machine (Gatan 691 precision ion polishing system) cooled with liquid nitrogen. The ion beam energy used was 2.5 keV and the ion milling duration was 3 - 4 h with an angle between 2° and 4°. Afterwards, the TEM is used to observe the microstructures using a Tecnai F30 microscope equipped with a field emission gun and operated at an accelerating voltage of 300 kV.

2.3 Thermal analysis

2.3.1 Differential scanning calorimetry

Differential scanning calorimetry (DSC) is a thermoanalytical device to measure the heat flow into or out of a sample relative to a reference upon heating [309]. Here, three DSC devices were employed: a Netzsch DSC 404 C, a Diamond DSC (Perkin Elmer), and a Pyris1 DSC (Perkin Elmer). All the devices were operated under Ar atmosphere. In order to investigate the phase transformation at high temperatures, a Netzsch DSC 404 C apparatus was used at heating rate of 20 K/min. Both the heating and cooling processes were recorded to determine the liquidus temperature, T_L. For the measurements, Al_2O_3 crucibles were used to heat to 1573 - 1773 K. Graphite crucibles were used if the samples react with the Al_2O_3 crucibles at high temperatures. In order to check the glass transition and crystallization behavior, a Diamond DSC (Perkin Elmer) device was used using Al or Al_2O_3 crucibles. In order to investigate the MT during heating, DSC measurements were conducted using a Pyris 1 DSC (Perkin Elmer) machine whose construction is similar to the Diamond DSC device except that it has a liquid nitrogen cooling system, which allows to access temperatures as low as 173 K.

2.3.2 Dilatometry

A dilatometer is an instrument to measure length changes as a function of temperature [310]. The dilatometer measurements were conducted using a Netzsch DIL402 C/1/G under an Ar atmosphere with a liquid nitrogen cooling system at a heating rate of 10 K/min. The length of the samples for the dilatometry was 25 mm and they had a diameter of 3 mm. The top and bottom of the samples were carefully ground to be parallel with each other and be perpendicular to the cylinder axis.

2.4 Measurement of the elastic constants

The elastic constants are measured by an ultrasound velocity detector (Olympus, Panametrics-NDT 5900PR) [302]. Before the measurement, the density of the sample was measured using an in-house designed apparatus based on the Archimedean principle. The height of the sample was measured by a micrometer screw. During the measurements, the longitudinal wave has a frequency of 100 MHz, while the shear wave processes a frequency of 20 MHz. The measurement for each wave was conducted for at least 100 times and then corresponding elastic constants can be calculated.

2.5 Compression and tensile tests

In order to determine the mechanical properties of the present samples at room temperature, compression and tension tests were conducted in an Instron 5869 testing machine with a laser-extensometer (Fiedler Optoelektronik GmbH). For compression tests, rods or plates were cut into a standard sample with an aspect ratio of approximately 2. The top and bottom were parallel to each other and must be perpendicular to the cylinder axis. During the compression tests, the initial strain rate is approximately 10^{-4} s^{-1}, while the cross-head speed is 0.001 mm/s. For the tensile test, the samples were cut into a dog bone shape and were fixed in custom-made grips. The length of the samples is about 4 cm and the gauge width is about 2 mm (Fig. 2.7). At a constant cross head speed of 0.015 mm/s during the tensile tests, the initial strain rate is approximately 10^{-4} s^{-1}. The yield strength is defined as the critical stress corresponding to the yielding plastic strain together with a 0.2% strain offset. The Young's modulus can be determined directly from the slope of the stress-strain curve in the elastic stage [311, 312].

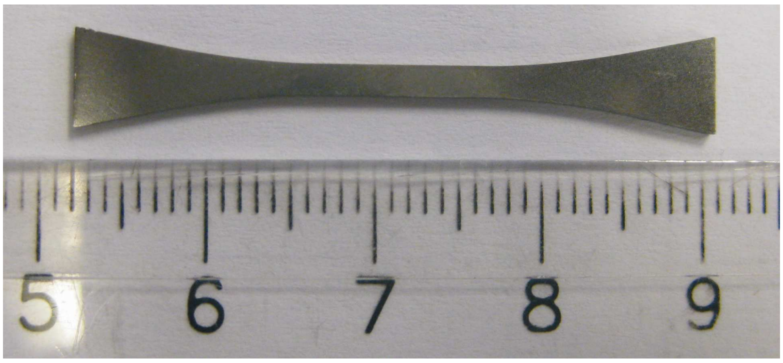

Fig. 2.7 Dimension of the tensile sample.

3 Strategy for pinpointing the formation of CuZr-based BMG composites

Even though significant plastic deformability and pronounced work hardening can be obtained in CuZr-based BMG composites containing B2 CuZr crystals in the glassy matrix under both compression and tension tests [295, 300, 301], one of the biggest challenges in developing new CuZr-based shape memory BMG composites is manipulating the formation of the B2 phase during rapid quenching. It is a particularly demanding task to establish a strategy for pinpointing the formation of CuZr-based BMG composites instead of performing tedious trial and error experiments. Consequently, it is necessary to establish a strategy for pinpointing the formation of ductile CuZr-based BMG composites.

3.1 Theoretical analysis for the formation of CuZr-based BMG composites

As shown in Fig. 3.1a, the B2 CuZr phase in the binary $Cu_{50}Zr_{50}$ alloy is a high-temperature line phase, which decomposes into the low-temperature equilibrium phases (LT-EPs), i.e. $Cu_{10}Zr_7$ and $CuZr_2$, in a eutectoid reaction at 988 K [293]. In order to preserve the B2 CuZr phase at room temperature, it is necessary to bypass this decomposition during quenching. Fig. 3.1b shows a schematic continuous cooling transformation (CCT) diagram for this alloy system. It can be seen that two important factors have to be considered for the formation of CuZr-based BMG composites, i.e. the formation of the amorphous phase and the B2 CuZr phase. On the one hand, the formation of amorphous phase is usually determined by the stability of the liquid phase and its resistance to crystallization [61, 62]. Different GFA parameters are available to evaluate the formation of the amorphous phase [61, 62], such as T_{rg} and γ (see **Chapter 1.2**). On the other hand, during quenching, the supercooled liquid (i.e. the predecessor of a glass) competes with the B2 CuZr phase and the LT-EPs. When the cooling rate is higher than the critical cooling rate for fully glass formation (R_c) (Fig. 3.1b), only the amorphous phase is observed. On the contrary, the LT-EPs are obtained under much lower cooling rates. In such a case, an appropriate cooling rate is required in order to obtain the B2 CuZr phase and the amorphous phase simultaneously (Fig. 3.1b). If some characteristic temperatures related to the formation of the B2 phase can be found, the formation of CuZr-based BMG composites might become predictable in combination with GFA parameters.

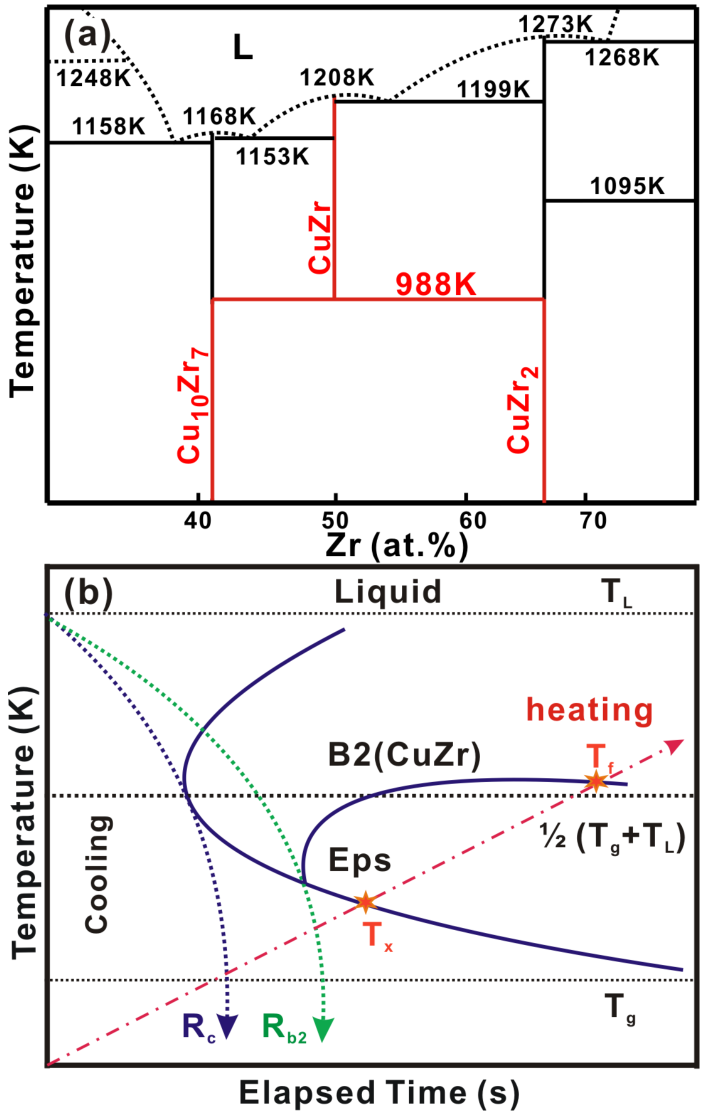

Figure 3.1 *(a) Phase diagram of Cu-Zr alloys, and (b) Schematic CCT diagram during the quenching process illustrating the formation of CuZr-based BMG composites. (a) Taken from [293].*

According to the binary Cu-Zr phase diagram (Fig. 3.1a) [293], there is a eutectoid transformation at a high temperature (i.e. 988 K). This eutectoid decomposition may be also influenced by adding minor elements to CuZr-based alloys. Therefore, the eutectoid transformation temperature may have a relationship with the formation of the B2 CuZr phase. As shown in Fig. 3.1b, when the eutectoid decomposition temperature (T_f) is relatively low, the thermal stability of the B2 CuZr phase becomes higher. Therefore, the B2 CuZr phase is prone to precipitate during cooling, which deteriorates the GFA. In this regard, 11 CuZr-based alloy systems, altogether 36 different compositions were chosen to check the effect of minor elements on this eutectoid decomposition (Table 3.1).

Table 3.1 *Thermodynamic parameters of the 36 different alloys investigated.*

Type	Alloy systems	No.	T_s (K)	T_f (K)	T_L (K)	T_f-T_s	T_s/T_L	K=T_f/T_L
I	$Cu_{45}Zr_{45}Co_{10}$	1	—	748±2	1399±2	—	—	0.535
	$Cu_{42}Zr_{46}Co_8Ti_4$	2	—	764±2	1343±2	—	—	0.568
	$Cu_{50}Zr_{45}Co_5$	3	—	764±2	1330±2	—	—	0.574
	$Cu_{42}Zr_{42}Al_{10}Co_6$	4	—	799±2	1249±2	—	—	0.640
	$Cu_{43}Zr_{43}Al_{10}Co_4$	5	—	803±2	1241±2	—	—	0.647
	$Cu_{42.5}Zr_{42.5}Al_{10}Co_5$	6	—	801±2	1239±2	—	—	0.647
II	$Cu_{50}Zr_{48}Co_2$	7	928±2	974±2	1275±2	46±2	0.728	0.764
	$Cu_{47.5}Zr_{48}Al_4Co_{0.5}$	8	957±2	985±2	1208±2	28±2	0.792	0.815
	$Cu_{50}Zr_{50}$	9	998±2	1013±2	1226±2	15±2	0.814	0.826
	$Cu_{48}Zr_{48}Al_4$	10	977±2	996±2	1206±2	19±2	0.810	0.826
	$Cu_{46}Zr_{46}Al_4Ni_4$	11	980±2	1000±2	1197±2	20±2	0.819	0.835
	$Cu_{45}Zr_{45}Al_5Ni_5$	12	981±2	1001±2	1196±2	20±2	0.820	0.837
	$Cu_{47}Zr_{47}Al_3Ni_3$	13	978±2	1003±2	1191±2	25±2	0.821	0.843
	$Cu_{50}Zr_{47.5}Ti_{2.5}$	14	1009±2	1028±2	1209±2	19±2	0.835	0.850
	$Cu_{49}Zr_{49}Al_1Ag_1$	15	998±2	1036±2	1211±2	38±2	0.824	0.855
	$Cu_{48}Zr_{48}Al_2Ag_2$	16	1006±2	1050±2	1194±2	44±2	0.843	0.874
	$Cu_{49}Zr_{49}Ag_2$	17	1029±2	1073±2	1212±2	44±2	0.849	0.885
	$Cu_{47.5}Zr_{47.5}Al_5$	18	981±2	1055±2	1184±2	74±2	0.828	0.891
	$Cu_{50}Zr_{42.5}Ti_{7.5}$	19	1039±2	1055±2	1167±2	16±2	0.89	0.903
	$Cu_{47}Zr_{47}Al_3Ag_3$	20	1021±2	1063±2	1174±2	42±2	0.870	0.906
	$Cu_{47}Zr_{47}Al_6$	21	981±2	1065±2	1174±2	84±2	0.836	0.907
	$Cu_{50}Zr_{40}Ti_{10}$	22	1055±2	1067±2	1151±2	12±2	0.917	0.927
	$Cu_{46}Zr_{46}Al_8$	23	981±2	1073±2	1158±2	92±2	0.848	0.927
	$Cu_{45}Zr_{45}Al_{10}$	24	966±2	1075±2	1158±2	109±2	0.834	0.929
III	$Cu_{46}Zr_{46}Al_4Ag_4$	25	1031±2	1090±2	1154±2	59±2	0.893	0.945
	$Cu_{47}Zr_{47}Ag_6$	26	1090±2	1116±2	1176±2	26±2	0.926	0.949
	$Cu_{46.25}Zr_{44.25}Al_{7.5}Er_2$	27	990±2	1096±2	1156±2	106±2	0.857	0.949
	$Cu_{43}Zr_{41.4}Al_{11}Y_{4.6}$	28	1048±2	1194±2	1194±2	146±2	0.877	1
	$Cu_{46}Zr_{46}Ag_8$	29	—	1214±2	1214±2	—	—	1
	$Cu_{42}Zr_{42}Al_8Ag_8$	30	—	1212±2	1212±2	—	—	1
	$Cu_{45}Zr_{45}Ag_{10}$	31	—	1145±2	1145±2	—	—	1
	$Cu_{45}Zr_{42.55}Al_9Y_{3.45}$	32	1059±2	1121±2	1121±2	62±2	0.945	1
	$Cu_{43}Zr_{43}Al_7Ag_7$	33	—	1184±2	1184±2	—	—	1
	$Cu_{45}Zr_{45}Al_5Ag_5$	34	1046±2	1133±2	1133±2	87±2	0.923	1
	$Cu_{44}Zr_{44}Al_6Ag_6$	35	—	1153±2	1153±2	—	—	1
	$Cu_{46}Zr_{42}Al_7Y_5$	36	—	1003±2	1003±2	—	—	1

3.2 Nature of the eutectoid B2 CuZr transformation

3.2.1 Shift of endothermic peak(s) related to the eutectoid B2 transformation

In order to investigate the eutectoid B2 CuZr transformation in CuZr-based alloys during heating, amorphous ribbons with a thickness of 35 ± 5 μm for the studied alloys were fabricated using melt spinning. Fig. 3.2a show the partial XRD results and it can be seen that no diffraction peaks corresponding to crystalline phases are seen, indicating the fully glassy nature of the studied ribbons. During heating, an endothermic event between the crystallization and the melting peaks is observed for most of the DSC traces in Figs. 3.2b (only selected data are presented). According to the binary Cu-Zr phase diagram [293] (Fig. 3.1a), these endothermic events connect with the eutectoid transformation. The start temperature and the final temperature of the phase transformation are indexed as T_s and T_f, respectively (Fig. 3.2b).

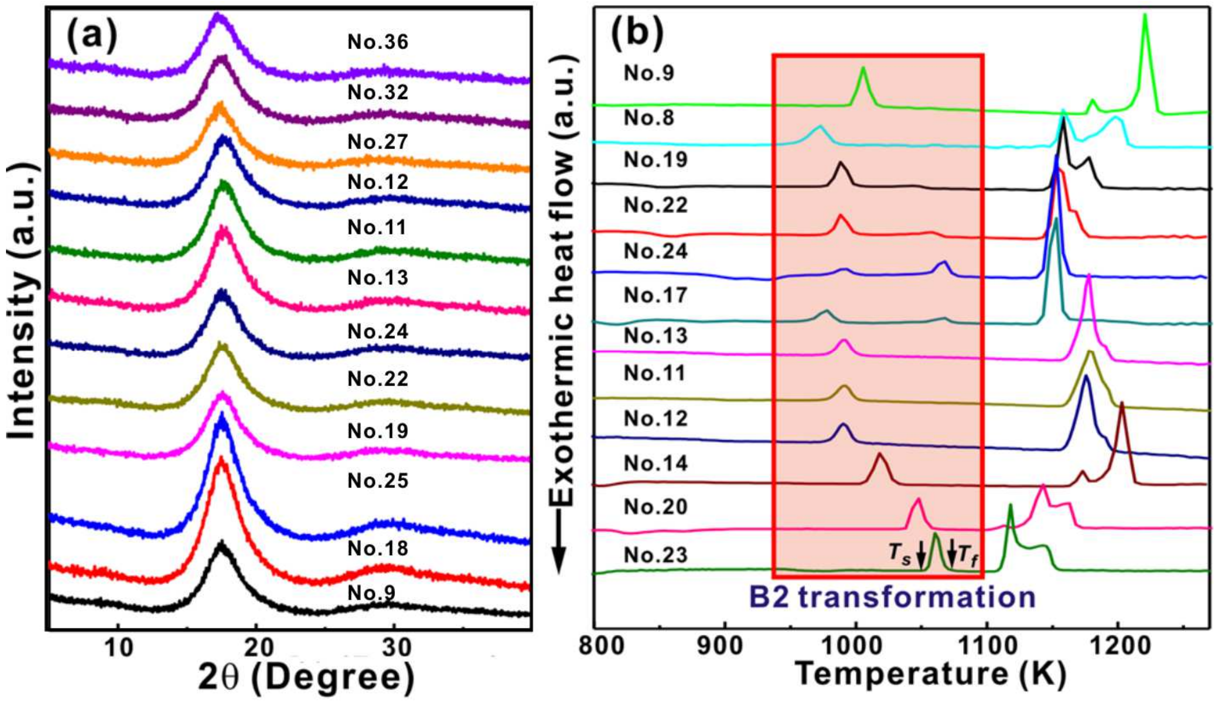

Figure 3.2 *(a) XRD patterns and (b) high-temperature DSC curves of as-quenched ribbons.*

In order to further validate this phase transformation, all the samples were annealed at temperatures below T_s and above T_f, respectively. Fig. 3.3 shows the XRD patterns of samples No. 13, No. 14 and No. 18 annealed below T_s and above T_f. It was found that the crystallization products below T_s are mainly $Cu_{10}Zr_7$ and

$CuZr_2$ (LT-EPs). Meanwhile, the samples annealed above T_f mainly consist of equiatomic CuZr intermetallics (i.e. the B2 CuZr and its martensites) and $Cu_{10}Zr_7$. For the latter samples, the formation of $Cu_{10}Zr_7$ and martensites is expected to result from to the relative slow cooling process in the DSC machine after annealing. As the cooling rate is low, the B2 CuZr phase partially transforms into (1) the thermodynamically more stable monoclinic martensites and (2) the LT-EPs such as $Cu_{10}Zr_7$, and $CuZr_2$. Furthermore, it is also seen that the minor alloying elements such as Al and Ti do not affect the phase formation remarkably compared with the binary $Cu_{50}Zr_{50}$ alloy.

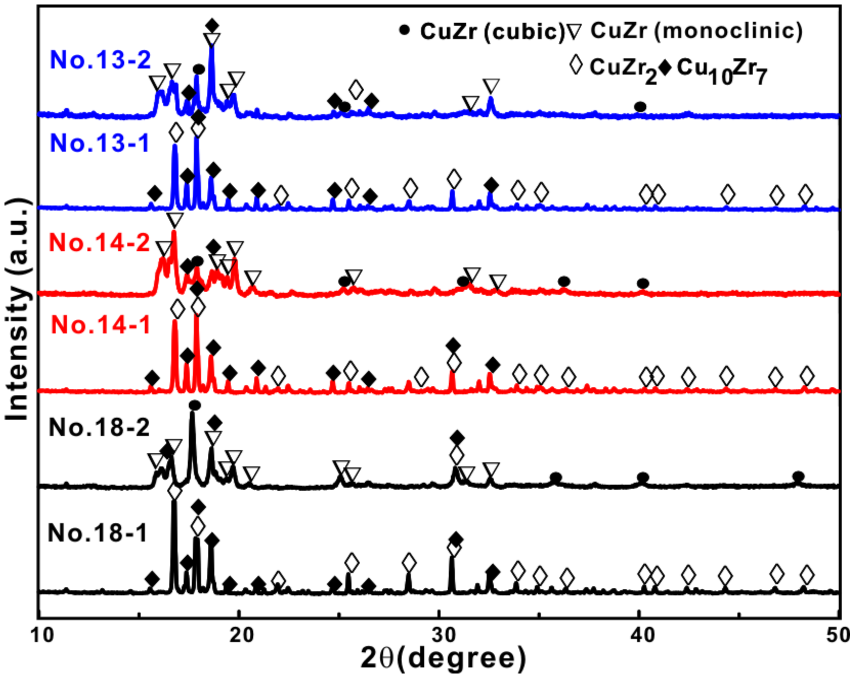

Figure 3.3 *XRD patterns of the as-quenched ribbons annealed below T_s and above T_f, for alloys including Nos. 14-1 and 14-2, 13-1 and 13-2, and 18-1 and 18-2, respectively. (The 14-1, 13-1, and 18-1 samples were obtained after being annealed below T_s, while the 14-1, 13-1, and 18-1 samples were obtained after being annealed below T_f).*

However, as shown in Figs. 3.4a-b, the endothermic peak(s) associated with the eutectoid B2 CuZr transformation in the alloys No. 1, No. 2, No. 4, No. 31 and No. 36 containing Co, Ag, AlAg, AlCo, Y or Er become lower or even disappear gradually with the content of these elements increasing. These samples were also annealed at temperatures exceeding the last crystallization peak (see $T_{cry\text{-}final}$ in Fig. 3.4b). The XRD results show that the B2 CuZr and $Cu_{10}Zr_7$ phases are observed after annealing the sample No. 1 with 10 at.% Co addition above $T_{cry\text{-}final}$

(Fig. 3.4c). For high Co addition, T_s and T_f of the B2 CuZr transformation decrease and eventually this solid phase transformation event starts to merge with crystallization peak(s) at low temperatures, implying that the B2 CuZr phase is stabilized to low temperatures.

In contrast, the B2 CuZr phase does not form any more but only $Cu_{10}Zr_7$, $CuZr_2$, and other crystalline phases are observed when the content of Ag or rare earth (RE) elements is relatively high (Fig. 3.4c). Compared with the DSC trace of $Cu_{50}Zr_{50}$ (No. 9 in Fig. 3.2b), the values of T_s and T_f of the eutectoid B2 CuZr transformation increase with Ti, Ag (AlAg), or AlRE (Er and Y) additions but decrease with the addition of AlNi. However, T_s is reduced while T_f increases with Al addition. For high Ag (AlAg) or low RE (Er and Y) addition, T_s and T_f of the B2 transformation increase and eventually reach T_L.

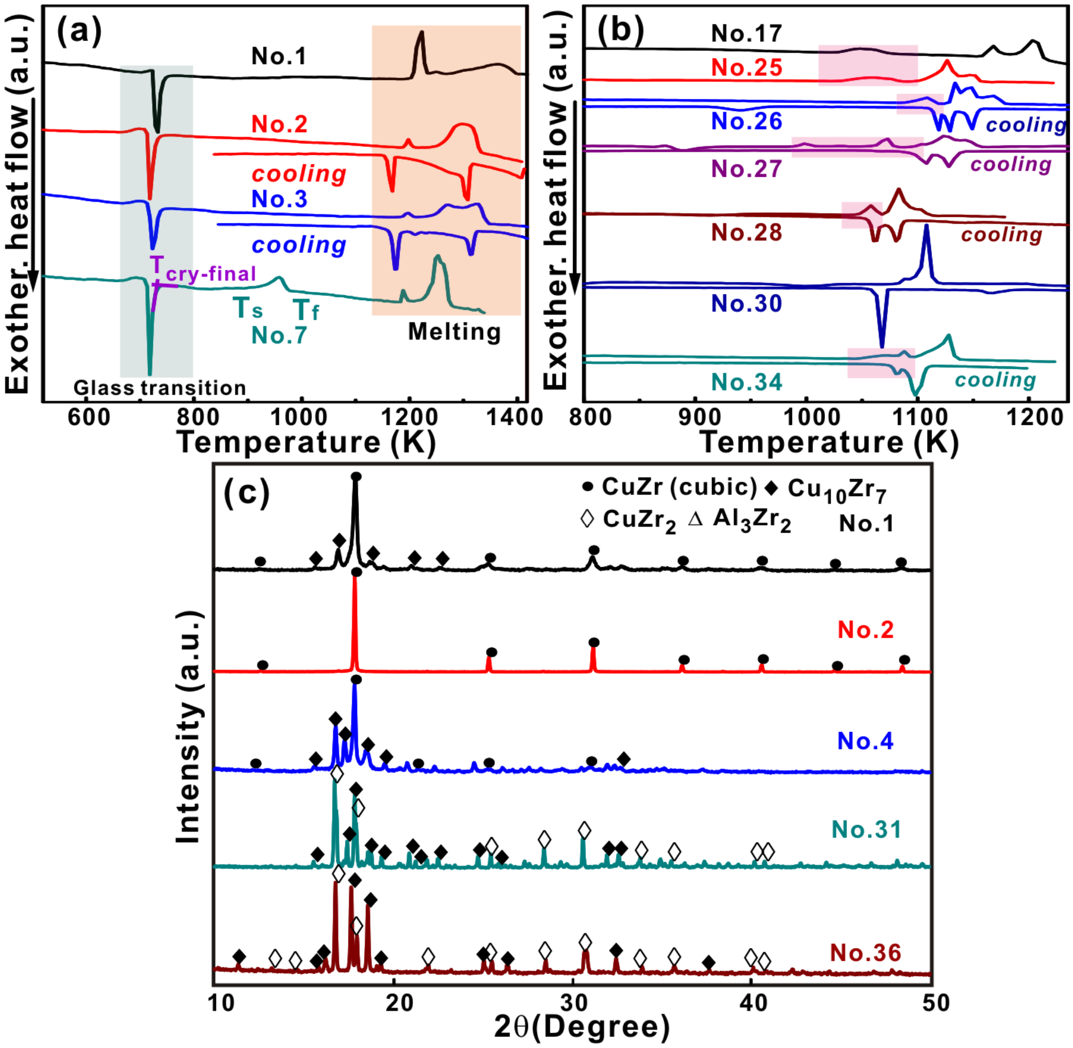

Figure 3.4 *(a-b) DSC curves of the amorphous ribbons with selected compositions and (a) XRD patterns of the sample annealed above $T_{cry\text{-}final}$ for alloys ribbons with selected compositions.*

Therefore, it can be concluded that the change of the decomposition of the B2 CuZr phase strongly depends on the type and the amount of the element addition, implying that the thermal stability of the B2 CuZr phase strongly depends on different (minor) element additions. According to this phenomenon, all the as-studied melt-spun CuZr-based alloys can be classified into three types (Fig. 3.5). For Type I alloys, the eutectoid B2 CuZr transformation starts to overlap and merge with the crystallization event at relatively low temperatures. For Type II alloys, the eutectoid B2 CuZr transformation appears at high temperatures. For Type III alloys, the eutectoid B2 CuZr transformation starts to merge with the melting peak(s) at higher temperatures.

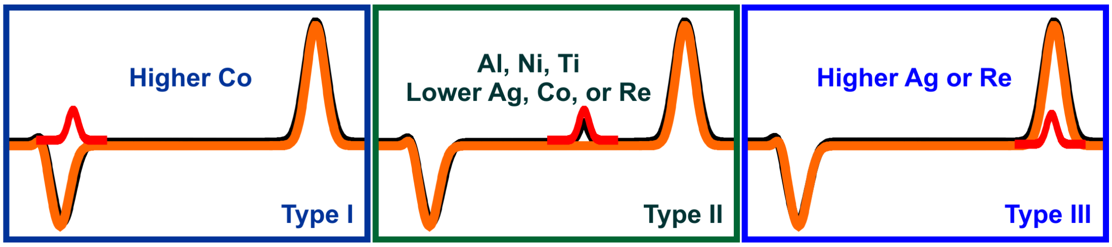

Figure 3.5 *Different types of CuZr-based alloys with the addition of different elements.*

3.2.2 Thermal stability of the B2 CuZr phase

Recent reports have shown that the stability of the B2 CuZr phase is closely associated with its electronic structures [313, 314]. Different minor elements addition can change the bonding nature and bond energies as the additional alloying elements are dissolved into the B2 CuZr phase matrix (Fig. 3.6a) [315]. In order to evaluate the impact of electronic structures on the thermal stability of the B2 phase, the average number of valence electrons per atom (e/a) of the alloys was calculated based on the following equation [316]:

$$e/a = f_A e^A + f_B e^B + f_C e^C , \tag{3.1}$$

where f_A, f_B and f_C represent the atomic fractions of the elements (A, B and C elements) in the alloy, and e^A, e^B and e^C are the number of valence electrons of the A, B and C elements, respectively. Furthermore, the bonding nature between the elements is also reflected by the enthalpy of mixing (ΔH_{mix}) [317] because the minimum in the enthalpy of mixing usually occurs at the compositions corresponding to stable intermetallics [318-322].

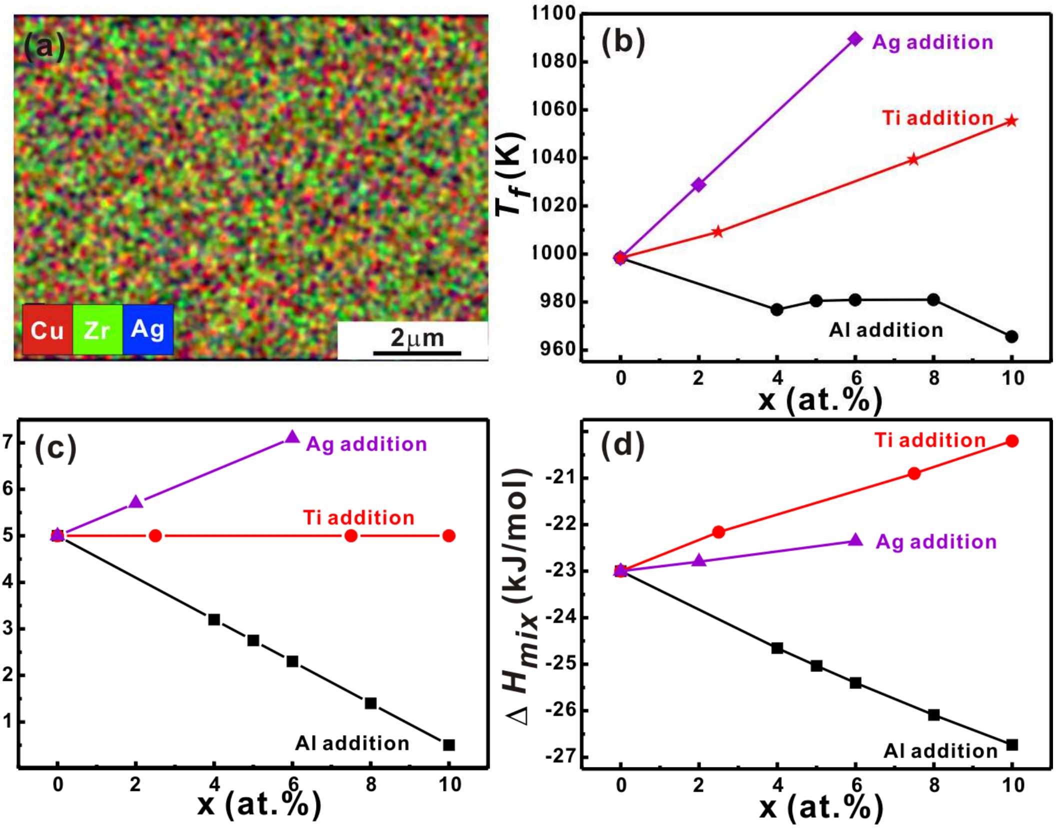

Figure 3.6 *EDX results for alloys (a) No. 29, and correlations between (b)* T_f, *(c) e/a, (d)* ΔH_{mix} *for Cu-Zr-Ag, Cu-Zr-Ti and Cu-Zr-Al alloy systems.*

Fig. 3.6b-d indicates that both the values of e/a and ΔH_{mix} correlate with the changes of T_f for Cu-Zr-Ag, Cu-Zr-Al and Cu-Zr-Ti alloy systems, implying that the T_f is closely related to the thermal stability of the B2 CuZr phase. On the other hand, from the thermodynamic point of view, the driving force for the precipitation from melts also governs the nucleation and growth rate of the B2 phase [318]. The Gibbs energy of the intermetallic CuZr can be expressed by the following equation [323, 324]:

$$ {}^{0}G_{m}{}^{CuZr} = 0.5\,{}^{0}G_{Cu}^{fcc} + 0.5\,{}^{0}G_{Zr}^{hcp} + \Delta G_{f}^{CuZr}, \tag{3.2} $$

where ΔG_f^{CuZr} is the Gibbs free energy of formation per mole of atoms, ${}^{0}G_{Cu}^{fcc}$ and ${}^{0}G_{Zr}^{hcp}$ are the molar Gibbs free energy of *fcc* Cu and *hcp* Zr in the CuZr intermetallics, respectively. Then ΔG_f^{CuZr} is given by $\Delta G_f^{CuZr} = a + bT$, where a and b are the parameters to be evaluated based on some thermodynamic models [323, 324]. According to equations above, the Gibbs free energy of the CuZr compound has a strong relationship with the phase transformation temperature. As additional elements are dissolved in the B2 CuZr phase, the electronic structure of the compound is changed, which results in a change of its Gibbs free energy. In turn, the changes of Gibbs free energy of the compound in different alloys may affect the values of T_f (Fig. 3.6b). Qiu *et al.* [313] calculated the formation energy, being defined as the total energy of the alloy minus the concentration weighted average of the total energies of the pure elements at their equilibrium volumes, for the B2 CuZr phase in Cu-Zr-Al alloys. With the Al content increasing, the formation energy for the B2 CuZr phase in Cu-Zr-Al alloys decreases [313], implying that Al addition plays a decisive role in controlling the formation and stability of B2 phase.

Generally speaking, minor additions are expected to change the formation energy of the B2 CuZr phase, which can impact the thermal stability of the B2 CuZr phase. Therefore, with different elements additions, it becomes difficult for the B2 CuZr phase to decompose into the LT-EPs and to transform into martensites during quenching.

3.3 Formation of the amorphous phase and the B2 CuZr phase

This interesting phenomenon during heating gives some hints to understand the formation of CuZr-based BMG composites. As shown in the CCT diagram (Fig. 3.1b), there are three types of phases, i.e. the metastable B2 phase, the amorphous phase and the LT-EPs, competing with each other during quenching, which are related to the formation of CuZr-based BMG composites. However, partial B2 CuZr phase can transform into martensites due to the thermal stress originating from rapid quenching [297], which also requires to be considered for the formation of CuZr-based BMG composites. However, it was found that CuZr-based BMG composites with the B2 CuZr phase less than 45 vol.% mainly contain the amorphous phase and the B2 CuZr phase. The amount of martensites is very little. Therefore, the competition among the metastable B2 phase, the amorphous phase and the LT-EPs during quenching is the dominant factor for the formation of CuZr-based BMG composites, as shown Fig. 3.1b, the formation of CuZr-based BMG composites is directly connected with the location and the shape of the "nose" of the competing phases in the CCT diagram. This means the actual cooling rate must fall between the R_c (the critical cooling rate for glass formation) and R_{B2} (the critical cooling rate for the B2 phase formation) in order to obtain both the B2 CuZr phase and the amorphous phase.

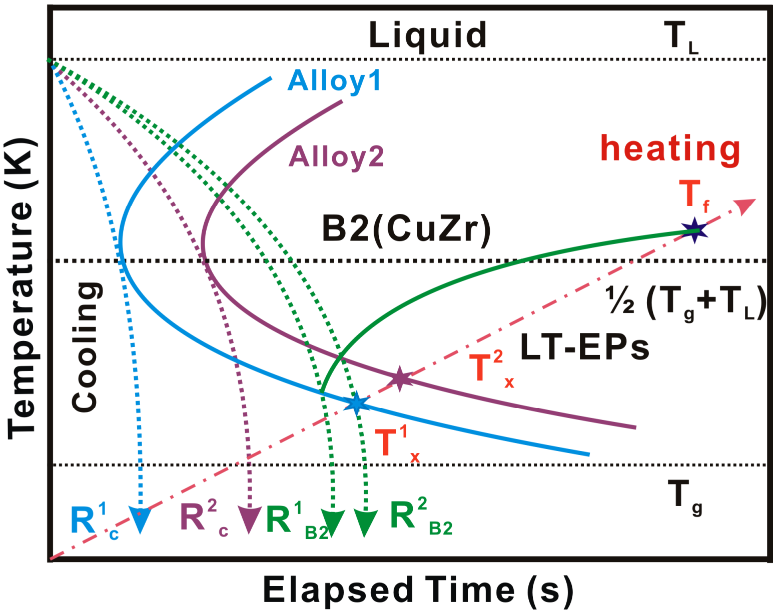

Figure 3.7 *Schematic CCT diagram during quenching process illustrating the formation of the B2 CuZr for two different alloys (Alloy 1 and Alloy 2) with a same T_f but different GFA.*

As shown in Fig. 3.7, the critical cooling rate to obtain a fully austenitic (B2 CuZr) phase for Alloy 1 is larger than that of Alloy 2, i.e. $R^1_{B2} > R^2_{B2}$, assuming T_f are almost the same for Alloy 1 and Alloy 2. This further implies that the formation of CuZr-based BMG composites is associated with the GFA to some extent. Previous results [75, 76] have also shown that the GFA of metallic alloys strongly depends on the thermal stability of supercooled liquid and the resistance to crystallization. By considering both of these factors, Lu and Liu [61, 62] proposed a GFA indicator (γ). Since the γ parameter is derived from the quantities T_x/T_g and T_x/T_L [61, 62], the formation of CuZr-based BMG composites is expected to be also proportional to T_x/T_g and T_x/T_L. T_x/T_g considers the competition between crystallization and vitrification, which is widely used to evaluate the GFA [61, 62]. However, as listed in Table 3.1, the values of T_g and T_x are almost identical for the investigated compositions becase all alloys are Cu-Zr rich. So the formation of CuZr-based BMG composites has a close relationship with the value of the T_x/T_L:

$$BMG\ composites \propto GFA \propto \frac{T_x}{T_L}, \tag{3.3}$$

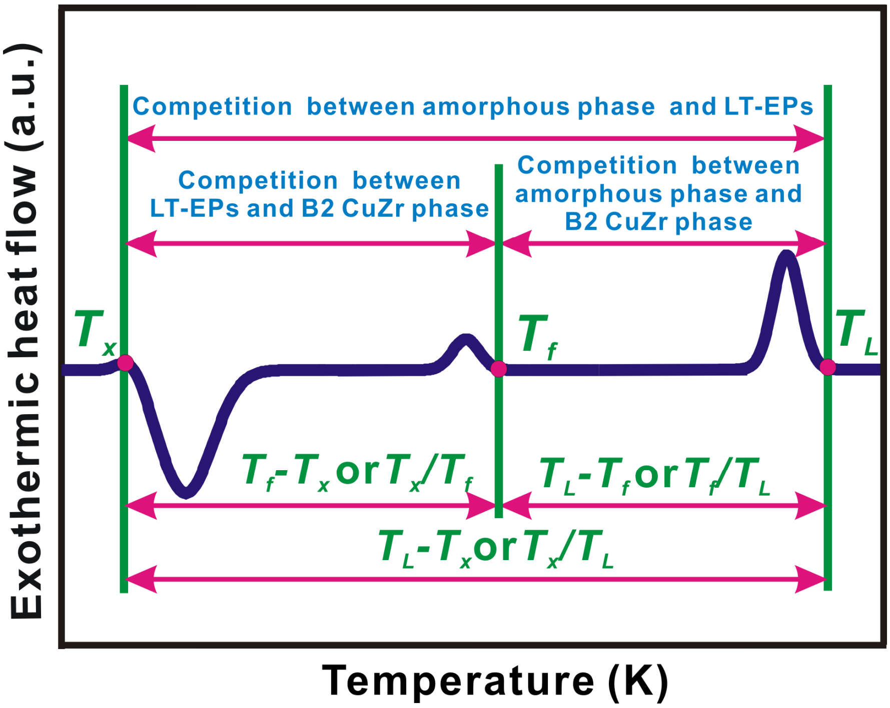

Figure 3.8 *Competitions among amorphous phase, B2 phase and LT-EPs for CuZr-based alloys.*

On the other hand, the formation of the B2 CuZr phase strongly depends on its thermal stability, which may have a relationship with the value of T_f. As the B2 CuZr phase becomes stable, it becomes difficult to decompose into the LT-EPs, leading to a smaller T_f. As listed in Table 3.1, with the value of T_f decreasing, the value of T_L also decreases. It is well know that a smaller T_L can reduce the homogeneous nucleation rate for crystals and then favor the glass formation (being called deep eutectic rule). Furthermore, the T_L of an alloy strongly depends on that of the primary crystalline phases and/or the eutectic structures [293]. In our case, the primary precipitates are the B2 CuZr phase, which indicates that the B2 CuZr phase is connected with the T_L of the alloys, i.e. being related to the formation of amorphous phase to some degree. These considerations can be schematically illustrated in Fig. 3.8, which shows the competition among the amorphous phase, the B2 phase and the EPs for CuZr-based alloys. Therefore, the values of T_f/T_L and T_x/T_f, also requires to be considered to evaluate the formation of the amorphous phase and the B2 CuZr phase.

As T_f shifts towards T_L and is far away from T_x, resulting in the decrease of temperature window between T_L and T_f, there is not enough time for the B2 CuZr phase to decompose into the LT-EPs during quenching. In the opposite case, the

B2 phase altogether with other LT-EPs competes with vitrification during quenching, which can reduce the GFA drastically. Hence, during quenching, for the alloys with a higher T_f and a lower T_x, the amorphous together with the B2 phase is prone to be preserved, while the LT-EPs and the phase B2 trend to be obtained for the samples with a lower T_f and a higher T_x. Therefore, the formation of CuZr-based BMG composites is supposed to be proportional to the values of T_f/T_L and to the inverse of T_x/T_f:

$$BMG\,composites \propto GFA \propto \frac{T_f}{T_L}\left(\frac{T_x}{T_f}\right)^{-1}, \tag{3.4}$$

3.4 A new parameter for pinpointing the formation of CuZr-based BMG composites

According to the discussions above, the formation of CuZr-based BMG composites is directly related to the values of T_f, T_x and T_L. According to Eqs. 3.3 and 3.4, a new dimensionless parameter can be deduced to evaluate the formation of CuZr-based BMG composites, which is given as follows:

$$BMG\,composites \propto \frac{T_x}{T_L} \times \frac{T_f}{T_L} \times \left(\frac{T_x}{T_f}\right)^{-1} = \left(\frac{T_f}{T_L}\right)^{2} \propto \frac{T_f}{T_L} = \boldsymbol{K}\,. \tag{3.5}$$

By collecting all the characteristic temperatures and calculating the thermodynamic parameters as well as the values of the ***K***-parameter of the 36 CuZr-based alloys, the relationship among the ***K***-parameter, the GFA, and characteristic temperatures is shown in Fig. 3.9. As shown in Table 3.1 and Fig. 3.9, the values of the ***K***-parameter can be categorized into three types, corresponding well with the classification in **Section 3.2.1**. The alloys possessing the clear eutectoid B2 CuZr transformation peak(s) are classified to be alloys Type II, while the alloys Type I do not show any eutectoid B2 CuZr transformation peak(s). For the alloys Type I, the B2 CuZr phase becomes the primary crystallization product of the amorphous ribbon during heating. Other alloys whose eutectoid B2 CuZr transformation events are close to the melting peaks or disappear in them, are defined as Type III alloys. Here, it was assumed that the values of T_f for Type I and for Type III are equal to $T_{cry\text{-}final}$ and T_L, respectively, due to the disappearance of the eutectoid B2 CuZr transformation peak(s). Furthermore, the values of the ***K***-parameter follow the tendency: ***K*** (Type III) > ***K*** (Type II) > ***K*** (Type I) (Fig. 3.9). Type I-alloys are alloys No. 1 to No. 6. The alloys from No. 7 to No. 24 belong to type II. Type III-alloys comprise of alloys No. 25 to No. 36.

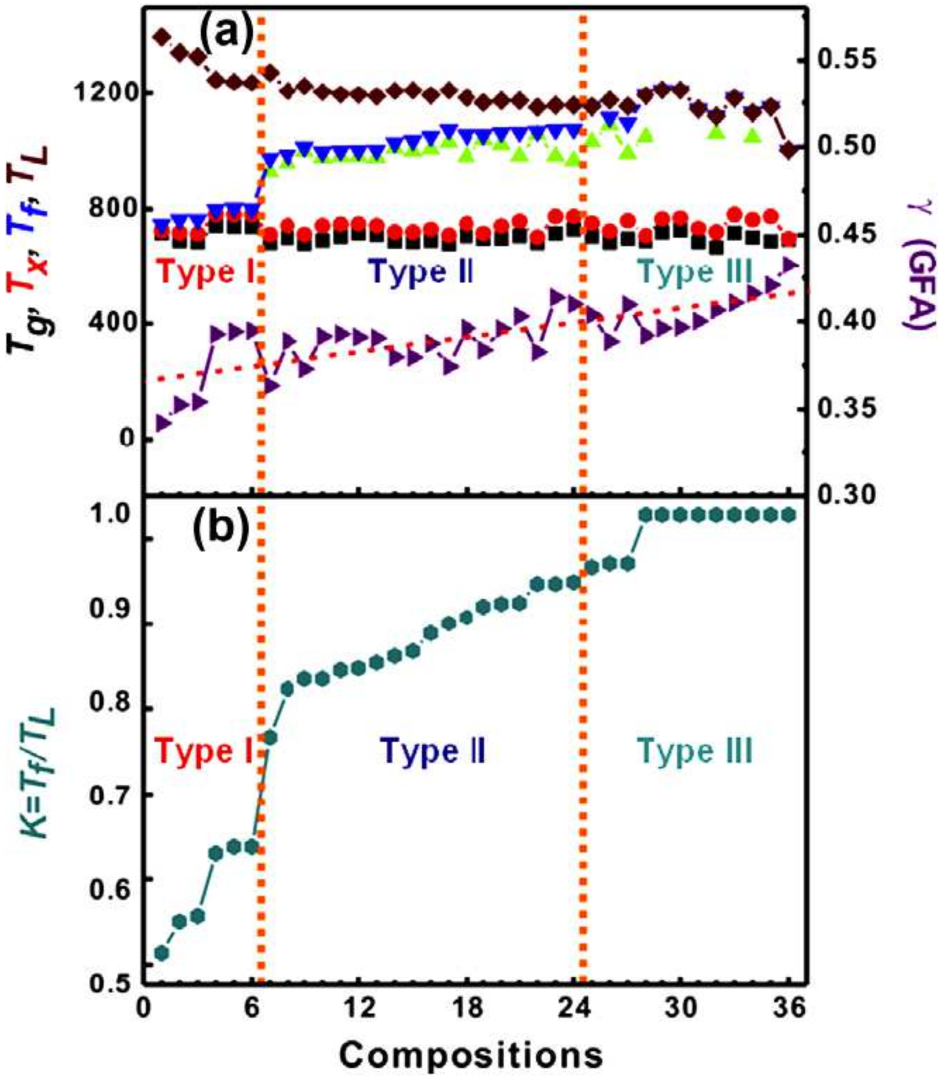

Figure 3.9 *(a) Effect of different element additions on the values of* T_g, T_x, T_f, T_L, *and* γ, *and (b) the values of the* ***K*** *criterion for different alloys. All the studied alloys can be classified into three types.*

According to the proposed strategy, it is expected to obtain BMGs or even BMG composites with small sizes. That be attributed to the limited GFA for Type I-alloys with low ***K*** values (less than 0.7 in Fig. 3.9), which leads to a larger driving force for the crystallization of the B2 phase and the LT-EPs and a smaller time window for the amorphous phase to form during quenching. Type II-alloys with medium ***K*** values from 0.77 to 0.93 have a sufficient time and temperature window (i.e. a lager value of T_f-T_S and a lower T_L in Table 3.1 and Fig. 3.9) to form the B2 CuZr phase alongside the amorphous phase. Medium-sized CuZr-based BMG composites are expected to be fabricated. As the ***K*** values further increase to above 0.94 (Fig. 3.9), a higher stability of the liquid promotes the increase of GFA due to a decreasing T_L. Hence, for Type III alloys, CuZr-based BMG composites with larger dimensions can be fabricated.

3.5 Conclusions

In this chapter, the eutectoid B2 CuZr transformation at high temperatures for 36 metastable CuZr-based alloys has been investigated using thermal analysis and X-ray diffraction. The shift of the phase transformation peak(s) with the addition of different elements is related to the thermal stability of the B2 CuZr phase. By considering the thermal stability of the supercooled liquid, the resistance against crystallization and the thermal stability of the B2 CuZr, a new parameter, $\boldsymbol{K} = T_f/T_L$, was proposed to select a compositional region, which allows to cast metastable CuZr-based BMG composites with different sizes. All the CuZr-based alloys were classified into three types according to the new strategy. It can be concluded: (1) When ***K*** is lower than 0.7, smaller BMG composites or even fully crystalline phases are expected to be obtained for Type I-alloys; (2) When ***K*** lies in the range from 0.7 to 0.94, Type II alloys may be cast into moderate dimensions; (3) when ***K*** is larger than 0.94, CuZr-based with larger dimensions may be fabricated. This new approach could be of great significance for the development of CuZr-based BMG composites with enhanced deformability.

4 Synthesis of CuZr-based BMG composites

According to our new strategy, the formation of CuZr-based BMG composites in different dimensions can be evaluated [315]. However, until now, only a limited number of CuZr-based BMG composites has been fabricated [295, 300, 301, 325, 326]. Thus it is necessary to develop additional ductile CuZr-based BMG composites. In this study, different compositions selected from three types of CuZr-based alloys proposed based on our prediction were used to fabricate CuZr-based BMG composites.

4.1 Formation of Type I alloys

For the Type I alloys, the eutectoid B2 CuZr transformation shifts to a lower temperature or even disappears in the crystallization event [315], implying that the B2 CuZr phase is stabilized to a low temperature. In such a case, the B2 phase becomes the dominant crystallization product, which collaborates with other LT-EPs and competes with the amorphous phase. Thus, this complicated competition facilitates the formation of the B2 CuZr phase, but deteriorates the GFA of CuZr-based alloys.

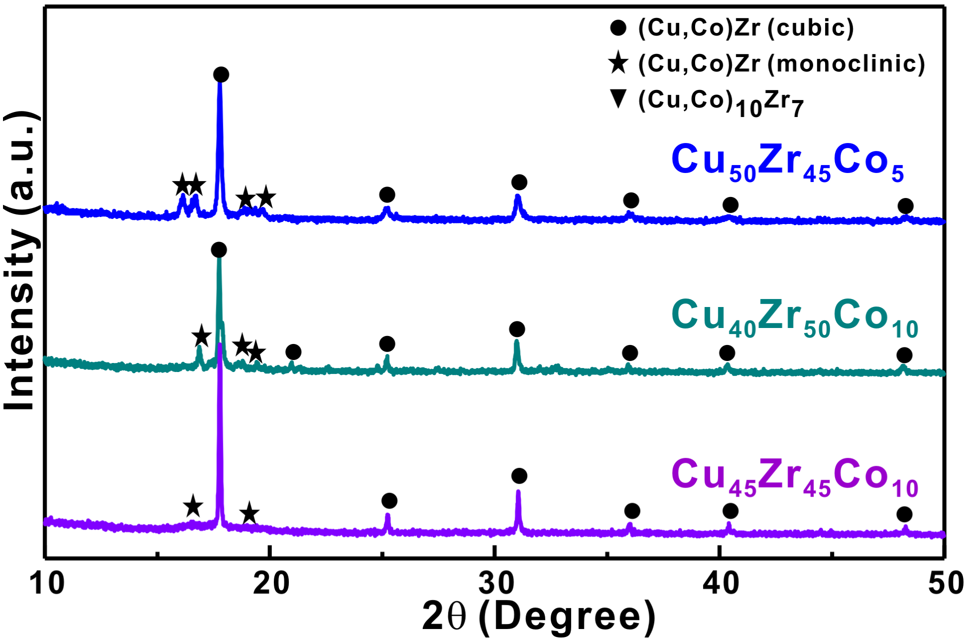

Figure 4.1 *XRD patterns of the as-cast Cu-Zr-Co rods with a diameter of 1.5 mm.*

As mentioned in **Chapter 3**, the Cu-Zr-Co alloy system is typical Type I alloys when higher content of Co (i.e. more than 2 at.%) is added into CuZr-based alloys.

Here, Cu-Zr-Co alloys, i.e. $Cu_{50}Zr_{45}Co_5$, $Cu_{40}Zr_{50}Co_{10}$, and $Cu_{45}Zr_{45}Co_{10}$, were chosen as a case study (Fig. 4.1). All the ingots were cast into rods with a diameter of 2 mm, whose XRD patterns are shown in Fig. 4.1. It was found that with the Co content increasing from 5 at. % to 10 at.%, the crystallization products upon cooling are determined to be the B2 (Cu,Co)Zr together with a small amount of $(Cu,Co)_{10}Zr_7$ crystals [327-330], implying that Co is dissolved in the B2 CuZr phase and stabilizes the B2 phase to room temperature.

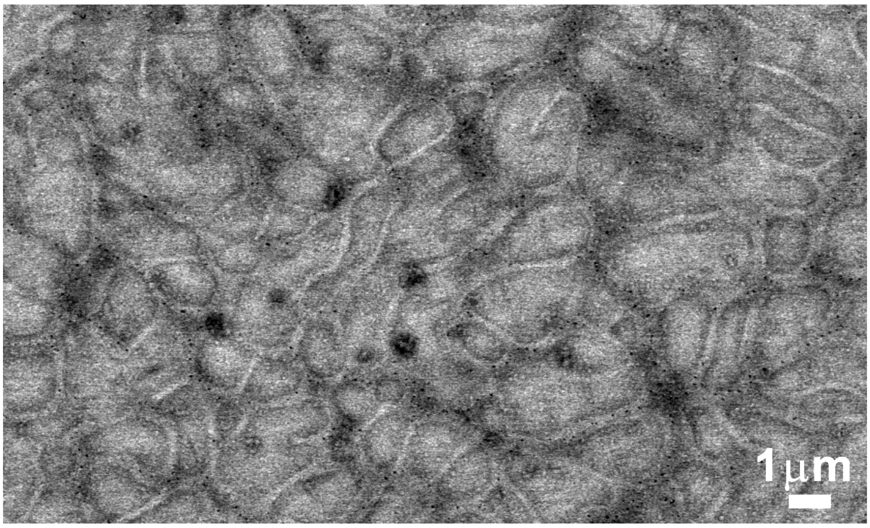

Figure 4.2 *Microstructure of the B2 phase for the as-cast for $Cu_{45}Zr_{45}Co_{10}$ rod.*

According to previous results [315], the glass transition and crystallization of Cu-Zr-Co amorphous ribbons with Co addition less than 10 at.% is located between 680 - 718 K and 711 - 724 K, respectively. In our case, the samples are rods in a diameter of 2 mm, whose corresponding cooling rate is less than that of the ribbons. Furthermore, the value of γ of these Cu-Zr-Co alloys lies between 0.34 and 0.36, while the ΔT_x is less than 37 K, being smaller than the γ-value (about 0.37) and ΔT_x (about 49 K) of the $Cu_{50}Zr_{50}$ alloy [291, 315, 327, 331], implying that the GFA and the thermal stability of CuZr-based amorphous alloys decreases with Co addition less than 20 at.%. Therefore, DSC curves (not shown here) for the present samples do not show any crystallization, further affirming their fully crystalline nature (Fig. 4.1) of the as-cast rods. Based on the SEM measurements, the B2 phase forms fine dendrites (Fig. 4.2) for the sample with a higher Co addition (i.e. $Cu_{45}Zr_{45}Co_{10}$).

Recently, it has been found [329, 332] that the crystallization products of the as-melt Cu-Zr-Co ribbons during heating, whose Co content is higher than 5 at.%, are mainly composed of B2 (Cu,Co)Zr phase. These facts indicate that the B2 (Cu,Co)Zr phase is the primary phase not only during quenching but also during heating, respectively, which changes the phase evolution of CuZr-based alloys, and strongly degrades the GFA of these alloys. During suction casting, the B2 phase forms in all the present alloys. However, the eutectoid reaction takes place at around 970K only with the Co being less than 5 at.% [327-330], but it will not happen for the CuZr-based alloys when the Co content is more than 5 at.%. As shown in Fig. 4.1, with the Co content increasing, the Bragg peaks corresponding to the B2 phase become obvious and the decomposition of the B2 CuZr phase becomes weak, implying that the B2 CuZr indeed becomes more stable with the addition of Co. Meanwhile, the higher thermal stability of the B2 CuZr phase assists the B2 CuZr to win the competition among the amorphous phase, the B2 CuZr phase and other LT-EPs [327-330]. In other words, the GFA becomes worse.

4.2 Formation of Type II alloys

As predicted using the ***K***-parameter, Type II alloys whose eutectoid B2 CuZr transformation temperature is larger than T_x but less than T_L can be fabricated into moderate sample sizes because of a complicated competition among the amorphous phase, the B2 CuZr phase, and the LT-EPs. In this section, $Cu_{50}Zr_{50}$, $Cu_{50}Zr_{50-x}Ti_x$ (x = 2.5, 5, 7.5, and 10) [326, 331, 333], $(Cu_{0.5}Zr_{0.5})_{100-x}Al_x$ (x = 2, 4, 5, and 8), and $(Cu_{0.5}Zr_{0.5})_{100-x}Ag_x$ (x = 2, 3, 4, and 5) alloys were chosen to investigate the formation of CuZr-based BMG composites.

4.2.1 Formation and microstructures of the $Cu_{50}Zr_{50}$ BMG composites

Previous results [291, 315, 331] have shown that the critical diameter of fully amorphous $Cu_{50}Zr_{50}$ rods is about 2 mm. However, different suction or injection casting machines have a strong influence on the glass formation of the same alloys even though the diameter of the copper mold is same [39, 135, 284, 334-337]. Meanwhile, the length of the as-cast rods is also critical [39, 135, 284, 334-337]. For the present experiments, all the rods, whose length is about 3.3 cm, were fabricated using a mini suction casting device (see **Chapter 2**).

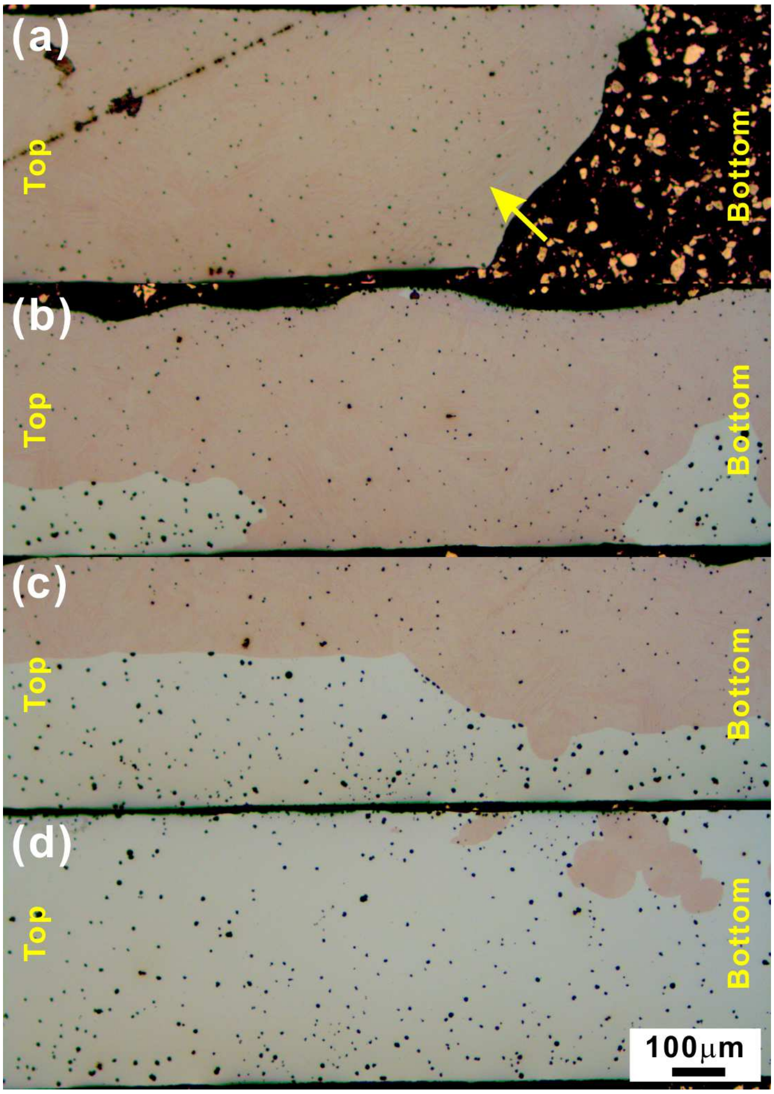

Figure 4.3 *Microstructure of the longitudinal cross sections from four* $Cu_{50}Zr_{50}$ *rods with a diameter of 1 mm. (the black dots in the samples originated from polishing solutions).*

Fig. 4.3 shows the OM pictures of the longitudinal sections of four $Cu_{50}Zr_{50}$ rods with a diameter of 1 mm. It was found that some parts are fully crystalline (see the arrow in Fig. 4.3), while some parts consist of amorphous phase (bright area) and crystals (orange area). Even for some parts, an almost fully amorphous rod (Fig. 4.3d) can be obtained. The phases were also analyzed by XRD, which will be shown below. The corresponding crystalline volume fraction (f_{cryst}) was estimated to be 100 vol.%, 83 ± 5 vol.%, 54 ± 5 vol.%, and 10 ± 2 vol.%, respectively, based on the areas of amorphous and crystalline phases extracted from the OM images (Fig. 4.3) of the longitudinal sections of the as-cast $Cu_{50}Zr_{50}$ rods. There are some reasons for the formation of crystals in the glassy matrix. On the one hand, it is worth noting that partial crystals prefer to precipitate around the rugged outside surfaces of the copper mold, which may be due to the insufficient filling of the melt into the copper mold, or the improper wetting between the melt and the copper mold during casting. When there are relatively large gaps between the rod and the copper mold, the corresponding cooling rate is expected to be reduced. Therefore, an amount of crystals prefer to precipitate around these surfaces (Figs. 4.3a-c). On the other hand, the cooling rates from top to bottom gradually increase during casting [338, 339]. As shown in Fig. 4.3, the f_{cryst} of the as-cast rods become large gradually.

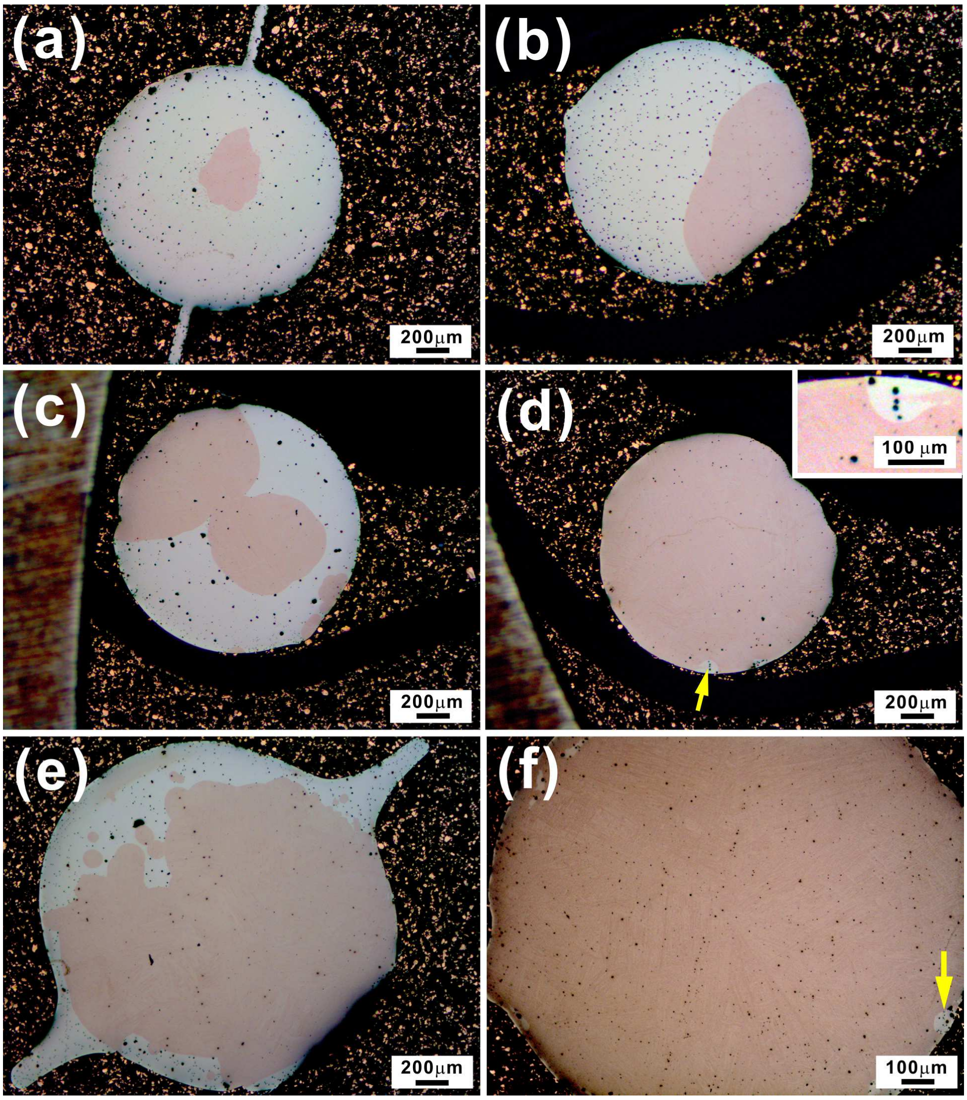

Figure 4.4 *Microstructure of cross sections from the as-cast* $Cu_{50}Zr_{50}$ *rods with a diameter of 1.5 mm, i.e. (a) top, (b) middle, (c) middle, and (d) bottom, and from the as-cast* $Cu_{50}Zr_{50}$ *rods with diameters of (e) 2 mm (middle position), and (f) 3 mm (middle position).*

When the diameter of the as-cast rods increases to 1.5 mm, different contents of crystals can be observed from different positions of a rod, which are shown in

Figs. 4.4a-d, respectively. For the bottom and top parts (Fig. 4.4a and d), the corresponding f_{cryst} was estimated to be 7.5 ± 2 vol.% and 99 ± 0.5 vol.%, respectively. As shown in the inset in Fig. 4.4, the amorphous phase can exist at the edge of the rods, where is closer to the copper mold and thus the cooling rate is relatively large. As shown in Fig. 4.4b-c, the f_{cryst} of two middle parts of the rod was calculate to be 35 ± 5 vol.% and 49.5 ± 5 vol.%, respectively. The change of the f_{cryst} can be attributed to the increasing cooling rates from the top to the bottom of the copper mold [325]. As the diameter of the as-cast rods increases to 2 mm and 3 mm (middle parts of the as-cast rods in Figs. 4.4e-f), the corresponding f_{cryst} was calculated to be 76.5 ± 5 vol.%, and 98 ± 1 vol.%, respectively. When the diameters of the as-cast rods increase from 2 mm and 3 mm, respectively, the cooling rate decreases gradually so that the content of amorphous phase is reduced (see white area in Fig. 4.4e and the arrow in Fig. 4.4f).

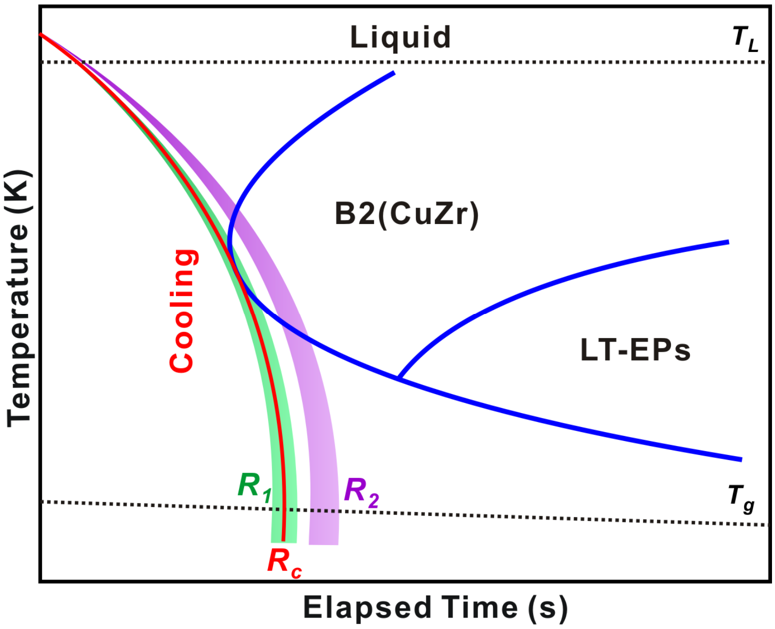

Figure 4.5 *Schematic CCT diagram during the quenching process illustrating the formation of* $Cu_{50}Zr_{50}$*BMG composites with diameters of 1 mm, 1.5 mm 2 mm, and 3 mm.*

For these rods with diameters of 2 mm and 3 mm, the volume fractions of crystals from the bottom to the top position of the rods (not shown) do not change too much compared with these of the samples with a diameter of 1.5 mm. The applied cooling rates for rods with a diameter of 2 mm and 3 mm are located in the "nose" region (see the region R_2 in Fig. 4.5) of the CCT diagram so that slight variations of the applied cooling rate do not strongly affect the f_{cryst} of the as-cast samples based on the CCT diagram of CuZr-based alloys. In contrast, for the rods with diameters of 1 mm and 1.5 mm, the applied cooling rates are close to the R_c (see the region R_1 in Fig. 4.5), and consequently small local differences in the cooling rates either result in vitrification or the precipitation of crystals.

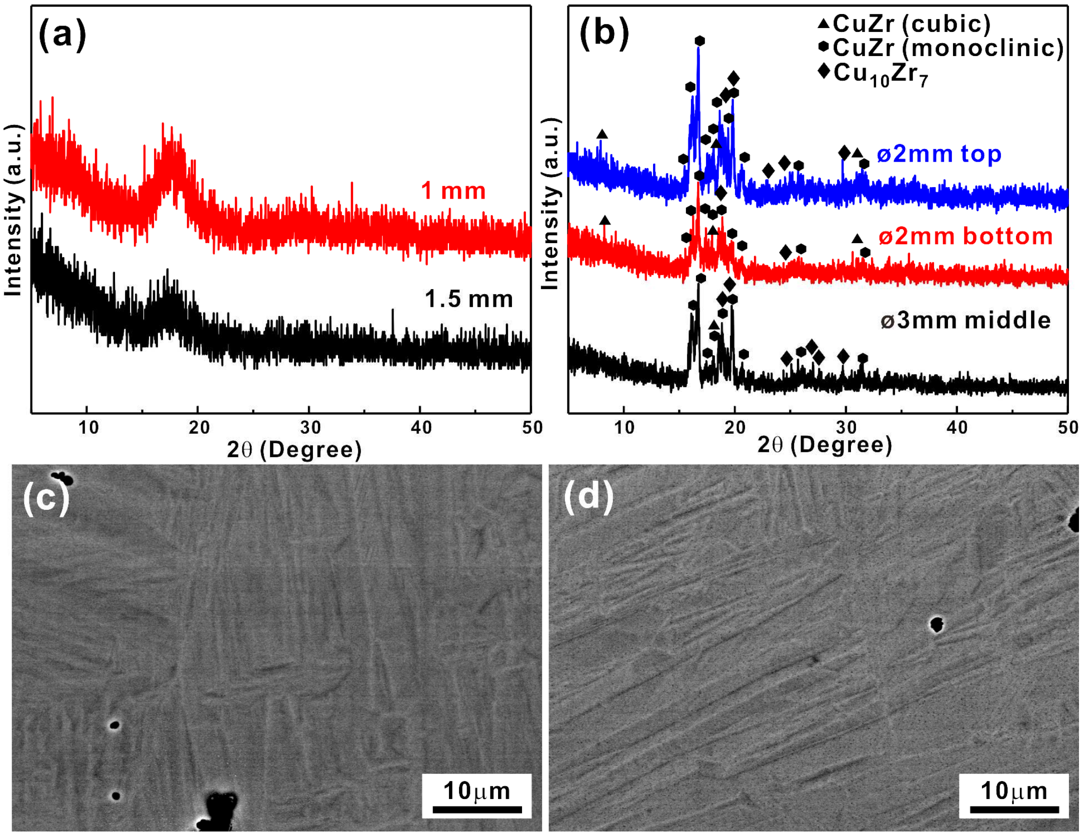

Figure 4.6 *XRD patterns of the as-cast $Cu_{50}Zr_{50}$ rods with diameters of (a) 1 and 1.5 mm, (b) 2 and 3 mm, and microstructures of the rods with diameters of (c) 1.5 mm, and (d) 2mm, respectively.*

XRD measurements were applied to further identify the phase formation of the as-cast rods with different diameters as shown in Figs. 4.6a-b. It can be seen that the crystals in the glassy matrix for the rods with diameters of 1.5 and 2 mm are very different. Even fully amorphous rods (only some parts in Fig. 4.3) with diameters of 1 mm and 1.5 mm can be fabricated. As shown in Fig. 4.6a, the XRD patterns show a broad peak, further confirming their fully amorphous nature for some parts of the rods. However, $Cu_{50}Zr_{50}$ BMG composites with larger diameters were obtained (Fig. 4.6b) and the crystals were indentified to be martensite as well as a minor amount of the B2 CuZr phase and $Cu_{10}Zr_7$ based on the XRD patterns. The existence of martensite was further proven by the SEM measurements shown in Figs. 4.6c-d. Obvious martensitic plates were observed. When the diameters of the samples increase from 1.5 mm to 2 mm, the martensitic plates become larger (Figs. 4.6c-d). Even though the equiatomic CuZr intermetallics, i.e. a little B2 CuZr phase and amount of martensites in Fig. 4.6b, is observed together with some amorphous phase, the size of $Cu_{50}Zr_{50}$ BMG composites is relatively small due to its low GFA and the limited thermal stability of the B2 CuZr phase. Therefore, the relatively high cooling rate for the present rods avoids the decomposition of most of the B2 phase into the LT-EPs, but cannot stop the transformation of most of the B2 CuZr phase into martensites. Meanwhile, some amorphous phase can be kept when the actual cooling rate near its R_c is sufficiently high to locally vitrify the melt.

4.2.2 Formation and microstructures of the Cu-Zr-Ti BMG composites

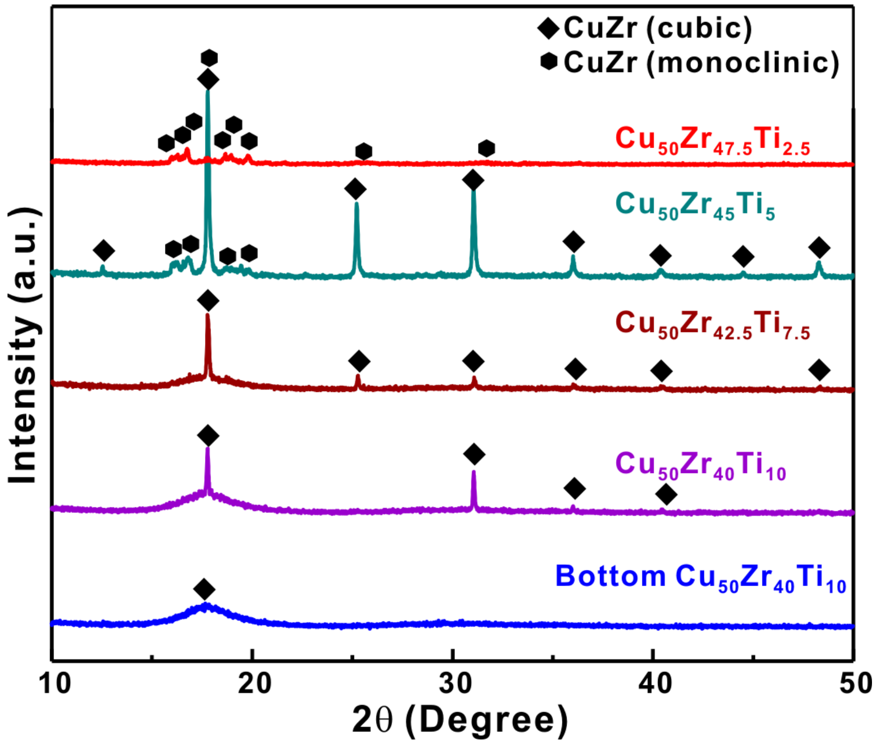

Figure 4.7 *XRD patterns of the as-cast Cu-Zr-Ti rods with a diameter of 3 mm.*

Fig. 4.7 show the XRD patterns of the $Cu_{50}Zr_{50-x}Ti_x$ (x = 2.5, 5, 7.5, and 10) rods with a diameter of 3 mm, which were fabricated using suction casting. It can be seen that with the Ti content decreasing from 10 at.% to 2.5 at.% for the as-cast Cu-Zr-Ti alloys, the f_{cryst} becomes large based on the increasing intensity of the crystalline peaks, implying that the GFA of Cu-Zr-Ti alloys gradually increases with the Ti addition. As the content of the Ti decreases from 10 at.% to 7.5 at.%, the crystals are identified to be the B2 CuZr phase, while the crystals in $Cu_{50}Zr_{50-x}Ti_x$ (x = 2.5 and 5) alloys are a mixture of the B2 CuZr phase and martensitic CuZr crystals. In order to confirm the microstructures of the $Cu_{50}Zr_{50-x}Ti_x$ (x = 2.5, 5, 7.5, and 10) alloys, OM measurements were also conducted (Fig. 4.8).

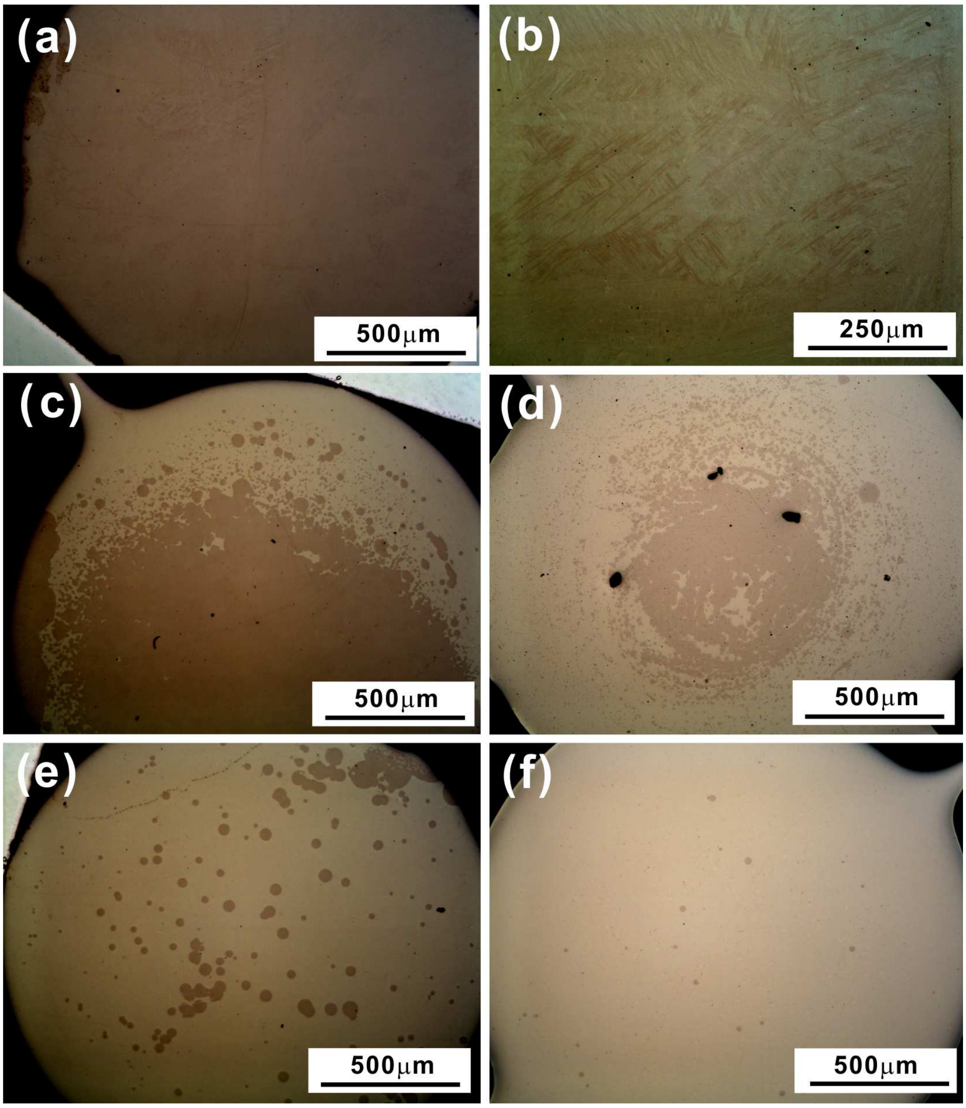

Figure 4.8 *OM pictures of the as-cast (a)* $Cu_{50}Zr_{47.5}Ti_{2.5}$ *rod, (b) the martensites in* $Cu_{50}Zr_{47.5}Ti_{2.5}$ *rod, (c)* $Cu_{50}Zr_{45}Ti_5$ *rod, (d)* $Cu_{50}Zr_{42.5}Ti_{7.5}$ *rod, and the (e) middle and (f) bottom of the* $Cu_{50}Zr_{40}Ti_{10}$ *rod with a diameter of 3 mm.*

It is noteworthy to mention that the XRD and the OM measurements were also performed on the middle position of all the rods in order to exclude the effect of different cooling rates from the copper mold on the microstructures. As shown in Fig. 4.8a, the $Cu_{50}Zr_{47.5}Ti_{2.5}$ sample shows an almost fully crystalline structure and only a little amorphous phase can be found close to the surfaces of the rods (not shown), whose f_{cryst} is estimated to be 97 ± 1 vol.%. As shown in Fig. 4.8b, martensitic plates are observed, which correspond well with the XRD patterns of the $Cu_{50}Zr_{47.5}Ti_{2.5}$ sample. When the Ti content increases to 5 at.% and 7.5 at.%, a larger area of amorphous phase (white areas in Figs. 4.8c-d) is found, while crystals precipitate in the glassy matrix and impinge. The corresponding f_{cryst} are determined to be 66.5 ± 5 vol.% and 40 ± 3 vol.%, respectively. As the Ti content increases to 10 at.%, the B2 phase distributes homogenously in the glassy matrix while the content of the B2 phase is not so high, i.e. 10 ± 2 vol.% (Fig. 4.8e). In addition to the effect of composition on the microstructures during quenching, the slight differences in the local cooling rate also lead to either vitrification or precipitation of crystals when the actual cooling rate is close to the R_c (see Fig. 4.5). As shown in Figs. 4.8e-f, less B2 phase (about 0.2 vol.%) is observed at the bottom position compared with the middle position of the as-cast $Cu_{50}Zr_{40}Ti_{10}$ rod.

The effect of Ti on microstructures of the $Cu_{50}Zr_{50-x}Ti_x$ (x =2.5, 5, and 7.5) BMG composites with a diameter of 1.5 mm [326, 333] together with the phase formation upon heating for the $Cu_{50}Zr_{50-x}Ti_x$ (x =2.5, 5, and 7.5) MGs has been investigated. Similar microstructures of the as-cast samples were also observed as the content of Ti is larger than 5 at.% [326, 333]. All these facts imply that it is difficult for the B2 CuZr phase to precipitate during quenching with the Ti addition into CuZr-based alloys. Furthermore, it was also found that the final crystallization products upon heating for the $Cu_{50}Zr_{50-x}Ti_x$ (x =2.5, 5, and 7.5) MGs are $Cu_{10}Zr_7$ and $CuZr_2$. Therefore, as shown in Fig. 4.6, the eutectoid B2 CuZr decomposition into $Cu_{10}Zr_7$ and $CuZr_2$ is also effectively suppressed for the present alloys during quenching. It has been demonstrated that the γ parameter and the liquid fragility of $Cu_{50}Zr_{50-x}Ti_x$ (x =2.5, 5, and 7.5) MGs do not monotonously increase [326, 333]. Furthermore, when the Ti content increases to 5 at. % [326, 333], metastable ternary Laves phase starts to precipitate in CuZr-based alloys during crystallization upon heating together with significant changes of the activation energies of crystallization. These observations demonstrate that the GFA of Cu-Zr-Ti MGs roughly increases with the addition of Ti from 0 at.% to 10% [326, 333]. In our prediction theory mentioned in **Chapter**

3, the formation of the $Cu_{50}Zr_{50-x}Ti_x$ (x =2.5, 5, 7.5, and 10) BMG composites depends on their GFA and the thermal stability of the B2 CuZr phase (i.e. T_f). Based on the calculation, the ***K***-values of $Cu_{50}Zr_{50-x}Ti_x$ (x = 2.5, 5, 7.5, and 10) alloys increase from 0.850 to 0.927 [315], implying that the dimensions of Cu-Zr-Ti BMG composites may increase gradually with the Ti content increasing. Actually, this assertion corresponds well with our observations.

4.2.3 Formation and microstructures of the Cu-Zr-Al and Cu-Zr-Ag BMG composites

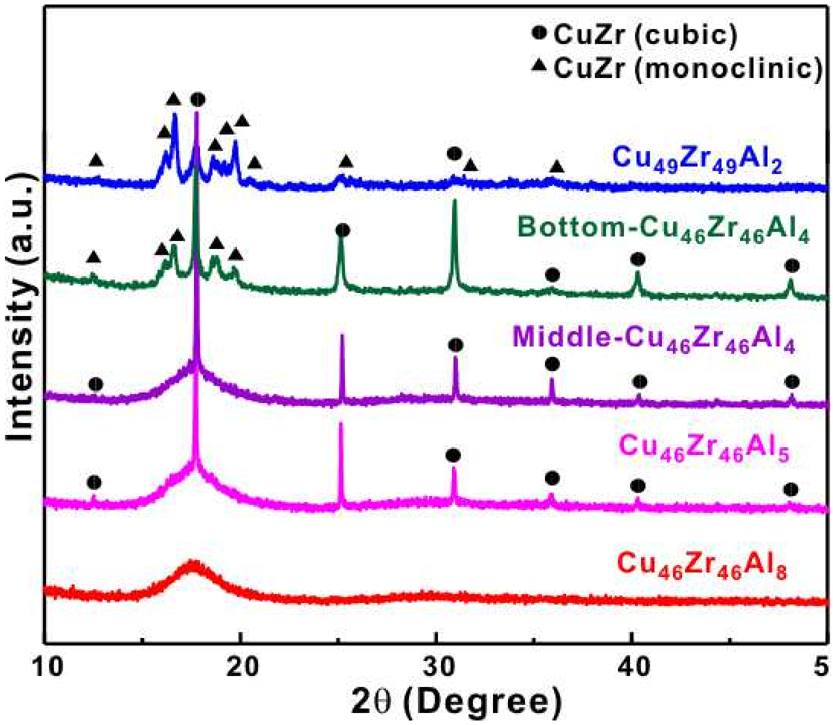

***Figure 4.9** XRD patterns of the as-cast Cu-Zr-Al rods with a diameter of 3 mm.*

According to our prediction [315], Cu-Zr-Al/Ag alloys also trend to be cast into relatively large dimensions. The XRD patterns of the as-cast $(Cu_{0.5}Zr_{0.5})_{100-x}Al_x$ (x = 2, 4, 5, and 8) rods with a diameter of 3 mm are shown in Fig. 4.9. With the Al addition to CuZr-based alloys, the content of the amorphous phase gradually increases based on the intensity of the crystalline peaks in the XRD patterns. As the content of Al is less than 4 at.% (Fig. 4.9), the Cu-Zr-Al BMG composites contain some martensitic crystals as well as some B2 CuZr phase. When the content of Al continues to increase from 4 at.% to 10 at.%, the martesitic phase starts to disappear and the content of the amorphous phase gradually increases (Fig. 4.9). Furthermore, the effect of different cooling rates from the top and bottom during quenching on the formation of CuZr-based BMG composites is also observed. As shown in Fig. 4.9, the precipitates of the bottom and middle parts for the $Cu_{48}Zr_{48}Al_4$ BMG composites are different. The bottom part has more martensitic crystals and less amorphous phase, whereas only the B2 CuZr phase and the amorphous phase can be observed in the middle parts.

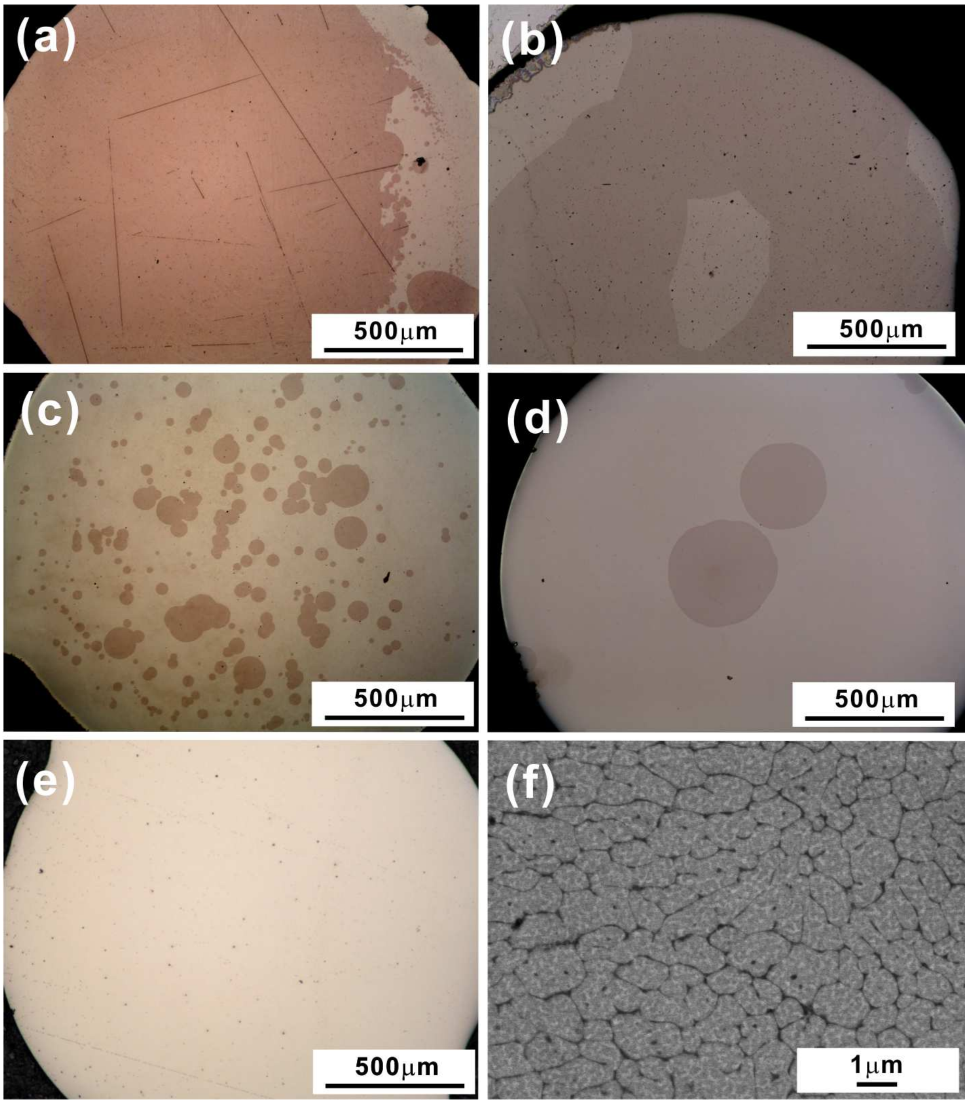

Figure 4.10 *OM pictures (a) of the as-cast* $Cu_{49}Zr_{49}Al_2$ *rod, (b) from the top part of* $Cu_{48}Zr_{48}Al_4$ *rod, (c) from the middle part of* $Cu_{48}Zr_{48}Al_4$ *rod, (d) of the as-cast* $Cu_{47.5}Zr_{47.5}Al_5$ *rod, and (e) of the as-cast* $Cu_{45}Zr_{45}Al_{10}$ *rod, and (f) the local dendritic structure of the B2 CuZr phase in* $Cu_{48}Zr_{48}Al_4$ *rod.*

In order to check the distribution, the size and the shape of the B2 CuZr crystals in the glassy matrix for the as-cast Cu-Zr-Al rods, OM measurements were carried out, which are shown in Fig. 4.10. For the $Cu_{49}Zr_{49}Al_2$ sample and the top part of the $Cu_{48}Zr_{48}Al_4$ BMG composites (Figs. 4.10a-b), the crystals accumulate with each other, and the f_{cryst} is estimated to be 84.5 ± 3 vol.% and

79.5 ± 3 vol.%, respectively. For the middle part of the $Cu_{48}Zr_{48}Al_4$ BMG composites, a relatively fine and homogenously dispersed B2 CuZr phase with a f_{cryst} of 16.5 ± 5 vol.% (Fig. 4.9c) is observed in the glassy matrix. As the content of Al increases further (e.g. $Cu_{47.5}Zr_{47.5}Al_5$ and $Cu_{45}Zr_{45}Al_{10}$), the volume fraction of the B2 phase continues to decrease to 9 ± 3 vol.% and then it eventually disappears (Figs. 4.10d-e). Fig. 4.10f shows that the B2 CuZr phase forms dendrites, being consistent with previous results [136, 295, 326, 333, 340].

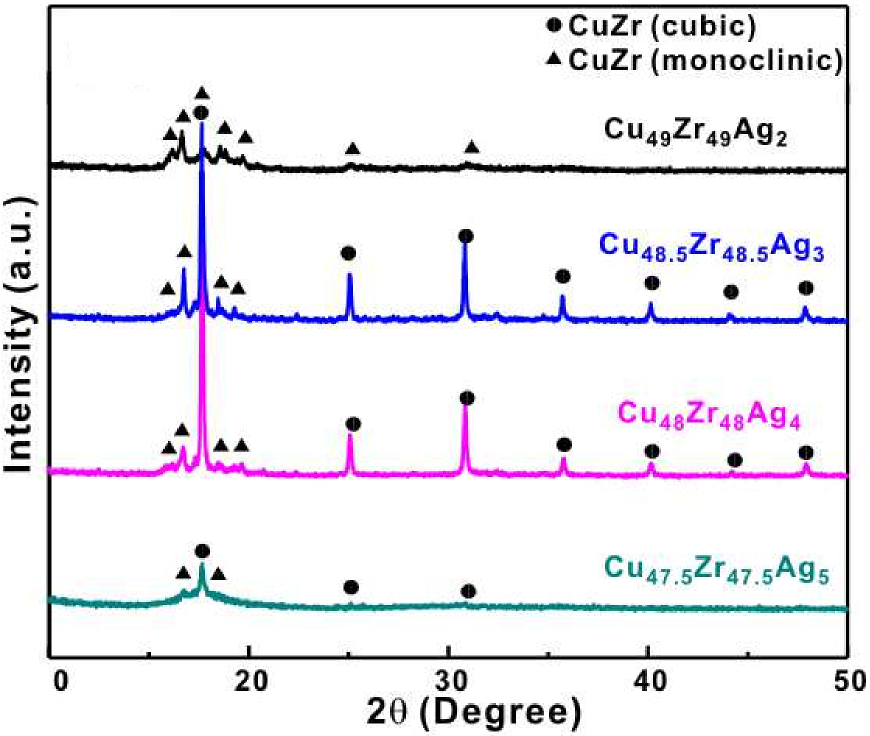

Figure 4.11 *XRD patterns of the as-cast Cu-Zr-Ag rods with a diameter of 3 mm.*

Fig. 4.11 shows the XRD patterns of the as-cast $(Cu_{0.5}Zr_{0.5})_{100-x}Ag_x$ (x = 2, 3, 4, and 5) rods with a diameter of 3 mm. It was found that when the content of Ag increases from 2 at.% to 5 at.%, the crystals (Fig. 4.11) in the glassy matrix start to disappear, implying that the addition of Ag induce the increase of the GFA of CuZr-based alloys. This observation corresponds well with previous results [336, 341]. Furthermore, as the content of Ag increases to more than 5 at.%, it was found that no martensitic crystals are observed and instead only the pure B2 CuZr phase together with the amorphous phase is found under the same cooling rate, implying the Ag addition may decrease the MT temperature.

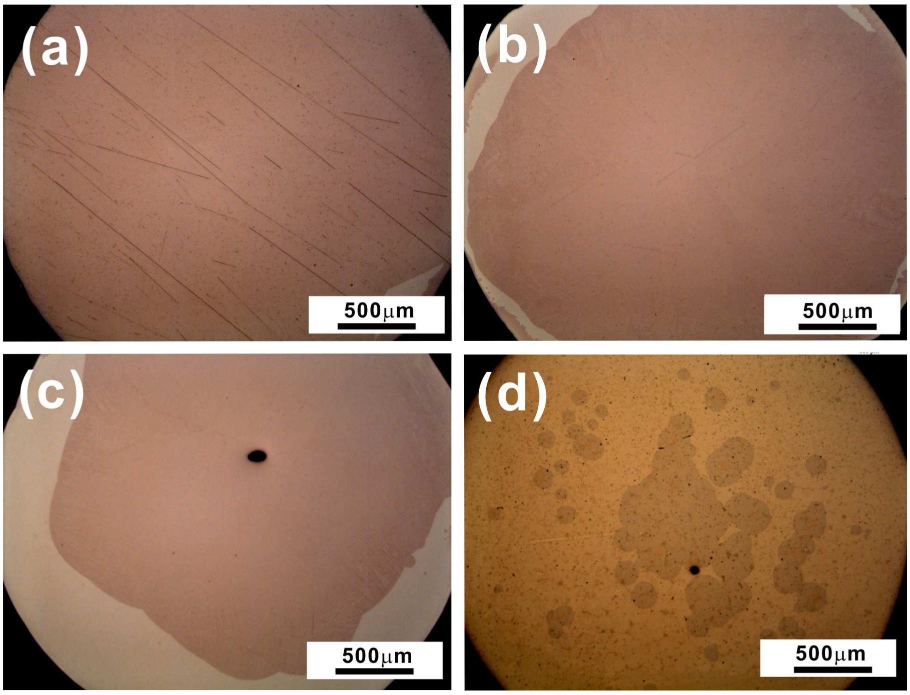

Figure 4.12 *OM pictures of (a) the as-cast* $Cu_{49}Zr_{49}Ag_2$ *rod, (b)* $Cu_{448.5}Zr_{48.5}Ag_3$ *rod, (c)* $Cu_{48}Zr_{48}Ag_4$ *rod, and (d) the as-cast* $Cu_{47.5}Zr_{47.5}Ag_5$ *rod.*

The OM pictures of the as-cast $(Cu_{0.5}Zr_{0.5})_{100-x}Ag_x$ (x=2, 3, 4, and 5) rods with a diameter of 3 mm are shown in Fig. 4.12. For the as-cast Cu-Zr-Ag samples, the f_{cryst} decreases from 99 ± 0.5 vol.%, 93 ± 3 vol.%, 72 ± 3 vol.%, and 23 ± 5 vol.%, respectively, with the Ag content increasing from 2% to 5%.. However, the B2 CuZr phase trends to show a relatively heterogeneous distribution in the glassy matrix compared with that in Cu-Zr-Al BMG composites. It has been demonstrated that Cu-Zr-Ag alloys with higher contents of Ag belong to a phase separated system [342-345]. During cooling of a phase separated liquid, the liquid becomes unstable and decomposes into two different liquids after it passes through a miscibility gap [346-349]. The decomposition initiates via the spontaneous formation and subsequent growth of coherent composition fluctuations. In the following step, a stationary state of the composition amplitude is achieved and a square-like composition profile can be observed [346-349]. Afterwards, the coarseness of the microstructure due to diffusion and coalescence can be induced with further cooling of the liquids and the flow in the liquids results in a coalescence of the droplets to larger domains [346-349]. Therefore, the heterogamous distribution for the primary B2 CuZr phase originating from the liquid during solidification may be due to the phase separated nature of Cu-Zr-Ag alloys with higher contents of Ag [342-345, 349]. However, since this exceeds the scope of the present observations, more studies will be carried out in the future.

4.3 Formation of Type III alloys

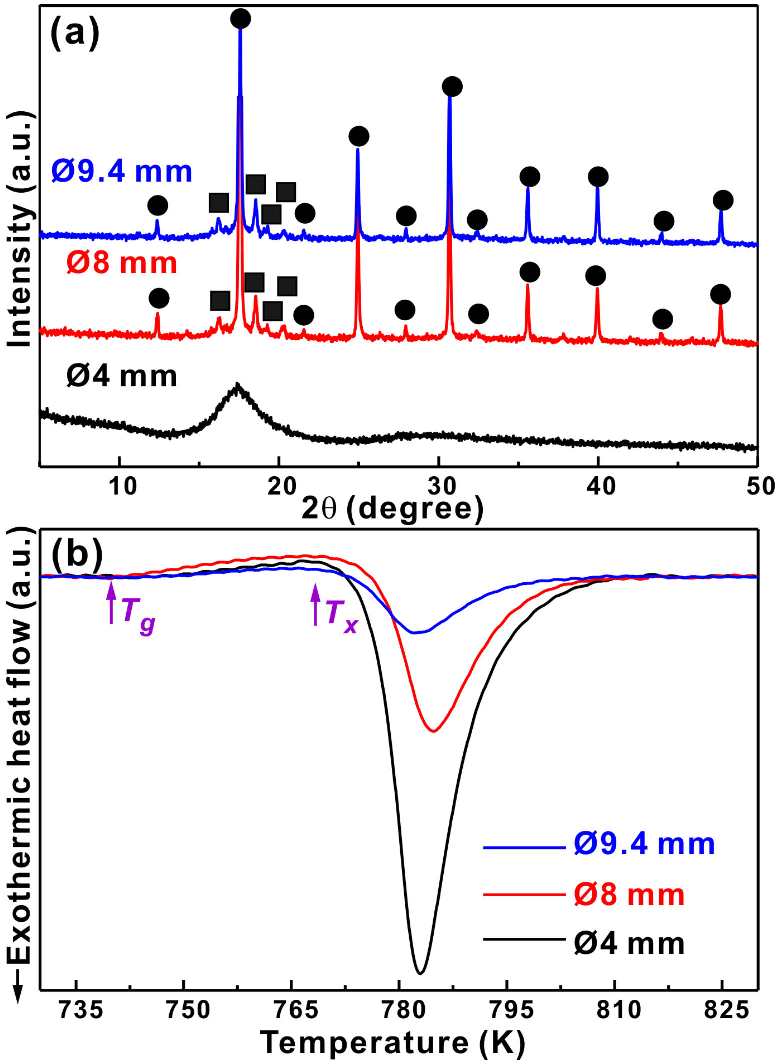

Figure 4.13 *(a) XRD patterns and (b) DSC curves of the as-cast $Cu_{46}Zr_{42}Al_7Y_5$ rods.*

For the Type III alloys, larger BMG composites can be fabricated according to our prediction. For example, the ***K***-values of $Cu_{46}Zr_{42}Al_7Y_5$ and $Cu_{46.25}Zr_{44.25}Al_{7.5}Er_2$ are 1 and 0.949 [315], respectively. In order to confirm this hypothesis, these glass-forming melts were suction-cast into copper molds whose internal cores with different diameters. Fig. 4.13a shows the XRD patterns of the as-cast $Cu_{46}Zr_{42}Al_7Y_5$ rods with different diameters, i.e. 4 mm (Y4), 8 mm (Y8), and 9.4 (Y94) mm. It can be seen that the Y4 sample is fully amorphous. When the diameter of the as-cast rods increases to 8 mm and 9 mm, the B2 CuZr phase together with a few martensitic crystals precipitates in the glassy matrix [315].

However, due to the large size of the present BMG composites, it is difficult to obtain the volume fraction of the amorphous phase based on the OM pictures. Therefore, the DSC measurements were conducted to check the existence of the amorphous phase. As shown in Fig. 4.13b, with the diameter of the rods increasing (i.e. the decrease of the cooling rates), the exothermic peaks associated with the crystallization of the amorphous phase gradually become small, further implying the volume fraction of the amorphous phase (f_{amor}) gradually decreases. The f_{amor} of the Y8 and Y94 samples can be calculated to be 47 ± 5 vol.% and 18 ± 5 vol.%, respectively, based on the ratio of the crystallization enthalpies of the as-cast samples and the corresponding BMG rod (Y4). Nevertheless, Cu-Zr-Al-Y BMG composites with large dimensions were fabricated, which confirms our strategy.

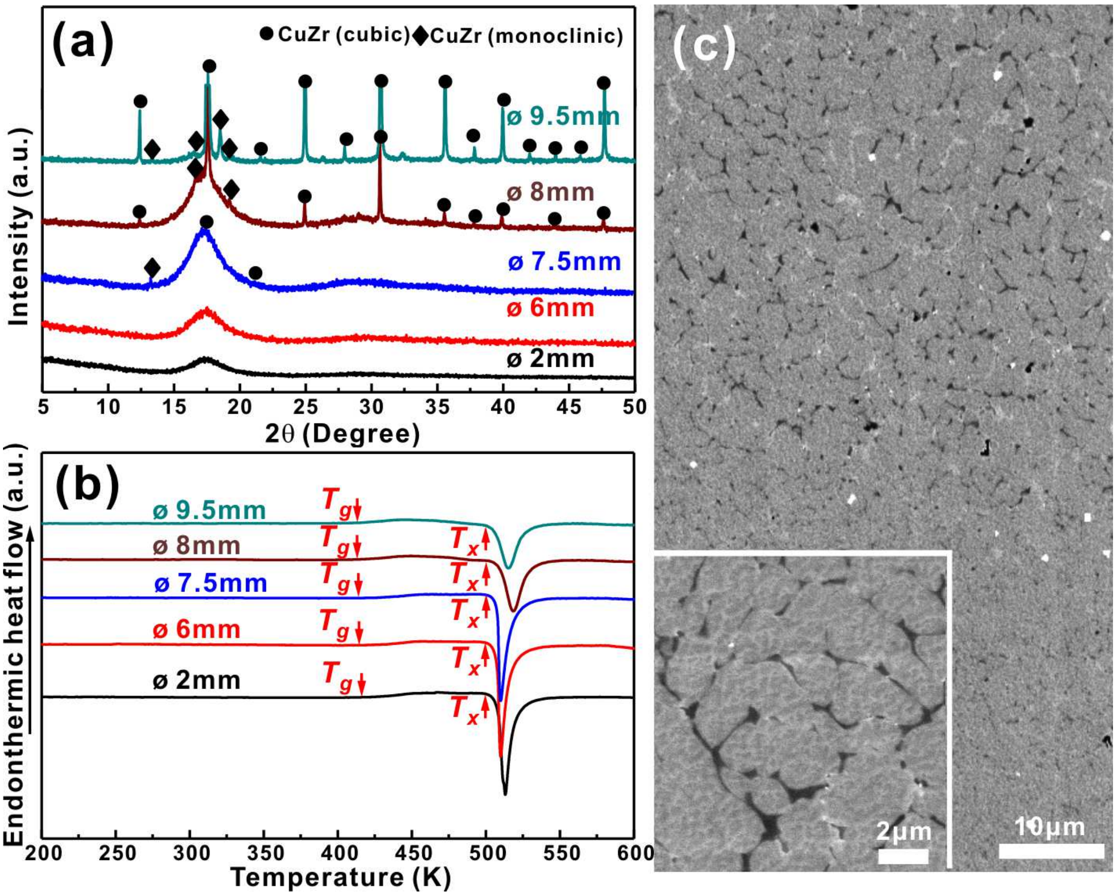

Figure 4.14 *(a) XRD patterns of the as-cast* $Cu_{46.25}Zr_{44.25}Al_{7.5}Er_2$ *specimens with different diameters, (b) DSC curves for the rods with different diameters, and (c) SEM picture of the partial cross-section of the specimen with a diameter of 9.5 mm (Insets: its amplificatory SEM picture of the B2 phase).*

For the $Cu_{46.25}Zr_{44.25}Al_{7.5}Er_2$ alloys, BMG composites containing different volume fractions of the B2 CuZr phase were also obtained. Fig. 4.14a shows the XRD patterns of the as-cast $Cu_{46.25}Zr_{44.25}Al_{7.5}Er_2$ alloys with different diameters [315]. No crystalline reflections can be detected for the rods with diameters less than 6 mm, implying that the D_c for the fully amorphous rod is about 6 mm under the present casting conditions. However, when the diameters increase to more than 6 mm (i.e. lowering the cooling rate), the B2 phase gradually starts to precipitate (Fig. 4.14a). Due to the thermodynamic instability of the B2 phase during quenching, i.e. a large T_f, it partially transforms into martensitic crystals as shown in Fig. 4.14a [350]. As shown in Fig. 4.14b, the DSC curves show that with the diameter of the sample increasing, the crystallization peaks decrease, implying that the content of the amorphous phase gradually decreases. The crystallization enthalpies of the as-cast specimens with different diameters were determined and are listed in Table 4.1.

Table 4.1 *The exothermic crystallization enthalpies, the f_{amor}, and the diameters for $Cu_{46.25}Zr_{44.25}Al_{7.5}Er_2$ metastable alloys [350].*

Composition	ΔH_{cryst} (J/g)	f_{amor} (vol.%)	Diameter (mm)
$Cu_{46.25}Zr_{44.25}Al_{7.5}Er_2$	-61±5	100	2
	-61±5	≤100	6
	-58±5	95±3	7.5
	-49±5	80±3	8
	-46±5	75±3	9.5

Thus, the f_{amor} of the present samples can be calculated, which is listed in Table 4.1. The SEM observations shown in Fig. 4.14c also reveal that the B2 CuZr phase in the glassy matrix forms micro-scaled dendrites, which is consistent with previous results [295]. All in all, by changing the cooling rate, i.e. the diameters of the copper mold, new CuZr-based BMG composites in different dimensions were successfully fabricated.

4.4 Conclusions

In this work, according to our strategy proposed to predict the formation of CuZr-based BMG composites, different types of CuZr-based BMG composites were successfully obtained, namely $Cu_{50}Zr_{50}$, $Cu_{50}Zr_{50-x}Ti_x$ (x = 2.5, 5, 7,5, and 10), $(Cu_{0.5}Zr_{0.5})_{100-x}Al_x$ (x = 2, 4, 5, and 8), and $(Cu_{0.5}Zr_{0.5})_{100-x}Ag_x$ (x = 2, 3, 4, and 5),

$Cu_{46}Zr_{42}Al_7Y_5$ and $Cu_{46.25}Zr_{44.25}Al_{7.5}Er_2$. This, in turn, verifies the applicability of the strategy for pinpointing the formation of CuZr-based BMG composites in different dimensions and is beneficial for the development of ductile CuZr-based BMG composites.

For Cu-Zr-Co alloys with a relatively small ***K***-value less than 0.7, it is difficult to fabricate CuZr-based BMG composites with the B2 CuZr precipitating in the glassy matrix. With the ***K***-value increasing for the Cu-Zr-AL/Ti/Ag alloys, moderate-sized CuZr-based BMG composites were obtained using the suction casting. When the value of ***K***-value is close to 1 as for Cu-Zr-Al-Y and Cu-Zr-Al-Er alloys, relatively large BMG composites with the presence of the B2 CuZr in the glassy matrix is prone to be fabricated. These new CuZr-based BMG composites with the presence of the B2 CuZr crystals in the glassy matrix can be good candidates as the structural materials due to their possible high strength and large plasticity, which is favorable for the development of BMGs.

5 Processing routes for CuZr-based BMG composites

Even though the formation of CuZr-based BMG composites can be pinpointed by using our new strategy [315], the distribution, size and the shape of the B2 CuZr phase, which is vital for the good deformability of CuZr-based BMG composites [131, 135, 191, 213, 295, 351-356], cannot be controlled well. In this chapter, different methods were explored to control the formation of the B2 CuZr phase in the glassy matrix, which may assist in the fabrication of the high-performance CuZr-based alloys.

5.1 Influence of the melting current/time

It was found that the thermal stability, the crystallization and the corresponding mechanical properties of BMGs can be affected by controlling the melting currents and melting times (i.e. changing the casting temperature), [338, 339, 357-362], implying that the casting process is very important for the formation of CuZr-based BMG composites [357, 359, 360]. It has been demonstrated that this method can also affect the precipitation of crystals during casting, which indicates that the formation of CuZr-based BMG composites may be tuned by changing the melting currents/times. $Cu_{47.5}Zr_{47.5}Al_5$ and $Cu_{46}Zr_{46}Ag_8$ alloys were chosen to investigate the formation and the distribution of the B2 CuZr phase in the glassy matrix.

Table 5.1 *The melting currents and melting times for different CuZr-based alloys.*

Samples	Melting current (A)	Melting time (s)	f_{amor} (vol.%)	Designation
$Cu_{47.5}Zr_{47.5}Al_5$	280 ± 2	15 ± 2	100	S0
$Cu_{47.5}Zr_{47.5}Al_5$	150 ± 2	10 ± 2	97.5 ± 0.5	S1
$Cu_{47.5}Zr_{47.5}Al_5$	86 ± 2	15 ± 2	78 ± 1	S2
$Cu_{47.5}Zr_{47.5}Al_5$	130± 2	10 ± 2	55 ± 3	S3
$Cu_{46}Zr_{46}Ag_8$	280 ± 2	18 ± 2	100	G0
$Cu_{46}Zr_{46}Ag_8$	150 ± 2	18 ± 2	73 ± 2	G1

$Cu_{47.5}Zr_{47.5}Al_5$ and $Cu_{46}Zr_{46}Ag_8$ rods with a diameter of 2 mm were fabricated by suction casting using different melting currents/times. The corresponding casting parameters for different alloys were listed in Table 5.1. Fig. 5.1 shows the

XRD patterns of the as-cast $Cu_{47.5}Zr_{47.5}Al_5$ and $Cu_{46}Zr_{46}Ag_8$ rods. As shown in Fig. 5.1a-b, CuZr-based BMG composites with different volume fractions of amorphous phase (f_{amor}) were successfully fabricated by adjusting the melting currents and melting times. When the melting current/time was 280 ± 2 A/15 ± 2 s and 280 ± 2 A/18 ± 2 s for the $Cu_{47.5}Zr_{47.5}Al_5$ and $Cu_{46}Zr_{46}Ag_8$ rods, respectively, the samples are fully amorphous (Fig. 5.1a-b). When the melting current/time decreases (see the Table 5.1) for each individual composition, as shown in Fig. 5.1, some crystalline peaks superimpose on a broad halo peak, which are identified to be the B2 CuZr phase together with little martensites. The corresponding f_{amor} can be obtained roughly from the OM pictures (Fig. 5.2). It can be seen that some crystals (orange area) precipitates in the glassy matrix as the melting currents/times is changing, further confirming the XRD results.

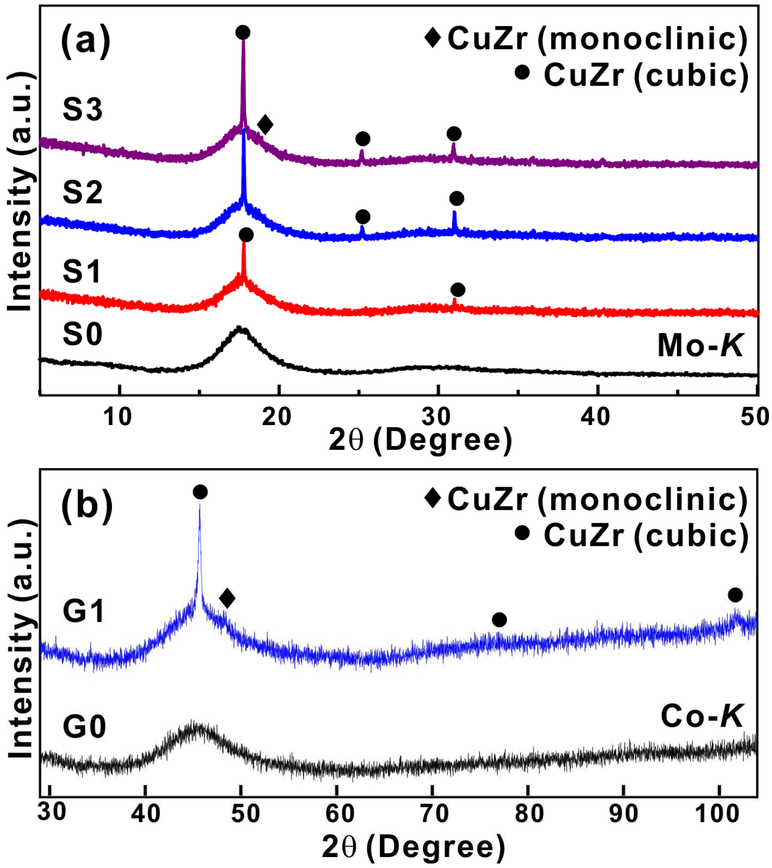

Figure 5.1 *XRD patterns of the as-cast (a)* $Cu_{47.5}Zr_{47.5}Al_5$*, and (b)* $Cu_{48}Zr_{48}Ag_8$ *rods with different contents of crystals.*

As shown in Fig. 5.2a, for the S1, S2, S3, and G1 samples with a large f_{amor} (Table 5.1 and Fig. 5.2a), the B2 CuZr crystals are few and well separated. When the f_{amor} decreases to about 55%, the spherical crystals start to accumulate with each other and gradually form a structural framework, corresponding well with the previous results [295]. The XRD and OM results indicate that the formation, the volume fraction, and the distribution of the B2 CuZr phase in the glass matrix for CuZr-based alloys are changed by changing the melting current/time. Furthermore, the substructures of the B2 CuZr phase exist in a form of dendrites (Fig. 5.2b-c). As the content of amorphous phase decreases to 55 ± 3 vol.%, the dendrites within the B2 CuZr crystals become more obvious.

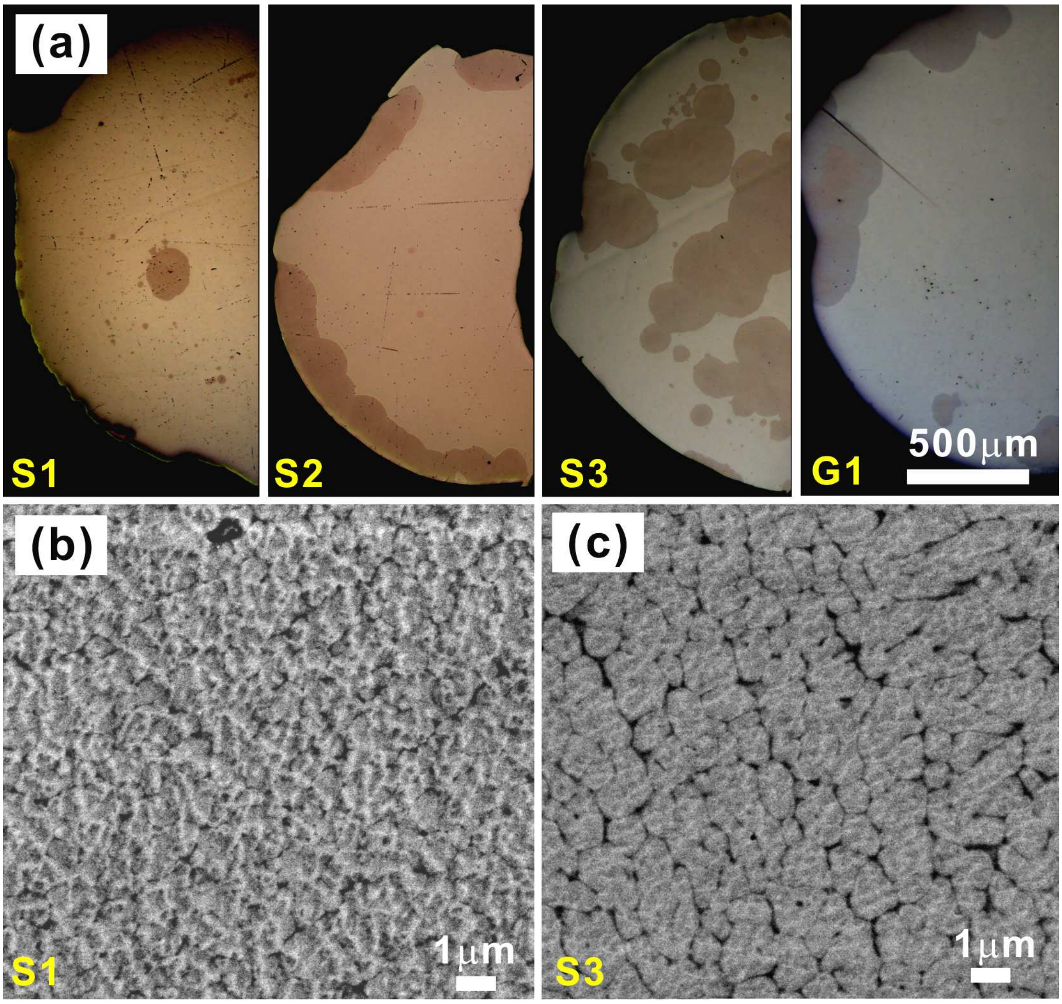

Figure 5.2 *(a) The distributions of the B2 CuZr phase of the S1, S2, S3, and G1 samples, and its internal dendrites in the glassy matrix for the as-cast (b) S1 and (c) G1 samples.*

During the experiments, the same copper mold was used during solidification, whose cooling capability is sufficient for the formation of fully amorphous $Cu_{47.5}Zr_{47.5}Al_5$ and $Cu_{46}Zr_{46}Ag_8$ rods. Only when the applied cooling rate is less than the critical cooling rate for fully amorphous rods (R_c), crystals in the glassy matrix start to precipitate because the nucleation of the glass-forming liquids is dominant by the steady state homogeneous nucleation [363]. However, when crystallization is dominant by the heterogeneous nucleation, the crystals can nucleate on heterogeneous nucleation sites and grow to different dimensions [57, 364, 365], which may result in different distributions and shapes of crystals in the glassy matrix. Therefore, it is reasonable to believe that the applied casting temperatures of the partial melts close to the copper mold during our experiments may locate in the semi-solid state region due to two possible reasons: (1) a low melting current and a short melting time can induce a low casting temperature of melts, and (2) the partial melts close to the copper mold may be cooled to a low temperature. Usually, when an alloy is heated between the liquidus and solidus temperatures and reaches an approximate thermal equilibrium state, it is in a diphasic state with some solid fraction. This state is defined as the semi-solid state [366]. When a metallic alloy is semi-solid [276], a high density of crystals precipitate and thus facilitates the further formation of the B2 CuZr phase in the glassy matrix during quenching. On the other hand, heterogeneous nucleation also occurs at preferential sites, i.e. impurities from mold walls or already solidified particles [367]. Hence, the B2 CuZr phase prefers to precipitate on the mold surfaces due to the lower free energy barrier for nucleation [367]. So the B2 CuZr phase can be obtained for $Cu_{47.5}Zr_{47.5}Al_5$ and $Cu_{46}Zr_{46}Ag_8$ BMG composites by changing the melting temperatures even though the applied cooling rate is enough to form the monolithic BMGs.

5.2 Adjusting the cooling rate

Based on the CCT diagram of CuZr-based alloys (Fig. 5.3), when the applied cooling rate (R_{com}) locates between the R_c (the critical cooling rate for fully glass formation) and R_{B2} (the critical cooling rate for the complete B2 CuZr phase formation), CuZr-based BMG composites can be fabricated during quenching. Different volume fractions of the B2 CuZr phase can precipitate under the same melting parameters but different R_{com}. However, it is worthy mentioning that the sizes of CuZr-based BMG composites also strongly depend on the GFA as does the thermal stability of the B2 CuZr phase as shown in Fig. 5.3. When the GFA of the glass-forming alloys becomes small, i.e. the value of R_c becomes large, it requires a higher R_{com} in order to fabricate CuZr-based BMG composites with a same f_{cryst}.

On the contrast, when the GFA of CuZr-based alloys become very large, CuZr-based BMG composites is prone to be fabricated by changing the actual cooling rate between R_c and R_{B2}.

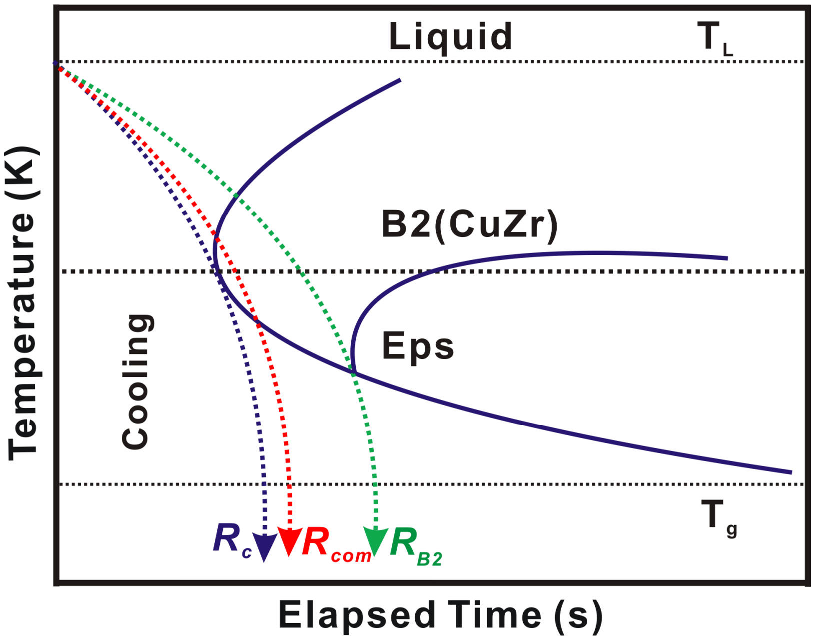

Figure 5.3 *Schematic CCT diagram during quenching for CuZr-based BMG composites.*

Actually, in **Chapter 4.3**, Cu-Zr-Al-Y and Cu-Zr-Al-Er BMG composites have been successfully fabricated by changing the diameters of the copper molds. In addition, it was also shown that a gradient microstructure can be observed in some cases because the local cooling rates are a little different from the top and bottom of the copper mold. As discussed in **Chapter 4**, this effect on the formation of crystals in the glassy matrix becomes more obvious when the applied cooling rate R_{com} is close to the R_c. In conclusion, it is a good method to control the volume fraction of the B2 CuZr phases in the glassy matrix even though it is difficult to adjust the distribution of crystals.

5.3 Re-melting of the pre-alloy

Here, a very effective way [368], i.e. the re-melting treatment of master alloys, was proposed to tune the microstructures of CuZr-based BMG composites. $Cu_{47.5}Zr_{47.5}Al_5$ alloy ingots with a similar weight of about 40 g were prepared, and were remelted for 4, 8, 12 and 20 times (M4, M8, M12, and M20, respectively), respectively, before they were injection-cast into a rod with a diameter of 3 mm. The melting duration for each time is approximately 1 min under a melting current of 410 A [368]. As shown in Fig. 5.4, SEM pictures show the microstructures of all the as-cast rods. Crystals (dark areas) distribute in the glassy matrix (white areas), which are indentified to be the B2 CuZr phase. For the M4 and M8 samples, the crystalline particles severely impinge with each other. When the remelting time increases to 12 and 20, respectively, a more homogenous distribution of crystals were observed for the M12 and M20 samples. For the M12 sample, a maximum tensile plasticity of about 13.6% was reached together with relatively high yield strength of about 1900 MPa [368]. Therefore, the optimum composite structure with the B2 particles distributing homogeneously in the glassy matrix was obtained for the M12 rod [368]. For the M20 rod, the f_{cryst} is very small even though the distribution of crystals is uniform.

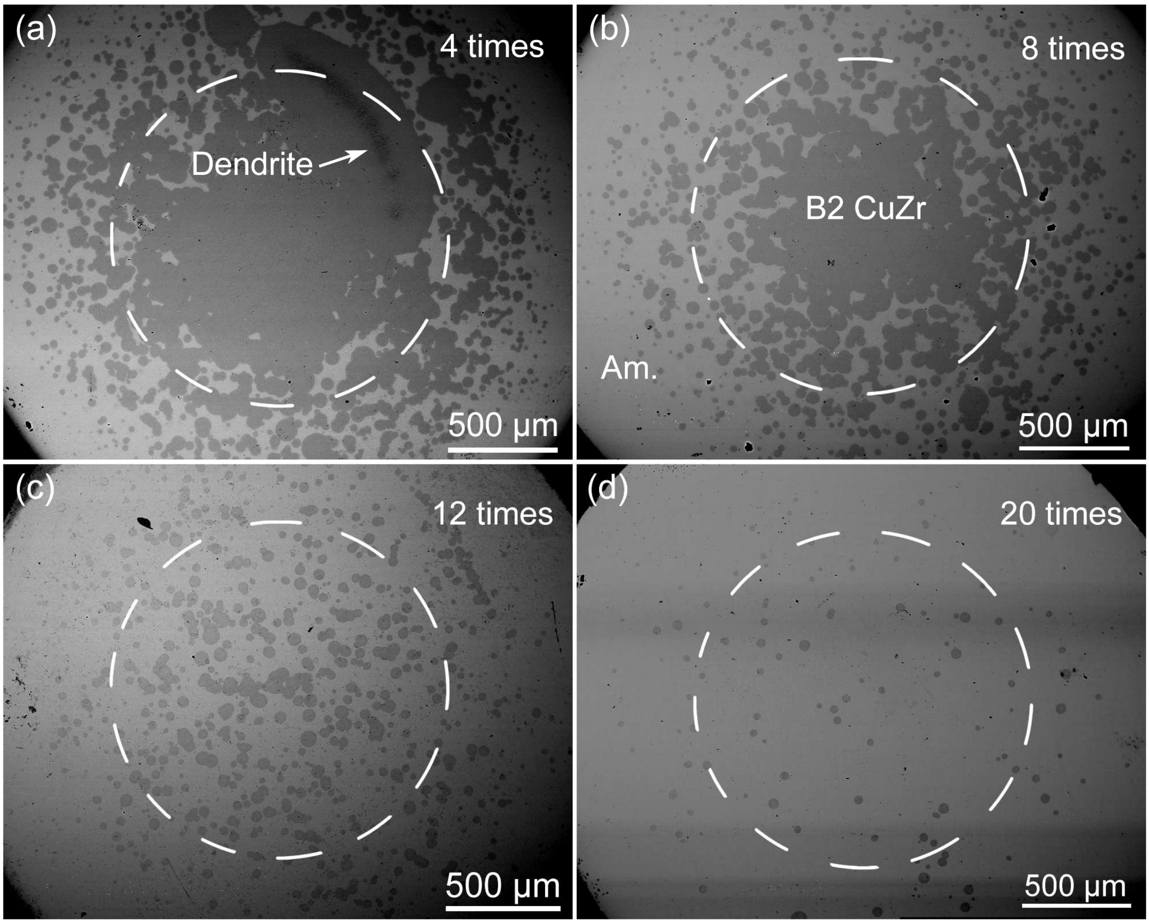

Figure 5.4 *SEM images of the as-cast* $Cu_{47.5}Zr_{47.5}Al_5$ *BMG rods with a diameter of 3 mm for the (a) M4, (b) M8, (c) M12, and (d) M20 samples [368].*

Therefore, it can be concluded that the remelting method indeed changes the nucleation of supercooled liquids during quenching. Usually, the nucleation of supercooled liquids is very sensitive to the compositions, refractory oxides and nitrides or oxygen/nitrogen stabilized phases [20, 369-373]. The oxides and nitrides which can act as heterogeneous nucleation sites may be dissolved by the remelting process [20, 369-375]. Therefore, the number and size of inclusions may decrease or even disappear with the remelting times increasing. Hence, the heterogeneous nucleation of the B2 CuZr crystals may be reduced, resulting in the homogenization of the structures. The dissolution of the oxygen and nitrogen in the solute state may induce a more efficient atomic packing structure of the alloys [370, 371, 374, 376, 377], leading to the increase of the GFA of the glassy matrix. Moreover, it has been proven [368] that with the remelting times increasing, the incubation times before crystallization become large, further confirming the suppression of the nucleation and the growth of the B2 CuZr crystals. Thus, the microstructures of the $Cu_{47.5}Zr_{47.5}Al_5$ BMG composites can be effectively tuned by controlling the remelting times of the master alloys. The more times the alloys were remelted, the smaller B2 CuZr particles become, and the more homogenous B2 CuZr phase distributes in the glassy matrix [368].

5.4 Introduction of boron nitride particles

As mentioned in **Section 5.3**, refractory oxides and nitrides or oxygen/nitrogen stabilized phases may play an important role in the nucleation of the B2 CuZr phase for CuZr-based alloys [20, 369-373]. When the foreign nucleation sites are introduced into the glassy matrix during solidification, the formation of crystals can be affected [20, 369-373, 378]. So the oxides and nitrides may have a large influence on the formation of the B2 CuZr phase in the glassy matrix for CuZr-based BMG composites. Previous results [377] have shown that after doping CuZr-based BMGs with nitrogen, the glass formation and the primary precipitating phase was changed. It was found [377] that the GFA of CuZr-based alloys can be improved with the addition of nitrogen of 1000 appm. However, excessive nitrogen deteriorated the GFA and simultaneously induced the formation of the B2 CuZr phase, $Cu_{10}Zr_7$ and other crystals, implying that the addition of the foreign nucleation sites can change the crystallization of the CuZr-based melts. In order to further illustrate the role of the foreign nucleation sites on the formation of crystals, boron nitride powders were chosen to check their effect on the formation of the B2 CuZr phase in CuZr-based alloys. Prior to the suction casting, as shown in Fig. 5.5, some boron nitride powders were painted on the copper mold surface. The suction casting device was used to cast the $Cu_{47.5}Zr_{47.5}Al_5$ alloy into the plate with dimensions of 1.5 or 2 mm × 10 mm × 60 mm under a vacuum atmosphere of about 2×10^{-5} mbar.

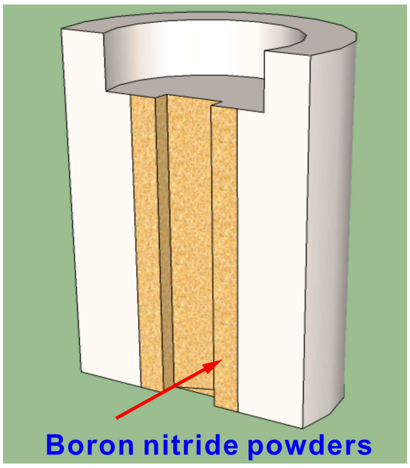

Figure 5.5 *Sketch map of the copper mold painted with boron nitride powders before casting.*

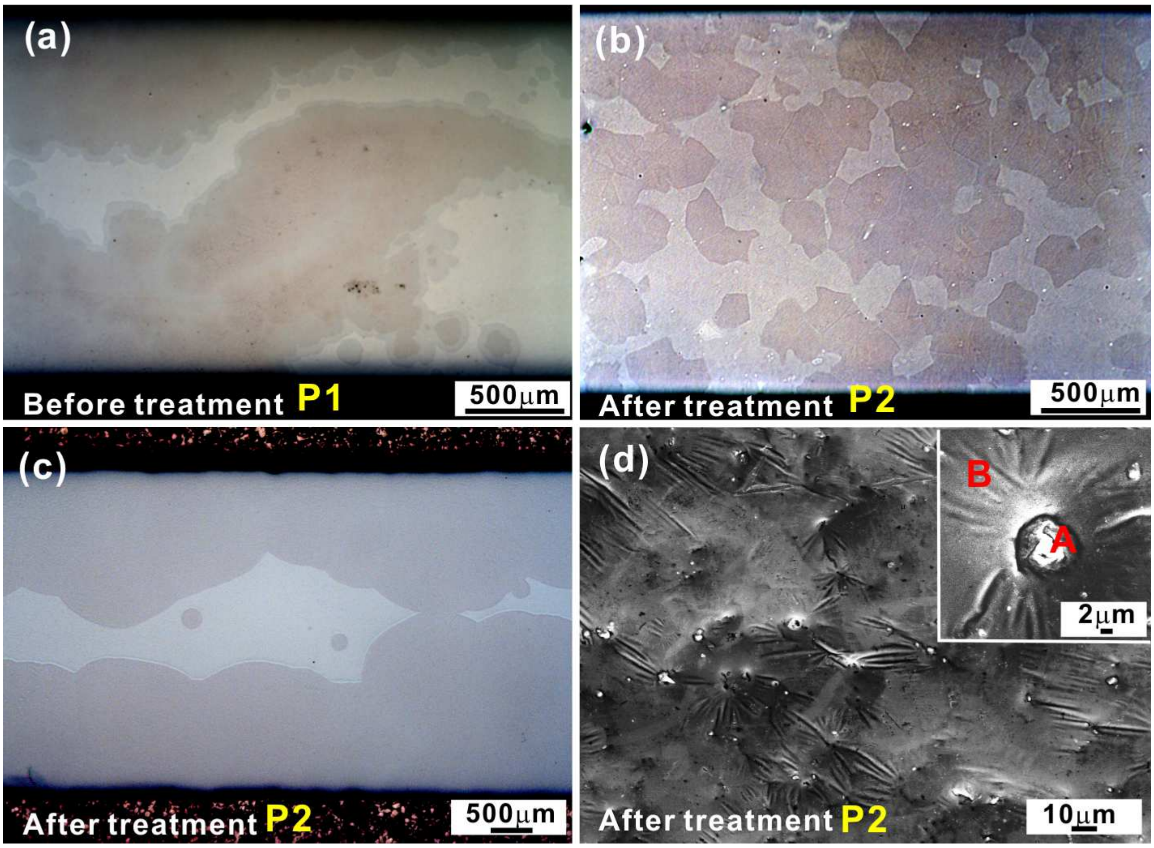

Figure 5.6 *(a) OM pictures of the area close the outside surface of the P1 plate, (b) of the area close the outside surface of the P2 sample, (c) of the structures in the center of the as-cast P2 sample, and (d) the surface morphology of the P2 plate.*

Usually, the critical thickness of a fully amorphous plate (D_c) for $Cu_{47.5}Zr_{47.5}Al_5$ alloy is about 1.5 mm [136, 254] without any boron nitride powders on the copper mold. Thus, as the thickness of the plate increases to 2 mm without the surface treatment (sample P1), it was found from Fig. 5.6 that a lot of crystals precipitate in the glassy matrix for the as-cast P1 plate. The crystals were identified to be the B2 CuZr phase by the XRD measurements (not shown). Many spherical B2 crystals interpenetrate with each other and distribute heterogeneously for the P1 sample (Fig. 5.6a) as the thickness of P1 is larger than D_c.

Meanwhile, the as-cast plates with a thickness of 1.5 mm (sample P2) with the surface treatment were also fabricated, which was shown in Fig. 5.6b. It was seen that a lot of crystals were observed in the glassy matrix for the P2 sample. Based on the XRD pattern (not shown), the microstructures were indentified to be the amorphous phase and the B2 CuZr phase. Compared with the microstructures for the P1 plate (thickness: 2 mm) and fully amorphous plate (thickness: 1.5 mm), the B2 crystals for the P2 sample (thickness: 1.5 mm) is not spherical but become a little sharp. Furthermore, it was also found that these B2 CuZr phase only form in the areas close the outside surface of the as-cast P2 sample. Interestingly, the size and distribution of these B2 phase in the glassy matrix become smaller and more relatively homogenous (Fig. 5.6b). However, the structures in the center of the P2 plate consist of the amorphous phase and the spherical B2 CuZr phase (Fig. 5.6c) again because the boron nitride powders on the surface of the copper mold cannot be dissolved into the melts during rapid solidification but only attached the surface of the melts.

Fig. 5.6d shows that the boron nitride powders attach to the outside surface of the P2 sample. Some “flower-like” structures can be observed on the surface with a white core (inset in Fig. 5.6d). Even though the EDX detector in a SEM cannot be used to accurately measure the content of boron and nitrogen due to their smaller atomic numbers [379], the EDX results can roughly indicate the change trend of the boron and nitrogen elements. It was found that the area A contains more oxygen than the area B in the inset in Fig. 5.6d. Furthermore, other elements in the area A are determined to be Cu: 32.48 at.%, Zr: 43.98 at.%, Al: 5.89 at.%, and O: 17.63 at.%. All these observations imply that after the boron nitride powders were adhered to the surface of the copper mold, the B2 CuZr phase trends to form around the surface of the copper mold. Furthermore, the boron nitride may also reduce the capability of heat transference during solidification, which may result in the decrease of the cooling rate of the copper mold.

Therefore, when the boron nitride is introduced into alloys during the casting processes, the heterogeneous nucleation of the B2 CuZr phase may form at preferential sites of impurities. Therefore, a lower effective surface energy can be obtained at such preferential sites and the free energy barrier needed for heterogeneous nucleation is lowered, which facilitate the nucleation of the B2 CuZr phase [370, 371, 374, 376, 377, 380].

5.5 Effect of TaW inoculation

Recently, finely dispersed B2 CuZr precipitates have been obtained in CuZr-based alloys after the addition of Ta [352]. During solidification, Ta precipitates from the melt due to its limited solubility in the form of *bcc* Ta or Ta-rich crystals with sub-nanometer sizes [293], which can serve as nuclei for the B2 CuZr precipitates. Even though the presence of Ta seems to positively affect the microstructures of CuZr-based BMG composites [352], it is not possible to artificially control the size and distribution of the B2 CuZr phase in the glass matrix. Furthermore, for CuZr-based alloys, it has not been tried to add refractory particles, which may act as heterogeneous nucleation sites for the formation of the B2 CuZr phase in the glassy sample, to the CuZr-based alloy melt using the *ex situ* method.

Here, as an alternative approach, ball-milled $Ta_{50}W_{50}$ (labeled TaW particles) were added to a CuZr-based glass-forming alloy to change the formation of the B2 CuZr phase. The $Cu_{47.5}Zr_{47.5}Al_5$ ingots were broken into pieces and mixed with 2 at.% TaW particles with different sizes (Table 5.2) obtained by the powder-metallurgical route. Firstly, a TaW ingot was prepared using arc melting, crushed manually by hammering, and then milled for 6 hours in a ball milling machine with a rotation velocity of 150 rpm under the protection of the argon atmosphere. Secondly, differently sized TaW particles were selected using different screens. Thirdly, $Cu_{47.5}Zr_{47.5}Al_5$ and TaW particles were mixed with each other and compacted into a bulk sample using an extrusion press for suction casting. Finally, the bulk sample was melted and simultaneously cast into copper molds with diameters of 2 mm and 3 mm by suction casting, respectively.

Table 5.2 *Crystalline volume fractions, sizes of the TaW particles, the volume fraction of amorphous phase and the casting parameters of the as-cast* $Cu_{47.5}Zr_{47.5}Al_5$ *rods with different diameter..*

Sample	Diameter (mm)	f_{amor} (vol.%)	Size of TaW particles (μm)	Melting Current (A) / time (s)
T1	2	87 ± 5	70 - 500	280 ± 2 / 18 ± 2
T2	3	55 ± 4		
T3	2	11 ± 2	2 - 20	
T4	3	2 ± 1		

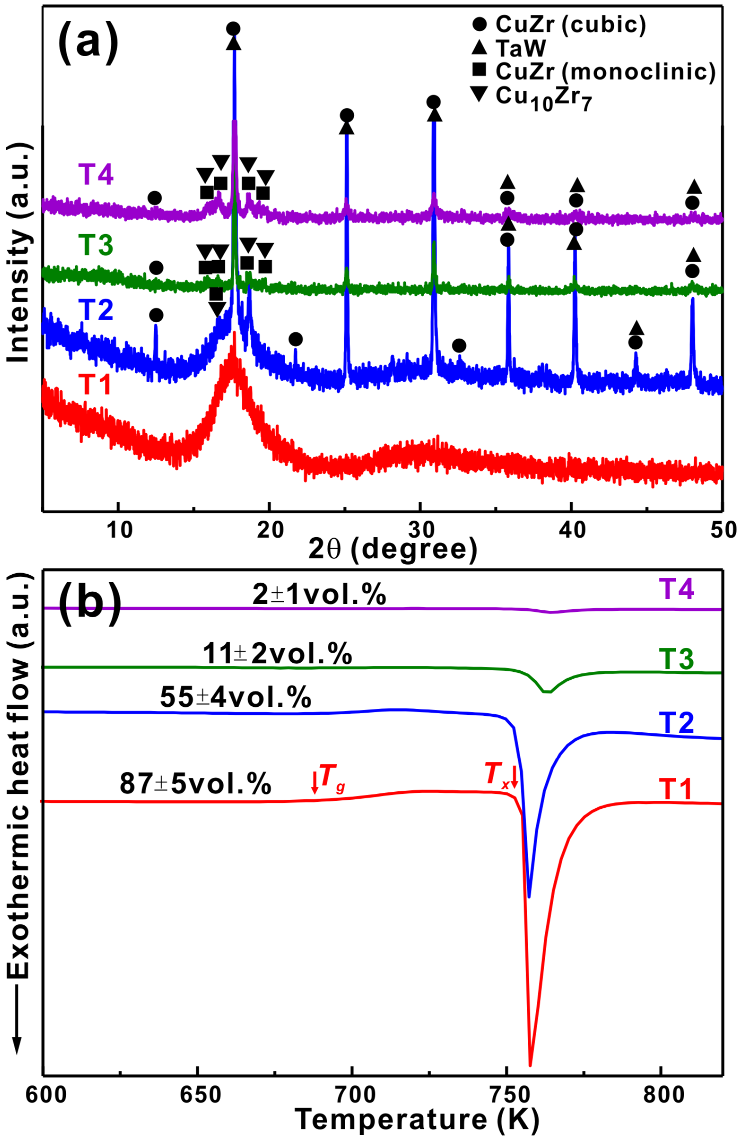

Figure 5.7 *(a) XRD patterns and (b) DSC curves (heating rate 20 K/min) for the as-cast rods with different diameters with the addition of TaW particles with different sizes.*

The detailed casting parameters are listed in Table 5.2. Fig. 5.7 shows the XRD patterns and DSC curves for the as-cast rods. The broad diffraction maximum in the XRD patterns proves the partially glassy structure of the T1 and T2 samples (Fig. 5.7a). For the T3 and T4 samples, sharp crystalline peaks superimposed on a small and diffuse diffraction maximum prove that the samples consist of a lot of crystals and small amount of amorphous phase. For all the as-cast samples, the B2 phase and a TaW solid solution can be identified, while other reflections belong to CuZr martensitic crystals and $Cu_{10}Zr_7$, respectively. It is well known that TaW is a solid solution of *bcc* Ta and *bcc* W, and its calculated lattice constant is 0.32316 nm [381], being nearly identical to that of the B2 CuZr phase (lattice constant: 0.3262 nm [295]), so that the reflections of the B2 phase and the TaW solid solution overlap in the XRD patterns.

The DSC curves (Fig. 5.7b) show that the decreasing crystallization peaks of the samples further confirm the decrease of the content of the amorphous phase. Based on the exothermic enthalpy extract from DSC curves, the corresponding f_{amor} were calculated, which is listed in Table 5.2. Furthermore, with the content of the amorphous phase decreasing, the glass transition temperature gradually disappears, implying that the crystallization of the supercooled liquid is accelerated when the TW particles were introduced into the liquids during casting.

As listed in Table 5.2 and shown in Fig. 5.7, the changes of not only the diameters of the as-cast rods but also the size of the TaW particles change the content of the amorphous phase. Basically, a larger rod diameter reduces the cooling rate under the same casting condition and leads to the increase of the f_{cryst} [382]. On the one hand, it can be seen that when TaW particles with an almost same size were introduced into CuZr-based alloys, the contents of the B2 CuZr phase and the amorphous phase increase and decrease, respectively, as the cooling rate decreases. On the other hand, as listed in Table 5.2, under the same cooling rate, the content of the amorphous phase decreases from 87 ± 5% vol.% to 11 ± 2% vol.% as the size of the TaW particles decreases from 70 - 500 μm to 2 - 20 μm, respectively (Fig. 5.7). Thus, it indicates that the *ex situ* addition of

TaW particles is favorable for the formation of the B2 phase for metastable CuZr-based alloys.

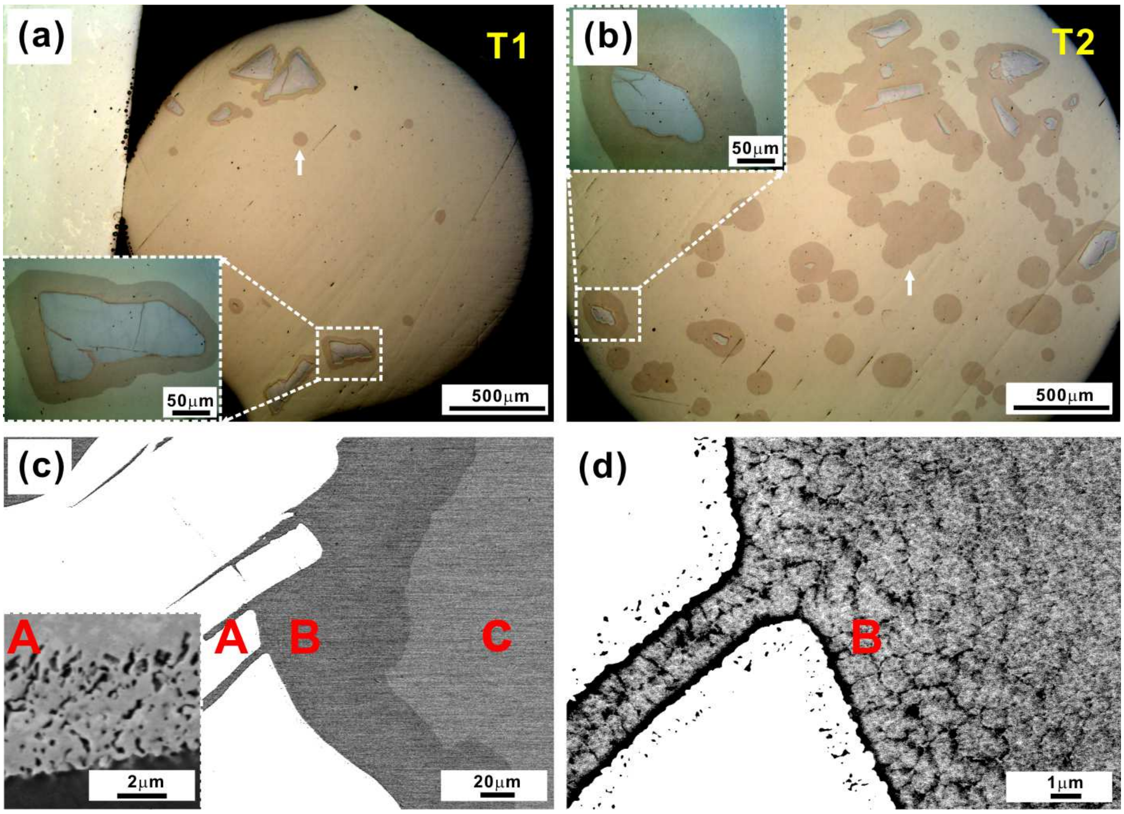

Figure 5.8 *OM images of the (a) T1 and (b) T2 rods (insets: magnified OM images of the B2 phase around the TaW particles), (c) the B2 CuZr phase (region B), and the glassy matrix (region C) of the samples with larger addition of TaW particles (Inset: magnified SEM picture of TaW particles (region A)), and (d) magnified structures within the B2 phase around the TaW particles.*

Figs. 5.8 and 5.9 show the OM images of the T1, T2, T3, and T4 rods containing TaW particles with different sizes. For the T1 and T2 samples with the addition of large-sized TaW particles, an amount of B2 crystals precipitate around the TaW particles (insets in Figs. 5.8a-b). As shown in Figs. 5.8c-d, for the T1 and T2 samples, B2 CuZr dendrites (region B in Figs. 5.8c-d) preferably nucleate and grow around the TaW particles (region A in Figs. 5.8c-d). The dendrite spacing becomes gradually smaller farther away from the TaW particles, and finally the dendrites disappear in the glassy matrix (region C in Figs. 5.8c-d).

For the T3 and T4 samples, when the size of TaW particles decreases to 2 - 20 μm, only a small volume fraction of amorphous phase can be obtained at the edge of the rods (Figs. 5.9a-b). As shown in Fig. 5.9c-d, B2 CuZr dendrites also nucleate and subsequently grow around smaller TaW particles for the T3 and T4 samples.

Compared with those in the T1 and T2 samples, the B2 dendrites in the T3 and T4 samples become more, and the dendrite arms become developed. The dendrites intersect with each other in the T3 and T4 samples. At the edge of the rods of the T3 and T4 samples, where a higher cooling rate is obtained, some smaller B2 CuZr precipitates can still nucleate around the smaller TaW particles (Fig. 5.9d).

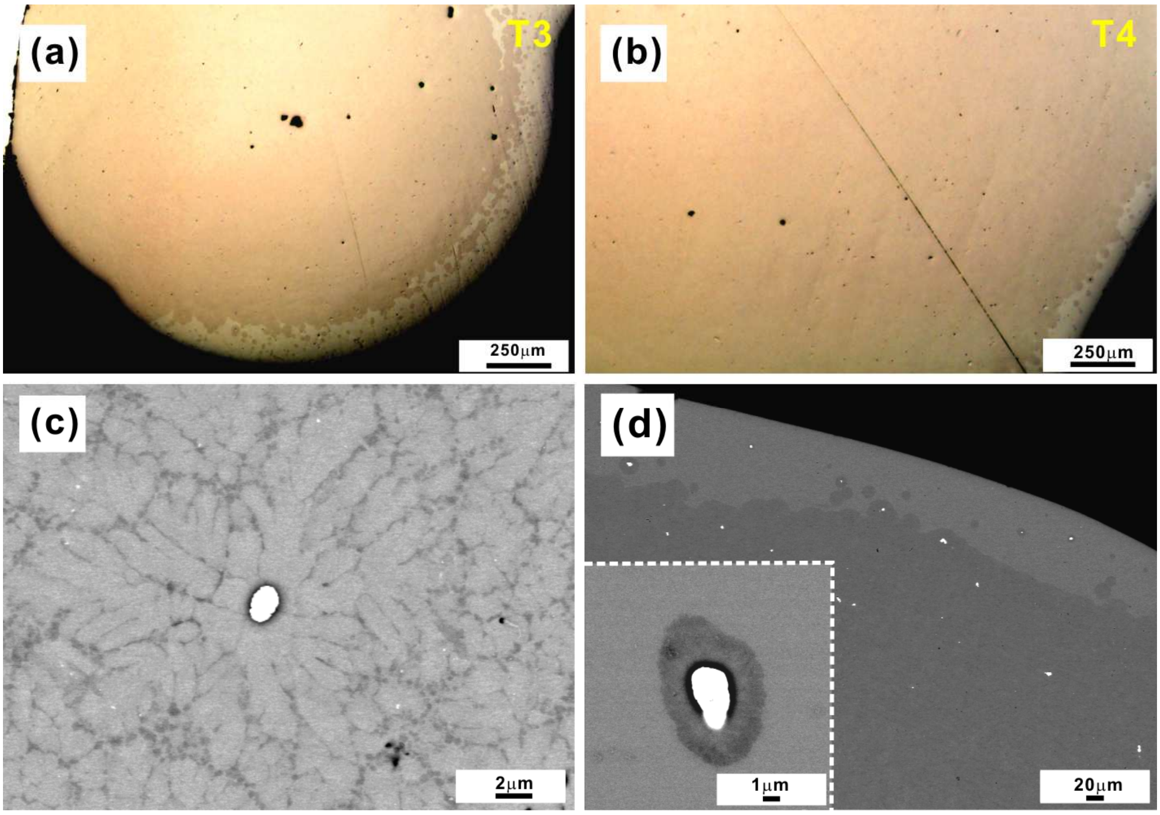

Figure 5.9 *OM images of the as-cast (a) T3 and (b) T4 rods, (c) microstructure of the B2 CuZr phase in the glassy matrix, and (d) microstructure at the edge of the T3 and T4 rods.*

However, besides the B2 phase around the TaW particles, some isolated B2 CuZr crystals also form in the glassy matrix at various places (see the arrows in Figs. 5.8a-b). Previous work has shown that the critical diameter of the fully amorphous $Cu_{47.5}Zr_{47.5}Al_5$ alloy is about 3 mm [288, 331]. Therefore, the addition of TaW particles also results in the decrease of the GFA of the glassy matrix. However, systematic research has shown that the thermal stability and the GFA of the glassy matrix are not deteriorated upon *ex-situ* addition of particles in Zr-based BMG composites [205, 207, 217, 383-390] because the elements in particles are not dissolved into the glassy matrix. Therefore, EDX measurements were conducted in the regions A (TaW particles), B (B2 CuZr phase), and C (glassy matrix) for the T1 sample (Fig. 5.8c). As listed in Table 5.3, a small amount of Cu (about 8.25 at.%) and Zr (about 0.89 at.%) are dissolved into the TaW solid solution, while a lot of Al can be detected within the TaW particles (region A) (Table 5.3).

Table 5.3 *The contents of Cu, Zr, Al, Ta, and W in Regions A, B, and C.*

Region	Cu (at.%)	Zr (at.%)	Al (at.%)	Ta (at.%)	W (at.%)
A	8.25 ± 1.4	0.89 ± 1	4.23 ± 2	44.51 ± 0.05	42.12 ± 0.06
B	42.70 ± 1.4	52.26 ± 1	4.47 ± 2	0.17 ± 0.05	0.41 ± 0.06
C	45.86 ± 1.4	50.06 ± 1	3.48 ± 2	0.15 ± 0.05	0.43 ± 0.06

Meanwhile, Ta and W appear to be hardly dissolved in the B2 CuZr phase and the glassy matrix (regions B and C) (Table 5.3). The relatively low solubility of Ta and W in the B2 phase and the glassy matrix may be due to the insufficient melting temperature/time during suction casting, the high melting point (around 3450 K) of the TaW particles [391], and the positive heats of mixing between Ta, W and the main elements Cu and Zr [392]. Furthermore, the efficiency of the heterogeneous crystal nucleation is associated with a range of microscopic properties, such as crystal structure, lattice mismatch, and other factors [393, 394]. The similar lattice constant of the $Ta_{50}W_{50}$ solid solution as the B2 CuZr phase [295, 381] may result in a low mismatch between these crystals which can reduce the effective surface energy between the B2 CuZr phase and the TaW particles. Therefore, the free energy barrier needed for the heterogeneous nucleation of the B2 CuZr phase around the TaW particles is decreased, resulting in the preferential nucleation of the B2 CuZr phase around these micro-scaled TaW particles.

Furthermore, previous results [284, 285, 292] have shown that as the Al content decreases from 6 at.% to 0%, the GFA decreases for CuZr-based alloys. Thus, in our case, when a certain amount of Al were dissolved into the TaW particles, the content of Al in the glassy matrix are decreased, which may result in the decrease of the GFA of the glassy matrix. Therefore, some isolated B2 CuZr crystals start to precipitate in the glassy matrix. It can be seen that the external surfaces of the TaW particles become porous (inset in Fig. 5.8c) for all samples, which may result from surface re-melting. This recrystallization behavior may support the nucleation of the B2 CuZr phase around TaW particles. Conversely, this reaction may also support the fact that a few TaW solid solutions are dissolved into the glassy matrix. All in all, it can be concluded that the TaW particles *ex situ* added to $Cu_{47.5}Zr_{47.5}Al_5$ can be used as nucleation agent to modify the precipitation of the B2 CuZr in CuZr-based BMG composites. In future work, further studies are needed to optimize the corresponding milling and casting processes.

5.6 "Flash annealing"

It has been demonstrated that partial devitrification of MGs upon heating is an effective method to improve their mechanical and physical properties [70, 225, 376, 395-399]. It is prone to control the volume fraction of crystals by adjusting the annealing temperature and the annealing time, respectively. However, an amount of free volume in the glassy matrix can be vanished due to the relatively slow heating and cooling rate [126, 152, 262, 400]. In 2011, a rapidly heating and cooling method has been used to shape amorphous metals, which utilizes Joule heating to uniformly heat MGs to a supercooled liquid state within milliseconds [401, 402]. It was found that when the heating rate and cooling rate are enough, the crystallization of MGs is avoided.

In 2009, Pauly *et al.* [302] first proposed a similar idea to control the crystalline phase and the amorphous phase in CuZr-based alloys, which contains three fabrication processes (Fig. 5.10): (1) Fabrication of CuZr-based BMGs, (2) Partial devitrification of CuZr-based BMGs at certain temperatures with different holding times at a very rapid heating rate, and (3) Rapid cooling of partially devitrified CuZr-based BMGs to room temperature. As shown in Fig. 5.10, when the cooling rate is larger than R_c, the fully amorphous CuZr-based alloys can be obtained from the melt. Furthermore, as CuZr-based BMGs are heated to a temperature T_B at a high heating rate, some of the amorphous phase transform into the B2 phase after a specific holding t_1 time. If the subsequent cooling rate (see R_{com} in Fig. 5.10) is enough and the holding time t_1 is well controlled, nano- or micro-scaled B2 CuZr phase in the glassy matrix will be obtained. The distribution, volume fraction, size and shape of the crystals are very important for the mechanical properties of BMG composites [131, 135, 191, 213, 295, 351-356]. Hence, this "flash annealing" method has a future prospect for the formation of CuZr-based BMG composites.

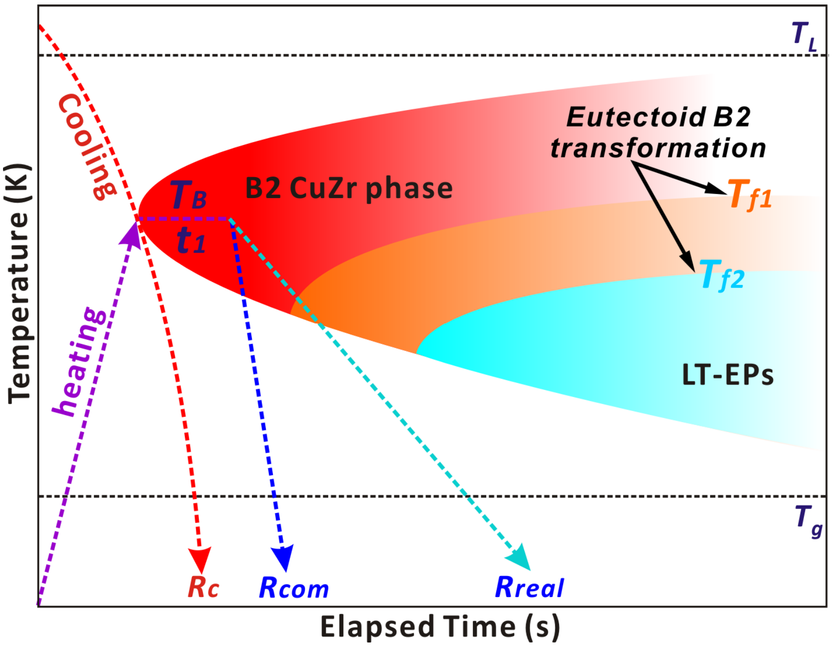

Figure 5.10 *CCT diagram during heating illustrating the formation of CuZr-based BMG composites.*

In order to obtain a high heating and cooling rate, a machine called MILA-3000 Mini Lamp Annealer made by ULVC-RIKO, Inc. in Japan (Fig. 5.11) was used, whose maximum heating and cooling rates are 50 K/s, respectively. As shown in Fig. 5.11, the MILA Mini Lamp annealing system uses an infrared lamp with a high density and high output as a heating element and permits rapid heating and cooling of a sample by reflection convergence under an atmosphere of 95%N_2+5%H_2 [403].

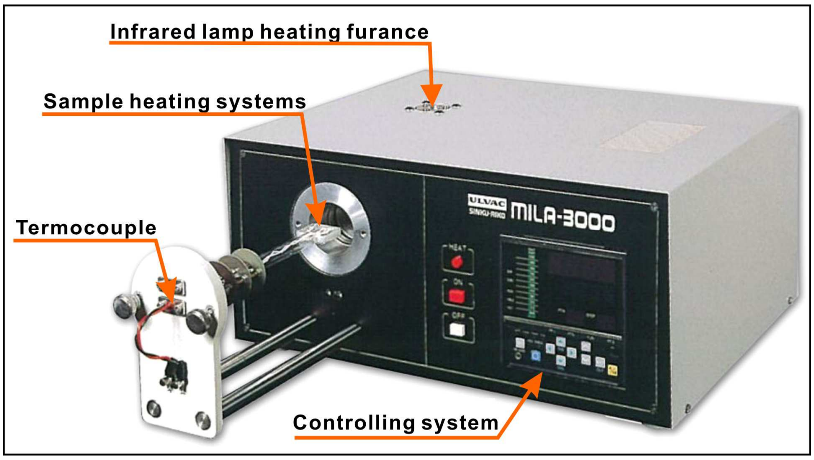

Figure 5.11 *The picture of the MILA-3000 Mini Lamp Annealer. Taken from Ref. [403].*

As discussed in **Chapters 3 and 4**, a large cooling rate during quenching is required to avoid the eutectoid decomposition of the B2 phase during the cooling process for most of CuZr-based BMGs. However, in our case, the cooling rate of 50 K/s (R_{real} in Fig. 5.10) is still not enough. As shown in Fig. 5.10, during cooling process, the B2 CuZr phase has a bad thermal stability at room temperature due to a higher T_f (i.e. T_{f1} in Fig. 5.10). As a result, the B2 CuZr phase is not prone to be kept during quenching. Therefore, it is necessary to fabricate new CuZr-based BMGs whose eutectoid B2 CuZr transformation occurs at relatively low temperatures (T_{f2} in Fig. 5.10). As shown in Fig. 5.10, the alloys whose B2 CuZr eutectoid transformation temperature (T_{f2}) of new alloys is lower than the T_{f1}, and thus, under a cooling rate of 50 K/s (R_{real}), new alloys can be fabricated into BMG composites with the presence of B2 phase in the glassy matrix (Fig. 5.10).

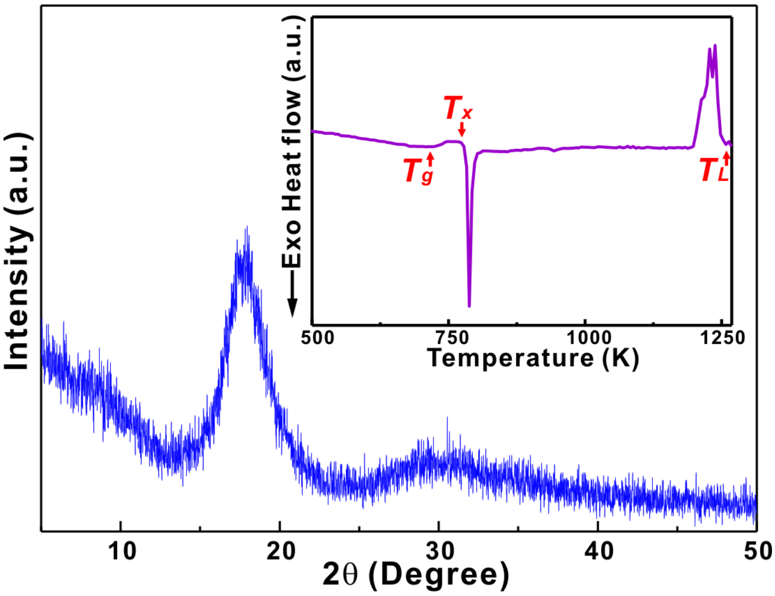

Figure 5.12 *XRD patterns of the as-cast* $Cu_{42}Zr_{42}Al_{10}Co_6$ *specimens (Insets: the corresponding high-temperature DSC curves).*

Recently, our group [329, 332] has found that with the content of Co addition increasing, the eutectoid B2 CuZr transformation shifts to a lower temperature [329, 332]. As the content of Co is more than 5 at.%, the main crystallization products are the B2 CuZr phase. However, with the content of Co increasing, the GFA of CuZr-based alloys become gradually worse [327, 328]. Usually, the GFA of CuZr-based alloys can be effectively enhanced with the addition of Al, Ag, and Re (rare metals) and so on [284, 285]. Here, 10 at.% Al was introduced into a CuZr-based alloy in order to improve the GFA, and simultaneously 6 at.% Co was also added in order to increase the thermal stability of the B2 CuZr phase. As shown in Fig. 5.12, the XRD pattern of the as-cast $Cu_{42}Zr_{42}Al_{10}Co_6$ specimens with a diameter of 2 mm indicates the nature of the fully amorphous phase. The DSC curve (inset in Fig. 5.12) shows that the eutectoid B2 CuZr transformation disappears, indicating that the B2 phase might become one of the main crystallization products at low temperatures or with the melting event at a higher temperature. Furthermore, the values of T_g, T_x, and T_L are determined to be 711 ± 2 K, 776 ± 2 K, and 1249 ± 2 K, respectively.

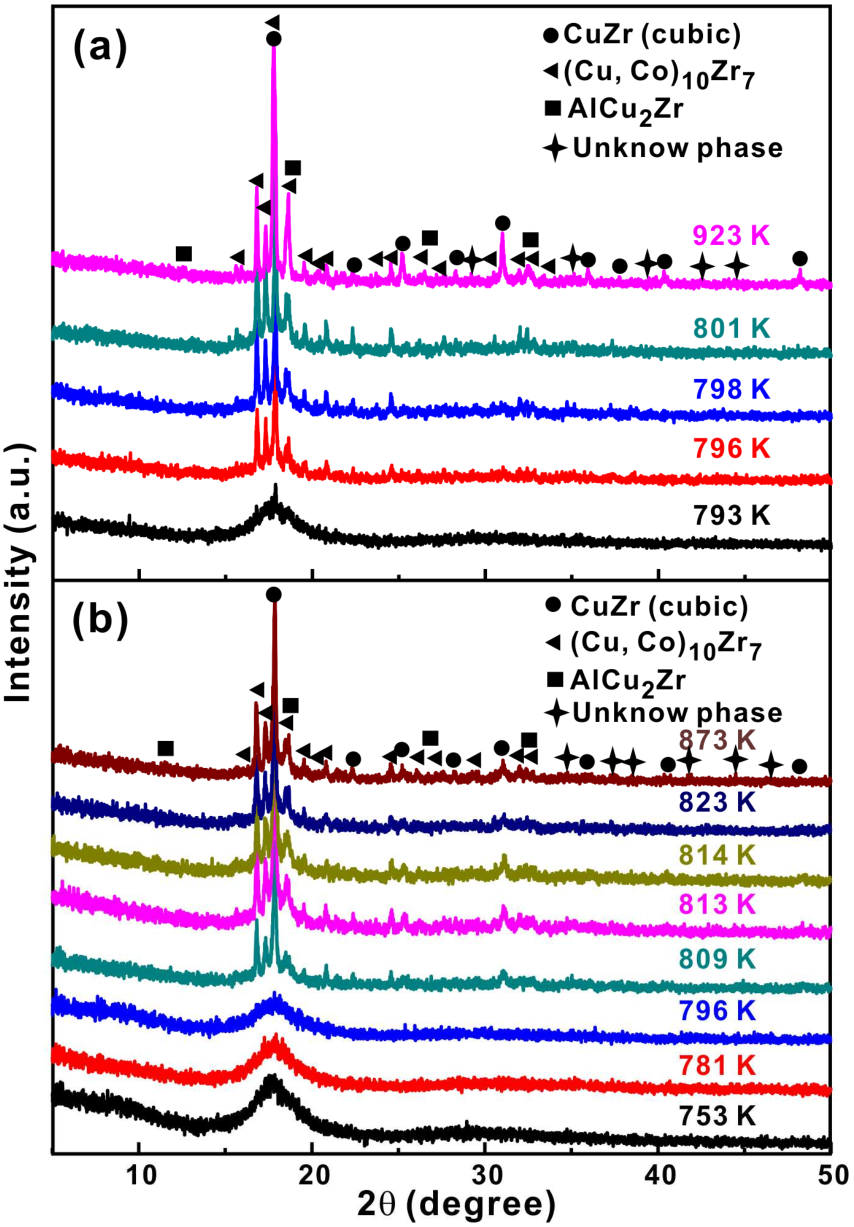

Figure 5.13 *XRD patterns of the as-cast* $Cu_{42}Zr_{42}Al_{10}Co_6$ *specimens annealed at different temperatures by the DSC device at heating rates of (a) 40 K/min, and (b) 60 K/min, respectively.*

In order to further confirm this result, an annealing treatment was applied to detect the crystallization products. Different heating rates (i.e. 40 K/min and 60 K/min) were used to check whether the crystallization shifts to higher temperatures. The XRD patterns of the as-cast $Cu_{42}Zr_{42}Al_{10}Co_6$ specimens annealed at different temperatures, i.e. 793 K, 796 K, 798 K, 801 K, and 923 K at the heating rate of 40 K/min are shown in Fig. 5.13a. Meanwhile, Fig. 5.13b exhibits the XRD of the as-cast $Cu_{42}Zr_{42}Al_{10}Co_6$ sample annealed at temperatures, i.e. 753 K, 781 K, 796 K, 809 K, 813 K, 814 K, 823 K, and 873 K, at the heating rate of 60 K/min. All the samples were cooled at a cooling rate of 100 K/min.

The primary crystallization products (Fig. 5.13a) of the as-annealed $Cu_{42}Zr_{42}Al_{10}Co_6$ samples annealed at 793 K at a heating rate of 40 K/min are identified to be the B2 CuZr phase, indicating that the eutectoid B2 CuZr transformation shifts to a relatively low temperature compared with these of Cu-Zr-Al and Cu-Zr-Ti alloys (See **Chapter 3**). With the annealing temperature increasing, $(Cu, Co)_{10}Zr_7$ phase together with a little $AlCu_2Zr$ and some unknown crystals start to precipitate. However, the B2 CuZr phase still exists and is very stable, implying that this new alloy system is a good candidate for the formation of CuZr-based BMG composites using the present flash annealing method.

On the other hand, the sample annealed at 793 K at the heating rate of 40 K/min consists of a little B2 CuZr phase together with amorphous phase, while for the sample annealed at 796 K at a heating rate of 60 K/min, only amorphous phase was observed. Furthermore, when the samples were heated to 796 K (Fig. 8.12a-b) at the heating rates of 40 K/min, some crystalline peaks can be observed. It was also noted that the onset temperature of the crystallization events also increases a little (not shown) with the heating rate increasing, which is of purely kinetic factors and can be described well by the Kissinger relation [404]. These observations indicate that the crystallization event is heating-rate dependent.[401, 402].

In the following, the as-cast $Cu_{42}Zr_{42}Al_{10}Co_6$ specimens were annealed at different temperatures with different holding times at the heating and cooling rate of 50 K/s (Fig. 5.14). The sample heated to 723 K and then kept at 723 K for 60 s prior to cooling is termed AC723-60. Other samples are indexed following this nomenclature rule.

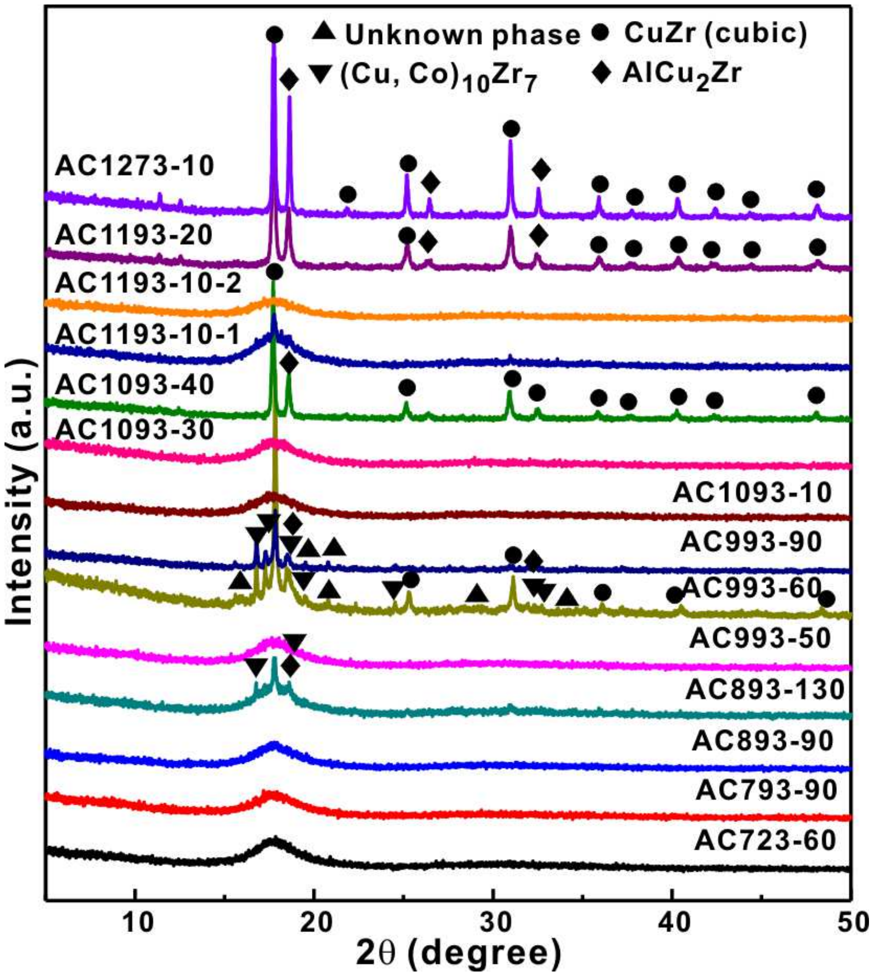

Figure 5.14 *XRD patterns of the as-cast* $Cu_{42}Zr_{42}Al_{10}Co_6$ *specimens annealed at different temperatures at heating and cooling rates of 50 K/s.*

As shown in Fig. 5.14, the as-cast sample (AC723-60) kept at a temperature less than T_x, i.e. 723 K for 60 s, is still fully amorphous. Even with the annealing temperature increasing to 793 K (above T_x), no crystalline reflections are observed after the sample was kept there for 90 s (AC793-90, Fig. 5.14). With the annealing temperature increasing to 893 K, it was found that the incubation time for the crystallization is about 130 s. As the annealing temperature increases to 993 K, 1093 K, and 1193 K, the incubation time reduces to about 60 s, 40 s, and 10s, respectively (Fig. 5.14). Furthermore, after the samples were heated to certain temperatures, the B2 CuZr crystals together with $(Cu,Co)_{10}Zr_7$ phase together with a little $AlCu_2Zr$ and some unknown crystals gradually form with the holding time increasing.

Furthermore, it is necessary to mention that as the samples are annealed at high temperature larger than 1193 K, the temperature cannot be controlled well by the present flash annealing machine so that a longer holding time will be spent on heating the sample than the planned time. After the required temperature is achieved, the machine may continue to heat the sample to a little higher temperature. Therefore, the uncertain heating times and annealing temperatures have an influence on the crystallization behavior. For example, as the sample was heated to 1193 K for 10 s (Fig. 5.14), some samples are still fully amorphous (AC1193-10-2), while the B2 CuZr phase starts to precipitate for others (AC1193-10-1). As the annealing temperature further increasing close to T_m, as shown in Fig. 5.14, the samples only contains the B2 CuZr phase and $AlCu_2Zr$ crystals. Therefore, the whole crystallization process is determined as follows: amorphous phase → amorphous phase + B2 CuZr → B2 CuZr + $(Cu,Co)_{10}Zr_7$ + unknown phase → B2 CuZr + $AlCu_2Zr$. Anyway, it can be concluded that CuZr-based BMG composites were successfully fabricated by controlling the annealing temperatures and holding times.

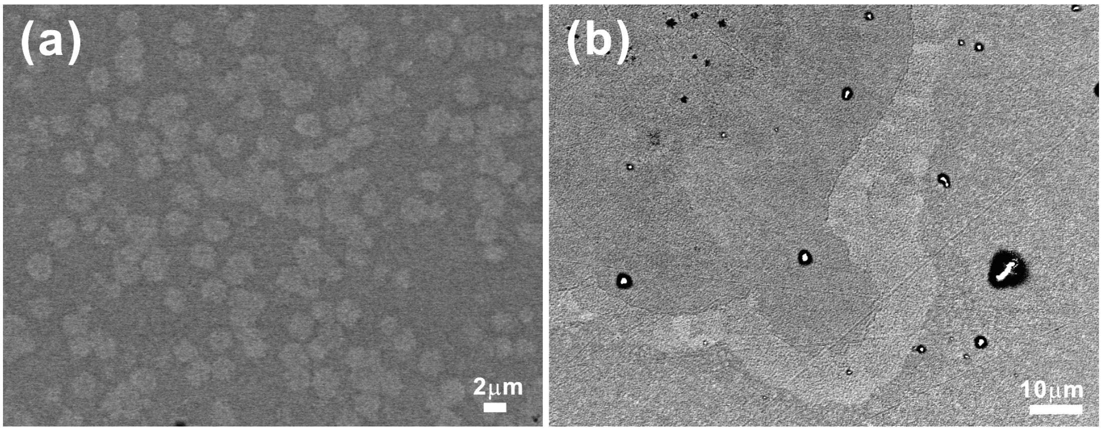

Figure 5.15 *The morphologies of the B2 CuZr phase from (a) the center and the outside surface (b) for the as-cast* $Cu_{42}Zr_{42}Al_{10}Co_6$ *specimens annealed at 893 K for 130 s.*

The morphologies of the B2 CuZr phase in the glassy matrix are shown in Fig. 5.15. It is obvious that the size of the B2 CuZr phase is 43 ± 5 μm with an approximately circular shape (white area in Fig. 5.15a). In addition, the micro-scaled B2 CuZr phase is distributed very homogenously in the glassy matrix. However, our method does not heat the sample very uniformly. Therefore, the B2 CuZr phase (dark area in Fig. 5.15b) preferentially forms near the outside surface where the sample is overheated and thus the B2 CuZr phase may nucleate and grow more quickly than those in the center of the rods. In such a case, the well separated B2 CuZr crystals begin to aggregate with each other, and then form a structural framework in the outside of the rods (Fig. 5.15b). Even though the heating and cooling rates of the present flash annealing machine are still not adequate, this idea for the fabrication of CuZr-based BMG composites has been proven to be feasible.

5.7 Conclusions

In this chapter, different methods were introduced or/and developed to fabricate the CuZr-based BMG composites containing the B2 CuZr phase in the glassy matrix: (1) Changing the melting current/time, (2) Adjusting the cooling rate, (3) The master alloy re-melting treatment, (4) Introducing boron nitride, (5) The effect of TaW inoculation, and (6) The flash annealing method. Multiple re-melting of the ingots seems to inhibit the heterogeneous nucleation, facilitating the homogenous nucleation and the formation of the amorphous phase. Furthermore, by using the “flash annealing”, the B2 CuZr phase precipitates uniformly in the CuZr-based glassy matrix after quenching. Other methods have a common characteristic during the fabrication process, i.e. the *ex situ* introduction of foreign nucleation sites in the melts during casting. It can be concluded that by using the methods above, the size, distribution, shape and volume fraction of the B2 CuZr phase can be effectively modified even though further studies need to be done to optimize the fabrication processes to ensure the formation of CuZr-based BMG composites with required microstructures.

6 Yielding and deformation mechanisms of CuZr-based BMG composites

As discussed above, a series of ductile CuZr-based BMG composites, in which B2 CuZr crystals precipitate in the glassy matrix, have been successfully fabricated [188, 218, 219, 221-223, 225, 228-230, 232-234, 237-241]. It has been reported that the MT and the multiplication of shear bands exerted by the micro-scaled B2 CuZr crystals lead to an enhanced deformability in these composites [188, 218, 219, 221-223, 225, 228-230, 232-234, 237-241]. Although the B2 CuZr phase and its MT are vital for the mechanical properties of the CuZr-based BMG composites, the deformation mechanism of these alloys, especially the interactions between the crystalline and amorphous phases as well as the details of the MT during deformation, have not been investigated in depth. In this chapter, the yield and plastic deformation of CuZr-based BMG composites is established.

6.1 Formation and microstructures of $Cu_{47.5}Zr_{47.5}Al_5$ BMG composites

In the past, different CuZr-based BMGs and their composites have been investigated, among which $Cu_{47.5}Zr_{47.5}Al_5$ alloy is a good candidate due to the following two reasons [136, 238, 295]: (1) the $Cu_{47.5}Zr_{47.5}Al_5$ BMG exhibits a large plasticity and a "work-hardenable" behavior resulting from the formation of multiple shear bands and a transformation from nanocrystals to nano-twinned crystals during deformation, and (2) the $Cu_{47.5}Zr_{47.5}Al_5$ BMG composites display a larger compressive plasticity and both plastic strain and yield strength scale with volume fractions of amorphous phase (f_{amor}). In order to further illustrate the yielding and subsequent plastic deformation mechanisms, $Cu_{47.5}Zr_{47.5}Al_5$ BMG and its composites with a diameter of 2 mm were fabricated by suction casting using different melting currents/times. The XRD and OM results for the samples obtained by adjusting the melting current/time were introduced in **Chapter 5**. The samples are S0, S1, S2, and S3 samples, respectively. In order to further decrease the volume fraction of the B2 CuZr phase in the glassy matrix, an injection casting machine was used to fabricate CuZr-based BMG composites. The casting temperature for all samples is 1470 ± 5 K. During the injection casting process, as the distance between the nozzle of the quartz tube and the mold is very close, the mold is warmed during the melting process of the ingots, which could affect the cooling rate of the copper mold. Furthermore, the cooling rate of the copper mold also can be decreased by stopping the water-cooling system. Therefore, different distances between the nozzle of the quartz tube and the mold and different water-cooled conditions were used (Table 6.1). It is worth noting that the S3 sample with a f_{amor} of 55 ± 3 vol.% can be also fabricated under a larger distance (i.e. 22 ± 5 mm) between the nozzle of the quartz tube and the water-cooled copper mold. Besides, another several samples were obtained, i.e. S4 and S5 (Table 6.1). When the melts were injected into a water-cooled copper mold with a smaller distance (i.e. 9 ± 3mm) between the nozzle of the quartz tube and the mold, the S4 sample was fabricated. The copper mold without water cooling, and a larger distance (i.e. 22 ± 5 mm) between the nozzle of the quartz tube and the mold were applied to obtain the S5 sample.

Table 6.1 *Casting parameters for the as-cast* $Cu_{47.5}Zr_{47.5}Al_5$ *rods with a diameter of 2 mm.*

Samples	Melting Temperature (K)	Distance between nozzle and mold (mm)	Water cooling system	f_{amor} (vol.%)
S3	1470 ± 5	22 ± 5	on	55 ± 3
S4	1470 ± 5	9 ± 3	off	19.5 ± 0.5
S5	1470 ± 5	22 ± 5	off	0%

As discussed in **Chapter 5**, the as-cast S0 sample is fully amorphous. Compared with S1, S2, and S3 samples, the S4 and S5 samples consist of the B2 CuZr phase and the monoclinic martensitic crystals, which were shown in Fig. 6.1a. For the S4 sample, as shown in Fig. 6.1b, compared with the fully amorphous $Cu_{47.5}Zr_{47.5}Al_5$ ribbon, the S4 sample exhibits a smaller exothermic peak associated with the crystallization, confirming the presence of the amorphous phase. Meanwhile, no amorphous phase was detected in S5 sample by the DSC method (not shown). The distribution of crystals in the glassy matrix for the S4 sample was investigated by OM measurements (Fig. 6.2c). An amount of relatively darker crystals interconnect and form a network in the glassy matrix (white area). As depicted in Fig. 6.2d, the substructures of the precipitates are very fine dendrites (dendrite arm spacing 0.6 - 2 μm), which is similar to the previous results [295, 315, 326]. Nevertheless, the enhanced crystalline peaks from the S1 to S5 samples imply that the f_{amor} (Table 6.1 and Table 5.1) gradually decreases, being roughly determined based on the area ratio of the amorphous and crystalline phases extracted from the OM pictures [353].

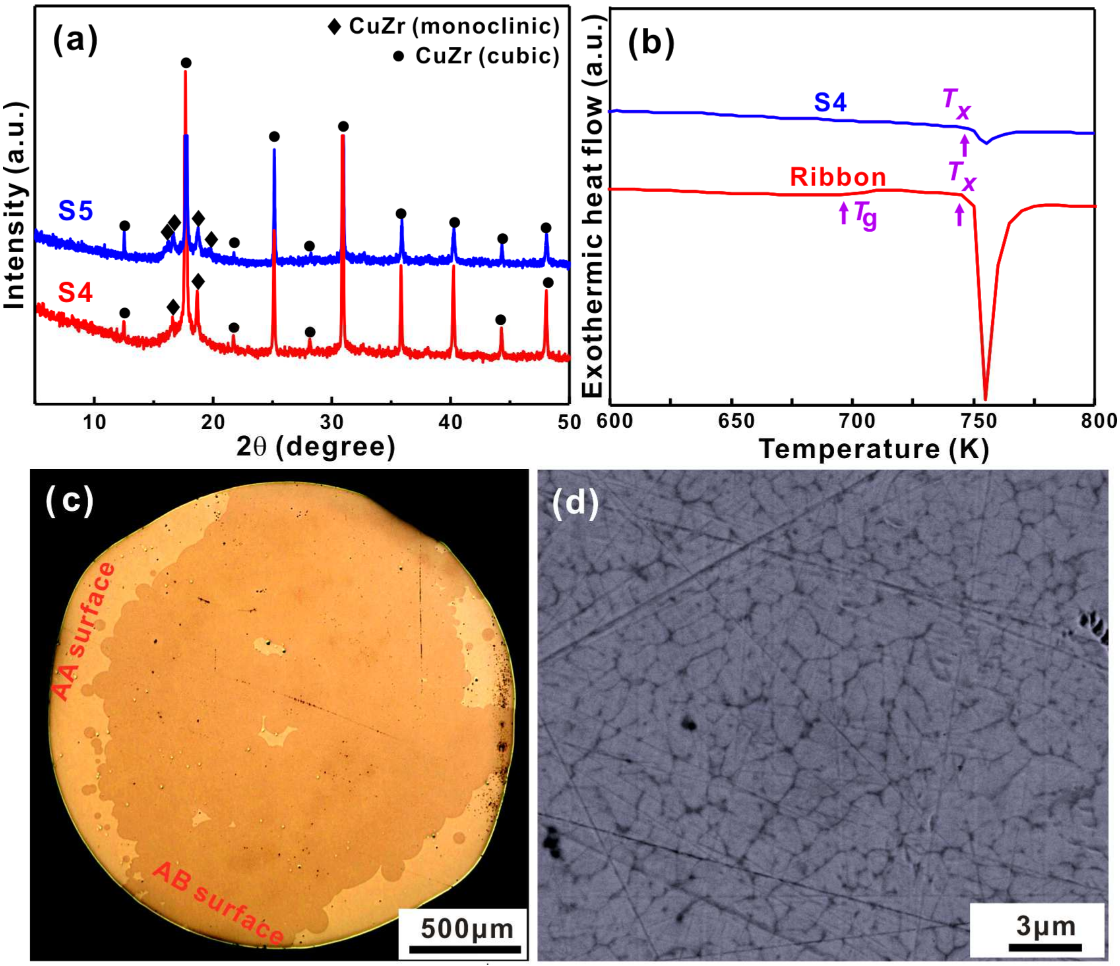

Figure 6.1 *(a) XRD patterns of the as-cast S4 and S5 rods, (b) DSC curves of the as-cast S4 rod and the fully amorphous ribbon, (c) OM picture (AA surface is fully amorphous, while AB surface is fully crystalline) and (d) SEM picture of the B2 CuZr phase in the as-cast S4 samples.*

In order to further check their microstructures, the TEM and HRTEM measurements were conducted for the S4 sample (Fig. 6.2). As shown in Fig. 6.2a, the observed lattice fringes and the disordered regions further confirm that the composite consist of crystals and the amorphous phase. Based on the Fast Fourier Transform (FFT) performed at the glassy interface (the inset in Fig. 6.2a) between crystals, typical diffuse halos indicative of the amorphous phase are observed.

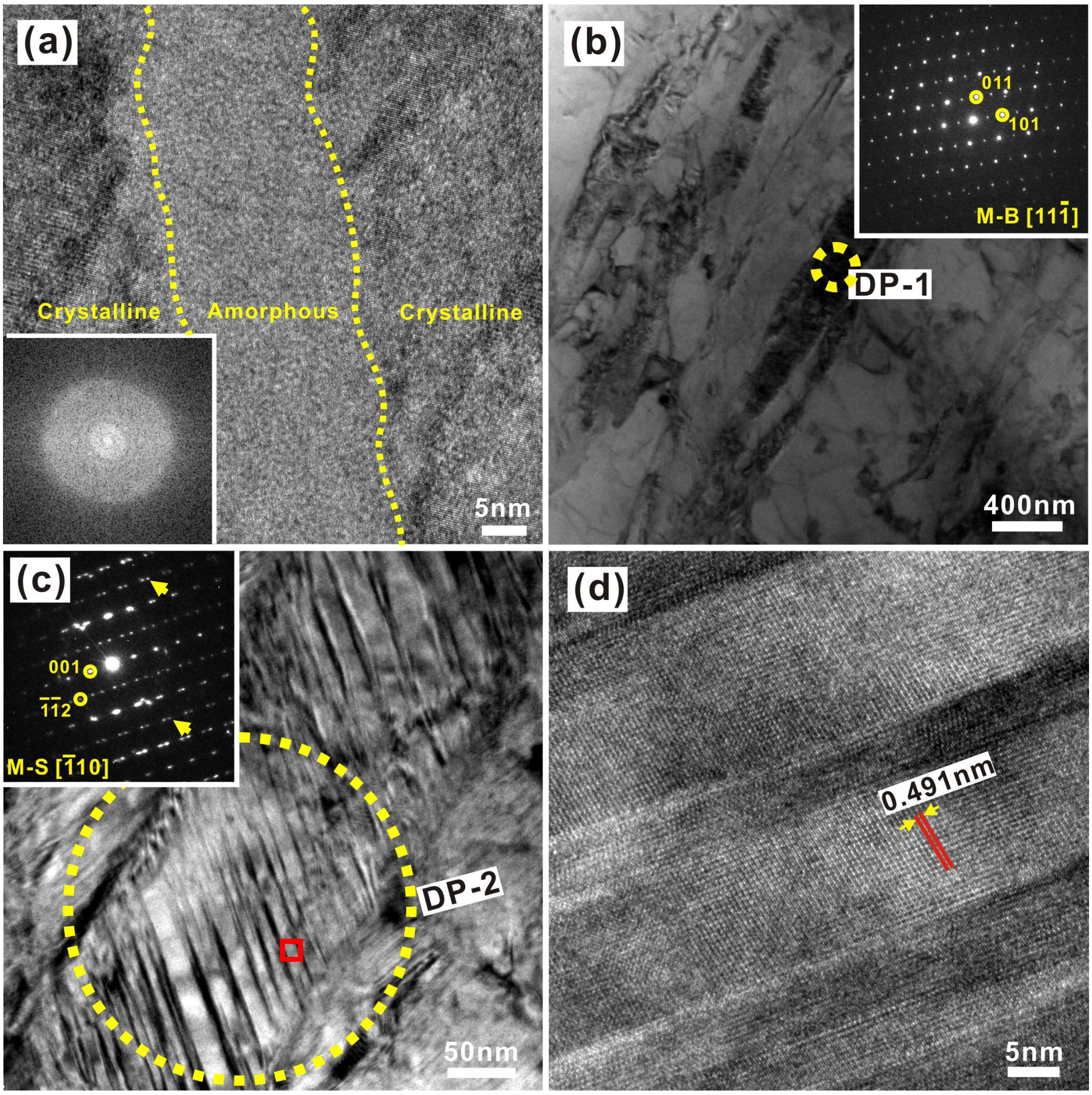

Figure 6.2 *(a) TEM and FFT images of the amorphous interface between crystals, (b) TEM image of the basic structure of martensite (M-B) and the SAED pattern from the area marked by DP-1, (c) the superstructure of martensite (M-S) and the SAED pattern from the area marked by DP-2, and (d) HRTEM image of twins from the area (the red square in Fig. 6.2(c)) for the as-cast S4 sample.*

Next to the B2 CuZr phase shown in Fig. 6.2a, the TEM results also reveal the presence of a very small amount of martensitic plates with sizes of about 200 nm - 300 nm (Figs. 6.3b-c). Previous results [297] have shown that the formation of martensitic phases may result from the thermal stress during rapid quenching. Selected area electron diffraction (SAED) analysis shows that the martensitic structures are composed of a basic structure (marked as M-B, P21/m space group, DP-1 in Fig 6.2b) and a superstructure (labeled as M-S, Cm space group, Fig. 6.2c) [294, 405]. Furthermore, the SAED measurement on the region DP-2 (see yellow arrows in Fig. 6.2c) exhibits additional twinning reflections, which give a hint for the existence of nano-scaled twins. As shown in Fig. 6.2d, the HRTEM image of this region (see the red square in Fig. 6.2c) indeed displays the symmetric arrangement of the lattice planes with different orientations, which is a direct evidence for the existence of nano-scaled twins. The lattice constants of the nano-scaled twins are estimated to be 0.491 nm, which is consistent with previous results [294]. Comparing the crystallographic data of the basic structure and of the martensitic superstructure [294], it is deduced that twinning preferentially occurs within the superstructures of the martensite.

6.2 Deformation behavior of $Cu_{47.5}Zr_{47.5}Al_5$ BMG composites

As shown in Fig. 6.3, the compressive stress-strain curves for all as-cast samples exhibit different yielding behaviors, significant plastic strains and obvious work hardening when different volume fractions of crystals precipitate in the glassy matrix [284, 285, 336].

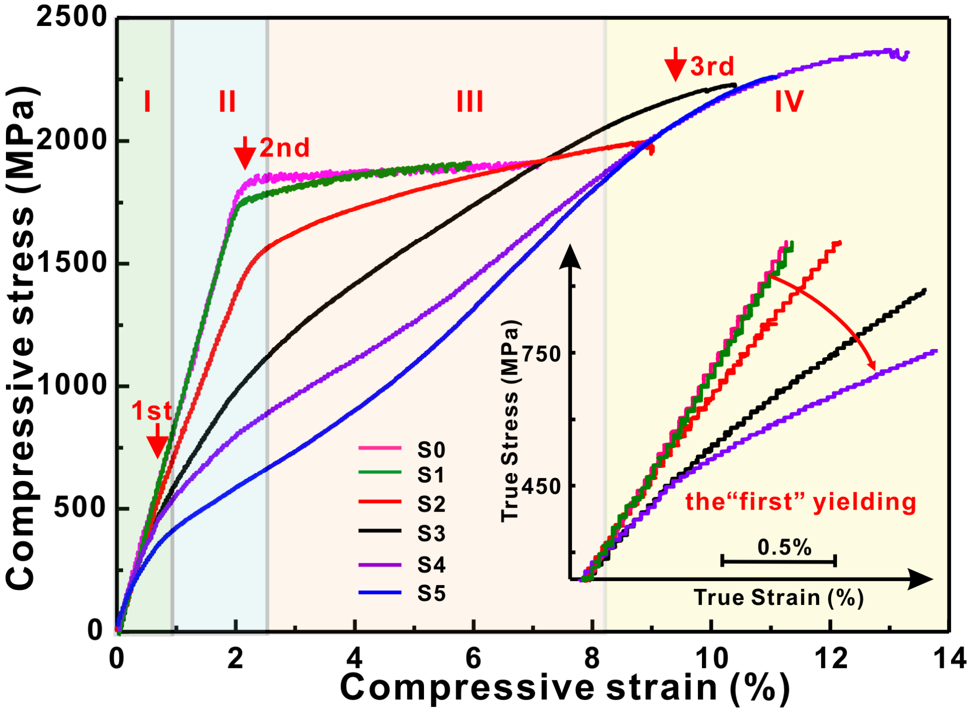

Figure 6.3 *compressive stress-strain curves of the samples (Inset: the magnified "first yielding").*

It can be seen from Fig. 6.3 that the S0 and S1 samples clearly yield at a strain of about 2%. However, with the f_{amor} gradually decreasing from 78 ± 1 vol.% to 19.5 ± 0.5 vol.%, the yielding of the composites (e.g. S2, S3 and S4) changes and then the yield strength becomes more difficult to identify. It is worth noting that at a strain of about 0.95%, a deflection is observed in the compressive curve of the S2 sample. The deflection stress is 734 MPa. With the compressive strain increasing to about 2%, the S2 sample yields again at a stress of about 1465 MPa. As the value of the f_{amor} decreases to 55 ± 3 vol.% (S3), this deflection becomes more obvious, which seems to become a "yielding". With the applied stress further increasing, the S3 sample yields again at a stress of about 734 MPa. However, for the S4 sample with a f_{cryst} of 80.5 ± 0.5%, the "first yielding" is more obvious while the "second yielding" becomes weak (Fig. 6.3). With the stress increasing, the S3 and S4 sample seems to yield at the strain > 8% for the third time. However, the fully crystalline sample (S5) only exhibits a double yielding behavior, which is different to that of the S2 sample. Previous results have shown that the double yielding of the S5 sample is quite common in shape memory alloys [295, 296, 406]. When the main crystalline phase is the B2 CuZr phase, the first yielding at the strain < 1% is due to the transformation from the B2 CuZr phase into martensitic phase, while the second yielding at the strain > 8% results from the occurrence of detwinning and/or dislocations with a high density [281, 295, 296, 406]. Therefore, it can be concluded that the "first yielding" is very sensitive to the existence of the B2 phase. Moreover, the "second yielding" shifts to higher stress and the "third yielding" becomes obscure as the amount of amorphous phase increases for $Cu_{47.5}Zr_{47.5}Al_5$ BMG composites.

In addition to the Cu-Zr-Al alloy system, the deformation behavior of other CuZr-based BMG composites with different content of crystals (Fig. 6.4) was also observed to further confirm the occurrence of this "yielding" behavior. The deformation behavior of $Cu_{47.5}Zr_{47.5}Al_5$ (labeled as S4-3 rod, ø3 mm, made using a different injection machine, the f_{cryst} is 80 ± 2 vol.%,), $Cu_{46.25}Zr_{44.25}Al_{7.5}Er_2$ [350] (ø2 mm, the f_{cryst} locates between 25 ± 3 vol.% and 20 ± 3 vol.%), $Cu_{46}Zr_{46}Ag_8$ [396] (ø2 mm) BMG composites containing 50 ± 10 vol.% amorphous phase were shown in Fig. 6.4. It was also found that the "first yielding" at a strain of about 1% becomes very clear with the f_{amor} decreasing. However, when the "first yield strength" slightly increases from 460 ± 10 MPa to 600 ± 10 MPa, the "first yielding" strain of the BMG composites is not strongly influenced. When the applied stress locates between 1000 and 1500 MPa, the "second yielding" of $Cu_{46.25}Zr_{44.25}Al_{7.5}Er_2$ and $Cu_{46}Zr_{46}Ag_8$ BMG composites with more amorphous phase are also observed. Meanwhile, as shown in Fig. 6.4, the S4-3 sample also shows a similar yielding behavior to the S4 sample.

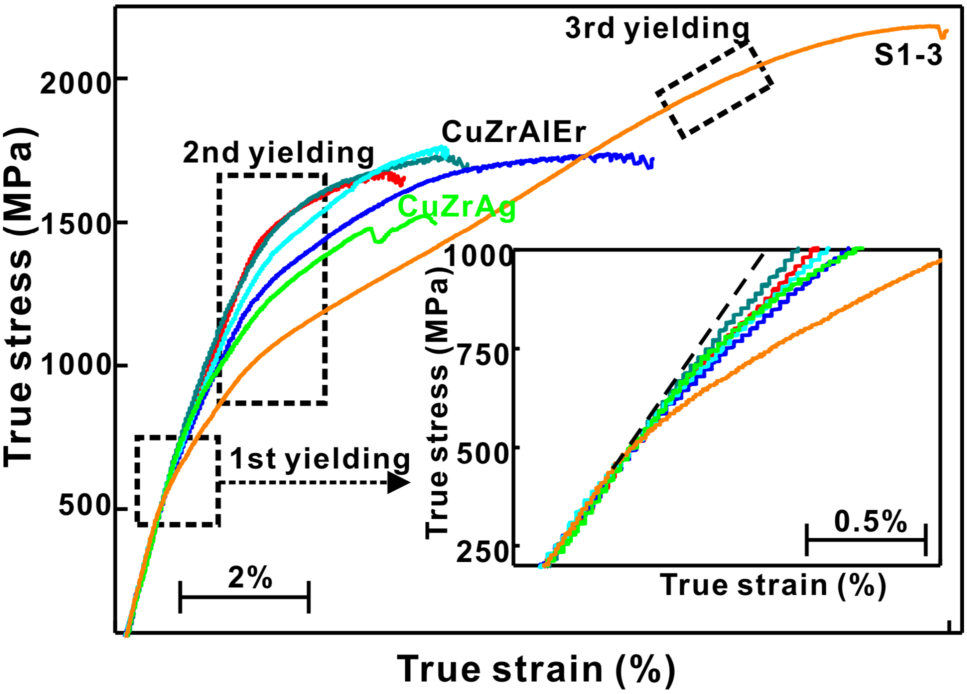

Figure 6.4 *The true stress-strain curves of* $Cu_{46.25}Zr_{44.25}Al_{7.5}Er_2$ *and* $Cu_{46}Zr_{46}Ag_8$ *rods with a diameter of 2mm, and* $Cu_{47.5}Zr_{47.5}Al_5$ *rod with a diameter of 3mm (Inset: enlarged part of the true stress-strain curves revealing the "first yielding").*

However, at a larger stress/strain for the as-cast S3, S4 and S4-3 samples, a "third yielding" point can be seen, while it is difficult to detect the "third yielding" points of $Cu_{46.25}Zr_{44.25}Al_{7.5}Er_2$ and $Cu_{46}Zr_{46}Ag_8$ BMG composites due to the early fail of the samples resulting from the rapidly shear localization of the glass matrix. However, for the monoclinic $Cu_{47.5}Zr_{47.5}Al_5$ BMG, only one yield point can be seen (Fig. 6.3). The observations above suggest that the existence of the amorphous phase and the B2 phase indeed play an important role on the "yielding" behavior during deformation. Different contents of the B2 CuZr phase and the amorphous phase can induce a "one" or "double" or "triple yielding" behavior.

In order to completely eliminate the effect of the amorphous phase and the B2 CuZr phase on the yielding behavior of CuZr-based BMG composites, the S4 specimen was annealed at 1073 K for 1 min and 6 h, denoted as S6 and S7, respectively (Fig. 6.5a), and the compressive results were also shown in Fig. 6.5.b. it can be seen that the S6 sample consists of the B2 CuZr phase, a small amount of martensitic crystals and LT-EPs, while the S7 sample contains a lot of martensitic crystals together with little LT-EPs. After the amorphous phase disappears in the S6 sample, only a double yielding behavior is observed, being similar to that of the S5 sample (Fig. 6.3).

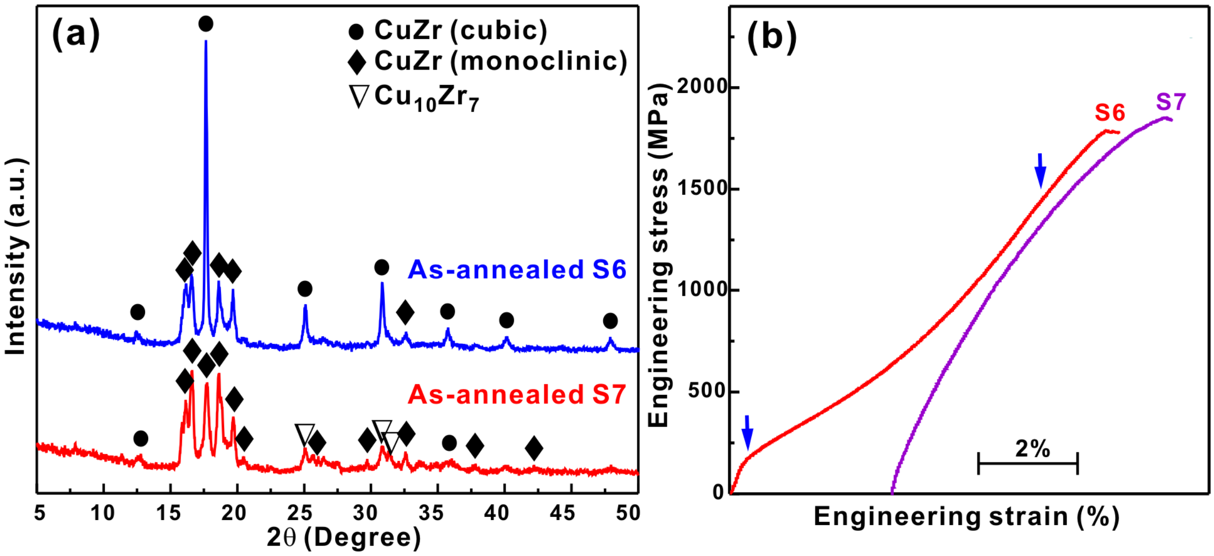

Figure 6.5 *(a) XRD patterns of the S6 and S7 samples, and (b) their compressive test results.*

The S5 and S6 samples yield at 390 ± 10 MPa and 150 ± 10 MPa, and then yield again at 1930 ± 10 MPa and 1630 ± 10 MPa, respectively. The lower yield strength of the S6 specimen is also related to the precipitations or different grain sizes of the crystalline phases (i.e. martensitic phase, $CuZr_2$ and $Cu_{10}Zr_7$ phases in Fig. 6.5a), chemical segregation or other influences [407-410] besides the MT. Nevertheless, the “second yielding” at a strain of about 2% for the S4 samples disappears in the S5 and S6 sample, implying the importance of the amorphous phase to the “second yielding” for the S4 sample. Furthermore, as the dominant crystals for the annealed samples change from the B2 CuZr phase to martensite, the annealed S7 sample just shows one yielding (Fig. 6.5b) with a lower yield strength, implying that the MT from the B2 CuZr phase into martensites may be responsible for the “first yielding” for the S2, S3, S4, S5, and S6 samples.

The “yielding” behavior of all the samples with the change of the f_{cryst} separate the whole deformation process in CuZr-based BMG composites into four different stages (Fig. 6.3). Moreover, the BMG composites show a relatively larger plasticity with obvious work hardening compared with the monolithic BMGs. In order to further illustrate the different stages, the as-cast S4 sample was chosen as an example because it processes all different yielding stages. Fig.

6.6 displays the response to mechanical loading in the curve of the work-hardening rate *vs.* the true strain. The work-hardening rate (Θ) is calculated using the equation ($\Theta = d\sigma_{true}/d\varepsilon_{true}$) [411], where σ_{true} and ε_{true} represent the true stress and true strain, respectively. The curve of Θ *vs.* ε_{true} of the as-cast S4 sample is also divided into four stages:

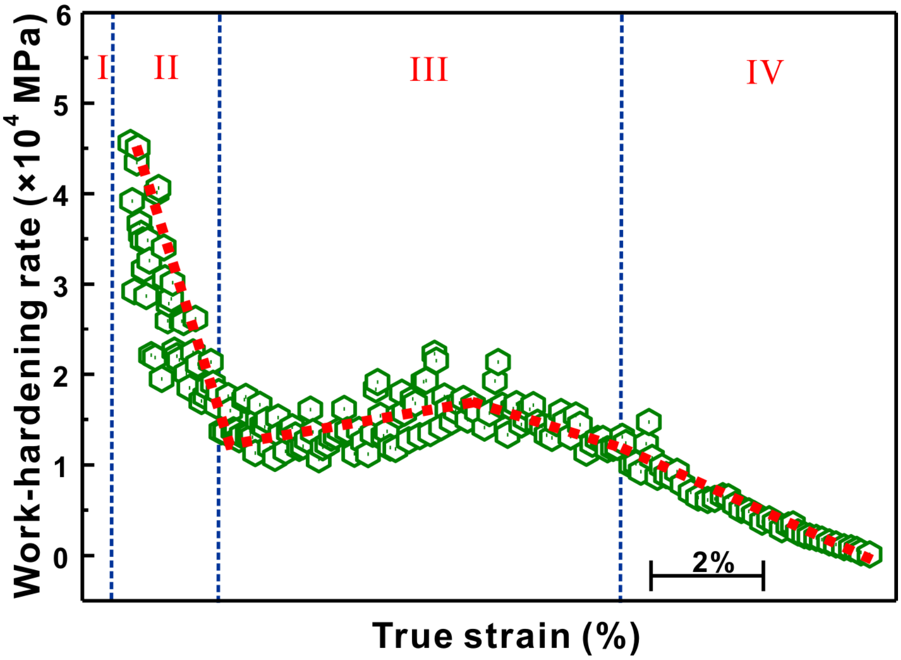

Figure 6.6 *Θ vs. true strain for the S4 sample during deformation.*

Stage I: During this stage, the amorphous phase and the crystals deform elastically. After reaching the elastic limit of 0.8 ± 0.2%, the S4 sample first yields at 460 ± 10 MPa (Fig. 6.3), which is much smaller compared to the elastic limit of 2% for monolithic BMGs due to the presence of 80.5 ± 0.5 vol.% CuZr crystals [8, 11, 127, 130].

Stage II: After the "first yielding", the slope of the stress-stain curve obviously deviates from the elastic stage I (Figs. 6.3 and 6.6), and then at a strain of about 2% a second yielding occurs at 820 ± 10 MPa (Fig. 6.3). The work-hardening rate Θ decreases from 4.5×10^4 MPa to 1.3×10^4 MPa.

Stage III: After the "second yielding", the plastic deformation of the sample continues to 9.1 ± 0.5%. With the applied stress further increasing to 2120 ± 10 MPa, a third yielding occurs (Figs. 6.3 and 6.6). The value of Θ slightly increases in the beginning and then decreases with the strain increasing.

Stage IV: During this stage, even though the work hardening still occurs, the value of Θ decreases and gradually approaches zero. At the stress of 2360 ± 10 MPa, the S4 sample finally fails at a compressive strain of 13.5 ± 0.5%. Compared with that of the BMG (Fig. 6.3), only very limited serrated flow is observed at a higher stress for the as-cast S4 alloy. The values of the Θ of the S4 sample during stage IV show a similar tendency with those of $Cu_{50}Zr_{45}Ti_5$ BMG composites containing a large amount of martensitic crystals together with a little amorphous phase and the B2 CuZr phase [333]. The discussions above indicate that the plastic flow is not dominated by shear banding.

6.3 Yielding and plastic deformation mechanisms

These "yielding" behaviors have been found in CuZr-based BMG composites and therefore it seems to a universal characteristic of these alloys. Thus, the yielding and subsequent plastic deformation of CuZr-based BMG composites with different contents of the B2 CuZr phase needs to be revealed. The $Cu_{47.5}Zr_{47.5}Al_5$ samples were chosen to check the yielding and plastic deformation.

6.3.1 Yielding and plastic deformation during stage I

Fig. 6.7 shows the microstructural changes of the S0, S1, S2, S3, S4, and S5 samples after pre-deformation at a strain of about 1 %. For the monolithic BMG (S0), no shear bands and other microstructural changes can be observed (Fig. 6.7a), implying that the S0 sample is still elastic in this region.

As shown in Figs. 6.7b-c and e-f, for the S1, S2, S4, and S5 samples, the SEM measurements reveal no obvious shear bands near the "first yielding" in the glassy matrix (white area). Meanwhile, martensitic laths (see the red arrows) and slip bands can be observed within crystals, indicating that the "first yielding" is mostly related to the yielding of the crystalline phases and the initiation of MT. The phase transformation in the S3 and S5 samples was also *in situ* investigated by high-energy X-ray diffraction [296]. Fig. 6.7d shows partial high-energy X-ray results between q = 37.5 nm^{-1} and q = 40.5 nm^{-1} of the S3 sample with the stress increasing. It was found that the deformation-induced MT indeed occurs at about 424 ± 1 MPa (before 2% strain) is reached, further confirming our SEM results. Moreover, it can be seen that with the content of amorphous phase decreasing, the characteristics of the occurrence of MT become more obvious (Fig. 6.7).

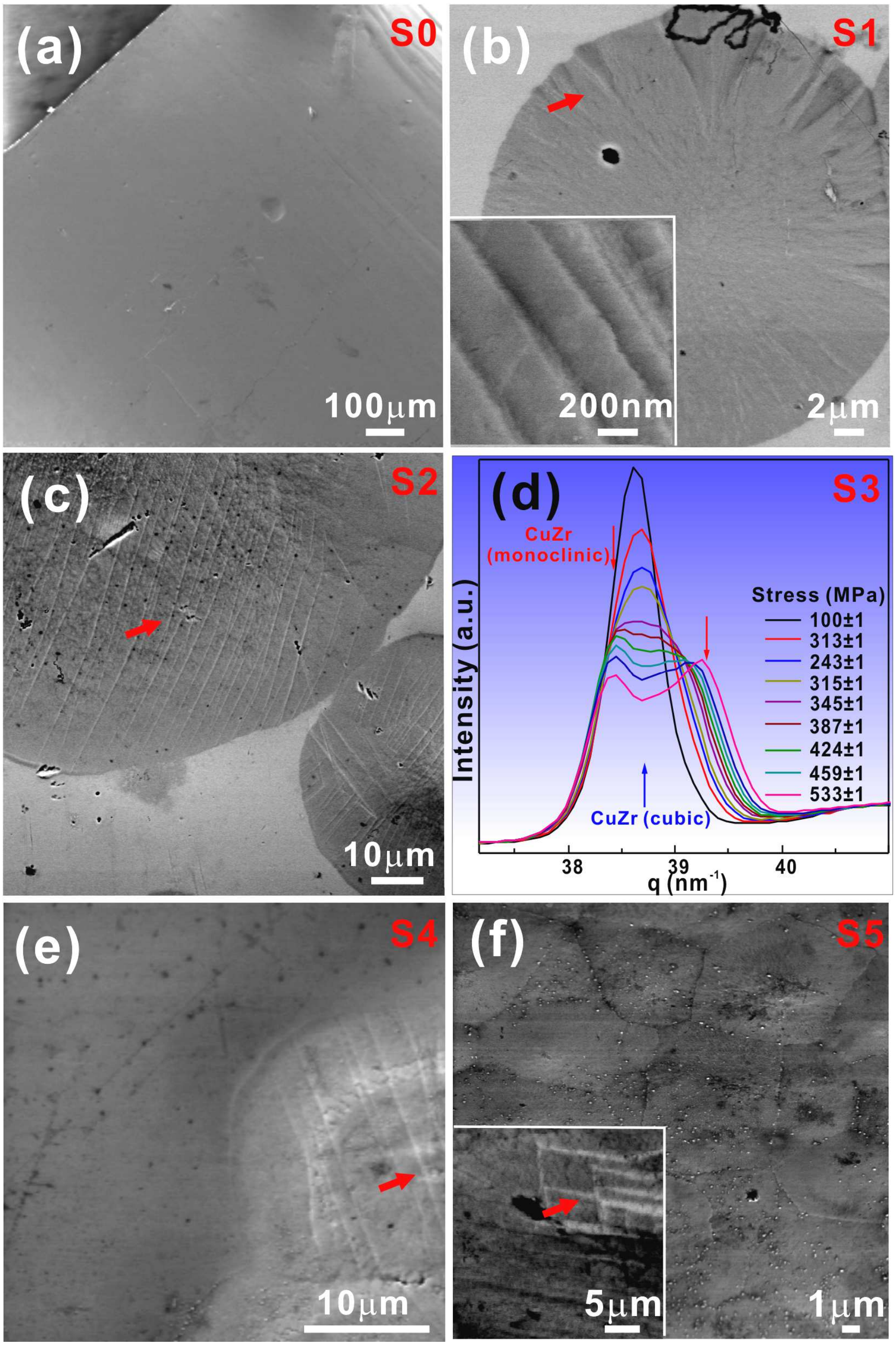

Figure 6.7 *The outside surfaces or the XRD pattern of the deformed (a) S0, (b) S1, (c) S2, (d) S3, (e) S4, and (f) S5 samples after the "first yielding", respectively.*

In order to investigate the microstructural evolution during this deformation stage, the deformed S4 sample after the "first yielding" was selected for TEM measurements. As shown in Fig. 6.8a, some martensitic plates start to prevail. As shown in Figs. 6.8b-d, some martensitic plates with sizes of about 200 ± 50 nm distribute within the B2 CuZr phase.

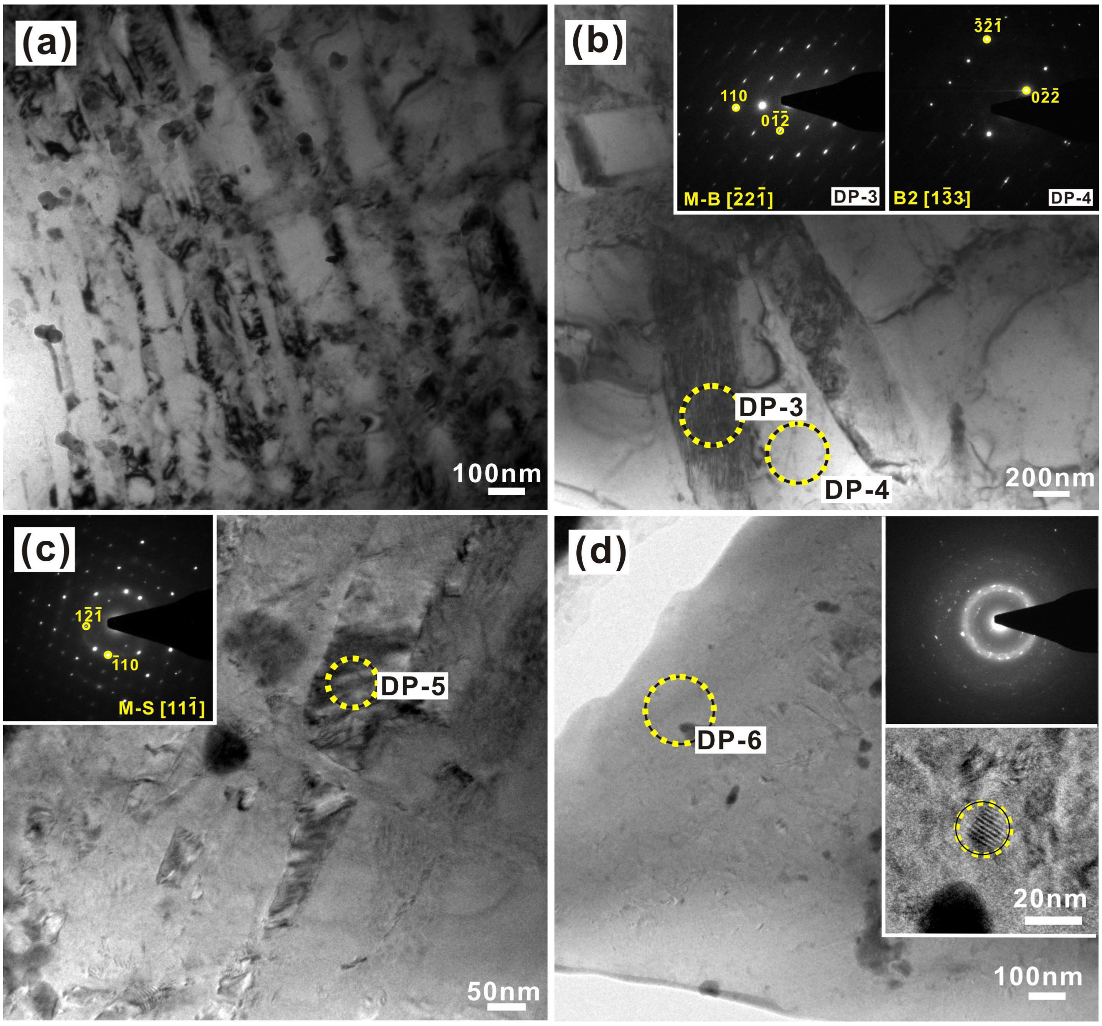

Figure 6.8 *(a) Overview of the martensites, (b) TEM of the mixed local structures and SAED patterns of M-B and M-S, (c) TEM and SAED images of M-S, and (d) the mixed local structures of amorphous phase and crystals.*

Based on the SAED patterns (insets in Figs. 6.8b-c), the structures of the deformation-induced martensites were identified to be the basic structure ($P2_1/m$) and the superstructure (Cm), respectively, proving that the MT indeed takes place at this stress. Especially, some nano-scaled crystals shown in the lower left inset in Fig. 6.8d can be observed within the amorphous matrix, which may be due to the deformation-induced crystallization and the local shear localization from either thermal or mechanical stresses [280, 412]. Furthermore, after a long-time annealing treatment (6 h at 1073 K) in order to eliminate most of the B2 CuZr phase, the S7 specimen mainly contains martensitic crystals. However, the S5 and S6 samples mainly containing the B2 phase show a "double yielding". Therefore, it can be inferred that the "first yielding" is due to the yielding of the B2 CuZr phase and the operation of the MT within the B2 phase.

6.3.2 Yielding and plastic deformation during stage II

After the "first yielding", the deformation of the S4 sample enters stage II. The BMG, i.e. the S0 sample, continues to be deformed elastically. For the other samples, however, at a strain of 2% (here the S4 sample is taken as an example), more peaks corresponding to martensitic phases can be observed from the XRD pattern (Fig. 6.9a), indicating an enhanced volume fraction of martensitic crystals because of the advancing MT.

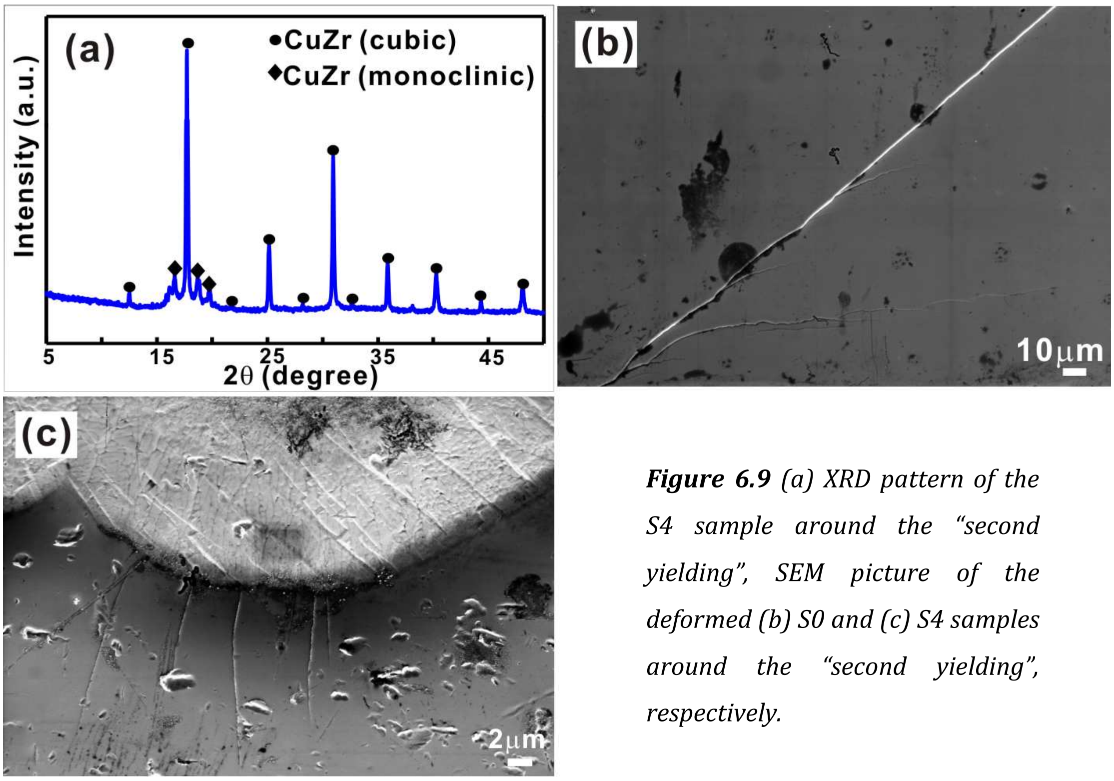

Figure 6.9 *(a) XRD pattern of the S4 sample around the "second yielding", SEM picture of the deformed (b) S0 and (c) S4 samples around the "second yielding", respectively.*

Furthermore, as shown in Fig. 6.7d, with the stress increasing, the intensity of the peaks corresponding to martensitic crystals for the S3 sample further increases during stage II, which corresponds well with the XRD observation for the S4 sample. During deformation, the MT is restricted by the stiff glassy matrix which is still deformed elastically. Thus, it is reasonable to believe that the stiff matrix slows down/confines the MT and then higher stresses are required to transform the B2 CuZr crystals into martensite. On the contrary, the work-hardening rate during the initial deformation stage of the fully crystalline alloys (S5 and S6 samples) is much lower when the confinement of the amorphous phases disappears. Based on the rule of mixtures (ROM), the strength of the composites will be increased with the addition of the high-strength particles into the low-strength matrix [295]. In our case, as the content of amorphous phase decreases to 19.5 ± 0.5 vol.%, the amorphous phase becomes the reinforced particles, which results in the increase of the strength of the composites. These facts demonstrate that the dominant deformation mechanism during stage II is the advance of the MT within the B2 CuZr phase under the restriction of the rigid amorphous matrix.

Ibarra *et al.* [413] have shown that the MT occurs through a heterogeneous nucleation and strongly depends on the lattice strain around the dislocations. The pre-existing martensitic plates and nano-scaled twins can lead to the reduction of the mean free path for dislocation glide. Therefore, the MT occurs faster at higher stresses when the transformation has already partially occurred. Furthermore, as shown in Fig. 6.9b, one main shear band can be observed at the surface of the S0 sample at a strain of about 2%, implying that the BMG starts to yield due to the shear localization within shear bands. For the S4 sample, multiple shear bands are observed at the interface of the crystals and the glassy matrix (Fig. 6.9c) together with the martensitic plates within the B2 CuZr phase at the beginning of stage III. Combined with the discussions in **Section 6.3.1**, the "second yielding" of CuZr-based BMG composites are attributed to the advance of the MT and the multiple shear bands.

6.3.3 Yielding and plastic deformation during stage III

The deformed microstructures of the S0, S1, S2, S3, S4, and S5 samples after the "second yielding" are shown in Fig. 6.10. It was found that for the fully amorphous S0 sample, multiple shear bands are observed in Fig. 6.10a, which suggests that the shear banding process dominates the deformation of the CuZr-based BMGs. With the applied load increasing, the BMG sample fails at a strain of about 7.1 %. Figs. 6.10b-h shows the XRD pattern and SEM pictures of the deformed S1, S2, S3, S4, and S5 samples after the "second yielding". It was seen that with the f_{cryst} increasing, more twinned martensitic plates were observed within the equiatomic CuZr crystals (Figs. 6.10b-f and h), implying that the MT also affects the whole deformation process.

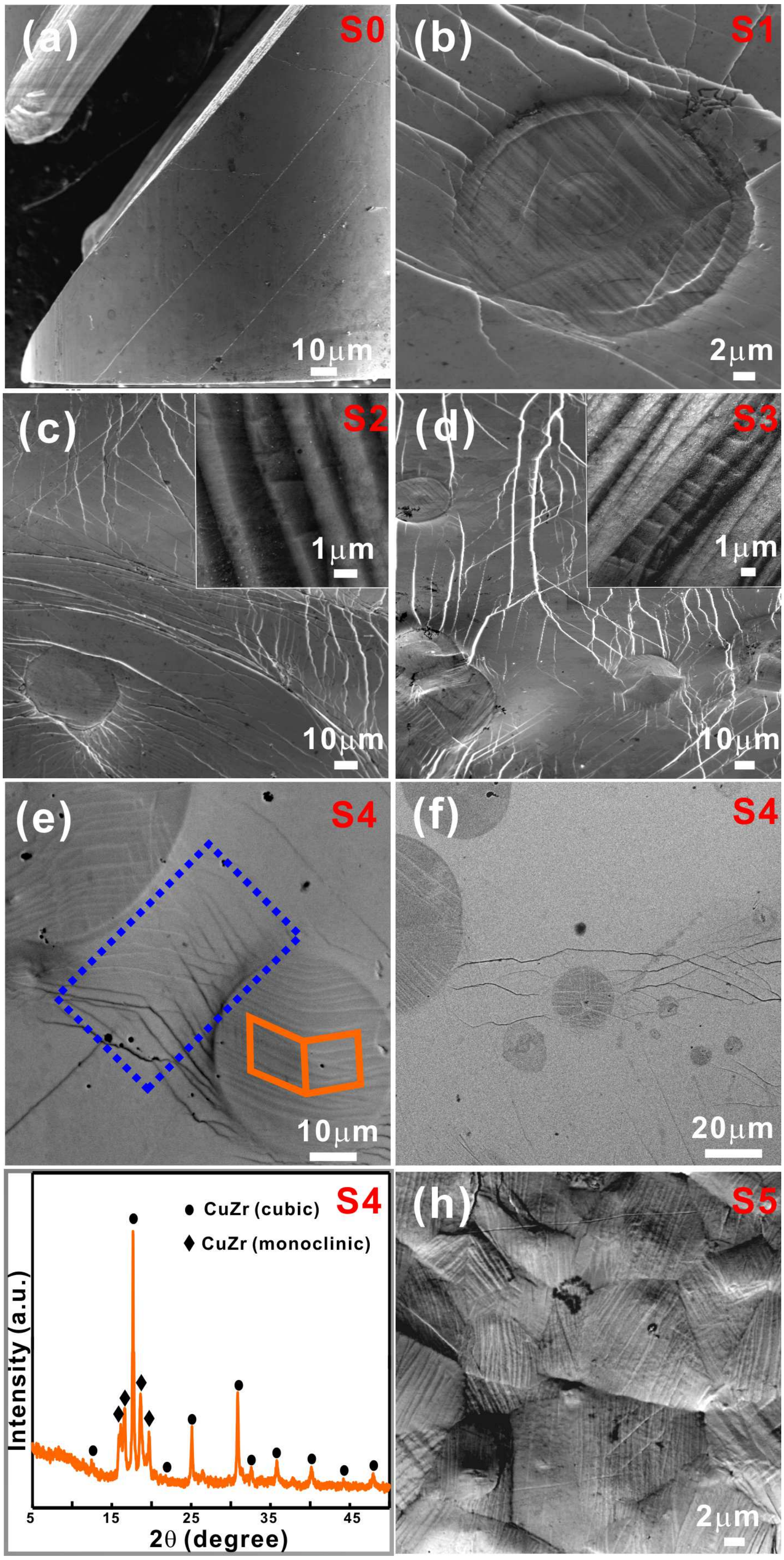

Figure 6.10 *(a) Outside surface of the S0 sample after the "first yielding" and after fracture, (b-f, h) SEM pictures of the S1-S5 samples after the "second yielding", and (g) XRD patterns of the deformed S4 samples.*

Furthermore, as shown in Fig. 6.10h, when the f_{amor} is close to 0 at.%, the MT completely dominates the whole deformation process. For the S4 sample, the enhanced intensity of the peaks corresponding to martensitic phases (Fig. 6.10g) in the XRD pattern implies that both the amount and the size of the martensite crystals increase, further demonstrating the rapid development of MT compared with the diffraction pattern of the as-cast sample (Fig. 6.1a).

Furthermore, following the MT, multiple shear bands are also be induced by the ductile phase (Fig. 6.10). As proposed by Johnson *et al*. [214, 300, 301], ductile crystalline phases in BMG composites may serve either as heterogeneous sites for the initiation of shear bands or act as pinning centers to hinder the shear band propagation. In such a case, in the beginning of stage III, shear bands initiate at the interface of the crystals and the glassy matrix (Fig. 6.9c). The observed shear bands lead to the yielding of the amorphous matrix at a strain of about 2%. As shown in Figs. 6.10b-f, multiple shear bands form after the "second yielding". Meanwhile, some shear bands cut through those B2 CuZr crystals smaller than 20 μm - 30 μm, but are stopped by some larger B2 CuZr precipitates, leading to the further formation of multiple shear bands (Figs. 6.10b-f). Even some of the martensitic crystals distribute symmetrically within the B2 CuZr phase (see the orange rectangle in Fig. 6.10e), whereas some shear bands around the interfaces intersect with other, and create a symmetric pattern (see the blue rectangle in Fig. 6.10e), implying a more serious "blocking effect" [214, 300].

With the stress further increasing, the S0, S1 and S2 samples fail, while the S3, S4, and S5 samples continue to deform. As shown in Figs. 6.11a-c, more martensitic crystals are induced within the B2 CuZr crystals compared with those in the S4 sample uploaded close to the "second yielding" (Fig. 6.10e-f), indicating that the MT has a strong influence on the deformation of the S3 sample during stage III. Furthermore, close to the "third yielding" for the S4 sample, much denser shear bands in some surface regions were observed and their average spacing of the primary shear bands is about 50 ± 30 μm (Fig. 6.11d). Meanwhile, more secondary and ternary shear bands were also induced. In addition, a typical triangular morphology of martensitic plates can be observed (see the yellow circle and the inset in Fig. 6.11c), which may be relevant to a self-accommodation effect due to the rearrangement of martensitic phases [281]. Especially, step-like martensitic plates within the B2 CuZr phase can be observed in Fig. 6.11b, implying the formation of twins. It has been shown that martensite usually becomes twinned after the MT through the self-accommodation [280], which is in accordance with our results.

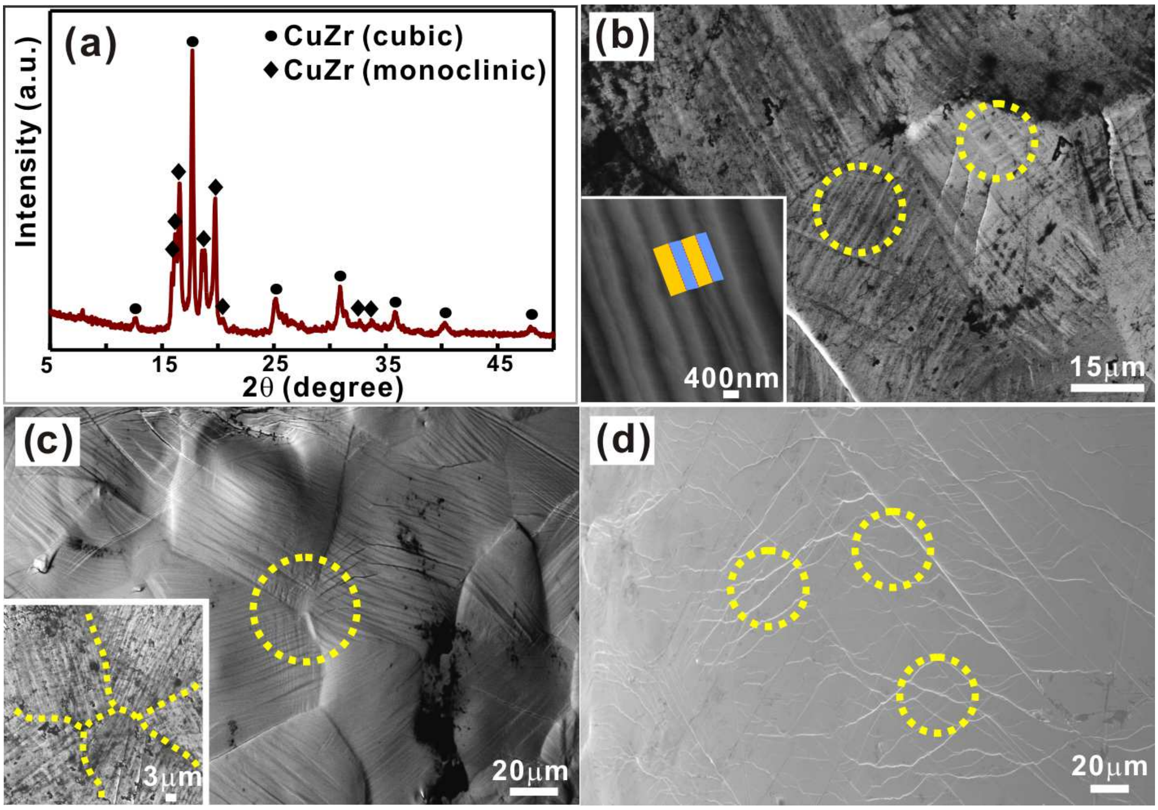

Figure 6.11 *(a) XRD pattern, and (b-d) SEM pictures of the S4 sample uploaded near the "third yielding".*

Furthermore, as shown in Fig. 6.6, the work-hardening rate first increases, and then decreases during stage III, which may be explained as follows: (1) The rapid development of the MT with the strain increasing is associated with the pronounced formation of martensite together with local dislocation pile-ups [407-410, 414, 415]. The generation of more defects and the increase of the local pile-up stress result in the increasing slope of the stress-strain curve [407-410, 414, 415]; (2) With the content of martensitic crystals increasing, the self-accommodation behavior of martensite, which is related to the release the transformation strain, becomes more intense, implying that more twins could be induced during stage III [280]. Hence, the work-hardening rate continues to decrease; (3) As the self-accommodation of the martensites approaches to finish, more shear bands generate quickly, which in turn induces a macroscopic strain softening of the glassy matrix. Then the deformation mechanism during stage III may be due to the competition and interaction between the MT and the shear banding processes. Meanwhile, the continuous development of the MT during this stage also affects the formation of shear bands, causing the raised plasticity.

6.3.4 Plastic deformation during stage IV

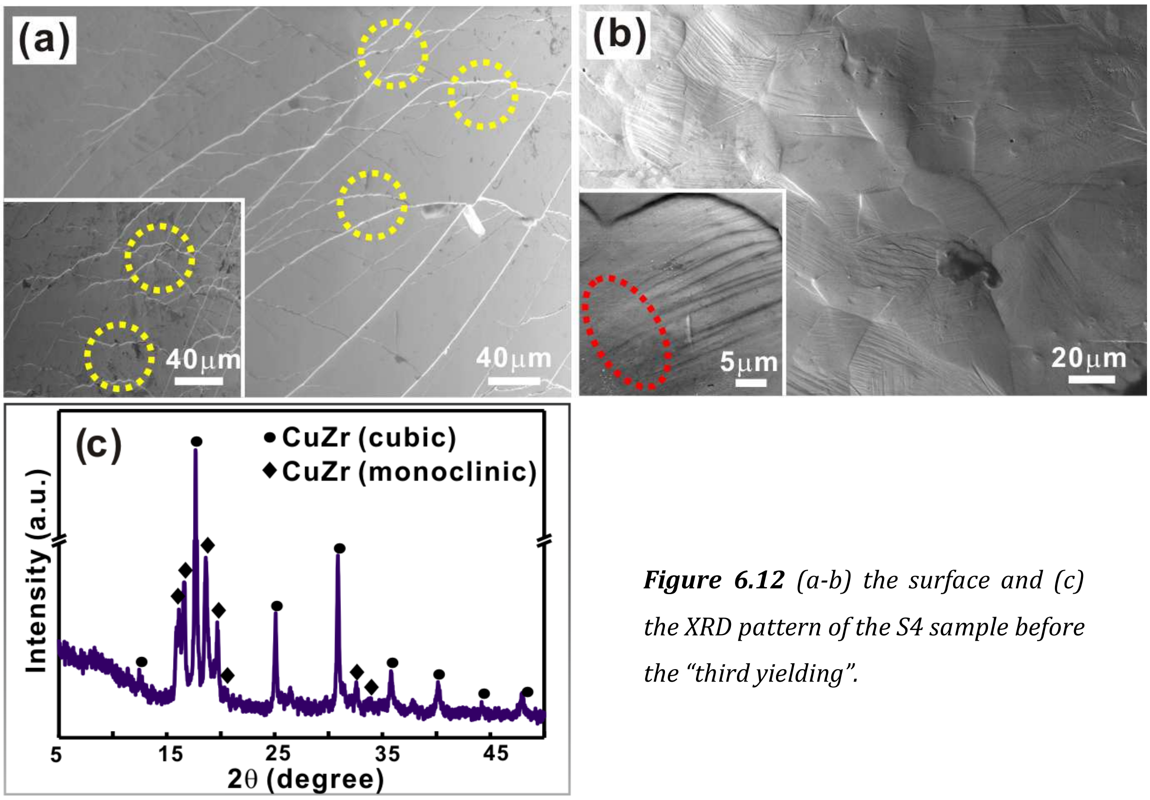

Figure 6.12 *(a-b) the surface and (c) the XRD pattern of the S4 sample before the "third yielding".*

For the S3, S4 and S5 samples, with the stress exceeding 2000 MPa and the strain being larger than 8%, the work-hardening rate continues to decrease and then the deformation enters stage IV. For these samples after fracture, the distribution of shear bands (Fig. 6.12a) does not change too much compared with the shear bands around the "third yielding" event (Fig. 6.12b), indicating that the macroscopic strain softening induced by shear bands does not mainly govern stage IV. Moreover, the stress increases slowly with the strain increasing during this stage, which is quite similar to the second yielding of TiNi-based shape memory alloys and the S5 sample, possibly implying that the deformation may be dominated by the formation of dislocations with a high density and/or detwinning [280, 295]. The existence of a larger amount of martensitic crystals after fracture was further confirmed by the XRD pattern (Fig. 6.12c). However, as shown Fig. 6.12b, CuZr phases with different structures still coexist, but some martensitic plates become indistinct, suggesting the possible formation of detwinning (inset in Fig. 6.12b).

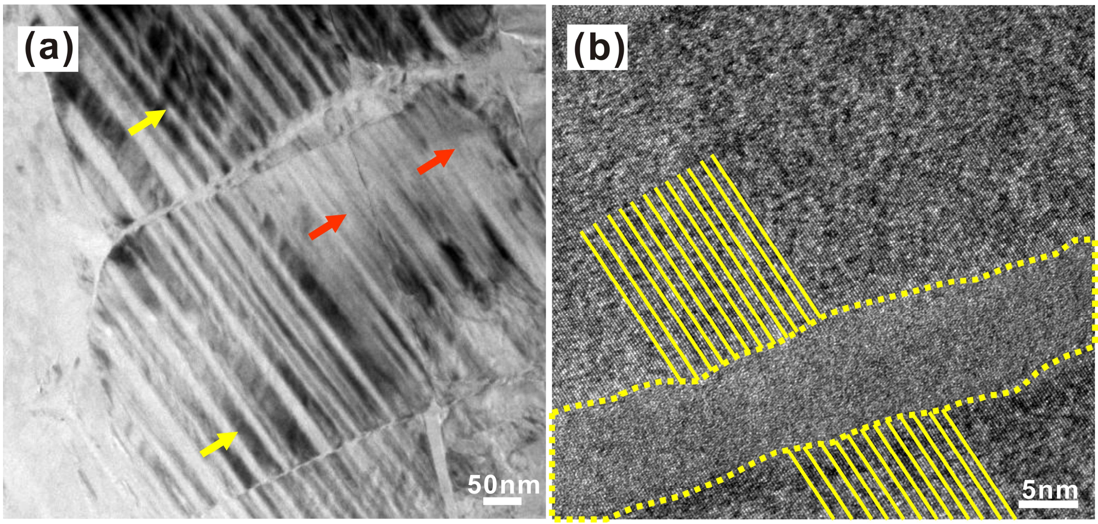

Figure 6.13 *(a) TEM images of martensites and (b) HRTEM related to detwinning after fracture.*

In order to elucidate the deformation mechanism during this stage, TEM measurements were conducted on the fractured sample. As shown in Fig. 6.13a (see the yellow arrows), the martensitic plates arrange side by side, implying that twinned martensite still exists. However, some twinned structures are broken in certain regions (indicated by red arrows). The HRTEM image (Fig. 6.13b) shows that some of the nano-scaled twins start to be dispelled, being unlike the typical characteristic of twinned structures observed in the as-cast sample, revealing that partial de-twinning occurs during stage IV [416]. With the twinned martensitic crystals being subjected to an external force, a resolved shear stress works along the twin plane and drives the twin boundary to move until it reaches a critical value by the formation and movement of dislocations with a high density [280, 417-420]. However, it is still difficult to study the dislocation mechanisms within the martensite using the TEM measurements. Based on the observation of Wang *et al.* [421], the detwinning process is accomplished through the collective glide of multiple dislocations that form an incoherent twin boundary [407]. Furthermore, the strong glassy matrix may also provide a larger strain/stress window for the occurrence of detwinning during deformation. Conversely, the formation of a high density of dislocations improves the fracture strength of the BMG composites. Hence, the "third yielding" may result from the operations of a high density of dislocations as well as the partial detwinning, the development of which result in the further increases of the plastic strain and fracture strength.

6.3.5 Fracture behavior

Fig. 6.14 shows the fracture surfaces of $Cu_{47.5}Zr_{47.5}Al_5$ BMG, BMG composites, and the fully crystalline alloy. As shown in Fig. 6.14a, for the fully amorphous CuZr-based sample (e.g. S0), some vein-like and river-like patterns are visible on the smooth fracture surface, which is a typical fracture characteristics of BMGs [422].

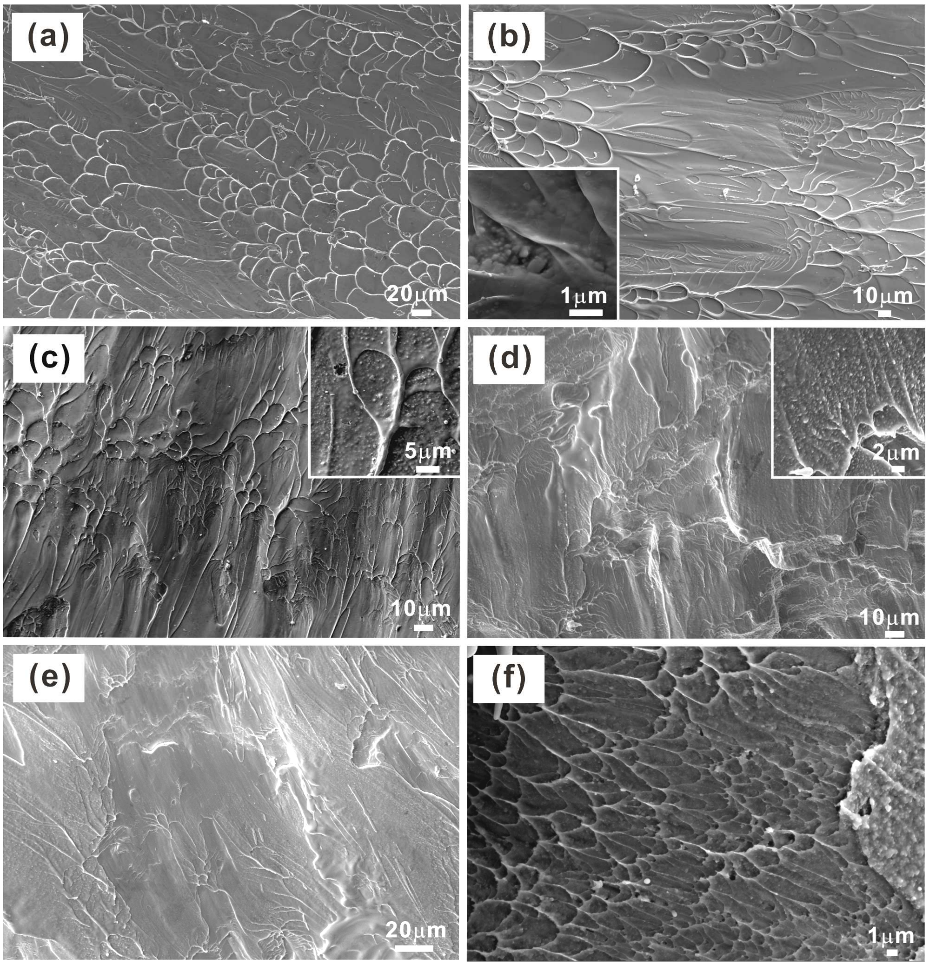

Figure 6.14 *The fracture surfaces of the (a) S0, (b) S1, (c) S2, (d) S3, (e)S4, and (f) S5 samples.*

However, with the precipitation of the B2 CuZr phase in the glassy matrix, some granulated structures (see the insets in Figs. 6.13b-c) can be observed within the vein-like structures (Figs. 6.13b-c). Furthermore, with the content of the B2 CuZr phase increasing, such kinds of structures become more. As the content of the B2 phase increases to more than 45 vol.%, the granulated structures dominate the whole fracture surface besides a little vein-like and river-like patterns. As the content of the amorphous phase totally disappears, dimples can be observed on the fracture surface of the S5 sample, which is the typical structure of the ductile metallic alloys. All the fracture surface morphology corresponds well with the evolution of the yielding and plastic deformation mechanisms with the f_{amor} decreasing. Namely, with the f_{cryst} increasing, the deformation mechanism of CuZr-based metastable alloys gradually changes from a shear-banding process to a mechanism being governed by the MT, resulting in different mechanical properties with different fracture characteristics.

6.4 Modeling of the "yielding" behavior

As described above, the yielding behavior of CuZr-based BMG composites is different from other dual-phase metal matrix composites [351, 423, 424]. For the other dual-phase metal matrix composites, the yield strength with the content of the reinforced phase increasing usually follows a simple ROM model or a load-bearing model [295, 425]. Recently, Pauly *et al.* [295] have found that the yield strength and fracture strain of CuZr-based BMG composites with different contents of amorphous phase can be described using a strength model, which considers the percolation and an empirical three microstructural element body approach. In our case, this theory model was employed to further model the yielding strength for the S0, S1, S2, S3, S4, and S5 samples. The variations of the yield strains/stresses as a function of the f_{cryst} for the as-cast $Cu_{47.5}Zr_{47.5}Al_5$ BMG composites are shown in Fig. 6.15. It can be seen from Fig. 6.15a that the "first yield" strain is about 1%, while the "second yielding" strain is approximately 2%. With the f_{cryst} increasing from 2.5 ± 0.5 vol.% to 100 vol.%, the fracture strain first increases from 6.1 ± 0.5% to 14.3 ± 0.5%, and then decreases to 11.7 ± 0.5%. The "yield" strength and the fracture strength are shown in Fig. 6.15b. The "first yield" strength of the composites can be modeled by the load-bearing model [425]:

$$\sigma_{Composite} = \sigma^{Crystalline}\left(1 + 0.5f_{Glass}\right), \tag{6.1}$$

where f and σ are the volume fractions of the constituent phases and the yield strength, respectively. However, the "second yield" strength can be described by the ROM model (Fig. 6.15b) [295]:

$$\sigma_{Composite} = f_{Cryst}\sigma^{Crystalline} + f_{Glass}\sigma^{Glass} . \tag{6.2}$$

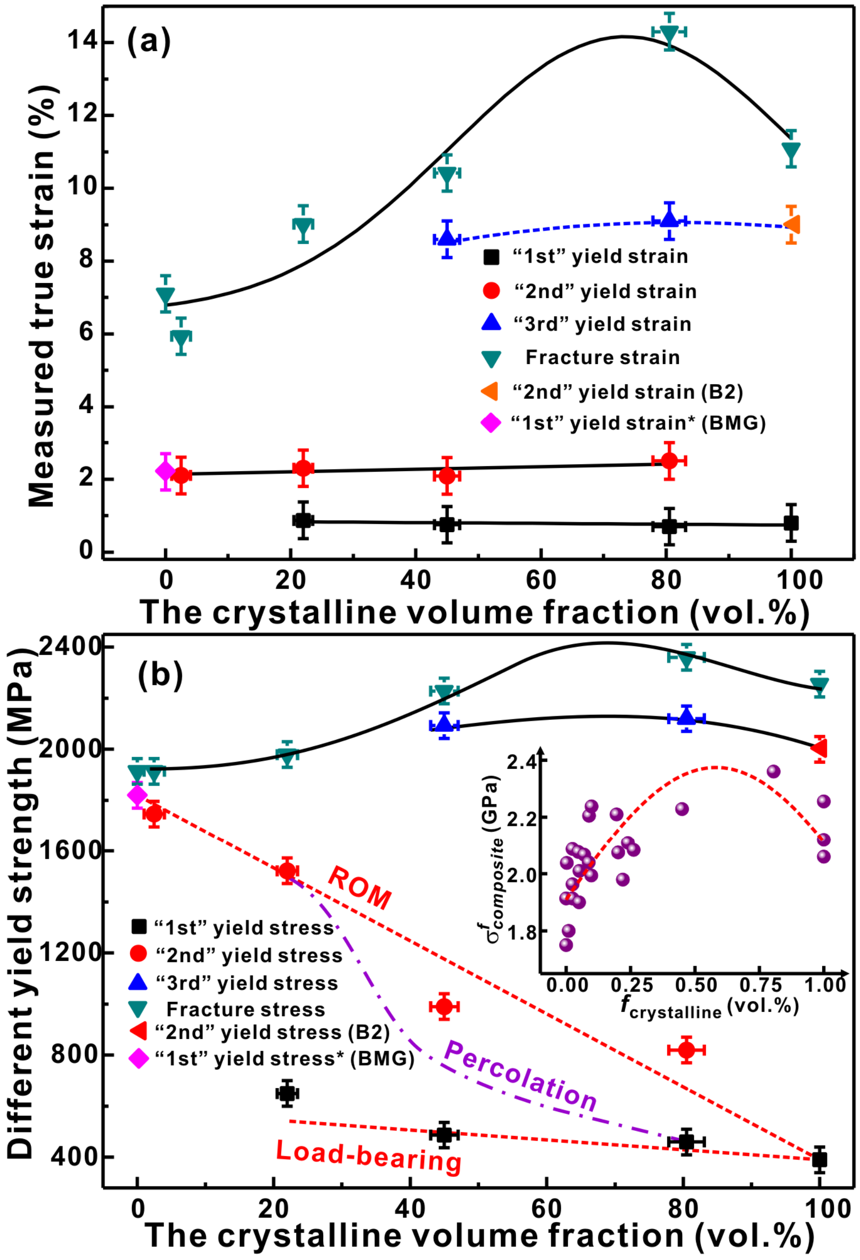

Figure 6.15 *(a) Different yielding and fracture strains, and (b) different yield strengths and fracture strengths with increasing* f_{cryst} *(Inset: fracture strengths for different* f_{cryst}*).*

As shown in Fig. 6.15b, when the f_{cryst} is larger than 22 ± 1 vol.%, it is difficult to separate the "first yielding" and the "second yielding" at a strain of about 2%, implying that the crystals start to aggregate with each other and a percolation threshold occurs [295, 351-353]. In the percolation theory, the percolation threshold generally locates between 10 vol.% and 50 vol.% for the second phase in the dual-phase metal matrix composites [135, 295, 351-353], which strongly depends on the morphology, size, distribution of the second phase and the volume fractions of the constituent phases. Pauly *et al.* found [295] that the critical f_{cryst} for the microstructural transition was determined to lie between 30 and 50 vol.%. Hence, the "second yielding" is not obvious below the percolation threshold, whereas the "first yielding" is blurred above it, leading to an actual yielding percolation transition in CuZr-based BMG composites. Usually for CuZr-based BMG composites, the interpenetration of the B2 crystals starts at a low f_{cryst} and in the vicinity of 50 vol.% the crystals form a structural framework [295].

Furthermore, the fracture strength of the CuZr-based BMG composites first increases and then decrease with the B2 CuZr phase increasing, being similar to the change of the fracture strain of the composites (Fig. 6.15). According to previous data [135, 295, 351-353] and the present observation for $Cu_{47.5}Zr_{47.5}Al_5$ BMG composites, the optimum f_{cryst} corresponding to the maximum fracture strength is found to lie between 20 vol.% and 80 vol.% (inset in Fig. 6.15b), which depends on different casting conditions [39, 135, 284, 295, 335-337, 351-353]. Based on the previous observations, the fracture strain/stress cannot be described by the ROM and the load-bearing models due to the following reasons [131, 135, 191, 213, 295, 351-356]: (1) the macroscopic softening from shear banding process and the work hardening induced by the MT are not considered, and (2) the interactions between shear bands and the crystals, and the length-scales of the microstructure inhomogeneities compared to the characteristic plastic zone size [151, 188, 426, 427] are not sufficiently taken into account. In such a case, the strength model based the percolation theory [295, 351] can be used to describe the change of the fracture strain/stress with the B2 CuZr phase changing. In the percolation theory [295, 351, 352] (Fig. 6.16), the composites can be topologically transformed into a three-microstructural element body. Element A only contains the amorphous phase and Element B represents the B2 phase. Element C consists of both the B2 phase and the amorphous phase in equal content and the two phases are partitioned by each other so as to form an ideal inter-dispersed structure as shown in Fig. 6.16. Then the fracture strain of the composites can be obtained [295]:

$$\varepsilon^f_{Composties} = f_A \varepsilon^f_A + f_B \varepsilon^f_B + k f_C \varepsilon^f_C \,, \tag{6.3}$$

where f_A, f_B and f_C are the volume fractions of the elements A, B and C, and ε^f_A, ε^f_B, and ε^f_C are the fracture strains of BMG, the B2 CuZr phase and C composite, respectively, and k is a constant. Based on the percolation theory, there is a maximum for the plastic/fracture strains for $Cu_{47.5}Zr_{47.5}Al_5$ BMG composites [135, 295, 351-353].

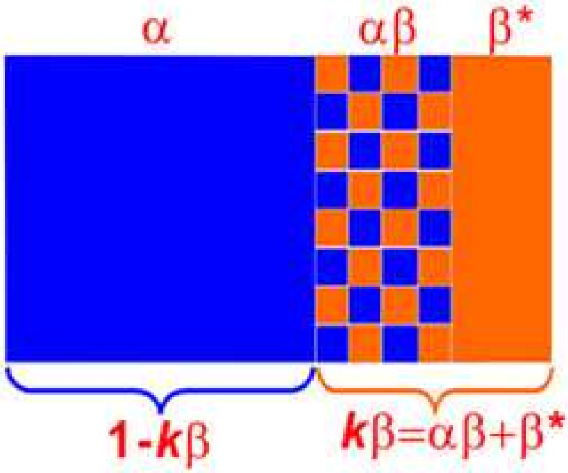

Figure 6.16 Schematic diagram of the transformation from microstructure to the three microstructural element bodies. Redrawn from [295].

As shown by the schematic dotted curves in Figs. 6.15a-b, the plastic/fracture strains of the studied samples indeed follow this rule. By collecting all the fracture strength from the compressive results [238, 295, 300, 301, 352, 353, 428], a maximum fracture strength was also observed (inset in Fig. 6.15b) when the volume fraction of the B2 CuZr phase locate between 20 vol.% and 80 vol.%.

6.5 Conclusions

Different yielding and plastic behaviors of the metastable CuZr-based alloys with the f_{cryst} increasing from 0 vol.% to 100 vol.% were investigated. The corresponding deformation mechanisms were investigated. For the fully amorphous rod, the sample yields at a strain of about 2% due to the occurrence of shear bands, and the sequent plastic stage is dominated by a shear banding process. As the B2 CuZr phase is introduced into the glassy matrix, the MT occurs at a strain of about 1%, while the shear bands forms at a strain of about 2%. With the content of the B2 CuZr increasing gradually, these microstructure changes become pronounced, which results in a "third yielding" at the strain > 8%, which is due to a detwinning process mediated by dislocation movements. For the samples containing the almost pure B2 CuZr phase, the first yielding can be observed at a strain less than 1%, while the second yielding occurs at a high stress of about 2000 MPa. However, due to the disappearance of amorphous phase, the "second yielding" at a strain of about 2% for CuZr-based BMG composites disappears. It can be concluded that with the f_{cryst} increasing from 0 vol.% to 100 vol.%, a "single-to-double-to-triple-to-double" yielding transition was found. The deformation mechanism gradually changes from a shear-banding dominated process, to being governed by the MT, resulting in different plastic deformation. The yield strengths of the composites are modeled as a function of the volume fractions of the constituents and a transition from a ROM model to a load-bearing model is observed based on a percolation model proposed by Pauly *et al.* [295]. Our results can assist in understanding the deformation behavior of metastable high-performance alloys.

7 Martensitic transformation behavior in CuZr-based alloys

The TRIP effect has been found in CuZr-based BMG composites containing the B2 CuZr phase in the glassy matrix during deformation [295, 300, 301, 315, 352, 353]. So far, much attention has been paid to their fabrication and deformation. However, the MT, which is important for the deformation of CuZr-based BMG composites, is still not clear. Furthermore, most B2 compounds are inherently brittle, which is due to a significant fraction of directional *d*-bonds near the Fermi level [429] and the MT within the B2 phase is also of electronic nature [430]. Therefore, it is necessary to illuminate the ductile nature and transformation information of the B2 CuZr phase and its martensites from the point of view of their electronic structures. Meanwhile, the microalloying effect and the effect from the glassy matrix on the MT also required to be illustrated.

7.1 Electronic structures and martensitic transformation

Experimental results have shown that the MT temperatures strongly depend on the chemical compositions, the elastic constants of the matrix crystal before MT and microstructural features such as precipitates [280, 281, 295, 431-435], which are of importance from a fundamental point of view. Under the same external and internal states, the MT has proven to be also connected with their special electronic structures [436-439], which may originate from the phonon softening to electron-phonon coupling and specific nesting properties of the Fermi surface [436-439]. In addition, it is necessary to mention that not all austenitic phases exhibiting the MT are quite ductile [418]. For AB-type intermetallics [316], as the element A with full *d* bonding is alloyed with an element B having incompletely filled *d* orbital, the A and B atoms move past one another when dislocations glide during the plastic deformation [440]. Therefore, the electronic structure of the equiatomic CuZr intermetallics is vital for their ductility or brittleness during deformation.

7.1.1 Electronic structures of the B2 CuZr phase

Electronic structure calculations for the B2 CuZr phase were performed by the full-potential linearized augmented plane wave plus local orbital method as implemented in the WIEN2k code [441-443]. The non-overlapping atomic spheres R_{MT} of 2.40 a.u. each were used for Cu and Zr. The value of $R_{MT}K_{Max}$, where K_{Max} corresponds to the largest plane wave vector, was set to 7.0 and spherical harmonics up to the tenth order were included in the expansion of the radial part of the wave function [441-443].

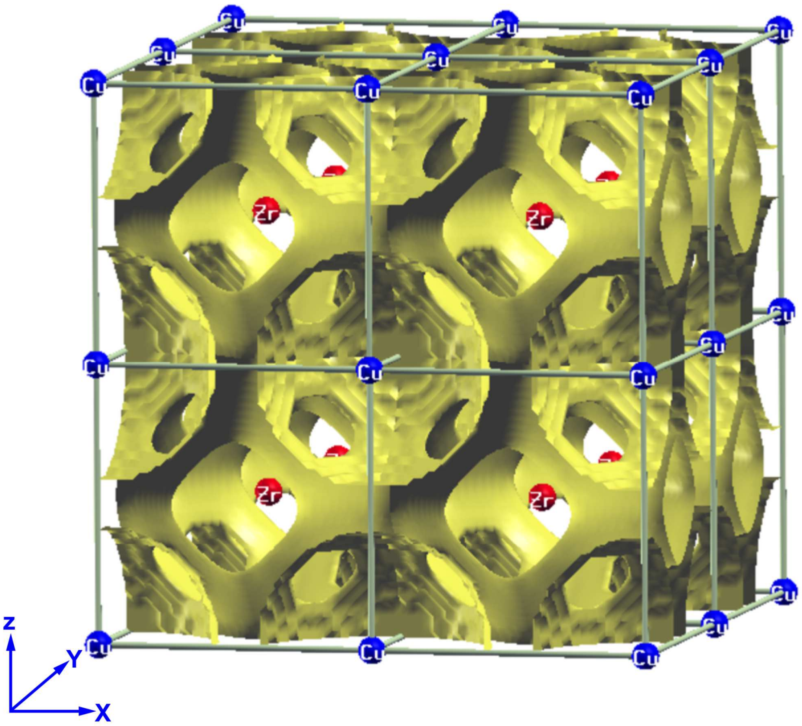

Figure 7.1 *The difference charge density (RCD) in the [001] plane of the structure modeling of the B2 CuZr intermetallics.*

The mesh of special k points in the irreducible Brillouin zone (IBZ) was selected to be 10×10×10. For the exchange-correlation energy functional the Perdew-Burke-Ernzerhof (PBE) version of the generalized gradient approximation (GGA) was used [441-443]. The structural parameters were taken from experimental values at room temperature [294]. The convergence is reached as the difference in the charge fluctuation becomes less than 0.0001 of an electron. For the two dimensional difference density slices a 500 × 500 mesh was used [353, 441-443]. Fig. 7.1 shows the difference charge density (RCD) in the plane [001] of the structure modeling of the B2 CuZr intermetallics.

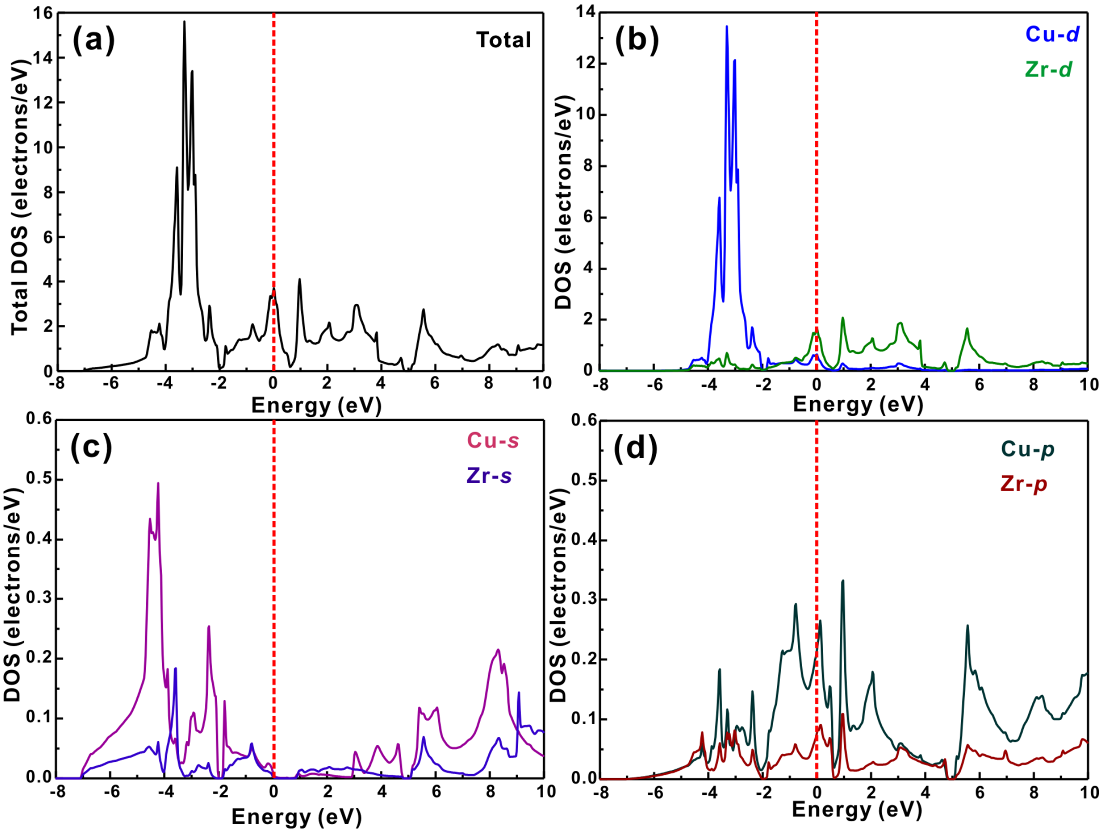

Figure 7.2 *(a) Total DOS of Cu and Zr elements for the B2 CuZr phase, and the projected DOS (b) of the Cu-d and Zr-d, (c) the Cu-s and Cu-s, and (d) of the Cu-p and Zr-p.*

The corresponding electronic densities of states (DOS) of Cu and Zr for the B2 CuZr phase were calculated, respectively (Fig. 7.2). It is obvious to distinguish the different Y-scales between *s*, *p*, and *d* components of the DOS. The Fermi level lies about 2 eV to the right of the pseudogap minimum, i.e. the bonding states are completely occupied. The total DOS at the Fermi level is rather high (3.7 the number of states eV^{-1} $atom^{-1}$). Compared with the total DOS, it can be seen that the bonding states are dominated by Cu-*d* lying well below the Fermi level and Zr-*d*, while the antibonding states are dominated by Zr-*d* (Figs. 7.2a-b). Below the Fermi level, pronounced peaks of Cu-*d* and Zr-*d* contribute more while the *s* and *p* contributions of both Cu and Zr are small (Figs. 7.2c-d).

As shown in Figs. 7.2a-b, the difference charge density (RCD) in the planes of [101] and [$\frac{1}{2}$01] shows the bonding characteristics more visually. In our case, the linear combination of the atomic charge density was subtracted from the converged charge density, denoting the lowest value as zero. The region with a higher charge density implies stronger bond formation. As shown in Fig. 7.3, different colors were used to represent differently relative values of the charge density, respectively. A significant delocalization of the bonding charge in the interstitial region in the B2 CuZr phase resembles the metallic bonding.

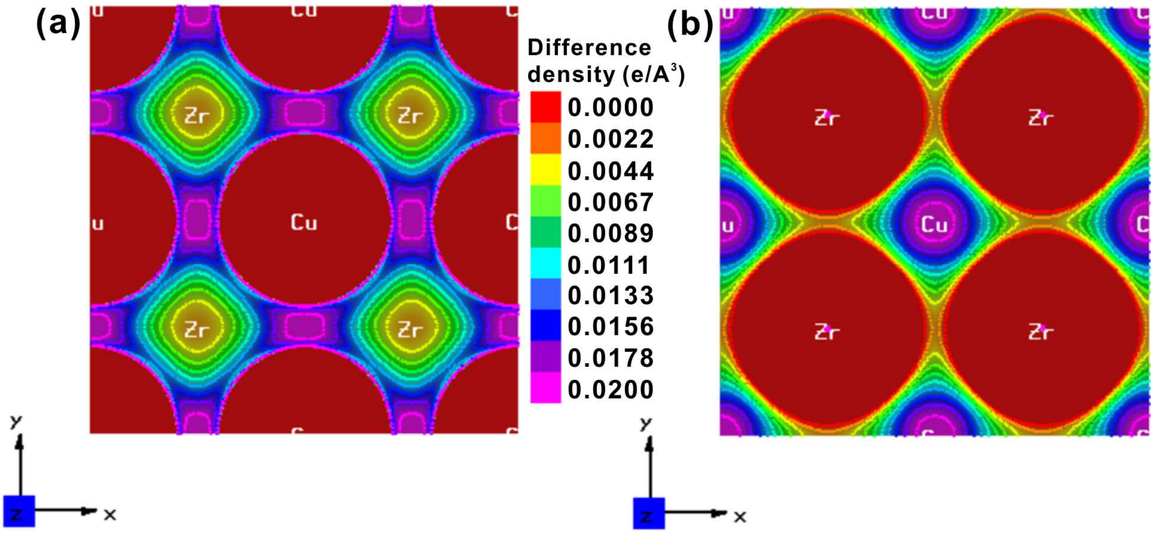

Figure 7.3 *Difference charge density on (a) [001] plane and (b)* $[\frac{1}{2}\ 0\ 1]$ *plane for the B2 phase.*

Recent reports [444] have shown that the elastic constants have an influence on the bonding characteristics between elements in phase. In such a case, the Zener's anisotropy factor of the B2 CuZr single-crystal, i.e. $A = 2C_{44}/(C_{11}-C_{12}) = 3.512$, is rather large, indicating a directional and intense bonding tendency. The distribution of the bonding charge densities of the B2 CuZr phase was also calculated by Ghosh [444] using all-electron PAW potentials, which corresponds well with the present results, further illustrating that the maximum in bonding charge density lies halfway along the Cu-Cu bonding direction rather than halfway along the Cu-Zr bonding direction. Gschneidner *et al*. [429] proposed a ductility criterion for B2 intermetallics based on the electronic structural information of 36 different B2 intermetallics. As the *d*-electrons lie well below the Fermi level, most of B2 intermetallics show a ductile deformation behavior. According to our simulation analysis, this ductility criterion is also applicable for the B2 CuZr phase.

7.1.2 Electronic structures of CuZr martensites

It has also been demonstrated that the MT within B2 phase is of electronic nature [430]. The splitting of the *d*-like electron energy bands in the pre-Fermi level under the conditions of non-hydrostatic deformation may have relations with the lattice instability of the high-temperature B2 CuZr phase [430, 445], which plays a stabilizing role relative to the shear deformation of the B2 CuZr phase. Recently, the relative formation energies of the B2 CuZr phase, B19' martensite and Cm martensite as well as their electronic structures have been calculated [446]. The mechanism of the MT within the B2 CuZr phase [447] has been proven to be the transformation from the high-temperature B2 CuZr phase into martensites (B19' and Cm). Even though the MT almost occurs simultaneously, B19' martensite forms first and then stops to form during further cooling. At the same time, Cm martensite proceeds to form until the end of the MT. When the two kinds of martensite phases are more stable than the austenite phase [446], new martensites trend to form from the B2 CuZr phase during shear deformation.

Firstov *et al.* [446] have also systematically calculated the DOS for Zr and Cu in B19' and Cm structures, respectively. The total DOSs of B19' and Cm intermetallics are also dominated by Cu-*d* below the Fermi level but not near the Fermi level, which implies that these two phases are also ductile. Based on the discussions in **Chapter 5**, almost purely martensitic samples (e.g. S7) indeed exhibit certain plasticity during the compression test. Furthermore, it is worth noting that compared with the *d*-DOS of Cu in the B2 CuZr structure, it can be seen that *d*-*d* interaction of Cu atoms in B19' and Cm structures increases [446], while the width of the *d*-Cu band in B19' and Cm structures becomes larger, which may be allied with their lower formation energies. Nevertheless, previous reports and our simulation results [429, 430, 446, 447] show that the B2 phase undergoes the MT due to their special electronic structures.

7.2 Effect of minor additions on the martensitic transformation

7.2.1 Formation of Cu-Zr-Ti crystalline samples

Recently, the phase formation and thermal stability in Cu-Zr-Ti(Al) MGs, as well as the deformation-induced MT in Cu-Zr-Ti(Al) BMG composites have been investigated [295, 326, 331]. So the related microstructure information during cooing and heating processes was provided. Therefore, the Cu-Zr-Ti(Al) alloy systems were good candidates to check the corresponding MT in the crystalline

CuZr-based alloys and the BMG composites. The as-cast $Cu_{50}Zr_{50-x}Ti_x$ (x = 2.5, 5, and 10) rods with a diameter of 3 mm were chosen. In order to fabricate fully crystalline alloys containing the equiatomic CuZr intermetallics, the temperatures of the eutectoid B2 CuZr decomposition (T_f) for the studied alloys have to be first considered, above which the B2 CuZr phase exists and below which the B2 CuZr phase decomposes into other stable LT-EPs.

In the Table 3.1 in **Chapter 3**, it has been shown that with the content of Ti increasing from 0 at.% to 10 at.%, the value of T_f increases from 1013 ± 2K to 1067 ± 2K, respectively [295, 315]. Thus, all the samples were annealed at 1073 K, above T_f but less than T_L for 36 h, and then quenched into water. Therefore, the equiatomic CuZr intermetallics (i.e. B2 CuZr phase and martensites) can be kept for the studied alloys.

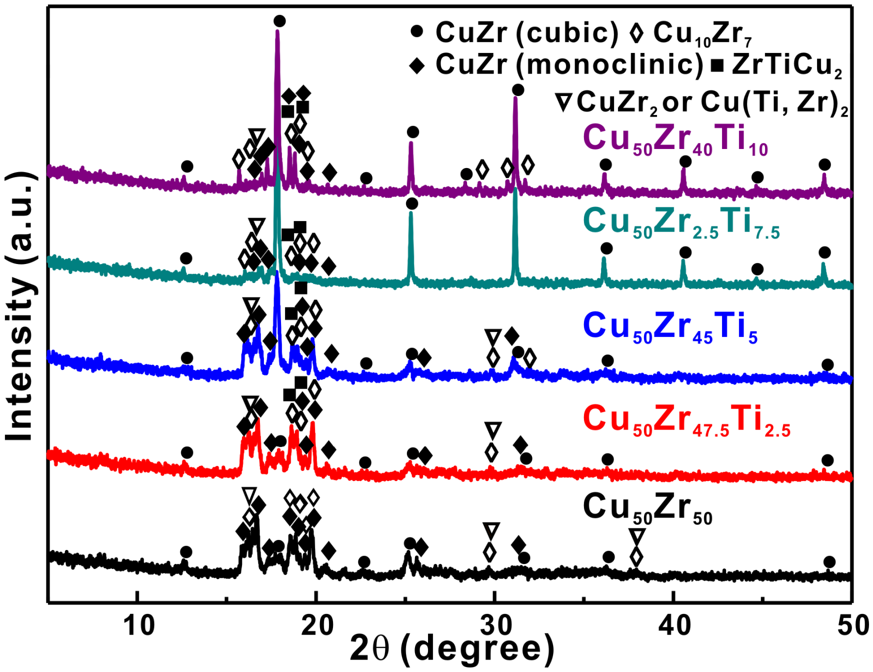

Figure 7.4 *XRD patterns of the annealed $Cu_{50}Zr_{50-x}Ti_x$ (x = 0, 2.5, 5, 7.5 and 10) rods.*

As shown in Fig. 7.4, the B2 CuZr phase and the martensitic phase are observed for all the samples. However, it is difficult to identify other stable EPs based on other crystalline peaks in the XRD pattern when the Ti may be dissolved into these phases. The crystalline peaks shift to a large 2θ when the Ti content gradually increases in CuZr-based alloys [448]. Recently, the Cu-Zr-Ti ternary phase diagram has been determined [449], which is shown in Fig. 7.5. When Ti is added into CuZr-based alloy, the B2 CuZr phase is not the unique crystalline phase above T_f and below T_L. As the content of Ti is less than 10 at%, a eutectic structure consisting of the B2 CuZr phase and τ_1 ($ZrTiCu_2$ [450]) is expected to form after quenching together with some primary B2 CuZr crystals. As the composition achieves a hypereutectic composition (10 at.% Ti), the eutectic structure is obtained during cooling together with τ_1. In other words, the primary crystallizing phase changes with the content of Ti increasing during solidification.

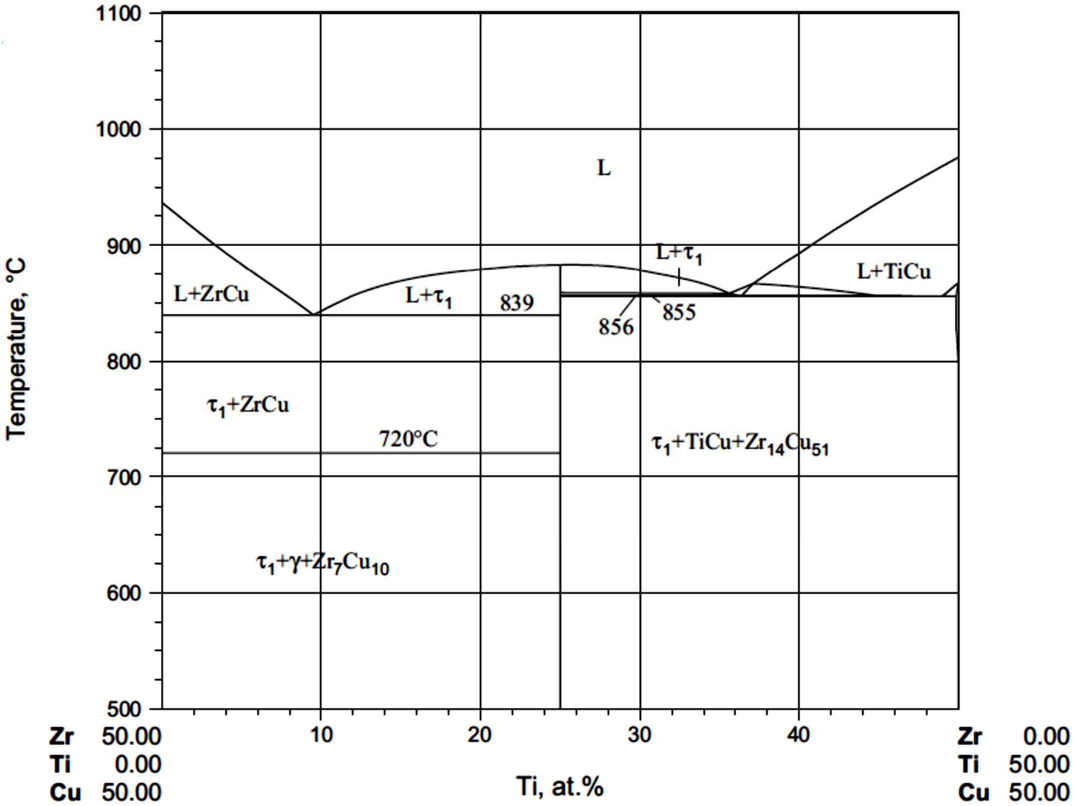

Figure 7.5 *Calculated temperature-composition ZrCu-TiCu section for Cu-Ti-Zr alloys [449].*

However, the B2 CuZr phase is a high-temperature crystalline phase. As the temperature is lower than 897 K [449], the eutectoid decomposition occurs during cooling. After this eutectoid decomposition, two crystalline phases (i.e. $Cu_{10}Zr_7$ and γ: $Cu(Ti,Zr)_2$) are observed. The γ phase was identified to be a continuous solid solution between the isostructural $CuZr_2$ and $CuTi_2$ phases [451]. Even though the cooling rate is very high, this transformation cannot be totally avoided. It was found that the B2 CuZr phase transforms into martensitic crystals during quenching due to the stresses that occur during solidification [295, 296, 326]. Therefore, after quenching, a mixture of equiatmoic CuZr intermetallics (i.e. B2 CuZr and martensites), τ_1, $Cu_{10}Zr_7$, and γ were obtained. As the content of Ti is 0 at.%, τ_1 will not exist, while the γ phase becomes $CuZr_2$. Nevertheless, the equiatomic CuZr compound is the dominant crystals for all the samples.

7.2.2 Effect of Ti element on the martensitic transformation

In this section, the MT for the annealed $Cu_{50}Zr_{50-x}Ti_x$ (x = 0, 2.5, 5, 7.5 and 10) alloys was investigated using a dilatometer. Fig. 7.6a shows the dilatation normalized with respect to the original sample length (dL/dL_0) of the annealed $Cu_{50}Zr_{50}$ alloy, which was thermally cycled between 153 K and 673 K at a heating and cooling rate of 10 K/min.

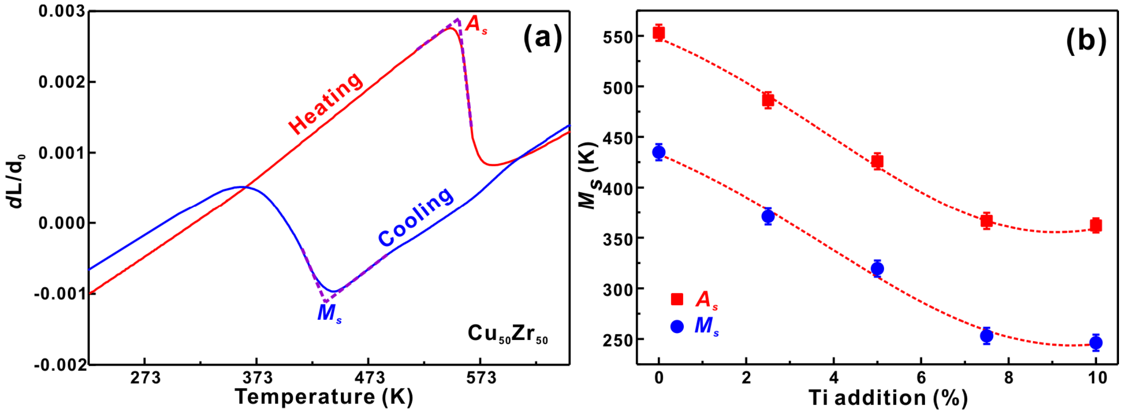

Figure 7.6 *(a) Thermal dilatation results of the annealed* $Cu_{50}Zr_{50}$ *alloy, and (b) the changes of* A_s *(austenite start temperature) and* M_s *(martensite start temperature) in the annealed Cu-Zr-Ti alloys.*

It has been found that the martensite transforms to austenite upon heating (Fig. 7.6a), being associated with a negative volume effect [295, 298, 326]. During cooling, the sample transforms back to the martensitic state, which is linked to a positive volume effect [295, 298, 326]. The thermal dilatation results of the annealed Cu-Zr-Ti alloys show that with the Ti content increasing, the transitions in the thermal dilatation curves associated with not only the reverse MT (AT) during heating but also the MT during cooling gradually shift to lower temperatures. The onset temperatures of AT and MT (A_s and M_s) were determined as shown in Fig. 7.6a and are plotted in Fig. 7.6b. It was found that the values of A_s and M_s gradually decrease from 553 ± 10 K and 435 ± 10 K to 362 ± 10 K and 246 ± 10 K, respectively, when the Ti content increases from 0 at.% to 10 at.% (Fig. 7.6b).

Additional low-temperature DSC measurements were conducted for each sample (Fig. 7.7) at a heating and a cooling rate of 10 K/min in order to confirm the trends observed in the dilatometry experiments. Again, as shown in Fig. 7.7, the peaks associated with the AT and MT indeed gradually shift to lower temperatures after the addition of Ti. Moreover, during the second thermal cycle, A_s becomes larger and M_s is lowered at the same time, which means the transformation hysteresis increases. The observation that an increasing number of thermal cycles leads to a decrease of M_s and can thus stabilize B2 CuZr (austenite) to lower temperatures is in good agreement with other reports [295, 326, 331].

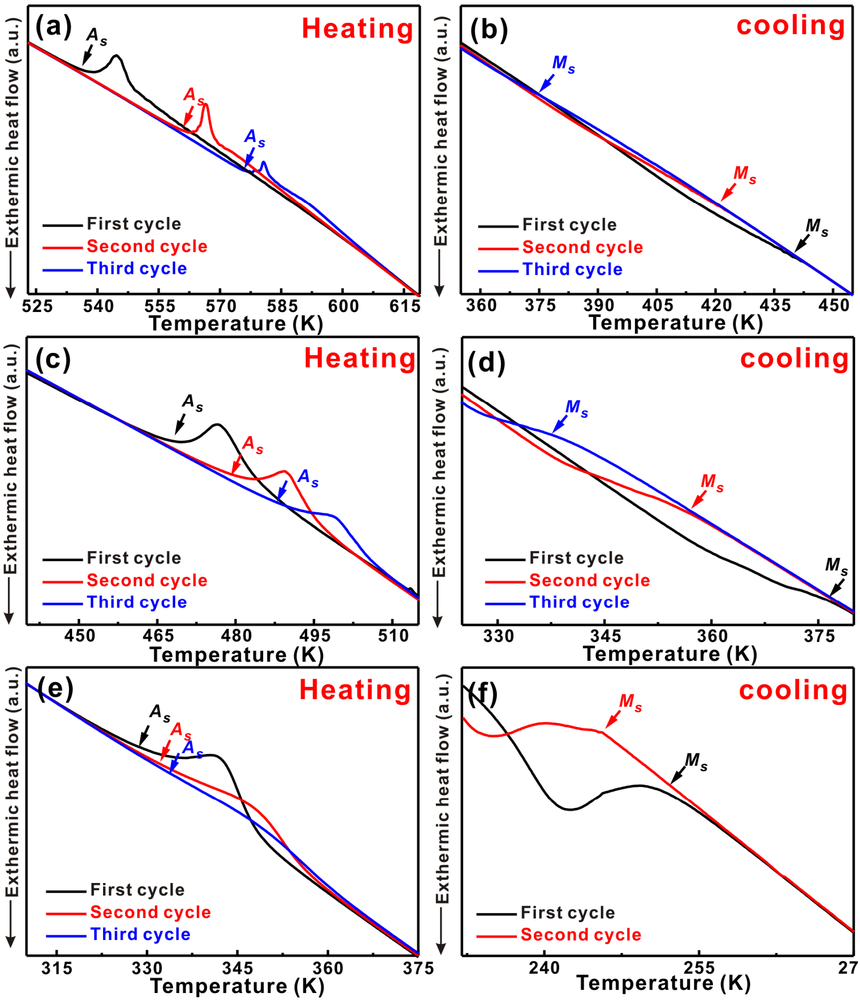

Figure 7.7 *Heating and cooling curves obtained in a DSC of the different annealed* $Cu_{50}Zr_{50-x}Ti_x$ *(x = (a-b) 0, (c-d) 2.5, and (e-f) 10) alloys.*

The A_s and M_s values obtained from the first heating and cooling process are consistent with those extracted from the thermal dilatation results even though their absolute values are a little different [302]. The difference between the transformation temperatures for the samples is 3-10 K, which may be due to different measuring machines.

It is also worthy noting that the peaks of the AT are much stronger but narrower than the ones of the MT, which aggravates an accurate determination of M_s. The dilatometry results already indicate that the reverse martensite-to-austenite transformation takes place in a slightly smaller temperature window than the forward transformation (Fig. 7.6a). This behavior becomes even more obvious in the DSC traces, where the austenite-to-martensite transformation is reflected in much broader but shallower peaks than the corresponding reverse transformation (Fig. 7.7 b, d, f).

As discussed in **Section 7.1**, the eutectoid decomposition temperatures for all the present alloys are lower than 900 K. Previous results [331] have shown that $Cu_{10}Zr_7$ forms prior to $CuZr_2$, the second LT-EP, in CuZr-based alloys. Therefore, it is expected that the B2 CuZr phase may partly decompose into the LT-EPs during thermal cycling, preferentially into $Cu_{10}Zr_7$. For the Cu-Zr-Ti alloys, this decomposition can be described as follows: τ_1 + B2 CuZr → τ_1 + B2 CuZr + $Cu_{10}Zr_7$ + γ [449] (see **Section 7.21**). Additionally, Pauly *et al.* and Koval *et al.* [295, 298, 326] have shown that some martensitic crystals remain in the alloy even after temperatures exceeding A_f (austenite finish temperature) are reached. This is because the shape recovery of CuZr-based alloys is generally not complete. The present DSC traces (Fig. 7.7) also prove that the enthalpies associated with the martensitic and its reverse transformation gradually decreases after the completion of a thermal cycle. The explanation for this behavior might be the partial decomposition of B2 CuZr into the more stable phases $Cu_{10}Zr_7$ and $CuZr_2$ as well as the incomplete transformation from austenite to martensite and back.

7.2.3 Effect of minor elements on the martensitic transformation temperature

In order to understand the change of the MT temperatures in shape memory alloys with addition of different elements, several parameters have been proposed based on the average concentration of valence electrons [316, 452-454], which are electrons in the outermost orbital of an atom. The valence electrons per atom of ternary and quaternary alloys, e_v/a [316, 452-454], can be calculated based on the atomic fraction of the elements in the alloy, which has been shown in **Chapter 3**. The M_s and the corresponding e_v/a for $Cu_{50-x}Zr_{50}Ni_x$ (x = 5, 10, 15, 20, and 25), $Cu_{50-x}Zr_{50}Al_x$ (x = 2, 4, 6, 8, and 10), $Cu_{50-x}Zr_{50}Co_x$ (x = 2, 3, 4, and 5), $Cu_{50}Zr_{50-x}Ti_x$ (x = 2.5, 5, and 10) alloys (Fig. 7.8a) were collected. For Cu-Zr-X (X=Al, Co, and Ni) alloys, with the content of minor elements increasing, the values of M_s and e_v/a decrease. However, for the Cu-Zr-Ti alloy system, this rule is not applicable. As the value of the M_s decreases, the value of e_v/a remains constant, implying that other factors need to be considered.

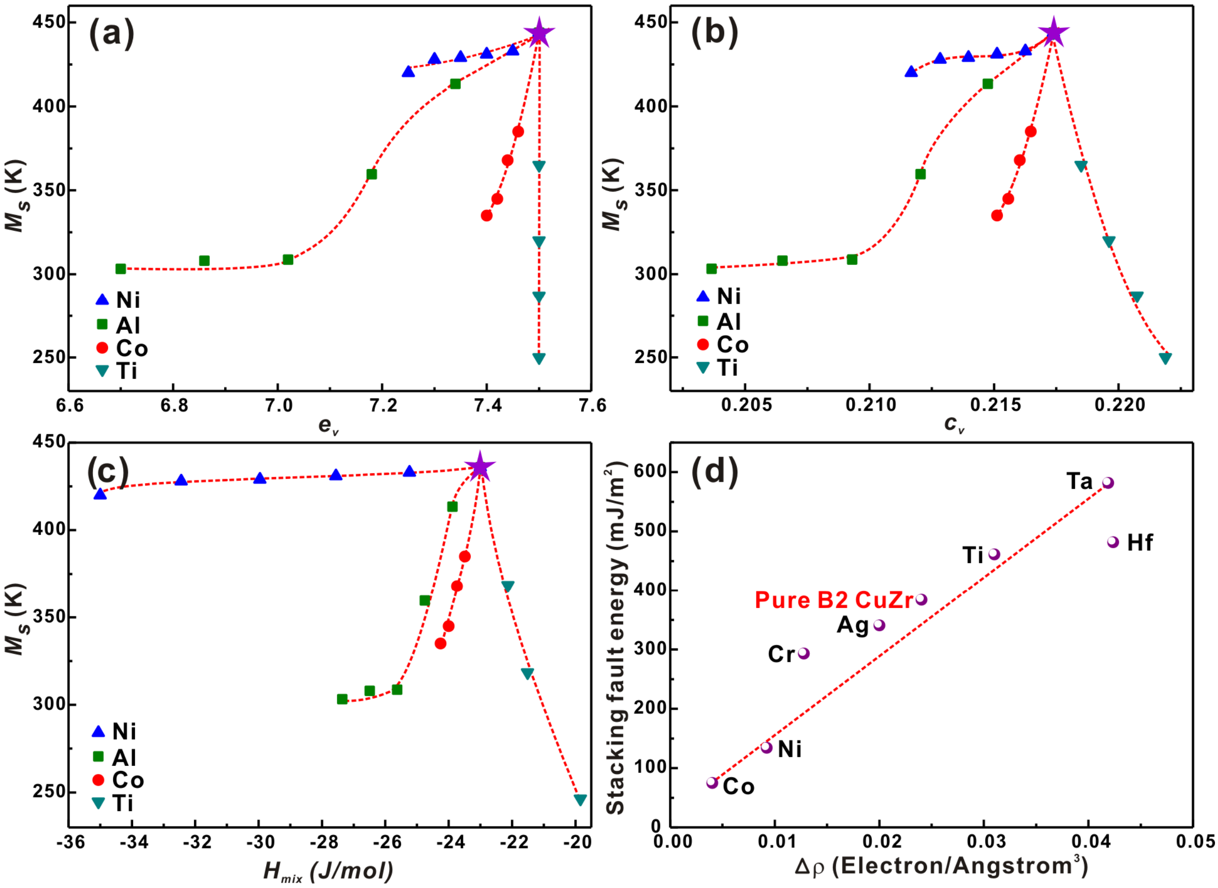

Figure 7.8 *Correlations between the values of M_s, (a) e_v/a, (b) c_v, and (c) ΔH_{mix}, Cu-Zr-X (X=Al, Co, Ti, and Ni) alloy systems, and (d) the correlations between the stacking fault energy and the electronic charge density redistribution of Cu. Fig. 7.8d was taken from [455].*

Recently, Zarinejad and Liu [316] have modified this theory and suggested another parameter to evaluate and explain the change of MT temperature. In their theory, the compositional dependence of the MT temperatures of shape memory alloys is connected with the variation of the average concentration of valence electrons, c_v, of an alloy, which is defined as the ratio of the number of valence electrons to the total number of electrons of the alloy, $c_v = e_v/e_t$, and is given by [316]:

$$c_v = \frac{e_v}{e_t} = \frac{f^A e_v{}^A + f^B e_v{}^B + f^C e_v{}^C}{f^A N^A + f^B N^B + f^C N^C}, \qquad (7.1)$$

where f^A, f^B and f^C are the atomic fractions of the different elements (A, B and C), $e_v{}^A$, $e_v{}^A$ and $e_v{}^A$ represent the corresponding number of valence electrons of the different elements, and N^A, N^B and N^C are the atomic numbers of the elements in the alloy, respectively.

As shown in Fig. 7.8b, with M_s of Cu-Zr-X (X=Al, Co, and Ni) alloy systems decreasing, the values of c_v decrease. However, the Cu-Zr-Ti alloys exhibit an increasing tendency for the c_v. Furthermore, since the enthalpy of mixing (ΔH_{mix}) also reflects the bonding nature between the elements, the ΔH_{mix} for the present alloys were calculated as shown in Fig. 7.8c. It has been reported that the change of ΔH_{mix} is consistent with the calculations of c_v [317-322]. For metallic alloys, the delocalized valence electrons hold the non-valence electrons and nuclei of ions together and form metallic bonds [316, 456, 457]. Non-valence electrons contribute to the total atomic volume of the alloy [456]. It is believed that the addition of minor elements changes the average strengths of the bonds in metallic alloys, which could be reflected from their electronic structures.

Furthermore, it has alos been proven that the valence electron concentration or electronic charge density is also correlated with the change of the bulk modulus (K) and the shear modulus (G) [458-463]. It has been shown that during cooling of austenite, the elastic moduli of austenite gradually decrease and finally reach a critical value before the MT [458-463]. Then the change of their electronic structures reflected by the values of c_v may induce the change of the elastic modules during cooling, and result in the change of the value of M_s.

Additionally, as proposed by Ogata *et al.* [464, 465], the variation of the energy of the created stacking faults also depends on their electronic structures and is particularly correlated with the electronic charge density during the stacking fault formation. The stacking fault energy represents the energy cost per unit area incurred by the relative displacement of two parts of a crystal through a shift vector across a certain slip plane [466, 467]. With the energy of the created stacking faults decreasing, the active plasticity mode will be dislocation glide, mechanical twinning and then MT [455, 464-467]. Hence, it can be concluded that the energy of the created stacking faults, the value of M_S, and the MT are correlated with each other to some degree. Fig. 7.8d shows the correlation between the stacking fault energy and the electronic charge density redistribution [455]. With the addition of Ta, Hf, and Ti to the equiatomic CuZr intermetallic compound, both the stacking fault energy and the electronic charge density increase. On the contrary, the addition of Cr, Co, and Ni decreases the stacking fault energy and the electronic charge density. The change trend of the stacking fault energy and the electronic charge density with the addition of minor elements corresponds well with our calculations.

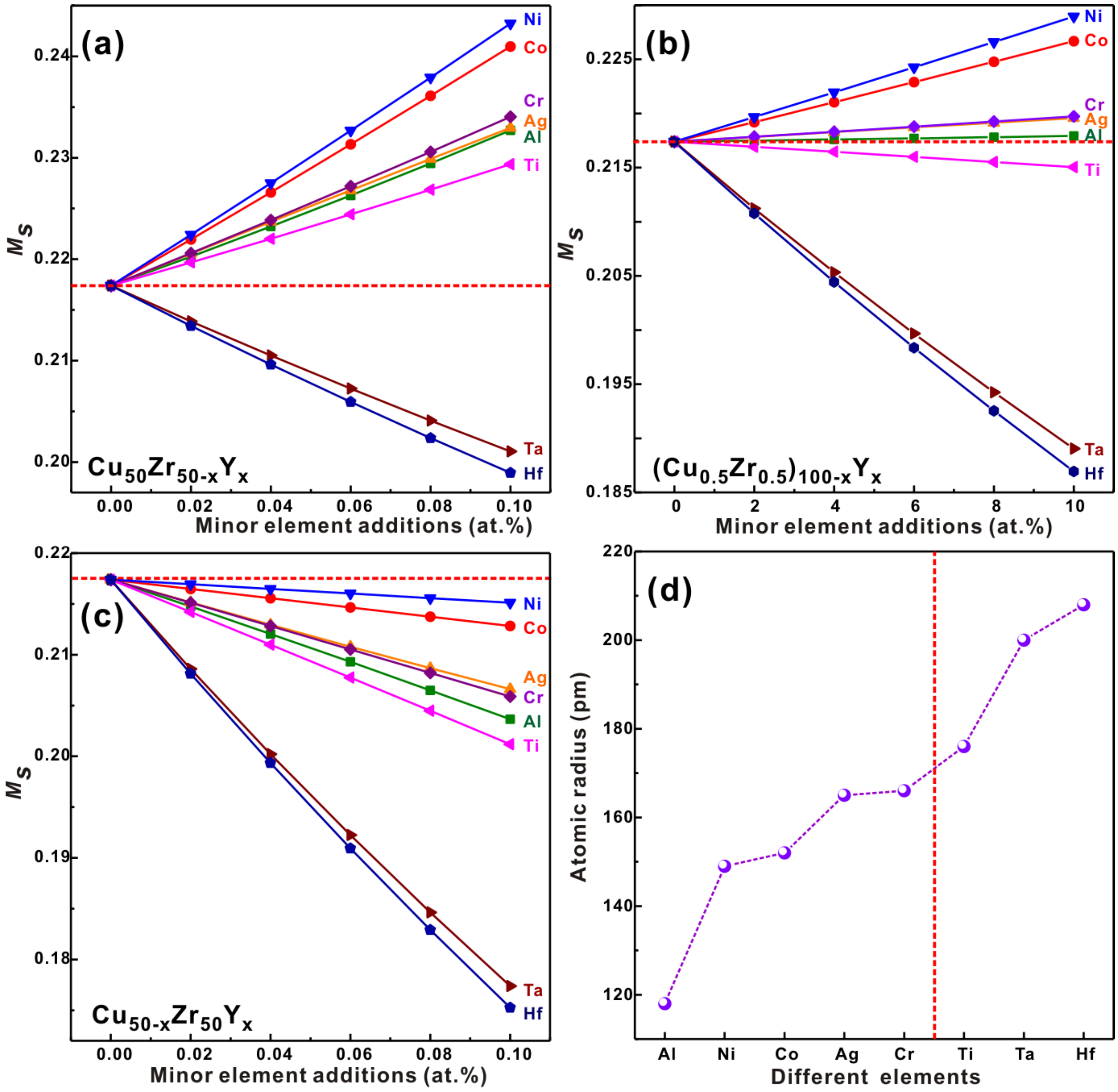

Figure 7.9 *The change of c_v for (a) $Cu_{50}Zr_{50-x}Y_x$, (b) $(Cu_{0.5}Zr_{0.5})_{100-x}Y_x$ (c) $Cu_{50-x}Zr_{50}Y_x$, (Y = Ni, Co, Ag, Cr, Al, and Ti; x= 0, 2, 4, 6, 8, and 10), and (d) the atomic radii of the elements.*

In order to further demonstrate these observations, the values of c_v of Cu-Zr-X (X=Ni, Co, Cr, Ag, Al, Ti, Ta, and Hf) were calculated, which is depicted in Fig. 7.9. For these alloy systems, different elements substitute Cu, Zr, or Cu and Zr. For the $Cu_{50}Zr_{50-x}Y_x$ (Y = Ta, and Hf; x= 0, 2, 4, 6, 8, and 10) alloys, the value of c_v always decreases with the content of Ta or Hf increasing, while the values of c_v for $Cu_{50}Zr_{50-x}Y_x$ (X=Ni, Co, Cr, Ag, Al, and Ti) alloys increase with the content of the minor alloying element increasing (Fig. 7.9a). Secondly, by using the minor element substituting Cu, all alloys show a decreasing tendency with the content of minor element increasing (Fig. 7.9b). At last, when the minor elements were used to substituting the Cu and Zr at the same time (Fig. 7.9c), it was found that the values of c_v for $Cu_{50}Zr_{50-x}Y_x$ (X=Ni, Co, Cr, Ag, and Al) alloys increase with the minor element addition, while the values of c_v for $Cu_{50}Zr_{50-x}Y_x$ (X=Ti, Ta, and Hf) alloys show an opposite tendency.

As shown in Fig. 7.9d, the atomic radii of the Ti, Ta, and Hf are relatively large, while the Ni, Co, Cr, Ag, and Al possess relatively small atomic radius. When minor elements with different atomic radii are added into the AB-type intermetallics, the elements can occupy the interstices or substitute A or B atoms, which indeed strongly depend on the sizes of the added atoms [468]. It has been found that the lattice parameters of the parent phase strongly affect the MT [469-471]. Usually, lattices generally have three lattice constants, referred as *a*, *b*, and *c*. For example, for Ni-Mn-Ga shape memory alloys, a global energy minimum of the martensitic phase for a ratio c/a >1 can be found [469], while a stable martensitic phase was reported at c/a =0.97 [472]. Nevertheless, as discussed above, the electronic structures of equiatomic CuZr intermetallics are associated with the MT behavior with the additions of different elements. Meanwhile, the atomic radii of the introduced elements also have a strong influence on the change of c_v, i.e. the electronic structures.

7.3 Martensitic transformation in rapidly solidified alloys

The B2 CuZr phase transforms into martensitic crystals upon deformation and thermal treatment [295]. However, the B2 CuZr phase and martensitic phase in CuZr-based BMG composites trend to decompose into other LT-EPs and simultaneously the amorphous phase devitrifies into crystals when the samples after certain heat treatments [295, 395]. Therefore, it is necessary to investigate the MT of CuZr-based BMG composites, which has not been done before. Here, $Cu_{50}Zr_{50}$ and $Cu_{47.5}Zr_{47.5}Al_5$ BMG composites were fabricated in order to measure the MT behavior.

7.3.1 Martensitic transformation in the as-cast $Cu_{50}Zr_{50}$ alloys

Fig. 7.10 shows the XRD patterns of the as-cast $Cu_{50}Zr_{50}$ rods with diameters of 2 mm (C2) and 3 mm (C3). For the C2 sample, sharp crystalline peaks superimposed on a small, diffuse diffraction maximum prove that the C2 sample consist of a little B2 CuZr phase, an amount of CuZr martensictic crystals and a little amorphous phase. The C3 sample mainly consists of CuZr martensictic crystals together with a little B2 CuZr phase. Actually, these the observations correspond well with the results in **Chapter 4**. For the C2 sample, the volume fraction of amorphous phase (f_{amor}) was determined to be 76.5 ± 5%. Meanwhile, the value of f_{amor} is about 98± 5% and the amorphous phase only exists around the outside surface of the C3 rod, where the cooling rate is relatively high.

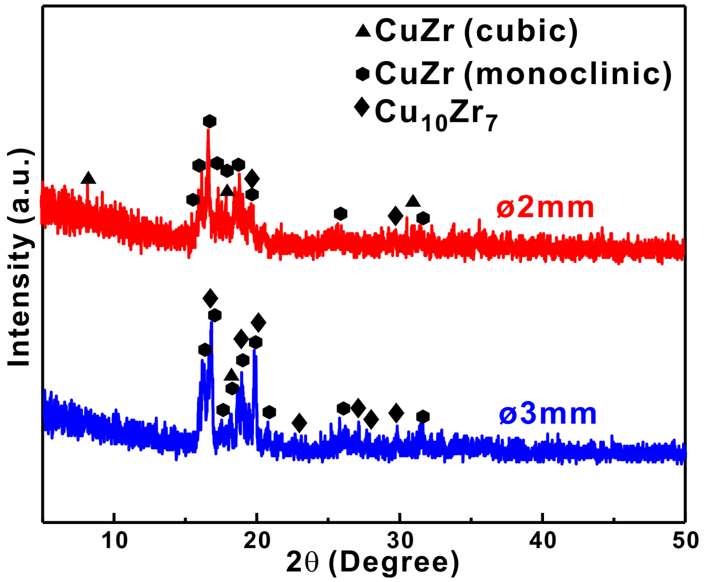

Figure 7.10 *XRD patterns of the as-cast $Cu_{50}Zr_{50}$ rods with diameters of 2 mm (C2) and 3 mm (C3).*

Fig. 7.11 shows the low-temperature DSC results of the C2 and C3 samples. All samples were cooled to 223 K, and then heated to 673 K below T_g. As shown in Fig. 7.11a, the C2 sample processes a reverse MT during heating to 673 K before T_g, and experiences the MT during cooling. Compared with the transformation temperatures of the full crystalline $Cu_{50}Zr_{50}$ sample in **Section**

7.2, the values of M_s of the C2 and C3 samples decrease to 424 ± 5 K and 435 ± 10 K, respectively (Figs. 7.11a-b).

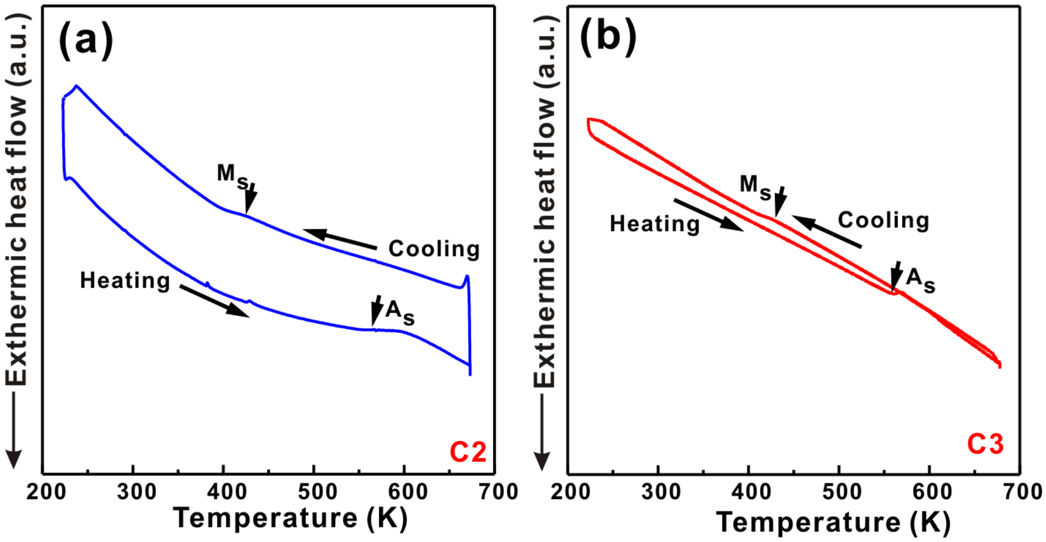

Figure 7.11 *The low-temperature DSC curves of the as-cast* $Cu_{50}Zr_{50}$ *rods with diameters of (a) 2 mm and (b) 3 mm.*

Based on the microstructural characteristics of these samples, several structural factors need to be considered: (1) the internal stress from quenching, (2) the precipitation of LT-EPs, such as $Cu_{10}Zr_7$, (3) the sizes of the martensitic crystals, and (4) the existence of amorphous phase. During the cooling process, large residual stresses are induced [281, 473], which will change the stress field and thereby facilitate the formation of preferred martensitic variants during cooling process. Secondly, pre-existing precipitates can reduce the mean free path for dislocation glide so that martensite prefers to nucleate around pre-existing precipitates [473]. With the precipitation of other LT-EPs, the composition of martensites may be also changed [474], which will result in the change of MT temperature. Thirdly, the grain sizes of martensites decrease with the applied cooling rate increasing [475, 476]. Thus, the value of M_s decreases with grain size decreasing because grain boundaries are believed to strengthen the parent phases [475, 476].

Furthermore, it has been shown that the AT is related to the positive volume effect and the MT is connected with a negative volume effect [295, 298, 326]. Therefore, the amorphous phase may restrict or impede the volume changes from the AT and MT during heating and cooling, respectively [295, 298, 302].

However, for the $Cu_{50}Zr_{50}$ alloy, four different phases exist in the samples. Therefore, it is necessary to remove the effect from the other LT-EPs and other factors [280, 281, 295, 431-435] in order to illustrate the effect of the amorphous phase on MT behavior.

7.3.2 Martensitic transformation in the as-cast Cu-Zr-Al alloys

The as-cast $Cu_{47.5}Zr_{47.5}Al_5$ alloy was chosen to investigate its MT temperature in more depth because the casting conditions can be adjusted this way that mainly the B2 CuZr phase and the amorphous phase precipitate (See **Chapters 4** and **5**). One sample was cut from an as-cast plate with a thickness of 2 mm, which is termed as A5-1. The XRD patterns of Fig. 7.12 show that this sample mainly consists of B2 crystals and amorphous phase next to a relatively small volume fraction of martensite. The amorphous volume fraction, f_{amor}, of the A5-1 sample was calculated to be 57 ± 5 vol.% based on the ratio of the crystallization enthalpies extracted from the A5-1 sample and the corresponding BMG rod (not shown here).

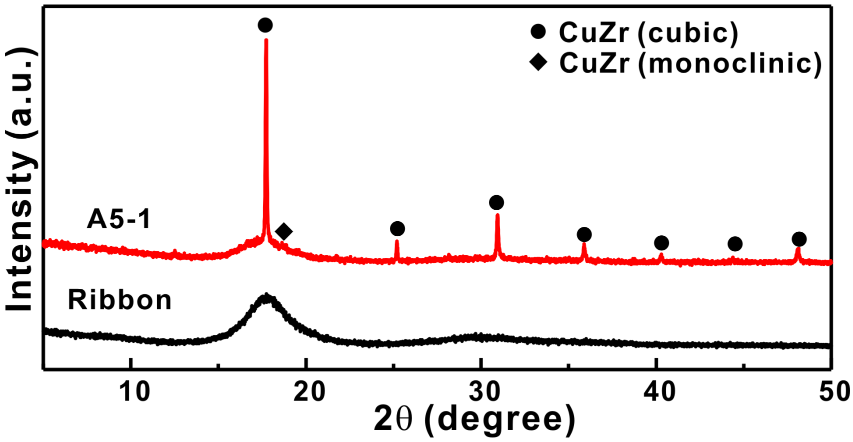

Figure 7.12 *XRD patterns of the $Cu_{50}Zr_{42.5}Ti_{7.5}$ ribbon and the A5-1 samples.*

In order to assess the MT in the crystals of the BMG matrix composite precisely, the resistance of the material was measured as a function of temperature. This approach is expected to yield additional information to the more conventional approach of heating the sample in a calorimeter, and then was applied here. Another advantage is the accessibility of temperatures close to 0 K. Furthermore, the corresponding fully amorphous ribbon was also measured for comparison (7.13). The resistance of the glass monotonously decreases with increasing temperature (Fig. 7.13), which is a typical behavior of MGs at temperatures below T_g [477-479].

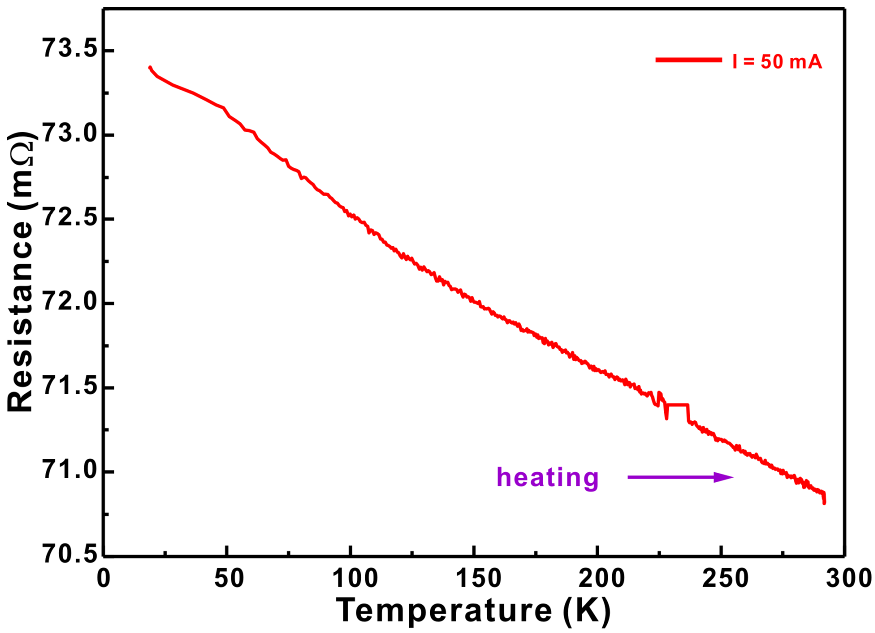

Figure 7.13 *Resistance of the* $Cu_{50}Zr_{42.5}Ti_{7.5}$ *fully amorphous ribbon.*

In order to guarantee the accuracy of the measurements for the A5-1 sample, different currents were applied during the measurements as shown in Fig. 7.14a, namely 1m A, 10 mA, 50 mA and 100 mA. As the B2 CuZr phase (austenitic phase) is embedded in the glassy matrix for the A5-1 sample, it is believed that the MT temperature is lower than room temperature [280, 281].

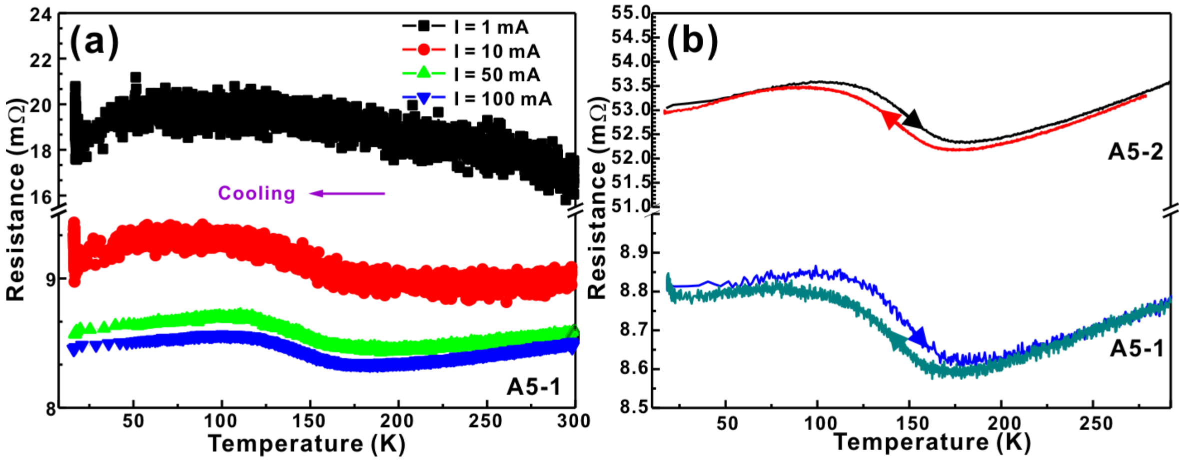

Figure 7.14 *Resistance of (a) the A5-1 sample during cooling under different currents, and of (b) the the A5-1 and A5-2 samplles under a current of 50 mA.*

As shown in Fig. 7.14a, the resistance of the composites is considerably smaller and depends on the currents. It is largest for the smallest current of 1 mA.

Not just the resistance becomes smaller with increasing current but also the scattering of the data (Fig. 7.14a). An accurate resistance is difficult to be obtained using such low currents. In contrast, at currents of 10 mA, 50 mA and 100 mA, the shape of the signal changes and one can see that the resistance upon cooling first decreases, goes through a minimum just to increase again at temperatures between 170 – 80 K. At temperatures below 80 K, the resistance decreases linearly again. In contrast, between 100 K and 250 K the resistance of MGs changes linearly and therefore the behavior of the composite must be caused by the crystalline phase. The change in its resistance could be caused by the MT in the crystalline phase.

If the MT indeed takes place in the A5-1 sample during cooling, the sample is expected to display a similar change in its resistance upon heating due to the occurrence of the AT. Therefore, the resistance of the A5-1 sample was also measured during heating, which is shown in Fig. 7.14b. It was found that the resistance of the A5-1 sample upon heating first increases to temperatures of about 100 K, goes through a maximum just to decrease at temperatures between 100 – 173 K. At temperatures above 173 K, the resistance decreases linearly again. Both of these asynchronous phase transformations during heating and cooling result in a transformation hysteresis in the curves (Fig. 7.14b). Furthermore, another A5-2 sample containing a smiliar content of the B2 CuZr phase was also measured and shows a similar change in its resistance during heating and cooling. All in all, these facts confirm the occurrences of MT upon cooling and AT upon heating.

Hence, the values of A_s and M_s can be estimated to be 118 ± 5 K and 168 ± 5 K, respectively, which is much lower that the crystalline $Cu_{47.5}Zr_{47.5}Al_5$ shape memory alloy (i.e. 321 ± 5 K) [302]. Previous results [475, 480-485] indicate that the grain size and the amorphous interface may have a large influence on the change of the MT temperature. During the transformation, martensite nucleates around the neighboring grains and the martensitic plates interact with the grain boundaries [480, 481, 483]. In our case, compared with these in the fully crystalline alloys, the grain size of the B2 CuZr phase in the A5-1 sample is finer due to the higher coolig rate during suction casting (see Fig.4.10 in **Chapter 4**) and then more grain boundaries may be induced. Wehn the grain boundaries become more, the local elastic energy is expected to be induced and then the nucleation sites for new martensitic plates may increase [480, 481, 483]. On the other hand, the amorphous interface plays a similar role on the MT, which induces a higher surface/volume ratio, minimizes the transformation strain and energies [475, 482, 484, 485], and consequently results in the decrease of A_s and M_s.

7.4 Conclusions

In this chapter, the electronic structures of the B2 CuZr phase, B19' and Cm in $Cu_{50}Zr_{50}$ binary alloy, which are connected with the MT. The minor elements on the MT behavior of $Cu_{50}Zr_{50}$ binary alloy were observed. With the content of Ti increasing, the A_s and M_s gradually decrease. Meanwhile, with the thermal cycling increasing, the A_s and M_s gradually shift to a lower temperature due to the incomplete of MT during heating and the instability of the B2 CuZr phase. The MT behavior of all the studied alloys can be evaluated by the value of c_v, i.e. the electronic structures. The samples with different element addition such as Ni, Co, Cr, Ag, Al, Ti, Ta, or Hf, the values of c_v for CuZr-based alloys show a different change trend, which may be due to the larger atomic radii of Ti, Ta, and Hf. The change of the lattice parameters of the parent phase may result in the difference of their electronic structures. Furthermore, the MT behavior of CuZr-based BMG composites was investigated. It can be seen that after quenching, with the addition of the amorphous phase, the value of M_s decreases to lower temperatures.

8 Shear banding process of CuZr-based BMG composites

Shear banding usually dominates the deformation process of BMGs under uniaxial, quasistatic loading at room temperature [126, 159, 486]. However, for CuZr-based BMG composites, as the ductile B2 CuZr phase is introduced into the glassy matrix, multiple shear bands are induced during deformation [295, 326, 331, 333, 340], which leads to a serrated flow behavior under compressive conditions [135]. It has been demonstrated in **Chapter 5** that when different volume fractions of the B2 CuZr phase precipitate in the glassy matrix, the shear banding process has a large influence on the plastic deformation. However, it is difficult to quantitatively describe the distribution of shear bands due to the stochastic formation and the fast propagation speed of the shear bands [146, 487-492]. Usually, the propagation and arresting of shear bands result in different stress drops in the compressive curves and then a serrated flow behavior is found in the plastic deformation for BMGs [146, 487-492]. The serrated flow behavior and the origin of serrations in BMGs have been investigated [146, 487-492], and a statistic analysis and dynamic analysis can be used to characterize the shear banding process [146, 487-492]. In this chapter, the shear banding process and the corresponding serrated flow behavior of CuZr-based BMGs and their composites are investigated in order to reveal the potential physical deformation mechanisms.

8.1 Serrated flow in CuZr-based BMG composites

The yielding and plastic deformations have been observed based on the TEM, SEM, and XRD observations presented in **Chapter 5**. Here, the compressive curves of the $Cu_{47.5}Zr_{47.5}Al_5$ BMG and its composites were used to check their shear banding process. Even though a few martensitic crystals were also found in the glassy matrix except the B2 phase, the overall deformation behavior of these composites is not strongly affected by a minor amount of martensites due to their limited ductility and strength [353]. As shown in Fig. 8.1, the serration events in the time-stress curves for $Cu_{47.5}Zr_{47.5}Al_5$ BMG (S0) and its composites (S1, S2, S3, and S4) with different contents of amorphous phase were observed. Firstly, the serration events were observed in the time-stress curves for the S0 sample (Fig. 8.1a). As the content of the B2 CuZr phase is introduced into the glassy matrix, the number and stress oscillations of the serration events become more and obvious, respectively. Their amplitudes become smaller (Figs. 8.1b-d). When the content of the B2 CuZr phase increases to about 22 vol.% (S2 sample), it is difficult to observe the serration events.

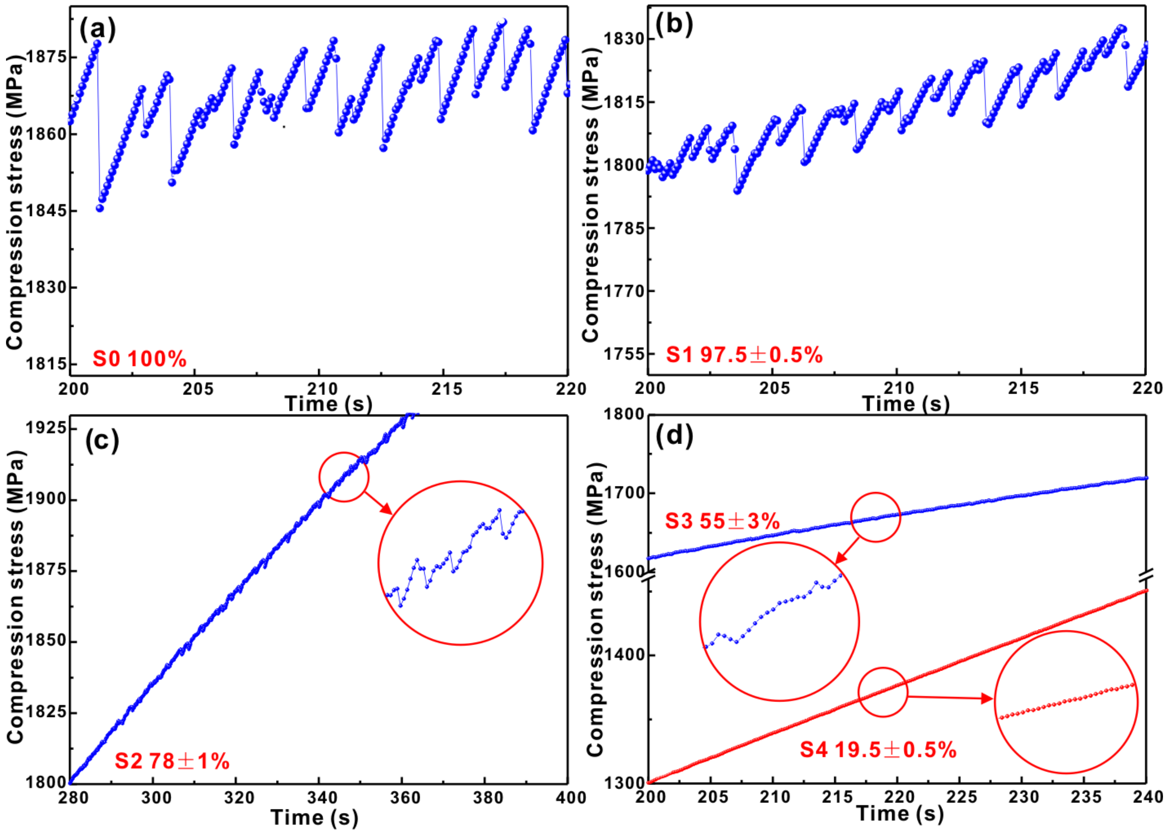

Figure 8.1 *The serrated flows vs. the time of the (a) BMG (S0) and the (b) S1, (c) S2, and (d) S3 and S4 samples with different f_{amor} (Insets: $N(\Delta\sigma_s)$ vs. the time and magnified serrations).*

In order to illustrate the serration events of these samples, the magnified serrated flows of different samples are shown in the insets in Figs. 8.1c-d. The serration events still exist but their intensity becomes weaker. Based on **Chapter 5**, with the content of the B2 CuZr phase increasing, the deformation mechanisms change from a shear banding process reflected by the serration events to a process dominated by the MT, resulting in the decrease of the serration events in the compressive curves with the content of the B2 phase increasing. However, the correlation between the shear banding and the serration events were only investigated in BMGs but not in BMG composites [146, 487-492]. By observing the serration flow in BMGs and the microstructural evolution associated with the fracture surface [493, 494], it was found that the serrated flow consists of two stages, which corresponds to the progressive sliding on the shear plane and a fast shear-off of the test sample. Nevertheless, prior to investigating the shear banding process in CuZr-based BMG composites, it is necessary to illustrate the serration flow for CuZr-based BMGs during deformation, which will be introduced and analyzed in the following section.

8.2 Statistical analysis of the serrations for brittle and ductile BMGs

Recently, statistical deformation analysis [146, 489, 490, 494-499] has been used to better understand the microscopic inhomogeneous deformation behavior of crystalline metals. It was found [146, 489, 490, 495-499] that the dislocation motions during the plastic deformation process for metallic crystalline solids are characterized by scale-free and intermittent avalanches, which follows a self-organized criticality. Recently, Wang *et al.* [146, 487, 489, 500, 501] have found that as the microcrystal size decreases to zero, i.e. a glassy state, the plastic flow also follows this scale-free, intermittent behavior during the plastic deformation of BMGs. By counting the numbers of stress drops $N(\Delta\sigma_S)$ with a given stress amplitude ($\Delta\sigma_S$) for the serration events during the plastic deformation, serration events for different BMGs exhibit a self-organized critical behavior or a chaotic behavior, respectively [146, 487, 489, 500, 501].

As shown in Fig. 8.2, each serrated flow behavior consists of two main deformation processes, i.e. a sudden stress drop and subsequent elastic reloading [146, 487, 489]. Based on these characteristics, the corresponding stress drop as a function of time can be obtained by statistical analysis. The compressive curve of the S0 sample was used to clarify the whole statistical theory associated with the serration flow behavior [146, 489, 502]. Each stress drop has an onset time (t_1) and an ending time (t_2), and the difference between both of these times is equal to Δt_s described in Fig. 8.2a. The value of the stress drop amplitude ($\Delta\sigma_S$) is taken as the difference between the maximum and the minimum of each serration event (Fig. 8.2a) [146, 489, 502].

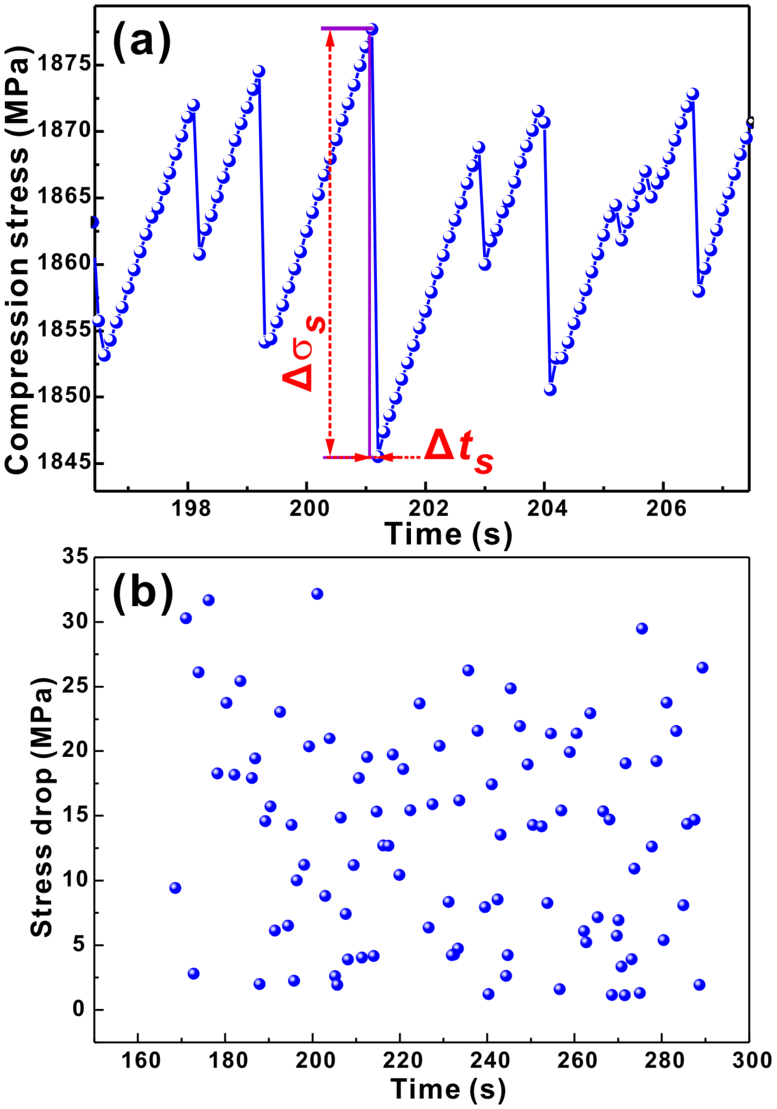

Figure 8.2 *(a) The amplifying stress-time curves, and (b) the correlation between the stress drop ($\Delta\sigma_s$) and the corresponding time (t) for the S0 sample.*

Hence, the increase of the stress drop amplitude with the corresponding time was calculated (Fig. 8.2b). It has been found [146, 489] that the serration size (i.e. the stress drop amplitude ($\Delta\sigma_s$)) which depends on the strain and time usually results in a systematic shift of the serration amplitude. Therefore, it is necessary to normalize the stress drop magnitude before statistical analysis. Firstly, the stress drop *vs*. time diagram was fitted using a linear regression and the equation of $\overline{\Delta\sigma_s} = f(t)$ was obtained [146, 489, 490]. Secondly, the stress drop amplitude can be calculated based on a relation of $\Delta\sigma_s/(f(t)/f(t_0))$, where $f(t_0)$ is the fitted value at the starting time of statistic t_0 [146, 489]. However, for the present samples, no obvious systematic shift of serration amplitudes can be observed

(Fig. 8.2). The linear regression fit was not used to normalize the serration amplitude [146, 489, 490].

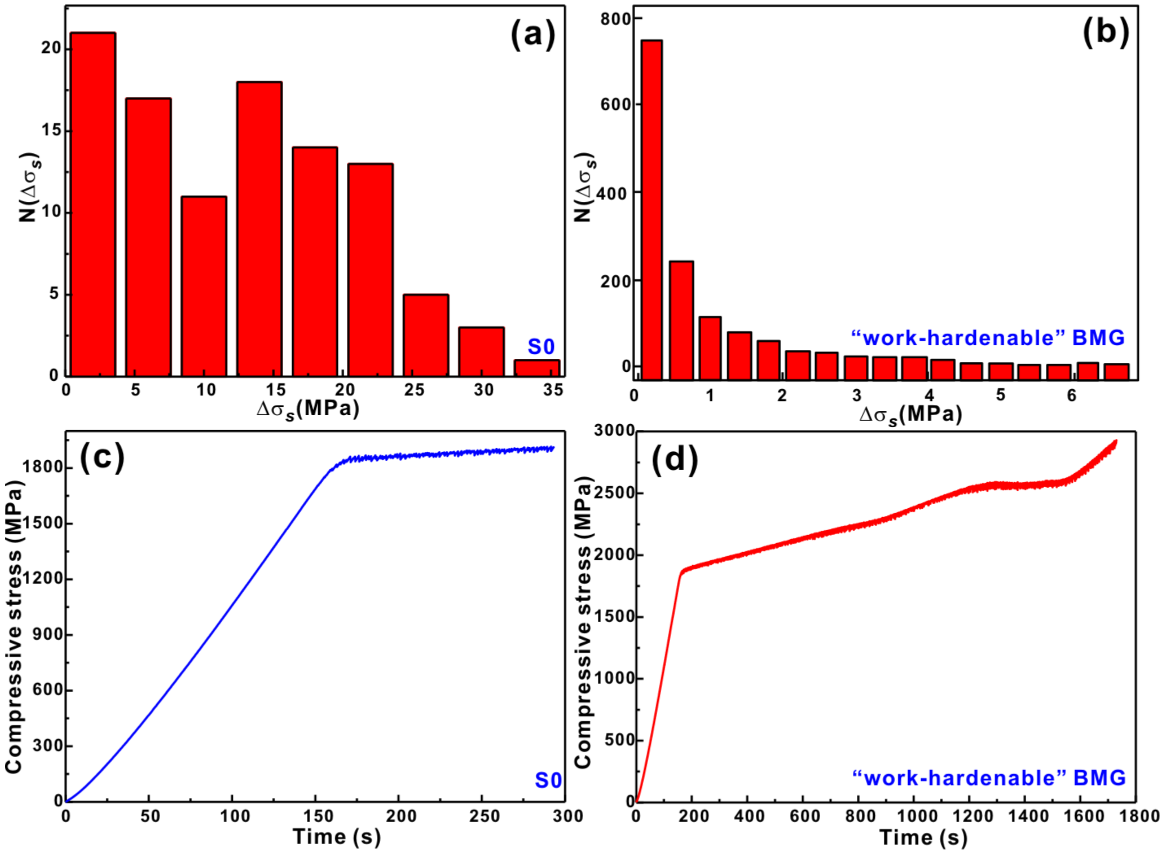

Figure 8.3 *The distribution histograms of the stress drops for (a) the relatively brittle* $Cu_{47.5}Zr_{47.5}Al_5$ *BMG and (b) the "work-hardenable" BMG, and the compressive stress vs. time for (c) the S0 and (d) the "work hardenable" BMG. Fig. 8.3b was taken from Ref. [489].*

In order to investigate the distribution of the different stress drops during the plastic deformation of the S0 sample, only the serrations in the stable plastic regime were chosen due to the following reasons: (1) the serrations in the initial plastic deformation mainly arise from the formation of highly localized shear bands [500], and (2) the operation of the dominant shear bands results in a stable plastic regime [146, 487, 489]. Nevertheless, the distribution histograms of the stress drops for the $Cu_{47.5}Zr_{47.5}Al_5$ BMGs samples were calculated, respectively, based on the statistical method shown in Figs. 8.3a-b. Two different serrated flow behaviors (e.g. S0, and "work-hardenable" BMG) can be observed. The distribution histogram of the stress drops for the S0 sample shows a peak shape with most stress drops concentrating in a range of 10 MPa < $\Delta\sigma_s$ < 25 MPa (Fig. 8.3a), implying that the serration size for this sample has a characteristic length scale [489, 500, 503]. The distribution of stress drops has been observed in metallic crystalline alloys, which was also applied into the description of the serrated flow behavior of BMGs [489, 500, 503]. It has been demonstrated that the serrated flow in S0 sample follows a chaotic stick-slip dynamics [489]. According to Sun's results [146, 489], these BMGs shear along a main shear banding plane during the plastic deformation, which usually results in the small plasticity of BMGs (Fig. 8.3c).

However, it also has been shown that the serration events for the more ductile BMGs become more complex [146, 489], and the corresponding distribution histogram of the "work-hardenable" ductile $Cu_{47.5}Zr_{47.5}Al_5$ BMG exhibits an exponentially decreasing distribution (Fig. 8.3b). Usually for these ductile BMGs (Fig. 8.3d), the operation of multiple shear bands is induced during one serration and then the multiple shear banding process dominates the whole plastic deformation [146, 489]. Actually, a decreasing distribution of the serration events for the ductile BMGs can be described by a power-law rules [146, 489]: $P(>\Delta\sigma_{s}^{-\alpha})$, where P is the cumulative probability distribution and α is the power-law relation an exponent. For the "work-hardenable" $Cu_{47.5}Zr_{47.5}Al_5$ BMG [238, 489], the value of α is about 1.49 [146, 489], implying that the plastic deformation of this ductile BMG indeed displays a self-organized critical state during the plastic deformation, and then the interacting shear bands dominate the whole plastic deformation.

Furthermore, as shown in Figs. 8.3c-d, the S0 sample shows a little plasticity, while a large plasticity with obvious "work hardening" are observed for the "work-hardenable" $Cu_{47.5}Zr_{47.5}Al_5$ BMG. It is worth noting that for the $Cu_{47.5}Zr_{47.5}Al_5$ BMGs (e.g. S0, and "work-hardenable" BMG) shown in Figs. 8.3c-d, which were fabricated under different casting conditions. Different casting conditions for an individual alloy can result in different internal states of BMGs and then induce different ductility [232, 334], which has been proven in $Zr_{56}Co_{28}Al_{16}$ alloy [504]. In our case, it was found that when microstructural heterogeneities exist in the glassy matrix, multiple shear bands can be induced and then a large plasticity for BMG samples can be obtained during the compressive test [504]. Therefore, in our case, it is reasonable to believe that the S0 sample is more homogenous than the "work-hardenable" BMG, which results in different plasticity of $Cu_{47.5}Zr_{47.5}Al_5$ BMGs. In fact, previous observations [428] have shown that the microstructure of the $Cu_{47.5}Zr_{47.5}Al_5$ BMGs with less ductility is homogeneous [238, 505], and no obvious nano-scaled structural inhomogeneities can be observed. However, the "work-hardenable" $Cu_{47.5}Zr_{47.5}Al_5$ BMG consists of an amount of nano crystals [238, 505]. For these alloys containing nano crystals, even a little tensile plasticity is achieved, which can be attributed to the transformation from nanocrystalline phase to nano twins, and the further nucleation and growth of the nanocrystalline crystals [136]. Furthermore, the multiple shear bands start to dominate the plastic deformation for the ductile samples [504], corresponding well with previous and our statistical results [135, 146, 487, 489].

Therefore, it can be concluded that the fundamental dynamics of the serration flow of $Cu_{47.5}Zr_{47.5}Al_5$ BMGs can be changed from chaotic dynamics to self-organized critical dynamics as nano-scaled structural heterogeneities are introduced into the glassy matrix. Therefore, the shear-band motions in ductile BMGs are in a scale-free, intermittent fashion so that the alloys show a stable plastic deformation for ductile BMGs.

8.3 Different statistical results of the serration events for CuZr-based BMG composites during deformation

As the scale of the structural heterogeneities increases from nano-scaled to micro-scaled, i.e. from the nanocrystals to the micrometer-sized ductile B2 CuZr crystals, the serration dynamics of the CuZr-based BMG composites is also changed. As shown in Figs. 8.4a-b, the stress drop ($\Delta\sigma_s$) and the corresponding time for the S1 and S2 BMG composites with different contents of the B2 CuZr phase (i.e. 97.5 ± 0.5 vol.% and 78 ± 1 vol.%, respectively) were calculated from their compressive stress-time curves. The corresponding distribution histograms of the stress drops for the S1 and S2 samples were also calculated (Figs. 8.4c-d), both of which display a decreasing distribution, being similar with these for ductile BMGs [146, 489, 490] mentioned above.

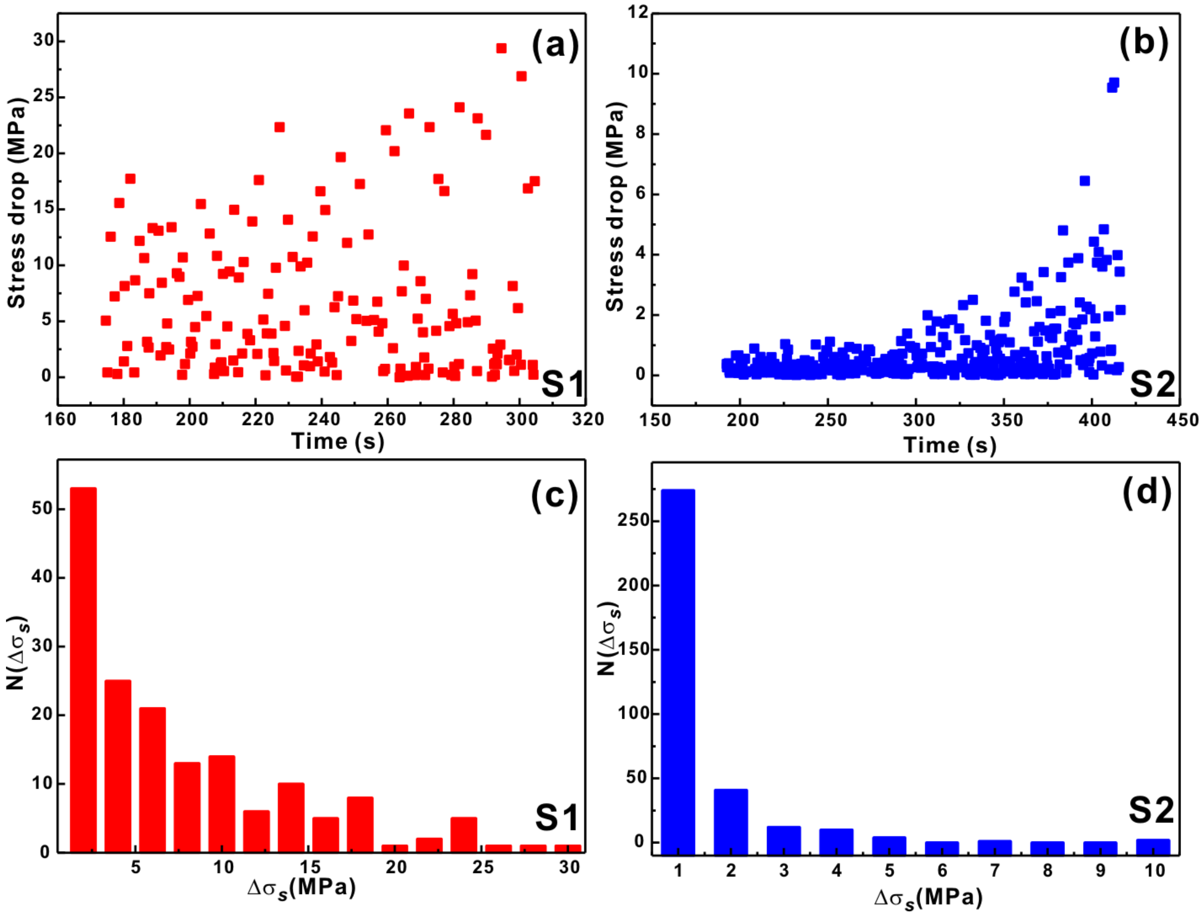

Figure 8.4 *The stress drop ($\Delta\sigma_S$) and the corresponding time for the (a) S1 and (b) S2 samples, and the distribution histograms of the stress drops for the (a) S1 and (b) S2 samples with different contents of the B2 CuZr phase.*

Therefore, the correlations between the cumulative probability distribution for the stress drop amplitude for the S1 and S2 samples were calculated as shown in Fig. 8.5, respectively, which also follow a power-law rule. These results imply that the shear banding process in CuZr-based BMG composites also displays a self-organized critical behavior and the effect of the shear-band interaction on the dynamics behavior during the plastic deformation needs to be considered. Multiple shear bands can be found on the side surface for the deformed S1 and S2 samples (Fig. 6.10 in **Chapter 6**), which further confirms our analysis. Recently, Sun *et al.* [146, 489] have proposed a simple model to explain this complex shear banding process based on the stress redistribution induced by each sliding shear band and the interactions from other pre-existing and operating shear bands, and have demonstrated that the sliding events in different serration events occur in a cooperative way.

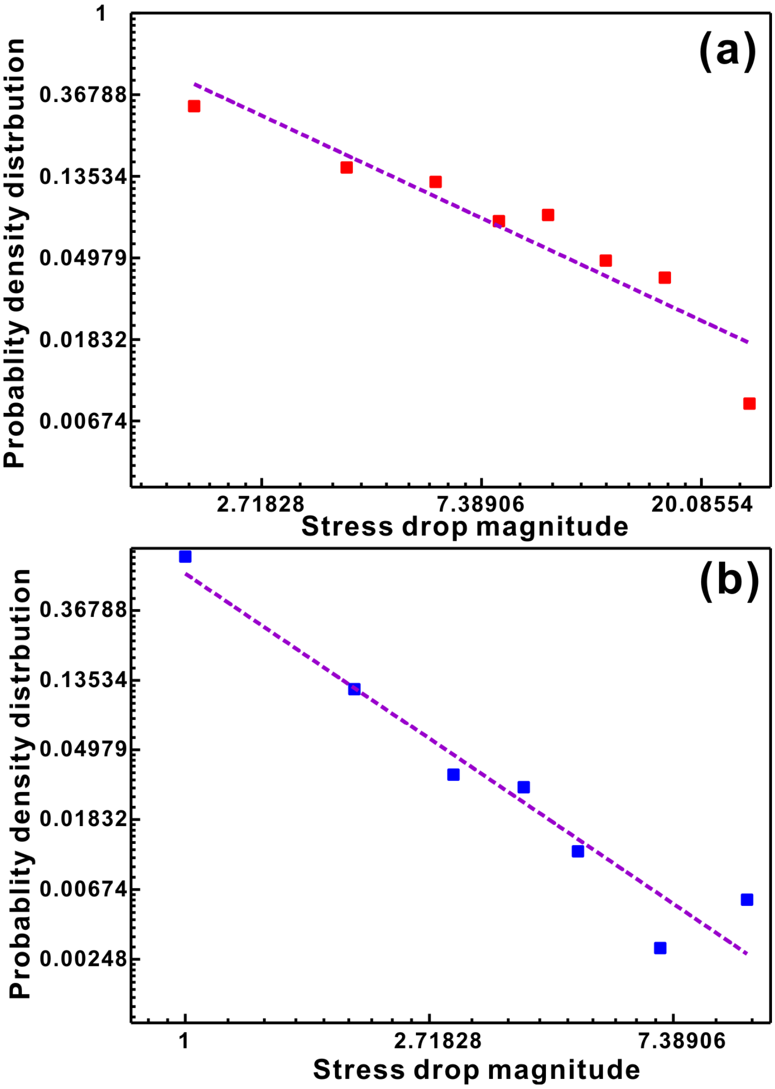

Figure 8.5 *Log-log plot of the cumulative probability density distribution vs. the stress drop magnitude for the (a) S1 and (b) S2 samples, which were fitted by a power-law scaling.*

For the CuZr-based BMG composites (e.g. S1, S2, S3, and S4 samples), with the volume fraction of B2 CuZr phase increasing, more shear bands can be induced (see **Chapter 6**). The primary shear bands are prone to form, which results in the occurrence of the small sliding events with an increasing number during the stable deformation stage. These small sliding events can effectively resolve the larger sliding events, which confirm the observations of smaller serration events in the compressive curves for the S3 and S4 samples with higher volume fractions of the B2 CuZr phase (Fig. 8.1d).

On the other hand, apart from the formation of multiple shear bands, the deformation is also affected by the phase transformation within the B2 CuZr phase (i.e. MT and detwinning), which is a first order, diffusionless, shear solid state structural changes [280, 281]. During the MT, the atoms rearrange through a shear process of the unit cell, resulting in the formation of large coherency strains in the lattice as the new crystalline phase forms [280, 281, 506]. As the phase transformation proceeds, partial elastic energy is accumulated and then dissipated [506]. The phase transformation is also controlled by heterogeneous micro-scaled dynamics [280, 281, 506], which has been proven using acoustic emissions, and electrical resistivity, and X-ray scattering transient [506-519]. Their kinetics is mainly controlled by discrete avalanches [506-519]. The spatial sizes of the avalanches change widely, and the distribution of the avalanche amplitudes also follows the power-law distribution with an exponent of about 1.7 for the cobalt-based shape memory alloys [506]. That suggests that the MT self-organizes into a critical state in order to release large coherency strains through the discrete but interacted avalanche motions. Therefore, when the MT and shear banding control the plastic deformation of the CuZr-based BMG composites, different avalanches with different scales are induced during deformation, i.e. the sliding motions of a single interface or the interfaces in different places of the crystal and the avalanches dominated from sliding motions of multiple shear bands [506-519].

8.4 Energy criteria for serrations in CuZr-based BMG and their composites

Disparate events, such as earthquakes, MTs, granular flow, movement of ferromagnetic domain walls, deformation of volcanic rocks, and serrated flow in some metallic crystalline alloys, have been proven to show a self-organized criticality [520-524]. The formation of avalanches leads to the irreversible release of the elastic energy in these systems [506-524]. Recently, Wang *et al.* [487] investigated the dissipated energy during shear banding process for ductile BMGs during plastic deformation. During deformation, the elastic energy is stored in the MG sample and testing machine system until the deformed sample achieves a critical point [492, 525, 526], i.e. the formation of shear bands.

The intermittent movement of shear bands in MGs during plastic deformation is reflected as a sequence of serration events, i.e. the increase and decrease of the local stress. Each serration event consists of the accumulation and the release of the elastic energy [487, 527], and the corresponding elastic energy density of each serration event, $\Delta\delta$, can be calculated by $\Delta\delta = \Delta\sigma\Delta\varepsilon/2$, where $\Delta\sigma$ and $\Delta\varepsilon$ are the elastic stress and strain in one serration event, respectively. When the elastic energy of the serration events mainly activates the local flow events in glassy metals (i.e. shear transformation zones (STZs), see **Section 1.4.1**), the elastic energy of serration events is consumed by the configurational hopping of STZs [152, 159, 166, 487, 527, 528]. The amount of the transformed STZs in one serration event can be calculated to be $\Delta\delta/W$, where W is the activation barrier for one STZ configurationally hopping between two stable states (Fig. 1.14c in **Chapter 1**) [152, 159, 166, 487, 527, 528]. Thus, the amount of the transformed STZs involved in a serration event reflects the volume of shear bands formed in one serration event. Thus the formation and propagation of shear bands, i.e. the serration flow, result in the relaxation of the partial elastic strain in the sample and the increase in the volume free energy between the shear bands and glassy matrix [492, 525, 526]. Simultaneously, the newly-generated interfaces between the shear bands and glassy matrix induce an additional interfacial free energy [529]. Therefore, for the monolithic BMG samples, the released elastic energy stored in a sample-machine system during the plastic deformation is mainly consumed by the initiation and the propagation of shear bands during deformation [146, 334, 487, 489]. Therefore, the elastic energy stored ($|\Delta G_E|$) for the BMGs during the stable plastic stage consists of the increase in the volume free energy ($|\Delta G_v|$) and the newly-generated interfacial free energy ($|\Delta G_I|$), and/or the dissipated energy in the form of heat within shear bands ($|\Delta G_h|$), which can be given as follows [525, 526, 530-533]:

$$|\Delta G_E| = |\Delta G_v| + |\Delta G_I| + |\Delta G_h|. \tag{8.1}$$

However, for the same sample-machine system, the dissipation of the stored energy during the stable plastic deformation could be affected by the introduction of nano- or micro-scaled structural inhomogeneities into the glassy matrix. For CuZr-based alloy systems, the phase transformation, i.e. the transformation of nanocrystals into nanotwins or the MT, may also consume partial $|\Delta G_E|$ in the form of heat and the newly-generated interfacial free energy and so on during phase transformation [280, 281, 534, 535]. Therefore, the elastic energy stored ($\left|\Delta G_E\right|$) for the CuZr-based BMG composites during the stable plastic deformation can be given by:

$$\left|\Delta G_E\right| = \left|\Delta G_v\right| + \left|\Delta G_I\right| + \left|\Delta G_h\right| + \left|\Delta G_P\right|, \tag{8.2}$$

where $\left|\Delta G_P\right|$ is the release of partial energy taken from the $\left|\Delta G_E\right|$ through the phase transformation. As the phase transformation becomes more pronounced before the initiation and propagation of shear bands, the dissipated energy can lead to a decrease of the total elastic energy density of serration events. Therefore, the plastic deformation of CuZr-based BMG composites is different to that of monolithic CuZr-based BMGs.

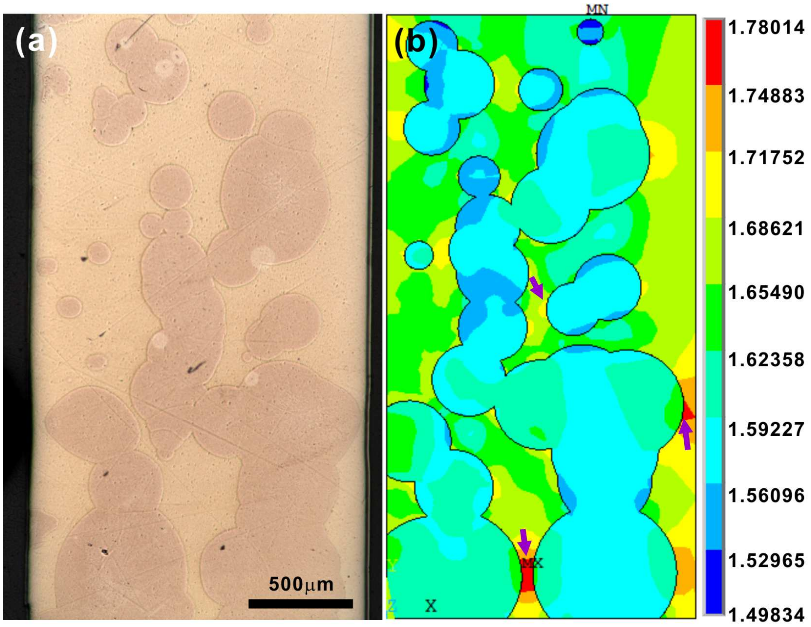

Figure 8.7 *(a) Distribution of crystals in the glassy matrix, and (b) stress concentrations at the interface between the glassy matrix and the crystals for CuZr-based BMG composites. The sites of maximum stresses are marked by arrows. The generation of shear bands is expected to begin here.*

During deformation of the CuZr-based BMG composites shear bands tend to initiate at the interface between the glassy matrix and the crystals due to the high interfacial energy and large stress concentrations at the interface [214, 534, 536-540]. These stress concentrations at the interface were simulated for the present CuZr-based BMG composites by finite element analysis (Fig. 8.7). A CuZr-based BMG composite in the elastic regime (at a strain of 1.9%) was chosen a stage just before the formation of shear bands commences. The distribution of the B2 CuZr phase along the length of a rod as seen in an optical microscope is shown in Fig. 8.7a. It can be seen that relatively high stresses can emerge at the interface between the glassy matrix and the crystals (see arrows in Fig. 8.7b).

Therefore, primary shear band preferentially form at the interface between the crystals and the glassy matrix. However, based on the conservation of energy for the same sample-machine system, less elastic energy is consumed in each shear banding event. The shear bands n the composites cannot extend to values possible in the monolithic BMGs where they are free to traverse the entire cross section without any obstacles. Therefore, for the ductile-phase reinforced CuZr-based BMG composites, shear banding gradually progresses in a more stable way. Hence, with the f_{cryst} increasing, the mean free path of the shear bands is reduced and the shear offset generated by each shear event is decreased, and then their dynamics is reflected by serrations in the respective stress-strain curves [130, 147, 487, 531]. These facts facilitate the formation of multiple shear bands but impede their rapid propagation. Nevertheless, combined with the serration analysis during deformation for CuZr-based BMG composites, the introduction of the B2 CuZr phase into the glassy matrix can redistribute the stress concentration and the dissipation of the elastic energy during the plastic deformation, resulting in the multiplication of shear bands.

8.5 Conclusions

In this chapter, the shear banding process of CuZr-based BMGs and their composites was analyzed during the plastic deformation. As the nano-scaled microstructural inhomogeneities are present in the glassy matrix, the ductility of CuZr-based BMGs can be changed. The shear banding process is dominated from one main shear banding process to a multiple shear banding process, which results in different serrated flow characteristics. Based on the statistical analysis of the serration events of two different CuZr-based BMGs, a serrated flow transition from a chaotic behavior to a self-organized critical state occurs with the introduction of the nano scaled microstructural inhomogeneities.

When the nano-scaled microstructural inhomogeneities increase to the micro-scaled B2 CuZr phase, the serrated flow during the plastic deformation become more stable compared with the corresponding BMGs, and also follows a power-law rule. The accumulation and the release of the partial elastic energy in the sample-machine system during the plastic deformation were investigated, which shows that the microstructural inhomogeneities can effectively induce the formation of primary shear band and the sequent multiplication of shear bands.

9 Summary and Outlook

In the present work, 36 CuZr-based metastable alloys were used to investigate the eutectoid B2 CuZr transformation at high temperature using thermal analysis methods, which has been proven to have relations with the thermal stability of the B2 CuZr phase. With different element additions, this phase transformation peak(s) can shift to low or high temperatures, and then all the CuZr-based alloys were separated into three different types. Based on competition among the amorphous phase, the B2 CuZr phase and other room-temperature stable crystalline phase, a new prediction ***K***-parameter is suggested to select a compositional region of differently sized CuZr-based BMG composites. Based on the prediction results, differently sized CuZr-based BMG composites were successfully fabricated. The formation and microstructures of these BMG composites were investigated in Cu-Zr-Co, $Cu_{50}Zr_{50}$, Cu-Zr-Al, Cu-Zr-Ag, Cu-Zr-Ti, Cu-Zr-Al-Y, and Cu-Zr-Al-Er alloy systems.

Furthermore, different methods or strategies were developed to control the distribution, size, and volume fraction of the B2 CuZr phase in CuZr-based BMG composites: (1) Changing the melting temperature or melting current/time; (2) Adjusting the cooling rate; (3) *Ex situ* introducing the foreign nucleation sites; and (4) Using the flash heating and cooling method.

In order to further illustrate the deformation mechanism of CuZr-based BMG composites, $Cu_{47.5}Zr_{47.5}Al_5$ BMG and its composites were selected. It was found that different yielding and plastic behaviors of the metastable CuZr-based alloys were changed with the f_{cryst} increasing, which can be attributed to the competitions among the MT, and/or the formation of multiple shear bands, and/or partial detwinning together with dislocations with a high density, leading to a single-to-“double”-to-“triple”-to-double” yielding transition and different plastic deformations.

In virtue of the importance to the MT to the deformation of CuZr-based BMG composites, the correlation among the special electronic structures of the B2 CuZr phase, B19’ and Cm in the $Cu_{50}Zr_{50}$ binary alloy were investigated. Furthermore, with minor elements being introduced into the $Cu_{50}Zr_{50}$ binary alloy, the change of MT temperatures was detected in different CuZr-based alloys.

Based our observation and previous results, it was found to be roughly evaluated by the value of c_v and the size factors induced by the adding elements.

Another important factor associated with the deformation behavior of CuZr-based BMG composites, i.e. the shear banding process, were also investigated. It was found that the elastic energy stored in the system is redistributed with the introduction of different microstructural inhomogeneities into the glassy matrix. The shear banding process is gradually dominated from a chaotic behavior to a self-organized critical behavior of shear avalanches. However, even though the present work shows certain understanding on the formation and deformation of CuZr-based BMG composites, lots of work is need to be done in the future. In our opinions, there are several questions opened for us:

(1) The methods to control the formation of the B2 CuZr in CuZr-based BMG composites should be further modified. For the addition of TaW particles during casting, the whole milling and casting process should be further refined. More work should be also done to improve the flash annealing method.

(2) The tensile experiments for the ductile CuZr-based BMG composites need to be finished. The symmetry between the compressive and tensile results should be further discussed. Furthermore, the correlation between the tensile response and the volume fraction of the B2 CuZr phase should be also considered.

(3) Owing to the outstanding deformability of CuZr-based BMG composites, the CuZr-based MG composites in a nano-scaled size should exhibit different but an interesting deformation behavior. In the future, this topic should be also focused.

Publications

1) ***K.K. Song***, S. Pauly, Z. Wang, U. Kühn, and J. Eckert, Materials Science and Engineering A, 587 (2013) 372.

2) ***K.K. Song***, S. Pauly, B. A. Sun, J. Tan, M. Stoica, U. Kühn, and J. Eckert, AIP Advances 3 (2013) 012116.

3) ***K.K. Song***, S. Pauly, Y. Zhang, B. A. Sun, J. He, G. Z. Ma, U. Kühn, and J. Eckert, Materials Science and Engineering A, 559(2013)711.

4) ***K.K. Song***, S. Pauly, Y. Zhang, R. Li, S. Gorantla, N. Narayanan, U. Kühn, T. Gemming, J. Eckert, Acta Materialia, 60 (2012)6000.

5) ***K.K. Song***, P. Gargarella, S. Pauly, G. Z. Ma, U. Kühn, and J. Eckert, Journal of Applied Physics, 112(2012) 063503.

6) ***K.K. Song***, S. Pauly, B.A. Sun, Y. Zhang, J. Tan, U. Kühn, M. Stoica, and J. Eckert, Intermetallics, 30 (2012) 132.

7) ***K.K. Song,*** S. Pauly, Y. Zhang, P. Gargarella, R. Li, N.S. Barekar, U. Kühn, M. Stoica, and J. Eckert, Acta Materialia, 59 (2011) 6620.

8) ***K.K. Song***, S. Pauly, Y. Zhang, S. Scudino, P. Gargarella, K. B. Surreddi, U. Kühn, and J. Eckert, Intermetallics, 19 (2011) 1394.

9) Z.J. Yan, W.X. Hao, Y. Hu, ***K.K. Song***, M. Stoica, S. Scudino, and J. Eckert, Applied Physics Letters **103** (2013) 021907.

10) G.Z. Ma, ***K. K. Song***, B. A. Sun, Z.J. Yan, U. Kühn, D. Chen, J. Eckert, Journal of Materials Science, 48 (2013) 6825.

11) P. Gargarella, S. Pauly, ***K.K. Song***, J. Hu, N.S. Barekar, M. Samadi Khoshkhoo, A. Teresiak, H. Wendrock, U. Kühn, C. Ruffing, E. Kerscher, and J. Eckert, Acta Materialia, 61(2013)151.

12) G.Z. Ma, B. A. Sun, S. Pauly, ***K. K. Song***, U. Kühn, D. Chen, J. Eckert, Materials Science and Engineering A, 563(2013)112.

13) Z.Q. Liu, R. Li, G. Liu, ***K.K. Song***, S. Pauly, J. Eckert, and T. Zhang, AIP Advances, 2 (2012) 032176.

14) J. Tan, Y. Zhang, B. A. Sun, M. Stoica, C. J. Li, ***K.K. Song***, U. Kühn, F. S. Pan, and J. Eckert, Applied Physics Letters, 98 (2011) 151906.

15) N. Barekar, P. Gargarella, ***K.K. Song***, S. Pauly, U. Kühn, and J. Eckert, Journal of Materials Research, 26 (2011) 1702.

Acknowledgements

I would take this opportunity to express my gratitude towards my supervising Professor Dr. Jürgen Eckert for giving me the opportunity to work and study at IFW and for his guidance and support. His leadership, attention to every detail, hard work, has set an example I hope to match some day.

I am very grateful to my supervisor, Dr. Simon Pauly, for his guidance, continuous supports, advices and patience. All of these contributions helped me very much in improving my research and study. It is not so easy to thank him with little words, but his input indeed has been crucial in my understanding of how to study CuZr-based BMG composites.

The supportive atmosphere inherent to the whole group of IFW Dresden contributed to the final outcome of my studies. I would like to thank Dr. Uta Kühn for guiding me in the research activity. Many thanks to Dr. Mihai Stoica, Dr. Thomas Gemming, Dr. Sergio Scudino, Dr. Narendirakumar Narayanan, Dr. Sandeep Madhukar Gorantla, Dr. Lars Giebeler, Dr. Stefan Roth, Dr. Jürgen Thomas, Dr. Ran Li, Piter Gargarella, Benjamin Escher, Konrad Kosiba, Julia Kristin Hufenbach, Hans-Jörg Klauß, Michael Frey, Dr. Golden Kumar, Dr. Ruijuan Xiao, Dr. Baoan Sun, Dr. Gang Wang, Dr. Qiang Luo, Dr. Fuping Dai, Dr. Zhijie Yan, Dr. Jie He, Dr. Jun Tan, Dr. Nilam Shankarrao Barekar, Birgit Bartusch, Dina Lohse, Sven Donath, Birgit Opitz, Uta Wilke, Michael Frey, Steffen Grundkowski, Prashanth Konda Gokuldoss, Fatemeh Asgharzadeh Javid, Mohsen Samadi Khoshkhoo, Hamed Shakur Shahabi, Dr. Jiong Zhao, GuoZhi Ma, Zhi Wang, Shilong Li, Dr. Na Zheng, Dr. Caiju Li, Kefeng Li, Zengqian Liu, Yang Zhang, Lixia Xi, Pan Ma, and Yandong Jia and others. Special thanks to Brit Präßler-Wüstling for her help. Thanks for the financial support of the Chinese Scholarship Council.

I would like to express all my sincere gratitude to my family for their constant love and continuous support. Thanks them to support and encourage me along my path to this very important point in my carrier. Thanks to my wife, Meiting Xie. She never lost her faith in me and she sustained and encouraged me from the very beginning until the very end. Special thanks for my daughter, Yixiao. Without her, I can not afford all these work until now.

References

[1] M. Cable, L.D. Pye, V.D. Frechette, N.J. Kreidl, Borate Glass: Structure, Properties, Applications, Plenum Press, New York, 1978.

[2] J.E. Shelby, Introduction to Glass Science and Technology, The Royal Society of Chemistry, Cambridge, 2005.

[3] http://www.fanpop.com/clubs/fruit/images/2500605/title/glass-apples-wallpaper-wallpaper.

[4] M. Telford, Materials Today, 7 (2004) 36.

[5] A.L. Greer, Science, 267 (1995) 1947.

[6] W.L. Johnson, MRS Bulletin, 24 (1999) 42.

[7] A. Inoue, Acta Materialia, 48 (2000) 279.

[8] W.H. Wang, C. Dong, C.H. Shek, Materials Science and Engineering: R: Reports, 44 (2004) 45.

[9] Y.Q. Cheng, E. Ma, Progress in Materials Science, 56 (2011) 379.

[10] E. Axinte, Materials & Design, 35 (2012) 518.

[11] W.H. Wang, Progress in Materials Science, 57 (2012) 487.

[12] W. Klement, R.H. Willens, P.O.L. Duwez, Nature, 187 (1960) 869.

[13] C.A. Angell, Science, 267 (1995) 1924.

[14] J.C. Dyre, Reviews of Modern Physics, 78 (2006) 953.

[15] M. Chen, NPG Asia Mater, 3 (2011) 82.

[16] A.L. Greer, E. Ma, MRS Bulletin, 32 (2007) 611.

[17] M. Chen, Annual Review of Materials Research, 38 (2008) 445.

[18] S. Kavesh, in: J.J. Gillman, H.L. Leamy (Eds.), Metallic Glasses, ASM International, Metals Park. OH, 1978.

[19] H.S. Chen, Acta Metallurgica, 22 (1974) 1505.

[20] A.J. Drehman, A.L. Greer, D. Turnbull, Applied Physics Letters, 41 (1982) 716.

[21] H.W. Kui, A.L. Greer, D. Turnbull, Applied Physics Letters, 45 (1984) 615.

[22] A. Inoue, K. Ohtera, K. Kita, T. Masumoto, Japanese Journal of Applied Physics, 27 (1988) L2248.

[23] A. Inoue, T. Zhang, and T. Masumoto, Materials Transactions, 30 (1989) 965.

[24] A. Inoue, T. Zhang, and T. Masumoto, Materials Transactions, 31 (1990) 177.

[25] A. Inoue and J.S. Gook, Materials Transactions, 36 (1995) 1180.

[26] A. Inoue, N. Nishiyama, and T. Matsuda, Materials Transactions, 37 (1996) 181.

[27] A. Inoue. T. Zhang, Materials Transactions, 37 (1996) 185.

[28] A. Inoue, T. Zhang, T. Itoi, and A. Takeuchi, Materials Transactions, 38 (1997) 359.

[29] A. Inoue, and T. Zhang, Materials Transactions, 39 (1998) 1001.

[30] A. Inoue, and T. Zhang, Materials Transactions, 40 (1999) 301.

[31] A. Peker, W.L. Johnson, Applied Physics Letters, 63 (1993) 2342.

[32] F. Guo, S.J. Poon, G.J. Shiflet, Applied Physics Letters, 83 (2003) 2575.

[33] F.Q. Guo, S.J. Poon, G.J. Shiflet, Applied Physics Letters, 84 (2004) 37.

[34] Z.P. Lu, C.T. Liu, J.R. Thompson, W.D. Porter, Physical Review Letters, 92 (2004) 245503.

[35] D. Xu, G. Duan, W.L. Johnson, Physical Review Letters, 92 (2004) 245504.

[36] F. Guo, H.-J. Wang, S.J. Poon, G.J. Shiflet, Applied Physics Letters, 86 (2005) 091907.

[37] H. Ma, L.L. Shi, J. Xu, Y. Li, E. Ma, Applied Physics Letters, 87 (2005) 181915.

[38] Q.K. Jiang, G.Q. Zhang, L. Yang, X.D. Wang, K. Saksl, H. Franz, R. Wunderlich, H. Fecht, J.Z. Jiang, Acta Materialia, 55 (2007) 4409.

[39] H.B. Lou, X.D. Wang, F. Xu, S.Q. Ding, Q.P. Cao, K. Hono, J.Z. Jiang, Applied Physics Letters, 99 (2011) 051910.

[40] N. Nishiyama, and A. Inoue, Materials Transactions, 38 (1997) 464.

[41] J.A. Alonso, S. Simozar, Solid State Communications, 48 (1983) 765.

[42] C.C. Koch, O.B. Cavin, C.G. McKamey, J.O. Scarbrough, Applied Physics Letters, 43 (1983) 1017.

[43] H. Schröder, K. Samwer, U. Köster, Physical Review Letters, 54 (1985) 197.

[44] L. Bai-Xin, Materials Letters, 5 (1987) 322.

[45] M.A. Hollanders, B.J. Thijsse, E.J. Mittemeijer, Physical Review B, 42 (1990) 5481.

[46] Y. Kawamura, H. Kato, A. Inoue, T. Masumoto, Applied Physics Letters, 67 (1995) 2008.

[47] A. Biswas, G.K. Dey, A.J. Haq, D.K. Bose, S. Banerjee, Journal of Materials Research, 11 (1996) 599.

[48] B.X. Liu, W.S. Lai, Q. Zhang, Materials Science and Engineering: R: Reports, 29 (2000) 1.

[49] C. Suryanarayana, Progress in Materials Science, 46 (2001) 1.

[50] M.D. Demetriou, J.P. Schramm, C. Veazey, W.L. Johnson, J.C. Hanan, N.B. Phelps, Applied Physics Letters, 91 (2007) 161903.

[51] R. Benedictus, K. Han, C. TrÆholt, A. Böttger, E.J. Mittemeijer, Acta Materialia, 46 (1998) 5491.

[52] H.W. Bergmann, H.U. Fritsch, G. Hunger, Journal of Materials Science, 16 (1981) 1935.

[53] A. Biswas, G.K. Dey, A.J. Haq, D.K. Bose, S. Banerjee, Journal of Materials Research, 11 (1996) 599.

[54] L.E. Rehn, P.R. Okamoto, J. Pearson, R. Bhadra, M. Grimsditch, Physical Review Letters, 59 (1987) 2987.

[55] A. Makaya, T. Tamura, K. Miwa, Metallurgical and Materials Transactions A, 41 (2010) 1646.

[56] W.H. Wang, P.W.Z. Bian, Y. Zhang, M.X. Pan, D.Q. Zhao, Intermetallics, 10 (2002) 1249.

[57] D. Turnbull, Contemporary Physics, 10 (1969) 473.

[58] G.H. Fredrickson, Annual Review of Physical Chemistry, 39 (1988) 149.

[59] J.C. Dyre, Journal of Non-Crystalline Solids, 235-237 (1998) 142.

[60] C.A. Angell, K.L. Ngai, G.B. McKenna, P.F. McMillan, S.W. Martin, Journal of Applied Physics, 88 (2000) 3113.

[61] Z.P. Lu, C.T. Liu, Physical Review Letters, 91 (2003) 115505.

[62] Z.P. Lu, C.T. Liu, Acta Materialia, 50 (2002) 3501.

[63] D.B. Miracle, W.S. Sanders, O.N. Senkov, Philosophical Magazine, 83 (2003) 2409.

[64] D.B. Miracle, Nature Materials, 3 (2004) 697.

[65] A.L. Greer, Nature, 366 (1993) 303.

[66] D. A. Porter, K.E. Easterling, Phase Transformation in Metals and Alloys, Van Nostrand Reinhold, New York, 1981.

[67] X.D. Hui, and G.L. Chen, Bulk Amorphous Alloys, Chemical Industry Press, Beijing, 2007.

[68] Y.Q. Gao, W. Wang, Journal of Non-Crystalline Solids, 81 (1986) 129.

[69] R. Busch, Y.J. Kim, W.L. Johnson, Journal of Applied Physics, 77 (1995) 4039.

[70] R. Busch, A. Masuhr, W.L. Johnson, Materials Science and Engineering: A, 304-306 (2001) 97.

[71] T.A. Waniuk, R. Busch, A. Masuhr, W.L. Johnson, Acta Materialia, 46 (1998)

[72] O. Kubaschewski, C.B. Alcock, and P. J. Spencer, Materials Thermo-chemistry, Pergamon, New York, 1993.

[73] R. Bormann, F. Gärtner, K. Zöltzer, Journal of the Less Common Metals, 145 (1988) 19.

[74] J.S. R. Busch, and W.H. Wang, MRS Bulletin, 32 (2007) 620.

[75] M.H. Cohen, D. Turnbull, Journal of Chemical Physics, 31 (1959) 1164.

[76] D. Turnbull, M.H. Cohen, Journal of Chemical Physics, 34 (1961) 120.

[77] R. Busch, JOM, 52 (2000) 39.

[78] M. Heilmaier, J. Eckert, JOM, 52 (2000) 43.

[79] J. Guo, X. Bian, Journal of Alloys and Compounds, 504, Supplement 1 (2010) S205.

[80] K.K. Song, X.F. Bian, X.Q. Lv, M.T. Xie, R. Jia, Journal of Applied Physics, 105 (2009) 024304.

[81] X.F. Bian, B.A. Sun, L.N. Hu, Y.B. Jia, Physics Letters A, 335 (2005) 61.

[82] B.A. Sun, X.B. Bian, J. Hu, T. Mao, Y.N. Zhang, Materials Characterization, 59 (2008) 820.

[83] Y. Zhao, X.F. Bian, X.L. Hou, Physica A: Statistical Mechanics and its Applications, 367 (2006) 42.

[84] R. Richert, C.A. Angell, Journal of Chemical Physics, 108 (1998) 9016.

[85] R. Busch, E. Bakke, W.L. Johnson, Acta Materialia, 46 (1998) 4725.

[86] R. Bohmer, K.L. Ngai, C.A. Angell, D.J. Plazek, Journal of Chemical Physics, 99 (1993) 4201.

[87] R. Brüning, K. Samwer, Physical Review B, 46 (1992) 11318.

[88] C.A. Angell, Journal of Physics and Chemistry of Solids, 49 (1988) 863.

[89] W.H. Wang, Journal of Applied Physics, 99 (2006) 093506.

[90] D.N. Perera, Journal of Physics: Condensed Matter, 11 (1999) 3807.

[91] M. L. F. Nascimento, C. Aparicio, Journal of Physics and Chemistry of Solids, 68 (2007) 104.

[92] S. Scudino, B. Bartusch, J. Eckert, Journal of Physics: Conference Series, 144 (2009) 012097.

[93] R. Busch, W. Liu, W.L. Johnson, Journal of Applied Physics, 83 (1998) 4134.

[94] R.D. Levine, Molecular Reaction Dynamics, Cambridge University Press, United Kingdom, 2005.

[95] X.L. Zhao, X.F. Bian, Y.W. Bai, X.X. Li, Journal of Applied Physics, 111 (2012) 103514.

[96] Y.W. Bai, X.F. Bian, X.Q. Lv, S.P. Pan, J.Y. Qin, X.B. Qin, L.N. Hu, Journal of Applied Physics, 112 (2012) 083524.

[97] X.F. Liu, X.F.Bian. X.G. Qi, J.J .Ma, JOM, 49 (1997) 40.

[98] S. Basak, S.R. Nagel, B.C. Giessen, Physical Review B, 21 (1980) 4049.

[99] G.S. Grest, S.R. Nagel, Physical Review B, 19 (1979) 3571.

[100] S. Basak, R. Clarke, S.R. Nagel, Physical Review B, 20 (1979) 3388.

[101] S.R. Nagel, Physical Review Letters, 41 (1978) 990.

[102] S.R. Nagel, Physical Review B, 16 (1977) 1694.

[103] S.R. Nagel, J. Tauc, Physical Review Letters, 35 (1975) 380.

[104] T. Egami, Y. Waseda, Journal of Non-Crystalline Solids, 64 (1984) 113.

[105] T. Egami, Materials Science and Engineering: A, 226-228 (1997) 261.

[106] C. He, P. Wu, Chemistry of Materials, 13 (2001) 4642.

[107] W.J. Botta, F.S. Pereira, C. Bolfarini, C.S. Kiminami, M.F. de Oliveira, Philosophical Magazine Letters, 88 (2008) 785.

[108] M.F. de Oliveira, F.S. Pereira, C. Bolfarini, C.S. Kiminami, W.J. Botta, Intermetallics, 17 (2009) 183.

[109] A. Inoue, A. Takeuchi, Acta Materialia, 59 (2011) 2243.

[110] A. Inoue, A. Takeuchi, Materials Transactions, 43 (2002) 1892.

[111] W.H. Wang, E. Wu, R.J. Wang, S.J. Kennedy, A.J. Studer, Physical Review B, 66 (2002) 104205.

[112] J. Saida, M. Matsushita, A. Inoue, Applied Physics Letters, 79 (2001) 412.

[113] H.W. Sheng, W.K. Luo, F.M. Alamgir, J.M. Bai, E. Ma, Nature, 439 (2006) 419.

[114] L.L. Shi, J. Xu, E. Ma, Acta Materialia, 56 (2008) 3613.

[115] D.B. Miracle, Acta Materialia, 54 (2006) 4317.

[116] D. Ma, A.D. Stoica, L. Yang, X.L. Wang, Z.P. Lu, J. Neuefeind, M.J. Kramer, J.W. Richardson, T. Proffen, Applied Physics Letters, 90 (2007) 211908.

[117] A. Hirata, P. Guan, T. Fujita, Y. Hirotsu, A. Inoue, A.R. Yavari, T. Sakurai, M. Chen, Nature Materials, 10 (2011) 28.

[118] Y. Wang, X. Zhang, J. Qiang, Q. Wang, D. Wang, D. Li, C.H. Shek, C. Dong, Scripta Materialia, 50 (2004) 829.

[119] K.K. Song, P. Gargarella, S. Pauly, G.Z. Ma, U. Kühn, J. Eckert, Journal of Applied Physics, 112 (2012) 063503.

[120] M.F. de Oliveira, Journal of Applied Physics, 111 (2012) 023509.

[121] M.F. de Oliveira, Philosophical Magazine Letters, 91 (2011) 418.

[122] R.D.S. Lisboa, C. Bolfarini, W.J.B. F, C.S. Kiminami, Applied Physics Letters, 86 (2005) 211904.

[123] P.H. Gaskell, Nature, 276 (1978) 484.

[124] J. Schroers, T.M. Hodges, G. Kumar, H. Raman, A.J. Barnes, Q. Pham, T.A. Waniuk, Materials Today, 14 (2011) 14.

[125] M. Carmo, R.C. Sekol, S. Ding, G. Kumar, J. Schroers, A.D. Taylor, ACS Nano, 5 (2011) 2979.

[126] M.M. Trexler, N.N. Thadhani, Progress in Materials Science, 55 (2010) 759.

[127] C.A. Schuh, T.C. Hufnagel, U. Ramamurty, Acta Materialia, 55 (2007) 4067.

[128] L. Tian, Y.Q. Cheng, Z.W. Shan, J. Li, C.C. Wang, X.D. Han, J. Sun, E. Ma, Nature Communications, 3 (2012) 609.

[129] Y.Q. Cheng, E. Ma, Acta Materialia, 59 (2011) 1800.

[130] W.L. Johnson, K. Samwer, Physical Review Letters, 95 (2005) 195501.

[131] M.F. Ashby, A.L. Greer, Scripta Materialia, 54 (2006) 321.

[132] W.H. Wang, Nature Materials, 11 (2012) 275.

[133] G.N. Greaves, A.L. Greer, R.S. Lakes, T. Rouxel, Nature Materials, 10 (2011) 823.

[134] D. Ma, A.D. Stoica, X.L. Wang, Z.P. Lu, B. Clausen, D.W. Brown, Physical Review Letters, 108 (2012) 085501.

[135] K.K. Song, S. Pauly, B.A. Sun, J. Tan, M. Stoica, U. Kühn, J. Eckert, AIP Advances, 3 (2013) 012116.

[136] S. Pauly, S. Gorantla, G. Wang, U. Kühn, J. Eckert, Nature Materials, 9 (2010) 473.

[137] F.H.D. Torre, A. Dubach, M.E. Siegrist, J.F. Loffler, Applied Physics Letters, 89 (2006) 091918.

[138] . Mukai, T.G. Nieh, Y. Kawamura, A. Inoue, K. Higashi, Intermetallics, 10 (2002) 1071.

[139] D. Klaumunzer, R. Maass, F.H.D. Torre, J.F. Loffler, Applied Physics Letters, 96 (2010) 061901.

[140] J.H. Chen, M.Q. Jiang, Y. Chen, L.H. Dai, Materials Science and Engineering: A, 576 (2013) 134.

[141] F. Yang, Applied Physics Letters, 91 (2007) 051922.

[142] Y.Q. Cheng, Z. Han, Y. Li, E. Ma, Physical Review B, 80 (2009) 134115.

[143] Z. Han, W.F. Wu, Y. Li, Y.J. Wei, H.J. Gao, Acta Materialia, 57 (2009) 1367.

[144] F.F. Wu, Z.F. Zhang, S.X. Mao, Journal of Materials Research, 22 (2007) 501.

[145] Z.F. Zhang, H. Zhang, X.F. Pan, J. Das, J. Eckert, Philosophical Magazine Letters, 85 (2005) 513.

[146] B.A. Sun, S. Pauly, J. Tan, M. Stoica, W.H. Wang, U. Kühn, J. Eckert, Acta Materialia, 60 (2012) 4160.

[147] B.A. Sun, S. Pauly, J. Hu, W.H. Wang, U. Kühn, J. Eckert, Physical Review Letters, 110 (2013) 225501.

[148] J.J. Lewandowski, W.H. Wang, A.L. Greer, Philosophical Magazine Letters, 85 (2005) 77.

[149] S.V. Madge, D.V. Louzguine-Luzgin, J.J. Lewandowski, A.L. Greer, Acta Materialia, 60 (2012) 4800.

[150] J. Schroers, Advanced Materials, 22 (2010) 1566.

[151] X.K. Xi, D.Q. Zhao, M.X. Pan, W.H. Wang, Y. Wu, J.J. Lewandowski, Physical Review Letters, 94 (2005) 125510.

[152] F. Spaepen, Acta Metallurgica, 25 (1977) 407.

[153] F. Spaepen, Nature, 408 (2000) 781.

[154] R. Becker, Zeitschrift für Physik, 33 (1925) 185.

[155] E. Orowan, Zeitschrift für Physik, 89 (1934) 634.

[156] I.-C. Choi, Y. Zhao, B.-G. Yoo, Y.-J. Kim, J.-Y. Suh, U. Ramamurty, J.-i. Jang, Scripta Materialia, 66 (2012) 923.

[157] D. Pan, A. Inoue, T. Sakurai, M.W. Chen, Proceedings of the National Academy of Sciences, 105 (2008) 14769.

[158] A.S. Argon, H.Y. Kuo, Materials Science and Engineering, 39 (1979) 101.

[159] A.S. Argon, Acta Metallurgica, 27 (1979) 47.

[160] V.V. Bulatov, A.S. Argon, Modelling and Simulation in Materials Science and Engineering, 2 (1994) 167.

[161] V.V. Bulatov, A.S. Argon, Modelling and Simulation in Materials Science and Engineering, 2 (1994) 185.

[162] V.V. Bulatov, A.S. Argon, Modelling and Simulation in Materials Science and Engineering, 2 (1994) 203.

[163] D. Srolovitz, V. Vitek, T. Egami, Acta Metallurgica, 31 (1983) 335.

[164] C.A. Schuh, A.C. Lund, Nature Materials, 2 (2003) 449.

[165] J.S. Langer, Scripta Materialia, 54 (2006) 375.

[166] M.L. Falk, J.S. Langer, Physical Review E, 57 (1998) 7192.

[167] J.D. Eshelby, Proceedings of the Royal Society of London. Series A. Mathematical and Physical Sciences, 241 (1957) 376.

[168] A.S. Argon, L.T. Shi, Philosophical Magazine A, 46 (1982) 275.

[169] A.C. Lund, C.A. Schuh, Acta Materialia, 51 (2003) 5399.

[170] P.S. Steif, F. Spaepen, J.W. Hutchinson, Acta Metallurgica, 30 (1982) 447.

[171] V.A. Khonik, Physica Status Solidi (a), 177 (2000) 173.

[172] F.H. Stillinger, P.G. Debenedetti, The Journal of Chemical Physics, 116 (2002) 3353.

[173] M. Goldstein, Journal of Chemical Physics, 51 (1969) 3728.

[174] M.D.D. William L. Johnson, John S. Harmon, Mary L. Lind, and Konrad Samwer, MRS Bulletin, 32 (2007) 644.

[175] S. Francesco, Journal of Statistical Mechanics: Theory and Experiment, 2005 (2005) P05015.

[176] S. Sastry, Nature, 409 (2001) 164.

[177] S. Büchner, A. Heuer, Physical Review E, 60 (1999) 6507.

[178] F.H. Stillinger, Science, 267 (1995) 1935.

[179] R.W. Hall, P.G. Wolynes, Journal of Chemical Physics, 86 (1987) 2943.

[180] S.G. Mayr, Physical Review Letters, 97 (2006) 195501.

[181] G. Gagnon, J. Patton, D.J. Lacks, Physical Review E, 64 (2001) 051508.

[182] D.L. Malandro, D.J. Lacks, Journal of Chemical Physics, 110 (1999) 4593.

[183] M.D. Demetriou, J.S. Harmon, M. Tao, G. Duan, K. Samwer, W.L. Johnson, Physical Review Letters, 97 (2006) 065502.

[184] J. Frenkel, Zeitschrift für Physik, 37 (1926) 572.

[185] A. Masuhr, T.A. Waniuk, R. Busch, W.L. Johnson, Physical Review Letters, 82 (1999) 2290.

[186] K.H. Tsang, S.K. Lee, H.W. Kui, Journal of Applied Physics, 70 (1991) 4837.

[187] K.J. Szczepanski, K.W. Becker, Zeitschrift für Physik B Condensed Matter, 89 (1992) 327.

[188] J. Schroers, W.L. Johnson, Physical Review Letters, 93 (2004) 255506.

[189] S.B. Biner, Acta Materialia, 54 (2006) 139.

[190] H. Choi-Yim, R. Busch, U. Köster, W.L. Johnson, Acta Materialia, 47 (1999) 2455.

[191] H. Choi-Yim, R.D. Conner, F. Szuecs, W.L. Johnson, Acta Materialia, 50 (2002) 2737.

[192] X. Hu, S.C. Ng, Y.P. Feng, Y. Li, Acta Materialia, 51 (2003) 561.

[193] X. Hui, W. Dong, G.L. Chen, K.F. Yao, Acta Materialia, 55 (2007) 907.

[194] J.C. Lee, Y.C. Kim, J.-P. Ahn, H.S. Kim, Acta Materialia, 53 (2005) 129.

[195] M.L. Lee, Y. Li, C.A. Schuh, Acta Materialia, 52 (2004) 4121.

[196] N. Nagendra, U. Ramamurty, T.T. Goh, Y. Li, Acta Materialia, 48 (2000) 2603.

[197] R.L. Narayan, P.S. Singh, D.C. Hofmann, N. Hutchinson, K.M. Flores, U. Ramamurty, Acta Materialia, 60 (2012) 5089.

[198] R.T. Ott, F. Sansoz, J.F. Molinari, J. Almer, K.T. Ramesh, T.C. Hufnagel, Acta Materialia, 53 (2005) 1883.

[199] F. Szuecs, C.P. Kim, W.L. Johnson, Acta Materialia, 49 (2001) 1507.

[200] K. Werniewicz, U. Kühn, N. Mattern, B. Bartusch, J. Eckert, J. Das, L. Schultz, T. Kulik, Acta Materialia, 55 (2007) 3513.

[201] W. Xu, R. Zheng, K.J. Laws, S.P. Ringer, M. Ferry, Acta Materialia, 59 (2011) 7776.

[202] Y.K. Xu, H. Ma, J. Xu, E. Ma, Acta Materialia, 53 (2005) 1857.

[203] Y. Zhang, W. Xu, H. Tan, Y. Li, Acta Materialia, 53 (2005) 2607.

[204] J. Eckert, J. Das, S. Pauly, C. Duhamel, Advanced Engineering Materials, 9 (2007) 443.

[205] H. Choi-Yim, W.L. Johnson, Applied Physics Letters, 71 (1997) 3808.

[206] J. Das, W. Loser, U. Kühn, J. Eckert, S.K. Roy, L. Schultz, Applied Physics Letters, 82 (2003) 4690.

[207] C. Fan, R.T. Ott, T.C. Hufnagel, Applied Physics Letters, 81 (2002) 1020.

[208] U. Kühn, J. Eckert, N. Mattern, L. Schultz, Applied Physics Letters, 80 (2002) 2478.

[209] H. Ma, J. Xu, E. Ma, Applied Physics Letters, 83 (2003) 2793.

[210] L.Q. Xing, J. Eckert, W. Löser, L. Schultz, Applied Physics Letters, 74 (1999) 664.

[211] H. Tan, Y. Zhang, Y. Li, Intermetallics, 10 (2002) 1203.

[212] J. Eckert, Das, J., Pauly, S., Duhamel, C., Journal of Materials Research, 22 (2007) 285.

[213] D.C. Hofmann, J.-Y. Suh, A. Wiest, G. Duan, M.-L. Lind, M.D. Demetriou, W.L. Johnson, Nature, 451 (2008) 1085-1089.

[214] C.C. Hays, C.P. Kim, W.L. Johnson, Physical Review Letters, 84 (2000) 2901.

[215] D.C. Hofmann, J.-Y. Suh, A. Wiest, M.-L. Lind, M.D. Demetriou, W.L. Johnson, Proceedings of the National Academy of Sciences, 105 (2008) 20136.

[216] G. Chen, X.L. Zhang, C.T. Liu, Scripta Materialia, 68 (2013) 150.

[217] R.D. Conner, R.B. Dandliker, W.L. Johnson, Acta Materialia, 46 (1998) 6089.

[218] Q.K. Jiang, X.D. Wang, X.P. Nie, G.Q. Zhang, H. Ma, H.J. Fecht, J. Bendnarcik, H. Franz, Y.G. Liu, Q.P. Cao, J.Z. Jiang, Acta Materialia, 56 (2008) 1785.

[219] E.S. Park, H.J. Chang, D.H. Kim, Acta Materialia, 56 (2008) 3120.

[220] E.S. Park, D.H. Kim, Acta Materialia, 54 (2006) 2597.

[221] D.D. Qu, K.D. Liss, Y.J. Sun, M. Reid, J.D. Almer, K. Yan, Y.B. Wang, X.Z. Liao, J. Shen, Acta Materialia, 61 (2013) 321.

[222] Y. Shi, M.L. Falk, Acta Materialia, 56 (2008) 995.

[223] X. Wang, Q.P. Cao, Y.M. Chen, K. Hono, C. Zhong, Q.K. Jiang, X.P. Nie, L.Y. Chen, X.D. Wang, J.Z. Jiang, Acta Materialia, 59 (2011) 1037.

[224] L. Zhang, Y.Q. Cheng, A.J. Cao, J. Xu, E. Ma, Acta Materialia, 57 (2009) 1154.

[225] Z.W. Zhu, L. Gu, G.Q. Xie, W. Zhang, A. Inoue, H.F. Zhang, Z.Q. Hu, Acta Materialia, 59 (2011) 2814.

[226] Q. Cao, J. Li, Y. Zhou, J. Jiang, Applied Physics Letters, 86 (2005) 081913.

[227] X.H. Du, J.C. Huang, K.C. Hsieh, Y.H. Lai, H.M. Chen, J.S.C. Jang, P.K. Liaw, Applied Physics Letters, 91 (2007) 131901.

[228] C. Fan, A. Inoue, Applied Physics Letters, 77 (2000) 46.

[229] K.B. Kim, J. Das, F. Baier, M.B. Tang, W.H. Wang, J. Eckert, Applied Physics Letters, 88 (2006).

[230] Y.C. Kim, J.H. Na, J.M. Park, D.H. Kim, J.K. Lee, W.T. Kim, Applied Physics Letters, 83 (2003) 3093.

[231] K.F. Yao, F. Ruan, Y.Q. Yang, N. Chen, Applied Physics Letters, 88 (2006) 122106.

[232] Z.W. Zhu, S.J. Zheng, H.F.Zhang, B.Z. Ding, Z.Q. Hu, P.K. Liaw, Y.D. Wang, Y. Ren, Journal of Materials Research, 23 (2008) 941.

[233] K. Hajlaoui, A.R. Yavari, A. LeMoulec, W.J. Botta, F.G. Vaughan, J. Das, A.L. Greer, A. Kvick, Journal of Non-Crystalline Solids, 353 (2007) 327.

[234] D.H. Bae, S.W. Lee, J.W. Kwon, X.D. Wang, S. Yi, Materials Science and Engineering: A, 449-451 (2007) 111-.

[235] H. Chen, Y. He, G.J. Shiflet, S.J. Poon, Nature, 367 (1994) 541.

[236] L.Q. Xing, Y. Li, K.T. Ramesh, J. Li, T.C. Hufnagel, Physical Review B, 64 (2001) 180201.

[237] L.Y. Chen, Z.D. Fu, G.Q. Zhang, X.P. Hao, Q.K. Jiang, X.D. Wang, Q.P. Cao, H. Franz, Y.G. Liu, H.S. Xie, S.L. Zhang, B.Y. Wang, Y.W. Zeng, J.Z. Jiang, Physical Review Letters, 100 (2008) 075501.

[238] J. Das, M.B. Tang, K.B. Kim, R. Theissmann, F. Baier, W.H. Wang, J. Eckert, Physical Review Letters, 94 (2005) 205501.

[239] Y.H. Liu, G. Wang, R.J. Wang, D.Q. Zhao, M.X. Pan, W.H. Wang, Science, 315 (2007) 1385-.

[240] M. Calin, J. Eckert, L. Schultz, Scripta Materialia, 48 (2003) 653.

[241] X. Hui, S.N. Liu, S.J. Pang, L.C. Zhuo, T. Zhang, G.L. Chen, Z.K. Liu, Scripta Materialia, 63 (2010) 239.

[242] J.C. Oh, T. Ohkubo, Y.C. Kim, E. Fleury, K. Hono, Scripta Materialia, 53 (2005) 165.

[243] S. Scudino, B. Jerliu, S. Pauly, K.B. Surreddi, U. Kühn, J. Eckert, Scripta Materialia, 65 (2011) 815.

[244] R. Raghavan, R. Ayer, H.W. Jin, C.N. Marzinsky, U. Ramamurty, Scripta Materialia, 59 (2008) 167.

[245] F.O. Méar, B. Lenk, Y. Zhang, A.L. Greer, Scripta Materialia, 59 (2008) 1243.

[246] M.H. Lee, K.S. Lee, J. Das, J. Thomas, U. Kühn, J. Eckert, Scripta Materialia, 62 (2010) 678.

[247] Y. Yokoyama, Y. Yamasaki, A.Inoue, Reviews on Advanced Materials Science, 18 (2008) 131.

[248] F.O. Méar, G. Vaughan, A.R. Yavari, A.L. Greer, Philosophical Magazine Letters, 88 (2008) 757.

[249] Y. Zhang, W.H. Wang, A.L. Greer, Nature Materials, 5 (2006) 857-860.

[250] L. He, M.B. Zhong, Z.H. Han, Q. Zhao, F. Jiang, J. Sun, Materials Science and Engineering: A, 496 (2008) 285.

[251] Y. Nishi, H. Harano, H. Ishizuki, M. Kawakami, E. Yajima, Materials Science and Engineering, 98 (1988) 505.

[252] T. Yamamoto, T. Takahashi, H. Kimura, A. Inoue, Journal of Alloys and Compounds, 430 (2007) 97.

[253] H. Shao, Y.L. Xu, B. Shi, C.S. Yu, H. Hahn, H. Gleiter, J.G. Li, Journal of Alloys and Compounds, 548 (2013) 77.

[254] K.K. Song, S. Pauly, Y. Zhang, S. Scudino, P. Gargarella, K.B. Surreddi, U. Kühn, J. Eckert, Intermetallics, 19 (2011) 1394.

[255] Z. Han, H. Yang, W.F. Wu, Y. Li, Applied Physics Letters, 93 (2008) 231912.

[256] J.X. Zhao, F.F. Wu, R.T. Qu, S.X. Li, Z.F. Zhang, Acta Materialia, 58 (2010) 5420.

[257] Y.B. Wang, D.D. Qu, X.H. Wang, Y. Cao, X.Z. Liao, M. Kawasaki, S.P. Ringer, Z.W. Shan, T.G. Langdon, J. Shen, Acta Materialia, 60 (2012) 253.

[258] D.L. Henann, L. Anand, Acta Materialia, 57 (2009) 6057.

[259] W. Dmowski, Y. Yokoyama, A. Chuang, Y. Ren, M. Umemoto, K. Tsuchiya, A. Inoue, T. Egami, Acta Materialia, 58 (2010) 429.

[260] Q.P. Cao, J.W. Liu, K.J. Yang, F. Xu, Z.Q. Yao, A. Minkow, H.J. Fecht, J. Ivanisenko, L.Y. Chen, X.D. Wang, S.X. Qu, J.Z. Jiang, Acta Materialia, 58 (2010) 1276.

[261] Q.P. Cao, J.F. Li, Y.H. Zhou, A. Horsewell, J.Z. Jiang, Acta Materialia, 54 (2006) 4373.

[262] A. Slipenyuk, J. Eckert, Scripta Materialia, 50 (2004) 39.

[263] J.W. Liu, Q.P. Cao, L.Y. Chen, X.D. Wang, J.Z. Jiang, Acta Materialia, 58 (2010) 4827.

[264] S.J. Cytron, Journal of Materials Science Letters, 1 (1982) 211.

[265] B. Clausen, S.Y. Lee, E. Üstündag, C.P. Kim, D.W. Brown, M.A.M. Bourke, Scripta Materialia, 54 (2006) 343.

[266] H. Choi-Yim, S.-Y. Lee, R.D. Conner, Scripta Materialia, 58 (2008) 763.

[267] J.W. Qiao, Y. Zhang, P.K. Liaw, G.L. Chen, Scripta Materialia, 61 (2009) 1087.

[268] S.F. Guo, L. Liu, N. Li, Y. Li, Scripta Materialia, 62 (2010) 329.

[269] Z. Zhu, H. Zhang, Z. Hu, W. Zhang, A. Inoue, Scripta Materialia, 62 (2010) 278.

[270] D.G. Pan, H.F. Zhang, A.M. Wang, Z.Q. Hu, Applied Physics Letters, 89 (2006) 261904.

[271] J.S.C. Jang, J.B. Li, S.L. Lee, Y.S. Chang, S.R. Jian, J.C. Huang, T.G. Nieh, Intermetallics, 30 (2012) 25.

[272] B.Y. Zhang, X.H. Chen, S.S. Wang, D.Y. Lin, X.D. Hui, Materials Letters, 93 (2013) 210.

[273] D.C. Hofmann, Doctoral thesis work: Designing bulk metallic glass matrix composites with high toughness and tensile ductility, California Institute of Technology, Pasadena, California, 2009.

[274] B. Zhang, H. Fu, P. Sha, Z. Zhu, C. Dong, H. Zhang, Z. Hu, Materials Science and Engineering: A, 566 (2013) 16.

[275] H.B. Wang, S.J. Li, T.Y. Yu, Polymer Engineering & Science, 33 (1993) 1027-

[276] D. Hofmann, H. Kozachkov, H. Khalifa, J. Schramm, M. Demetriou, K. Vecchio, W. Johnson, JOM, 61 (2009) 11.

[277] J.W. Qiao, A.C. Sun, E.W. Huang, Y. Zhang, P.K. Liaw, C.P. Chuang, Acta Materialia, 59 (2011) 4126.

[278] F. Abdeljawad, M. Haataja, Physical Review Letters, 105 (2010) 125503.

[279] I.Y. Georgieva, Metal Science and Heat Treatment, 18 (1976) 209.

[280] K. Otsuka, C.M. Wayman, Shape memory materials, Cambridge University Press, Cambridge, 1998.

[281] D.C. Lagoudas, Shape memory alloys: modeling and engineering applications, Springer Science, New York, 2008.

[282] www.keytometals.com/page.aspx?ID=CheckArticle&site=kts&LN=EN&NM=207.

[283] S. Zhu, G. Xie, F. Qin, X. Wang, A. Inoue, Materials Transactions, 53 (2012) 500.

[284] B.W. Zhou, X.G. Zhang, W. Zhang, H. Kimura, T. Zhang, A. Makino, A. Inoue, Materials Transactions, 51 (2010) 1003151032.

[285] Q. Zhang, W. Zhang, G. Xie, A. Inoue, Materials Transactions, 48 (2007) 0706180019.

[286] V. Ponnambalam, S.J. Poon, G.J. Shiflet, Journal of Materials Research, 19 (2004) 1320.

[287] Y.C. Kim, W.T. Kim, D.H. Kim, Materials Science and Engineering: A, 375–377 (2004) 127.

[288] P. Yu, H.Y. Bai, M.B. Tang, W.L. Wang, Journal of Non-Crystalline Solids, 351 (2005) 1328.

[289] D. Xu, B. Lohwongwatana, G. Duan, W.L. Johnson, C. Garland, Acta Materialia, 52 (2004) 2621.

[290] D. Wang, Y. Li, B.B. Sun, M.L. Sui, K. Lu, E. Ma, Applied Physics Letters, 84 (2004) 4029.

[291] M.B. Tang, D.Q. Zhao, M.X. Pan, W.H. Wang, Chinese Physics Letters, 21 (2004) 901.

[292] Y.Y. Cui, T.L. Wang, J.H. Li, Y. Dai, B.X. Liu, Physical Chemistry Chemical Physics, 13 (2011) 4103.

[293] www1.asminternational.org/AsmEnterprise/APD.

[294] J.W. Seo, D. Schryvers, Acta Materialia, 46 (1998) 1165.

[295] S. Pauly, G. Liu, G. Wang, U. Kühn, N. Mattern, J. Eckert, Acta Materialia, 57 (2009) 5445.

[296] S. Pauly, J. Bednarčik, U. Kühn, J. Eckert, Scripta Materialia, 63 (2010) 336.

[297] D. Schryvers, G.S. Firstov, J.W. Seo, J. Van Humbeeck, Y.N. Koval, Scripta Materialia, 36 (1997) 1119.

[298] Y.N. Koval, G.S. Firstov, A.V. Kotko, Scripta Metallurgica et Materialia, 27 (1992) 1611.

[299] A.W. Nicholls, I.R. Harris, W. Mangen, Journal of Materials Science Letters, 5 (1986) 217.

[300] Y. Wu, H. Wang, H.H. Wu, Z.Y. Zhang, X.D. Hui, G.L. Chen, D. Ma, X.L. Wang, Z.P. Lu, Acta Materialia, 59 (2011) 2928.

[301] Y. Wu, Y. Xiao, G. Chen, C.T. Liu, Z. Lu, Advanced Materials, 22 (2010) 2770.

[302] S. Pauly, Doctoral thesis work: Phase formation and mechanical properties of metastable Cu-Zr-based alloys, TU dresden, 2009.

[303] J. Das, Doctoral thesis work: Heterostructureed copper- and titanium- base ultrafine and glassy alloys, TU dresden, 2007.

[304] M. Stoica, Doctoral thesis work: Casting and characterization of Fe-(Cr,Mo,Ga)-(P,C,B) soft magnetic bulk metallic glasses, TU dresden, 2005.

[305] W. G. Lidman, and K. H. Moyer, Hot Pressing of Electrolytic Grade CR Beryllium, Modern Developments in Powder Metallurgy, Plenum Press, New York, 1966.

[306] www.icdd.com.

[307] G.D. Danilatos, in: W.H. Peter (Eds.), Advances in electronics and electron physics: Foundations of environmental scanning electron microscopy, Academic Press, 1988, pp. 109-250.

[308] www.ammrf.org.au/myscope/sem/background

[309] R.F. Speyer, Thermal analysis of materials, Marcel Dekker Inc., New York-Basel-Honk Kong, 1994.

[311] G. Gottstein, Physikalische Grundlagen der Materialkunde, Springer,Verlag Berlin Heidelberg, 2007.

[312] D. R. Askeland, and P. P. Phulé, The Science and Engineering of Materials, Thomson Brooks, Cole, USA, 2003.

[313] F. Qiu, P. Shen, T. Liu, Q. Lin, Q. Jiang, Journal of Alloys and Compounds, 491 (2010) 354.

[314] N. Barekar, P. Gargarella, K.K. Song, S. Pauly, U. Kühn, J. Eckert, Journal of Materials Research, 26 (2011) 1702.

[315] K.K. Song, S. Pauly, Y. Zhang, P. Gargarella, R. Li, N.S. Barekar, U. Kühn, M. Stoica, J. Eckert, Acta Materialia, 59 (2011) 6620.

[316] M. Zarinejad, Y. Liu, Advanced Functional Materials 18 (2008) 2789.

[317] A. Takeuchi, and A. Inoue, Materials Transactions, 41 (2000) 1372.

[318] Z.Y. Liu, M. Aindow, J.A. Hriljac, I.P. Jones, I.R. Harris, Journal of Materials Science, 37 (2002) 745.

[319] A.R. Miedema, F.R. Deboer, P.F. Dechatel, Journal of Physics F: Metal Physics, 3 (1973) 1558.

[320] A.R. Miedema, Journal of Physics F: Metal Physics, 3 (1973) 1803.

[321] T. Maekawa, T. Yokokawa, K. Niwa, Journal of Chemical Thermodynamics, 3 (1971) 143.

[322] T. Maekawa, T. Yokokawa, K. Niwa, Journal of Chemical Thermodynamics, 3 (1971) 707.

[323] N. Wang, C.R. Li, Z.M. Du, F.M. Wang, W.J. Zhang, Calphad, 30 (2006) 461.

[324] X.C. He, H. Wang, H.S. Liu, Z.P. Jin, Calphad, 30 (2006) 367.

[325] Y.F. Sun, B.C. Wei, Y.R. Wang, W.H. Li, T.L. Cheung, C.H. Shek, Applied Physics Letters, 87 (2005) 051905.

[326] S. Pauly, J. Das, J. Bednarcik, N. Mattern, K.B. Kim, D.H. Kim, J. Eckert, Scripta Materialia, 60 (2009) 431.

[327] K. Kosiba, P. Gargarella, S. Pauly, U. Kuhn, J. Eckert, Journal of Applied Physics, 113 (2013) 123505.

[328] F. Javid, N. Mattern, S. Pauly, J. Eckert, Metall and Mat Trans A, 43 (2012) 2631-2636.

[329] F.A. Javid, N. Mattern, S. Pauly, J. Eckert, Metallurgical and Materials Transactions A, 43 (2012) 2631.

[330] B. Schwarz, U. Vainio, N. Mattern, S.W. Sohn, S. Oswald, D.H. Kim, J. Eckert, Journal of Non-Crystalline Solids, 357 (2011) 1538.

[331] S. Pauly, J. Das, N. Mattern, D.H. Kim, J. Eckert, Intermetallics, 17 (2009) 453.

[332] F.A. Javid, N. Mattern, S. Pauly, J. Eckert, Metallurgical and Materials Transactions A: Physical Metallurgy and Materials Science, 43A (2012) 2631.

[333] S. Pauly, J. Das, C. Duhamel, J. Eckert, Metallurgical and Materials Transactions A: Physical Metallurgy and Materials Science, 39A (2008) 1868.

[334] H. Wang, Materials Science Forum, 638-642 (2010) 1671.

[335] W. Zhang, Q. Zhang, C. Qin, A. Inoue, Materials Science and Engineering: B, 148 (2008) 92.

[336] W. Zhang, A. Inoue, Journal of Materials Research, 21 (2006) 234.

[337] Q.S. Zhang, W. Zhang, A. Inoue, Materials Transactions, 48 (2007) 629.

[338] R. M. Srivastava, J. Eckert, W. Löser, B.K. Dhindaw, and L. Schultz, Materials Transactions, 43 (2002) 1670.

[339] H. Hermann, V. Kokotin, J. Eckert, EPL (Europhysics Letters), 98 (2012) 16003.

[340] S. Pauly, J. Das, C. Duhamel, J. Eckert, Advanced Engineering Materials 9 (2007) 487.

[341] W. Zhang, F. Jia, Q. Zhang, A. Inoue, Materials Science and Engineering: A, 459 (2007) 330.

[342] D.V. Louzguine-Luzgin, K. Georgarakis, A.R. Yavari, G. Vaughan, G. Xie, A. Inoue, Journal of Materials Research, 24 (2009) 274.

[343] A.A. Kündig, M. Ohnuma, T. Ohkubo, T. Abe, K. Hono, Scripta Materialia, 55 (2006) 449.

[344] T. Fujita, K. Konno, W. Zhang, V. Kumar, M. Matsuura, A. Inoue, T. Sakurai, M.W. Chen, Physical Review Letters, 103 (2009) 075502.

[345] T. Fujita, P.F. Guan, H.W. Sheng, A. Inoue, T. Sakurai, M.W. Chen, Physical Review B, 81 (2010) 140204.

[346] J.H. Han, N. Mattern, B. Schwarz, D.H. Kim, J. Eckert, Scripta Materialia, 67 (2012) 149.

[347] J.H. Han, N. Mattern, I. Kaban, D. Holland-Moritz, J. Bednarĉik, R. Nowak, N. Sobczak, D.H. Kim, J. Eckert, Journal of Physics: Condensed Matter, 25 (2013) 245104.

[348] J. He, N. Mattern, J. Tan, J.Z. Zhao, I. Kaban, Z. Wang, L. Ratke, D.H. Kim, W.T. Kim, J. Eckert, Acta Materialia, 61 (2013) 2102.

[349] N. Mattern, T. Gemming, J. Thomas, G. Goerigk, H. Franz, J. Eckert, Journal of Alloys and Compounds, 495 (2010) 299.

[350] K.K. Song, S. Pauly, B.A. Sun, Y. Zhang, J. Tan, U. Kühn, M. Stoica, J. Eckert, Intermetallics, 30 (2012) 132.

[351] C.W. Nan, Progress in Materials Science, 37 (1993) 1.

[352] Z.Q. Liu, R. Li, G. Liu, W.H. Su, H. Wang, Y. Li, M.J. Shi, X.K. Luo, G.J. Wu, T. Zhang, Acta Materialia, 60 (2012) 3128.

[353] K.K. Song, S. Pauly, Y. Zhang, R. Li, S. Gorantla, N. Narayanan, U. Kühn, T. Gemming, J. Eckert, Acta Materialia, 60 (2012) 6000.

[354] S.F. Corbin, D.S. Wilkinson, Acta Metallurgica et Materialia, 42 (1994) 1311.

[355] Z. Li, S. Schmauder, M. Dong, Computational Materials Science, 15 (1999) 11.

[356] Z. Fan, A.P. Miodownik, Scripta Metallurgica et Materialia, 28 (1993) 895.

[357] C. Fan, C.T. Liu, G. Chen, G. Chen, P.K. Liaw, H.G. Yan, Scripta Materialia, 68 (2013) 534.

[358] Z. Zhu, H. Zhang, H. Wang, B. Ding, Z.Q. Hu, H. Huang, Journal of Materials Research, 24 (2009) 3108.

[359] A.A, Antonysamy, S. Pauly, B.K. Dhindaw, J. Eckert, Journal of Materials Engineering and Performance, 20 (2011) 1196.

[360] W. Löser, J. Das, A. Güth, H.J. Klauß, C. Mickel, U. Kühn, J. Eckert, S.K. Roy, L. Schultz, Intermetallics, 12 (2004) 1153.

[361] K.B. Kim, S. Yi, I.S. Hwang, J. Eckert, Intermetallics, 14 (2006) 972.

[362] J. Mao, H.F. Zhang, H.M. Fu, A.M. Wang, H. Li, Z.Q. Hu, Advanced Engineering Materials, 11 (2009) 986.

[363] J. Saida, A.D. Setyawan, M. Matsushita, A. Inoue, Materials Transactions, 51 (2010) 1188.

[364] A. Inoue, in: A.R. Yavari (Eds.), Mechanically Alloyed and Nanocrystalline Materials, 179 (1995) 691.

[365] W. Wang, B. Zhou, Materials Science and Engineering: A, 366 (2004) 45.

[366] J.C. Barbé, M. Perez, M. Papoular, Journal of Physics: Condensed Matter, 12 (2000) 2567.

[367] M.E. Glicksman, Principles of Solidification: An Introduction to Modern Casting and Crystal Growth Concepts, Springer, 2011.

[368] Z.Q. Liu, R. Li, G. Liu, K.K. Song, S. Pauly, T. Zhang, J. Eckert, AIP Advances, 2 (2012) 032176.

[369] Y.J. Kim, R. Busch, W.L. Johnson, A.J. Rulison, W.K. Rhim, Applied Physics Letters, 65 (1994) 2136.

[370] Z. Lin, W. Youshi, B. Xiufang, W. Si, L. Hui, Journal of Materials Science Letters, 18 (1999) 1977.

[371] V. Manov, P. Popel, E. Brook-Levinson, V. Molokanov, M. Calvo-Dahlborg, U. Dahlborg, V. Sidorov, L. Son, Y. Tarakanov, Materials Science and Engineering: A, 304-306 (2001) 54.

[372] S. Mukherjee, Z. Zhou, J. Schroers, W.L. Johnson, W.K. Rhim, Applied Physics Letters, 84 (2004) 5010.

[373] J. Schroers, W.L. Johnson, Journal of Applied Physics, 88 (2000) 44.

[374] A. Gebert, J. Eckert, L. Schultz, Acta Materialia, 46 (1998) 5475.

[375] L.Q. Xing, D.M. Herlach, Journal of Materials Science, 34 (1999) 3795.

[376] J. Schroers, W.L. Johnson, R. Busch, Applied Physics Letters, 76 (2000) 2343.

[377] Z.Q. Liu, R. Li, H. Wang, T. Zhang, Journal of Alloys and Compounds, 509 (2011) 5033.

[378] H. Fredriksson, U. ÅkerlindUlla, Solidification and Crystallization Processing in Metals and Alloys, John Wiley and Sons, Ltd, United Kingdom, 2012.

[379] L. Reissig, U. Czubayko, N. Wanderka, R. Völkl, U. Glatzel, Materials Characterization, 55 (2005) 153.

[380] H. Biloni, W.J. Boettinger, in: R.W. Cahn, P. Haasen (Eds.), Physical Metallurgy, Elsevier, Amsterdam, 1996, pp. 669-842.

[381] Z.L. Lin, J.M. Zhang, Y. Zhang, V.C. Ji, Pramana-journal of Physics, 76 (2011) 127.

[382] X.H. Lin, W.L. Johnson, Journal of Applied Physics, 78 (1995) 6514.

[383] H. Choi-Yim, R.D. Conner, F. Szuecs, W.L. Johnson, Scripta Materialia, 45 (2001) 1039.

[384] R.D. Conner, H. Choi-Yim, W.L. Johnson, Journal of Materials Research, 14 (1999) 3292.

[385] R.D. Conner, R.B. Dandliker, V. Scruggs, W.L. Johnson, International Journal of Impact Engineering, 24 (2000) 435.

[386] J. Eckert, A. Kubler, L. Schultz, Journal of Applied Physics, 85 (1999) 7112.

[387] H. Li, G. Subhash, L.J. Kecskes, R.J. Dowding, Materials Science and Engineering: A, 403 (2005) 134.

[388] J. Li, L. Wang, H. Zhang, Z. Hu, H. Cai, Materials Letters, 61 (2007) 2217.

[389] R.T. Ott, C. Fan, J. Li, T.C. Hufnagel, Journal of Non-Crystalline Solids, 317 (2003) 158.

[390] K.Q. Qiu, A.M. Wang, H.F. Zhang, B.Z. Ding, Z.Q. Hu, Intermetallics, 10 (2002) 1283.

[391] T.B. Massalski, H. Okamoto, P.R. Subramaniam, L. Kacprzak, Binary Alloy Phase Diagrams, 2nd ed., ASM International, Ohio,1990.

[392] F.R. De Boer, R. Room, W.C.M. Mattens, A.R. Miedema, A.K. Niessen, Cohesion in Metals, North-Holland publishing, Amsterdam, 1989.

[393] K. F. Kelton, A.L. Greer, Nucleation in Condensed Matter, Elsevier, Amsterdam, 2010.

[394] L. Gránásy, T. Pusztai, D. Saylor, J.A. Warren, Physical Review Letters, 98 (2007) 035703.

[395] K. Song, X. Bian, J. Guo, X. Li, M. Xie, C. Dong, Journal of Alloys and Compounds, 465 (2008) L7.

[396] K.K. Song, S. Pauly, Y. Zhang, B.A. Sun, J. He, G.Z. Ma, U. Kühn, J. Eckert, Materials Science and Engineering: A, 559 (2013) 711.

[397] K. Lu, J.T. Wang, Journal of Non-Crystalline Solids, 117-118, Part 2 (1990) 716.

[398] M.H. Bhat, V. Molinero, E. Soignard, V.C. Solomon, S. Sastry, J.L. Yarger, C.A. Angell, Nature, 448 (2007) 787.

[399] W.Z. Chen, P.L. Ryder, Materials Science and Engineering: B, 34 (1995) 204.

[400] Z. Evenson, R. Busch, Acta Materialia, 59 (2011) 4404.

[401] W.L. Johnson, G. Kaltenboeck, M.D. Demetriou, J.P. Schramm, X. Liu, K. Samwer, C.P. Kim, D.C. Hofmann, Science, 332 (2011) 828.

[402] X. Liu, M.D. Demetriou, G. Kaltenboeck, J.P. Schramm, G.R. Garrett, W.L. Johnson, Acta Materialia 61 (2013) 3060

[403] www.pascaltechnologies.com/category.cfm?GroupID=24&CategoryID=211.

[404] H.E. Kissinger, Analytical Chemistry, 29 (1957) 1702.

[405] S.H. Zhou, R.E. Napolitano, Scripta Materialia, 59 (2008) 1143.

[406] S. Pauly, G. Liu, G. Wang, J. Das, K.B. Kim, U. Kühn, D.H. Kim, J. Eckert, Applied Physics Letters, 95 (2009) 101906.

[407] T. Ezaz, H. Sehitoglu, H.J. Maier, Acta Materialia, 59 (2011) 5893.

[408] T. Ezaz, H. Sehitoglu, H.J. Maier, Acta Materialia, 60 (2012) 339.

[409] T. Ezaz, J. Wang, H. Sehitoglu, H.J. Maier, Acta Materialia, 61 (2013) 67.

[410] K. Gall, H. Sehitoglu, Y.I. Chumlyakov, I.V. Kireeva, H.J. Maier, J Eng Mater-T Asme, 121 (1999) 19.

[411] X.H. Chen, L. Lu, Scripta Materialia, 57 (2007) 133.

[412] M. Chen, A. Inoue, W. Zhang, T. Sakurai, Physical Review Letters, 96 (2006) 245502.

[413] A. Ibarra, D. Caillard, J. San Juan, M.L. No, Applied Physics Letters, 90 (2007) 101907.

[414] H. Sehitoglu, I. Karaman, R. Anderson, X. Zhang, K. Gall, H.J. Maier, Y. Chumlyakov, Acta Materialia, 48 (2000) 3311.

[415] L. Bataillard, J.E. Bidaux, R. Gotthard, Philosophical Magazine A, 78 (1998) 327.

[416] Y. Liu, Z.L. Xie, Acta Materialia, 51 (2003) 5529.

[417] Y. Liu, Z. Xie, J. Van Humbeeck, L. Delaey, Acta Materialia, 46 (1998) 4325.

[418] K. Otsuka, X.B. Ren, Intermetallics, 7 (1999) 511.

[419] M.L. Young, M.F.X. Wagner, J. Frenzel, W.W. Schmahl, G. Eggeler, Acta Materialia, 58 (2010) 2344.

[420] R.F. Hamilton, H. Sehitoglu, Y. Chumlyakov, H.J. Maier, Acta Materialia, 52 (2004) 3383.

[421] J. Wang, N. Li, O. Anderoglu, X. Zhang, A. Misra, J.Y. Huang, J.P. Hirth, Acta Materialia, 58 (2010) 2262.

[422] Z.F. Zhang, J. Eckert, L. Schultz, Acta Materialia, 51 (2003) 1167.

[423] J.Y. Koo, M.J. Young, G. Thomas, Metallurgical Transactions A, 11 (1980) 852.

[424] S.H. Xia, J.T. Wang, International Journal of Plasticity, 26 (2010) 1442.

[425] X.L. Fu, Y. Li, C.A. Schuh, Scripta Materialia, 56 (2007) 617.

[426] C.C. Yuan, J. Ma, X.K. Xi, Materials Science and Engineering: A, 532 (2012) 430.

[427] U. Ramamurty, S. Jana, Y. Kawamura, K. Chattopadhyay, Acta Materialia, 53 (2005) 705.

[428] Q.P. Cao, J.F. Li, Y.H. Zhou, J.Z. Jiang, Scripta Materialia, 59 (2008) 673.

[429] K.A. Gschneidner, M. Ji, C.Z. Wang, K.M. Ho, A.M. Russell, Y. Mudryk, A.T. Becker, J.L. Larson, Acta Materialia, 57 (2009) 5876.

[430] V.V. Nemoshkalenko, A.V. Zhalko-Titarenko, Y.N. Koval, Y.V. Kudryavtsev, E.V.G. EV, Metallofizika 15 (1993) 18.

[431] S.W. Kang, Y.H. Lee, Y.M. Lim, J.M. Nam, T.H. Nam, Y.W. Kim, Scripta Materialia, 59 (2008) 1186.

[432] L. Chen, F.X. Hu, J. Wang, J.L. Zhao, J.R. Sun, B.G. Shen, J.H. Yin, L.Q. Pan, Journal of Physics D: Applied Physics, 44 (2011) 085002.

[433] M. Grujicic, P. Dang, Materials Science and Engineering: A, 201 (1995) 194.

[434] M. Ahlers, Materials Science and Engineering: A, 481-482 (2008) 500.

[435] K. Seki, H. Kura, T. Sato, T. Taniyama, Journal of Applied Physics, 103 (2008) 063910.

[436] C. Jiang, G. Feng, S. Gong, H. Xu, Materials Science and Engineering: A, 342 (2003) 231.

[437] K. Shimizu, Materials Transactions, 43 (2002) 2050.

[438] A. Chakrabarti, C. Biswas, S. Banik, R.S. Dhaka, A.K. Shukla, S.R. Barman, Physical Review B, 72 (2005) 073103.

[439] S. Rubini, C. Dimitropoulos, S. Aldrovandi, F. Borsa, D.R. Torgeson, J. Ziolo, Physical Review B, 46 (1992) 10563.

[440] D. Gignoux, D.Schmitt, in: Jr. K.A. Gschneidner, L. Eyring (Eds.), Handbook on the Physics and Chemistry of Rare Earths, Elsevier, Amsterdam, 1995, pp. 297.

[441] P. Blaha, K.H. Schwarz, G. Madsen, D. Kvasnicka, and J. Luitz., WIEN2k. An Augmented Plane Wave plus Local Orbitals Program for Calculating Crystal Properties, TU Wien, Austria, 2001.

[442] J.P. Perdew, K. Burke, M. Ernzerhof, Physical Review Letters, 77 (1996) 3865.

[443] J.W. Seo, D. Schryvers, Acta Materialia, 46 (1998) 1177.

[444] G. Ghosh, Acta Materialia, 55 (2007) 3347.

[445] A.V. Zhalko-Titarenko, M.L. Yevlashina, V.N. Antonov, B.Y. Yavorskii, Y.N. Koval, G.S. Firstov, Physica Status Solidi (b), 184 (1994) 121.

[446] G.S. Firstov, A.N. Timoshevskii, Y.N. Koval, S. Kalkuta, J. Van Humbeeck, Esomat 2009, DOI: http://dx.doi.org/10.1051/esomat/200902008.

[447] G.S. Firstov, J. Van Humbeeck, Y.N. Koval, Journal de Physique IV, 11 (2001) 481.

[448] H. Okamoto, Journal of Phase Equilibria, 23 (2002) 549.

[449] www.springermaterials.com/docs/pdf/978-3-540-47004-5_37.html?queryterms=%22cu-ti-zr%22.

[450] Y.K. Kovneristyi, A.G. Pashkovskaya, Bulk Amorphization of Alloys in the Intermetallic-Containing System Ti-Cu-Zr: Amorphous Glassy Metallic Materials, Baikov Inst. Metallurgy, Ros. Akad. Nauk, 1992, pp. 153-157.

[451] V.N. Chebotnikov, V.V. Molokanov, Inorganic Materials, 26 (1990) 808.

[452] G. Jakob, T. Eichhorn, M. Kallmayer, H.J. Elmers, Physical Review B, 76 (2007) 174407.

[453] X. Jin, M. Marioni, D. Bono, S.M. Allen, R.C. O'Handley, T.Y. Hsu, Journal of Applied Physics, 91 (2002) 8222.

[454] N. Lanska, O. Soderberg, A. Sozinov, Y. Ge, K. Ullakko, V.K. Lindroos, Journal of Applied Physics, 95 (2004) 8074.

[455] Y. Wu, D.Q. Zhou, W.L. Song, H. Wang, Z.Y. Zhang, D. Ma, X.L. Wang, Z.P. Lu, Physical Review Letters, 109 (2012) 245506.

[456] W.D. Callister, Materials Science and Engineering: An Introduction, John Wiley and Sons, Asia, 2007.

[457] K. Parlinski, M. Parlinska-Wojtan, Physical Review B, 66 (2002) 064307.

[458] X. Ren, N. Miura, J. Zhang, K. Otsuka, K. Tanaka, M. Koiwa, T. Suzuki, Y.I. Chumlyakov, M. Asai, Materials Science and Engineering: A, 312 (2001) 196.

[459] L. Mañosa, M. Jurado, A. Planes, J. Zarestky, T. Lograsso, C. Stassis, Physical Review B, 49 (1994) 9969.

[460] L. Mañosa, J. Zarestky, T. Lograsso, D.W. Delaney, C. Stassis, Physical Review B, 48 (1993) 15708.

[461] J.J. Gilman, R.W. Cumberland, R.B. Kaner, International Journal of Refractory Metals and Hard Materials, 24 (2006) 1.

[462] J.J. Gilman, Electronic Basis of the Strength of Materials, Cambridge University Press, Cambridge, United Kingdom, 2003.

[463] K. Otsuka, X. Ren, Progress in Materials Science, 50 (2005) 511.

[464] Y. Qi, R.K. Mishra, Physical Review B, 75 (2007) 224105.

[465] S. Ogata, J. Li, S. Yip, Science, 298 (2002) 807.

[466] A. Frøseth, H. Van Swygenhoven, P.M. Derlet, Acta Materialia, 52 (2004) 2259.

[467] N. Hatcher, O.Y. Kontsevoi, A.J. Freeman, Physical Review B, 80 (2009) 144203.

[468] W.D. Callister, Jr.David, G. Rethwisch, Materials Science and Engineering: An Introduction, John Wiley and Sons, 2009.

[469] S.R. Barman, S. Banik, A. Chakrabarti, Physical Review B, 72 (2005) 184410.

[470] G.V.K. Jumov, Metallurgical Transactions A, 7 (1976) 999.

[471] K.M. Knowles, D.A. Smith, Acta Metallurgica, 29 (1981) 101.

[472] A.T. Zayak, P. Entel, J. Enkovaara, A. Ayuela, R.M. Nieminen, Journal of Physics: Condensed Matter, 15 (2003) 159.

[473] J. Hufenbach, L. Giebeler, M. Hoffmann, S. Kohlar, U. Kühn, T. Gemming, S. Oswald, B. Eigenmann, J. Eckert, Acta Materialia, 60 (2012) 4468.

[474] G. B. Olson, and M. Cohen, Journal de Physique 43 (1982) C4-75.

[475] T. Waitz, H.P. Karnthaler, Acta Materialia, 52 (2004) 5461.

[476] G.P. Cheng, Z.L. Xie, Y. Liu, Journal of Alloys and Compounds, 415 (2006) 182.

[477] D. Korn, H. Pfeifle, G. Zibold, Zeitschrift für Physik, 270 (1974) 195.

[478] J. Willer, G. Fritsch, W. Rausch, E. Lüscher, Zeitschrift für Physik B: Condensed Matter, 50 (1983) 39.

[479] A.J. Kailath, K. Dutta, T.C. Alex, A. Mitra, Journal of Materials Science & Technology, 27 (2011) 275.

[480] J.B. Leblond, J. Devaux, Acta Metallurgica, 32 (1984) 137.

[481] F.J. Gil, J.M. Manero, J.A. Planell, Journal of Materials Science, 30 (1995) 2526.

[482] R. Santamarta, D. Schryvers, Scripta Materialia, 50 (2004) 1423.

[483] T. Waitz, D. Spišák, J. Hafner, H.P. Karnthaler, EPL (Europhysics Letters), 71 (2005) 98.

[484] N. Resnina, S. Belyaev, A. Shelyakov, European Physical Journal Special Topics, 158 (2008) 21.

[485] W.J. He, G.H. Min, Y.S. Yin, O. Tolochko, Transactions of Nonferrous Metals Society of China, 19 (2009) 1464.

[486] J.J. Gilman, Journal of Applied Physics, 46 (1975) 1625.

[487] G. Wang, K.C. Chan, L. Xia, P. Yu, J. Shen, W.H. Wang, Acta Materialia, 57 (2009) 6146.

[488] Y.F. Sun, B.C. Wei, Y.R. Wang, W.H. Li, C.H. Shek, Journal of Materials Research, 20 (2005) 2386.

[489] B.A. Sun, H.B. Yu, W. Jiao, H.Y. Bai, D.Q. Zhao, W.H. Wang, Physical Review Letters, 105 (2010) 035501.

[490] M.A. Lebyodkin, Y. Brechet, Y. Estrin, L.P. Kubin, Physical Review Letters, 74 (1995) 4758.

[491] H.M. Chen, C.J. Lee, J.C. Huang, T.H. Li, J.S.C. Jang, Intermetallics, 18 (2010) 1240.

[492] H.M. Chen, J.C. Huang, S.X. Song, T.G. Nieh, J.S.C. Jang, Applied Physics Letters, 94 (2009) 141914.

[493] H.S. Chen, Scripta Metallurgica et Materialia, 7 (1973) 931.

[494] T. Mukai, T.G. Nieh, Y. Kawamura, A. Inoue, K. Higashi, Intermetallics, 10 (2002) 1071.

[495] J.J. Gilman, Dislocation in solids, Amsterdam, North-Holland, 1983, pp. 185.

[496] M.C. Miguel, A. Vespignani, S. Zapperi, J. Weiss, J.R. Grasso, Nature, 410 (2011) 667.

[497] A. Portevin, F.L. Chatelier, Comptes Rendus de l'Académie des Sciences, 176 (1923) 507.

[498] T. Richeton, J. Weiss, F. Louchet, Nature Materials, 4 (2005) 465.

[499] F.F. Csikor, C. Motz, D. Weygand, M. Zaiser, S. Zapperi, Science, 318 (2007) 251.

[500] S.X. Song, T.G. Nieh, Intermetallics, 17 (2009) 762.

[501] S.X. Song, T.G. Nieh, Intermetallics, 19 (2011) 1968.

[502] K. Chihab, Y. Estrin, L.P. Kubin, J. Vergnol, Scripta Metallurgica, 21 (1987) 203.

[503] G. Ananthakrishna, S.J. Noronha, C. Fressengeas, L.P. Kubin, Physical Review E, 60 (1999) 5455.

[504] J. Tan, Y. Zhang, B.A. Sun, M. Stoica, C.J. Li, K.K. Song, U. Kühn, F.S. Pan, J. Eckert, Applied Physics Letters, 98 (2011) 151906.

[505] J. Das, S. Pauly, C. Duhamel, B.C. Wei, J. Eckert, Journal of Materials Research, 22 (2007) 326.

[506] C. Sanborn, K.F. Ludwig, M.C. Rogers, M. Sutton, Physical Review Letters, 107 (2011) 015702.

[507] R. Ahluwalia, G. Ananthakrishna, Physical Review Letters, 86 (2001) 4076.

[508] L. Carrillo, J. Ortín, Physical Review B, 56 (1997) 11508.

[509] B. Cerruti, E. Vives, Physical Review E, 80 (2009) 011105.

[510] U. Chandni, A. Ghosh, H.S. Vijaya, S. Mohan, Physical Review Letters, 102 (2009) 025701.

[511] M.C. Gallardo, J. Manchado, F.J. Romero, J. del Cerro, E.K.H. Salje, A. Planes, E. Vives, R. Romero, M. Stipcich, Physical Review B, 81 (2010) 174102.

[512] R. Niemann, J. Baró, O. Heczko, L. Schultz, S. Fähler, E. Vives, L. Mañosa, A. Planes, Physical Review B, 86 (2012) 214101.

[513] F.J. Pérez-Reche, E. Vives, L. Mañosa, A. Planes, Physical Review Letters, 87 (2001) 195701.

[514] F.J. Pérez-Reche, M. Stipcich, E. Vives, L. Mañosa, A. Planes, M. Morin, Physical Review B, 69 (2004) 064101.

[515] I. Ràfols, E. Vives, Physical Review B, 52 (1995) 12651.

[516] E. Vives, J. Ortín, L. Mañosa, I. Ràfols, R. Pérez-Magrané, A. Planes, Physical Review Letters, 72 (1994) 1694.

[517] E. Vives, A. Planes, Physical Review B, 50 (1994) 3839.

[518] E. Vives, I. Ràfols, L. Mañosa, J. Ortín, A. Planes, Physical Review B, 52 (1995) 12644.

[519] E. Vives, D. Soto-Parra, L. Mañosa, R. Romero, A. Planes, Physical Review B, 80 (2009) 180101.

[520] A.R. Abate, D.J. Durian, Chaos: An Interdisciplinary Journal of Nonlinear Science, 17 (2007) 041107.

[521] P. Cizeau, S. Zapperi, G. Durin, H.E. Stanley, Physical Review Letters, 79 (1997) 4669.

[522] M.D. Ediger, Annual Review of Physical Chemistry, 51 (2000) 99.

[523] H. Guo, G. Bourret, M.K. Corbierre, S. Rucareanu, R.B. Lennox, K. Laaziri, L. Piche, M. Sutton, J.L. Harden, R.L. Leheny, Physical Review Letters, 102 (2009) 075702.

[524] D.H. Kim, S.B. Choe, S.C. Shin, Physical Review Letters, 90 (2003) 087203.

[525] R. Maaß, D. Klaumünzer, J.F. Löffler, Acta Materialia, 59 (2011) 3205.

[526] Z.Q. Liu, R. Li, G. Wang, S. Wu, X. Lu, T. Zhang, Acta Materialia, 59 (2011) 7416.

[527] X.F. Pan, H. Zhang, Z.F. Zhang, M. Stoica, G. He, J. Eckert, Journal of Materials Research, 20 (2005) 2632.

[528] J.S. Langer, Physical Review E, 70 (2004) 041502.

[529] C.N.R. Rao, K.J. Rao, Phase transitions in solids: An Approach to the Study of the Chemical and Physics of Solids, McGraw-Hill, New York, 1978.

[530] B. Yang, C.T. Liu, T.G. Nieh, M.L. Morrison, P.K. Liaw, R.A. Buchanan, Journal of Materials Research, 21 (2006) 915.

[531] J. J. Lewandowski, A.L. Greer, Nature Materials, 5 (2006) 15.

[532] K. Georgarakis, M. Aljerf, Y. Li, A. LeMoulec, F. Charlot, A.R. Yavari, K. Chornokhvostenko, E. Tabachnikova, G.A. Evangelakis, D.B. Miracle, A.L. Greer, T. Zhang, Applied Physics Letters, 93 (2008) 031907.

[533] F.H. Dalla Torre, A. Dubach, J. Schällibaum, J.F. Löffler, Acta Materialia, 56 (2008) 4635.

[534] Q.S. Zhang, W. Zhang, G.Q. Xie, A. Inoue, Materials Transactions, 48 (2007) 2542.

[535] M. Ahlers, R. Pascual, R. Rapacioli, W. Arneodo, Materials Science and Engineering, 27 (1977) 49.

[536] H.L. Duan, J. Wang, Z.P. Huang, Z.Y. Luo, Mechanics of Materials, 37 (2005) 723.

[537] A.G. Evans, A.H. Heuer, Journal of the American Ceramic Society, 63 (1980) 241.

[538] A.H. Heuer, M. Rühle, Acta Metallurgica, 33 (1985) 2101.

[539] Z.K. Lu, G.J. Weng, Journal of the Mechanics and Physics of Solids, 45 (1997) 1905.

[540] J.H. Serebrinsky, Solid-State Electronics, 13 (1970) 1435.

Schriftliche Erklärung gemäß Promotionsordnung Fakultät Maschinenwesen/ TU Dresden

Hiermit versichere ich, dass ich die vorliegende Arbeit ohne unzulässige Hilfe Dritter und ohne Benutzung anderer als der angegebenen Hilfsmittel angefertigt habe; die aus fremden Quellen direkt oder indirekt übernommenen Gedanken sind als solche kenntlich gemacht.

Weitere Personen waren an der geistigen Herstellung der vorliegenden Arbeit nicht beteiligt. Insbesondere habe ich nicht die Hilfe eines kommerziellen Promotionsberaters in Anspruch genommen. Dritte haben von mir keine geldwerten Leistungen für Arbeiten erhalten, die in Zusammenhang mit dem Inhalt der vorgelegten Dissertation stehen.

Die Arbeit wurde bisher weder im Inland noch im Ausland in gleicher oder ähnlicher Form einer anderen Prüfungsbehörde vorgelegt und ist auch noch nicht veröffentlicht worden.

Diese Promotionsordnung wird anerkannt.

Kaikai Song
Dresden, 25.11.2013